

**Coarse-Grained Discretized Description of  
Magneto-Responsive Elastomers:  
Mesoscopic Modeling as a Bridge Pillar  
between Microscopic Simulations  
and Macroscopic Behavior**

Inaugural dissertation

for the attainment of the title of doctor  
in the Faculty of Mathematics and Natural Sciences  
at the Heinrich Heine University Düsseldorf

presented by

**Giorgio Pessot**  
from Pordenone

Düsseldorf, December 2017

from the Institute for Theoretical Physics II: Soft Matter  
at the Heinrich Heine University Düsseldorf

Published by permission of the  
Faculty of Mathematics and Natural Sciences at  
Heinrich Heine University Düsseldorf

Supervisor: Priv.-Doz. Dr. Andreas M. Menzel

Co-supervisor: Prof. Dr. Hartmut Löwen

Date of the oral examination: 21.12.2017

# Abstract

Ferrogels and magnetoelastomers are hybrid materials that combine the reversible deformability typical of polymeric elastomers with the responsiveness in the presence of external magnetic fields characteristic of ferrofluids. They are often realized by embedding mesoscopic (nano- to micrometer sized) ferro- or paramagnetic particles into a crosslinked polymeric network.

The described procedure results in a “magnetomechanically” coupled material with properties—e.g. strain, viscosity, or elastic moduli—controllable via magnetic interactions. This is a consequence of the particles adjusting their positions and orientations due to: i) field–particle interactions leading to rotations, ii) forces arising from magnetic field gradients, or iii) magnetic interactions between the particles.

This dissertation is structured by two different measures. On the one hand, we start from the coarse-grained microscopic scale and work ourselves via mesoscopic modeling up to the macroscopic level. On the other hand, beginning with basic reduced minimal models, we build our path towards increasing complexity describing the properties of realistic many-particles experimental sample systems.

First, we “coarse-grain” the fast-evolving degrees of freedom of a single polymer chain connecting two magnetic particles to obtain effective pair interactions between the particles. This represents a first basis step of our scale-bridging description.

Then, we increase the degree of complexity and study an exemplary problem of several magnetic particles aligned into a chain-like structure and embedded in a soft elastic gel. As has been demonstrated experimentally, such chains buckle in the presence of a transversal magnetic field. We derive a coarse-grained, phenomenological description of this effect. Via a variational method, we reproduce the buckled chains morphologies.

Finally, arrangements of many particles linked by linear springs to elastic networks are studied to connect the particle-resolved description to the macroscopic scale. As a first approximation, elastic and magnetic effects are represented, respectively, by harmonic springs connecting the particles and dipole moments assigned to each of them. These approximations for the elastic and magnetic components correspond to the linear elasticity regime and to low-volume fractions of the embedded particles, respectively.

In the simplified case of 2D lattices, the central role played by nearest neighbors is demonstrated. Furthermore, we remark the importance of non-affine particle displacements especially in disordered or finite-sized distributions. Moving on to 3D arrangements of dipolar particles, we explicitly connect the normal modes of deformation of the system to the overall elastic moduli. Particularly, we calculate the frequency-dependent elastic moduli as a function of the magnetic interactions between the particles.

As a final step, the particle positions and volumes are taken as input from micrometer-resolved experiments employing X-ray tomography. We set a fine network of springs to represent the elastic matrix. The magnetic particles are attached to a small fraction of the network nodes while other nodes serve to smoothen the elastic response of the discretized network. Here, we investigate the effect of varying magnetization, frequency, or volume fraction of magnetic particles on the overall strain behavior and elastic moduli.

---

In summary, our discretized mesoscopic models serve to study the rearrangement of magnetic particles in elastic environments as a function of the magnetic interactions between them. Our simplified dipole–spring models are linked to both the micro- and macroscale. On the latter level, they serve to analyze the adjustable static and dynamic elastic moduli of magnetic gels and elastomers tuned by magnetic interactions also for particle arrangements in real experimental samples.

# Zusammenfassung

Ferrogele und magnetorheologische Elastomere sind Hybridmaterialien, welche die typischen Eigenschaften zweier komplexer Materialklassen miteinander verbinden. Einerseits sind dies Elastomere, die sich durch ihre häufig sehr ausgeprägte reversible Deformierbarkeit auszeichnen, andererseits Ferrofluide mit ihrer ausgeprägten Adressierbarkeit durch externe Magnetfelder. Typischerweise werden derartige magnetische Gele und Elastomere durch Einbetten mesoskopischer (nano- bis mikrometergroßer) magnetischer Partikel in ein chemisch vernetztes Polymernetzwerk hergestellt.

Dieses Verfahren führt zu einem „magnetomechanisch“ gekoppelten Material, dessen Eigenschaften durch äußere Magnetfelder über magnetische Wechselwirkungen reversibel gesteuert werden können. Beispiele für solche einstellbaren Eigenschaften sind die Dehnung, Viskosität oder Elastizitätsmoduln. Dem liegt zugrunde, dass die Partikel ihre Positionen und Orientierungen durch i) Orientierungswechselwirkungen mit einem äußeren Magnetfeld, ii) Kräfte, die durch Magnetfeldgradienten entstehen, oder iii) magnetische Wechselwirkungen zwischen den Partikeln ändern.

Die Gliederung dieser Dissertation zur Beschreibung solcher Effekte folgt zwei verschiedenen Schemata. Einerseits gehen wir von einer „vergrößerten“ mikroskopischen Skala aus und arbeiten uns über die mesoskopische Modellierung bis zur makroskopischen Ebene vor. Andererseits entwickeln wir die Komplexität der Beschreibung, indem wir zunächst ein einfaches Zweiteilchensystem untersuchen und schließlich die Eigenschaften realistischer experimenteller Vielteilchensysteme beschreiben.

Auf der Mikroebene verfolgen wir dabei zunächst die sich schnell entwickelnden Freiheitsgrade einer einzelnen Polymerkette, die zwei magnetische Partikel verbindet. Aus der resultierenden Statistik leiten wir auf der Mesoskala effektive Paarwechselwirkungen zwischen den beiden Partikeln her. Dies ist ein erster Schritt zu unserer skalenübergreifenden Beschreibung.

Im nächsten Schritt untersuchen wir auf der Mesoskala kettenartige Strukturen, die jeweils aus mehreren solcher magnetischer Teilchen zusammengesetzt und in ein weiches elastisches Gel eingebettet sind. Wie experimentell gezeigt wurde, krümmen sich solche Ketten in Gegenwart eines transversalen Magnetfeldes in eine oszillatorische Form. Unter Entwicklung einer phänomenologischen Beschreibung und mit Hilfe von Variationsrechnung reproduzieren wir die Morphologien der gebogenen Ketten.

Schließlich werden Anordnungen vieler Teilchen, die durch elastische Federn zu elastischen Netzwerken verbunden sind, untersucht. In erster Näherung verwenden wir harmonische Federn und modellieren die magnetischen Beiträge der Partikel durch Dipolmomente. Dadurch können Deformationen im Rahmen linearer Elastizität in Systemen mit ausreichendem Abstand zwischen den Partikeln untersucht werden. Die Ergebnisse dieser mesoskopischen, partikel aufgelösten Vielteilchenbeschreibung dienen zur Charakterisierung von makroskopischen Eigenschaften als Funktion der mesoskopischen Struktur.

Im vereinfachten Fall zweidimensionaler Grundzustandspartikelanordnungen auf regelmäßigen Gitterstrukturen tritt die zentrale Bedeutung der magnetischen Wechselwirkung mit den nächsten Nachbarn für das makroskopische Gesamtverhalten hervor.

---

Darüber hinaus weisen wir auf die Bedeutung nicht-affiner Partikelverschiebungen unter aufgeprägter Deformation hin, insbesondere bei ungeordneten oder räumlich stark begrenzten Verteilungen. Für dreidimensionale Partikelanordnungen verbinden wir explizit das Spektrum der Deformationsnormalmoden mit den Elastizitätsmoduln, welche charakteristische aufgeprägte Deformationen des gesamten Systems beschreiben. Insbesondere berechnen wir die frequenzabhängigen dynamischen Elastizitätsmoduln als Funktion der magnetischen Wechselwirkungen zwischen den Teilchen.

Schließlich analysieren wir das Verhalten von Systemen, welche wir aus experimentell durch mikrometere aufgelöste Röntgentomographie ermittelten Partikelpositionen und -volumina konstruieren. Hierzu ist eine feinere Struktur des elastischen Federnetzwerks notwendig. Die magnetischen Partikel sind an einen Bruchteil der Knotenpunkte des Netzwerks gebunden, während zusätzliche Knoten eingefügt werden, um eine homogene Elastizität der umgebenden elastischen Matrix abzubilden. Wir bestimmen die Auswirkungen variierender Magnetisierung, Frequenz und Volumenanteile magnetischer Partikel auf die Gesamtdehnung unter Magnetisierung und auf die dynamischen Elastizitätsmoduln.

Zusammengefasst dienen unsere diskretisierten mesoskopischen Modelle dazu, die Bedeutung der mesoskopischen Partikelanordnung in magnetischen Gelen und Elastomeren für deren Eigenschaften als Funktion der magnetischen Wechselwirkungen zu untersuchen. Dabei verknüpfen unsere vereinfachten Dipolfedermodelle Charakteristika der Mikro- mit der Mesoskala und weiter die mesoskopischen Eigenschaften mit der Makroskala. Im letzteren Fall dienen sie insbesondere dazu, die reversibel anpassbaren Auswirkungen der durch äußere Magnetfelder induzierten magnetischen Wechselwirkungen auf die statischen und dynamischen Elastizitätsmoduln zu analysieren. Dies gilt vor allem auch für mesoskopische Partikelanordnungen aus realen experimentellen Proben bei der Charakterisierung tatsächlicher Materialien.

# Affidavit

I declare under oath that I have compiled my dissertation independently and without any undue assistance by third parties under consideration of the “Principles for the Safeguarding of Good Scientific Practice at Heinrich Heine University Düsseldorf”.

Düsseldorf, January 10, 2018,

Giorgio Pessot

---

# Preface

This cumulative thesis incorporates and summarizes my PhD investigations at the *Institut für Theoretische Physik II: Weiche Materie, Heinrich-Heine-Universität Düsseldorf*. The work has been performed in cooperation with and under the supervision of Priv.-Doz. Dr. Andreas M. Menzel and Prof. Dr. Hartmut Löwen.

Many of the published works are the result of fruitful cooperations with members of the DFG SPP 1681 program, namely (listed by institution): D. Y. Borin, J. Nowak, M. Schümann, T. Gundermann, and S. Odenbach (*Technische Universität Dresden*); R. Weeber and C. Holm (*Universität Stuttgart*); S. Huang and G. K. Auernhammer (*Max Planck Institute for Polymer Research, Mainz*).

The references of the resulting publications are:

- Paper I  
G. Pessot, R. Weeber, C. Holm, H. Löwen, and A. M. Menzel, Towards a scale-bridging description of ferrogels and magnetic elastomers, *J. Phys.: Condens. Matter*, **32**, 325105 (2015).
- Paper II  
S. Huang, G. Pessot, P. Cremer, R. Weeber, C. Holm, J. Nowak, S. Odenbach, A. M. Menzel, and G. K. Auernhammer, Buckling of paramagnetic chains in soft gels, *Soft Matter*, **12**, 228 (2016).
- Paper III  
G. Pessot, P. Cremer, D. Y. Borin, S. Odenbach, H. Löwen, and A. M. Menzel, Structural control of elastic moduli in ferrogels and the importance of non-affine deformations, *J. Chem. Phys.*, **141**, 124904 (2014).
- Paper IV  
G. Pessot, H. Löwen, and A. M. Menzel, Dynamic elastic moduli in magnetic gels: Normal modes and linear response, *J. Chem. Phys.*, **145**, 104904 (2016).
- Paper V  
G. Pessot, M. Schümann, T. Gundermann, S. Odenbach, H. Löwen, and A. M. Menzel, Tunable dynamic moduli of magnetic elastomers: from X- $\mu$ CT characterization to mesoscopic modeling, *arXiv:1711.04165 [cond-mat.soft]* (Submitted to *Smart Mater. Struct.*).

A detailed statement on my contributions to each of these works can be found before each paper in chapter 2.

---

# Contents

<b>1</b>	<b>Introduction</b>	<b>1</b>
1.1	Soft Matter, Polymers, and Magnetoelastomers . . . . .	1
1.2	Magnetic Particles and their Interactions . . . . .	3
	1.2.1 Magnetism and Magnetic Particles . . . . .	3
	1.2.2 Magnetic Interactions . . . . .	5
1.3	Polymers and Elasticity . . . . .	6
	1.3.1 Coarse-Graining of Microscopic Simulations . . . . .	9
1.4	Buckling of Paramagnetic Chains of Particles . . . . .	13
1.5	Static Linear Elasticity . . . . .	17
	1.5.1 Homogeneous Isotropic Materials . . . . .	17
	1.5.2 Homogeneous Deformations . . . . .	19
	1.5.3 Elasticity and Compliance Tensors: Voigt Notation . . . . .	20
1.6	Viscoelasticity . . . . .	21
	1.6.1 Hookean and Dashpot Elements . . . . .	22
	1.6.2 Kelvin-Voigt Model . . . . .	22
1.7	Elasticity of Spring Lattices . . . . .	23
	1.7.1 Square and Rectangular Lattices . . . . .	25
	1.7.2 Cubic Lattice . . . . .	28
	1.7.3 Face-Centered-Cubic Lattice . . . . .	28
	1.7.4 Scaling of the Spring Constants . . . . .	29
1.8	Ferrogels and Magnetoelastomers . . . . .	30
	1.8.1 2D and 3D Field-Induced Deformation . . . . .	31
	1.8.2 Static Elastic Moduli . . . . .	34
	1.8.3 Dynamic Elastic Moduli . . . . .	37
<b>2</b>	<b>Publications</b>	<b>41</b>
Paper I	Towards a scale-bridging description of ferrogels and magnetic elastomers . . . . .	43
Paper II	Buckling of paramagnetic chains in soft gels . . . . .	61
Paper III	Structural control of elastic moduli in ferrogels and the importance of non-affine deformations . . . . .	93
Paper IV	Dynamic elastic moduli in magnetic gels: Normal modes and linear response . . . . .	105
Paper V	Tunable dynamic moduli of magnetic elastomers: from X- $\mu$ CT characterization to mesoscopic modeling . . . . .	129
<b>3</b>	<b>Conclusions</b>	<b>131</b>

*Contents*

---

# 1 Introduction

## 1.1 Soft Matter, Polymers, and Magnetoelastomers

Soft matter physics studies systems the building blocks of which are larger than atoms but smaller than macroscopic objects. In such cases and on those lengthscales usually quantum effects are small and the classical treatment suffices. However, and differently from the macroscopic level, other effects play a major role, e.g., thermal fluctuations, viscous friction, many-body effects, or hydrodynamic interactions. Exemplary cases of soft matter include colloids [1], liquid crystals, active systems [2], polymers [3], as well as biological systems like DNA or blood. The typical lengthscale in soft matter is commonly referred to as mesoscopic, coming from the ancient Greek  $\mu\acute{\epsilon}\sigma\omega\varsigma$ , “middle”, because it is intermediate between the *micro*- and the *macroscopic*.

One of the most prominent sub-branches of soft matter is the study of polymeric materials. Polymers are macromolecules, i.e., very large molecules, composed of a sequence of repeating subparts named monomers [3]. Polymers exist in nature, biological examples being nucleic acids and proteins, but artificial ones are very common as well, e.g., plastics, rubbers and synthetic fibers like nylon. Perhaps the most interesting feature of polymers is that their elastic behavior follows from entropic effects, rather than from strong chemical bonding or ordering as in “hard” condensed matter. Because of their size, the sections of the polymer are strongly subject to thermal fluctuations. Thus, polymer chains usually assume looped, curled up configurations favored by higher entropy and seldom evolve into extended shapes.

The chains can be reversibly stretched, lowering their entropy, and later return to a coiled state of higher entropy. This is reflected by a change in free energy that penalizes deviations from the curled states. Thus, elastic behavior derives from the entropic forces that oppose stretching. Nevertheless, since the energetic intensity of entropic effects is of the order of  $\sim k_B T$ , polymeric materials are “soft” compared to “hard” condensed matters like crystalline materials. Such a difference is revealed by the typical orders of magnitudes of the elastic moduli:  $\lesssim 10^9$  Pa and  $\gtrsim 10^9$  Pa, respectively [4].

Interestingly, the elastic properties of polymers had been long known to the natives of central and south America, who used the secretions of the rubber tree to fabricate waterproof boots and shoes [5, 6]. The duration and resilience of natural rubber is, however, limited and especially at low temperatures becomes hard and brittle [7]. It is, in fact, a tangle of non-connected polymer chains, possibly swollen with water (a “noodle soup”, in the words of de Gennes [6]). Charles Goodyear made a breakthrough in 1839 by heating natural rubber with sulfur. He discovered that rather than melting, the rubber would become stiffer and tougher. In such a process, the polymer chains chemically link to each other (“crosslinking”) and the process is usually referred to as “polymerization”, “curing”, or “vulcanization”. After curing, the polymer chains are linked to each other at their crossing points, and compose an interconnected 3D network.

The polymer network or matrix then behaves like an elastic solid and resists compres-

sions or shape deformations. The elastic modulus, i.e., the stiffness of the material per unit volume, depends on the amount of crosslinking, quantified by the number of links per unit volume. Starting from the fluid phase, there is a minimum amount of links necessary to turn the fluid into a solid of nonvanishing long-time shear modulus. This corresponds to the amount of curing required to transition the polymer from a fluid to a solid phase and is usually indicated as “gelation” or “sol-gel” transition. Although the crosslinking can occur by many ways (e.g. high-temperature curing [8], irradiation with electrons [9], or the action of chemicals catalysts [10]), the phase transition is characterized by the elastic moduli (i.e., the second derivatives of the free energy density) switching from zero to a finite value.

On the one hand, “rubbers” and “elastomers” are polymer networks characterized by relatively large moduli (Young’s modulus  $E > 10^4$  MPa [10, 11]) and strong memory of their initial shape. On the other hand, the term “gel” typically indicates that the polymer network, or “matrix”, is swollen with a solvent, e.g., water (hydrogel) or oil. To this purpose, a viscous polymer solution can be cured up to the gelation transition to form a gel, or a “solid” crosslinked polymer can absorb a sufficient amount of solvent until it becomes a gel. In either case, the elastic moduli of gels are typically lower,  $E \sim 10^{-1} - 10^4$  Pa [12].

Since polymeric materials are extremely versatile and adaptive, they represent an ideal medium into which to embed other substances to obtain composite materials [13]. One benefit of these composite “smart polymers” [14] is the possibility to combine responses from different kinds of stimuli. For instance, dielectric elastomer composites [15–17] integrate the elasticity of rubbers with the response to electrical fields, leading to effects such as piezoelectricity or electrostriction [18] and applications ranging from soft actuators [19] to smart power generators [20]. Another example of hybrid materials are ferrofluids, combining the rheology of viscous fluids with the susceptibility to magnetic fields [21–27], resulting in many applications from sensors [28] to damping devices [29].

Ferrogels and magnetic elastomers combine the elastic, reversible deformability with the responsiveness to external magnetic fields [2, 30–33]. Similarly to the tunable viscosity [34, 35] in ferrofluids, magnetic fields affect the properties of the magneto-elastic composite. Such a feature, known as “magneto-mechanical” coupling [36–38], allows to control the material deformation [39–43] and stiffness [10, 11, 44–50], as well as vibration modes [51] or impedance [52].

This thesis is structured as follows. Section 1.2 reviews the kinds of magnetic particles typically employed in magnetic elastomers. Then, a short derivation of the dipole–dipole magnetic interaction is presented. After that, we introduce in section 1.3 the statistical description of polymer chains and the entropic origin of elasticity. In this context, our microscopic minimal approach to magnetic elastomers is summarized (Paper I). Then, as a first step in increasing complexity, in section 1.4 we investigate and model the exemplary case of buckling chains of paramagnetic particles in soft magnetic gels (Paper II). Furthermore, in section 1.5 the main notions of linear elasticity such as strain, stress, and elastic moduli are presented and then, in section 1.6, extended via basic viscoelastic

models to describe the time-dependent response to external stimuli. In section 1.7 we calculate the elastic moduli of some selected regular spring networks in 2- and 3D as a reference point for subsequent calculations. Moving on to presenting our investigation results, section 1.8 combines our investigated dipole–spring networks in two- and three-dimensions to describe deformations and changes in elastic moduli (Paper III and Paper IV). Moreover, the integration of experimental, particle-resolved data into mesoscopic simulations is outlined, together with the resulting magneto-mechanical effects (Paper V). Finally, chapter 2 includes our published papers before we summarize our findings and draw the final conclusions in chapter 3.

In the following we use the Latin alphabet  $i, j, k, l, \dots = 1, 2, 3, \dots$  to index the different particles or components, while the spatial degrees of freedom are labeled by Greek letters  $\alpha, \beta, \gamma, \dots = x, y, z$ . Furthermore, we denote vectors lying in 2- or 3D space by bold font, e.g.,  $\mathbf{r} = (r^x, r^y, r^z)$ . The bra-ket notation, instead, indicates a phase-space vector representing the positions of  $N$  three-dimensional points. Its  $D$  components are, e.g.,  $|\mathbf{r}\rangle = (r_1^x, r_1^y, r_1^z, r_2^x, r_2^y, \dots, r_N^y, r_N^z)$  with  $D = 3N$ . Finally, we denote tensors either by a double overline (e.g.,  $\overline{\overline{\Delta}}$ ) or, when possible, by the `\mathcal` uppercase font  $\mathcal{D}$  and their respective components by  $\Delta_{ij}^{\alpha\beta}$  and  $\mathcal{D}_{ij}^{\alpha\beta}$ .

## 1.2 Magnetic Particles and their Interactions

The crucial ingredient of magnetoelastic materials are the embedded magnetic or magnetizable particles. They are the origin of the responsiveness to external magnetic fields. In this section, we briefly review the properties of magnetic materials with particular emphasis on the ones typically employed in ferrogels. Finally, a short derivation of the often used dipole–dipole potential will be presented.

### 1.2.1 Magnetism and Magnetic Particles

Magnetic materials can be roughly divided into ferromagnetic and paramagnetic. Important parameters to distinguish them are the saturation magnetization  $M_s$ , the retentive (or remnant) magnetization  $M_r$ , the coercive field  $H_c$ , as well as the magnetic susceptibility and permeability  $\chi$  and  $\mu = \mu_0(1 + \chi)$ , respectively [53].

Macroscopic ferromagnetic materials are composed of multiple grains, each divided into several magnetized domains. Upon introduction of an external magnetic field  $H = |\mathbf{H}|$ , see Fig. 1.1 (a), the magnetization of the domains start to reorient along it, significantly increasing the overall magnetization of the material with initial permeability  $\mu_f$ . When all domains are oriented in the field direction, the magnetization  $\mathbf{M}$  reaches the saturation magnitude  $|\mathbf{M}| = M_s$ , after which it only increases proportionally to  $\sim \mu_0 H$ . If the external field is switched off, some of the magnetic domains will remain aligned, resulting into a the retentive magnetization  $M_r$ , see Fig.1.1 (b). To compensate for such residual magnetization, an external field must be applied in the opposite direc-

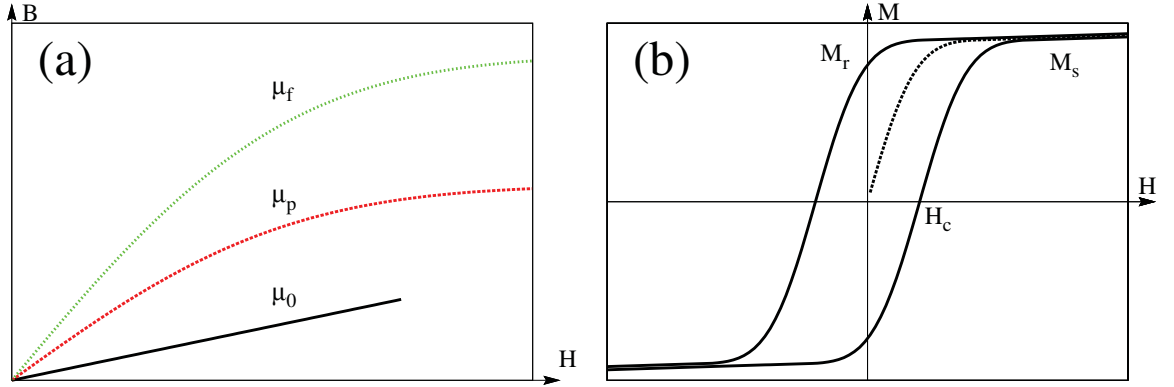


Figure 1.1: Sketch of magnetization curves for different magnetic materials. Panel (a) shows the qualitative initial  $B(H)$  behavior for reference vacuum ( $\mu_0$ ), paramagnetic ( $\mu_p$ ), and ferromagnetic  $\mu_f$  materials. Panel (b) illustrates a qualitative, simplified hysteresis curve  $M(H)$  of a ferromagnetic material. The dashed line represents the initial behavior depicted in panel (a). After the saturation magnetization  $M_s$  is reached, cyclical increase and decrease of  $H$  leads to the hysteresis loop (solid line). Coercive field and retentive magnetization are indicated in the plot by  $H_c$  and  $M_r$ , respectively.

tion. The intensity of the field required to cancel the retained magnetization is  $H_c$ , the coercive field. For cyclical increases and decreases of the  $H$ -field, the typical hysteresis curve as in Fig.1.1 (b) is obtained.

Ferromagnetic materials can be further divided into hard and soft ones. The former are characterized by relatively large magnetization retained  $M_r$  compared to the saturation value  $M_s$  and large coercive fields  $H_c$  as well. The latter, instead, present little magnetization retained and are easy to re-magnetize, thus drawing hysteresis curves with smaller areas. Carbonyl iron particles are examples of soft ferromagnetic particles and are often employed to prepare magnetoelastomers [8, 54–56]. Their relative permeability  $\mu/\mu_0$  ranges from 2.77 to 4.82 [57], the saturation magnetization is  $M_s \sim 1360$  kA/m, the remnant magnetization  $M_r \sim 104$  kA/m, and the coercive field  $H_s \sim 27.5$  kA/m [58].

In paramagnetic materials the moments of the atoms also align in presence of external magnetic fields. However, after the external field is switched off, they do not retain any magnetization. For increasing external fields the magnetization increases linearly, with proportionality constant  $\mu = \mu_0(1 + \chi)$ , larger than the vacuum magnetic permeability  $\mu_0$ . Porous particles containing paramagnetic iron oxide [12] can have up to  $M_s \sim 141$  kA/m and virtually no retentive magnetization or coercive field, with subsequent absence of hysteresis [59].

In magneto-elastic composites, the particles can range from nano- [60] to several micrometers [10] in size and, additionally can vary from regularly spherical [30, 61] to oval, irregular [8, 10] shapes. A special case is represented by very small ferromagnetic

particles, known as superparamagnetic [62]. They typically have diameters of a few nanometers [63] and consist of a single magnetic domain.

### 1.2.2 Magnetic Interactions

The magnetic field  $\mathbf{B}$  generated at position  $\mathbf{r}$  by a distribution of electric current density  $\mathbf{j}(\mathbf{r}')$  reads [53]

$$\mathbf{B}(\mathbf{r}) = \partial_{\mathbf{r}} \times \mathbf{A}(\mathbf{r}) = \frac{\mu_0}{4\pi} \int \partial_{\mathbf{r}} \times \frac{\mathbf{j}(\mathbf{r}')}{|\mathbf{r} - \mathbf{r}'|} d\mathbf{r}', \quad (1.1)$$

where  $\times$  indicates the cross product and  $\mathbf{A}$  the vector potential.

In our case of magnetic particles, the current density  $\mathbf{j}$  is non-vanishing only on their insides. Furthermore, we are interested in far-field interactions, i.e., for interparticle distances much larger than the particle size. Thus, we expand in multipoles for  $|\mathbf{r}| \gg |\mathbf{r}'|$

$$\frac{1}{|\mathbf{r} - \mathbf{r}'|} = \frac{1}{r} + \frac{\mathbf{r} \cdot \mathbf{r}'}{r^3} + \dots, \quad (1.2)$$

obtaining the far-field  $\mathbf{B}$  generated by a dipolar particle  $i$ , with volume  $V_i$ , and centered in the origin of our reference system

$$\mathbf{B}_i(\mathbf{r}) = \frac{\mu_0}{4\pi} \partial_{\mathbf{r}} \times \frac{1}{r^3} \int_{V_i} \mathbf{r} \cdot \mathbf{r}' \mathbf{j}(\mathbf{r}') d\mathbf{r}' + \dots, \quad (1.3)$$

where the integral is performed over the volume  $V_i$  occupied by the particle. The monopole contribution vanishes and the lowest order term is the dipolar one:

$$\mathbf{B}_i(\mathbf{r}) = \frac{\mu_0}{4\pi} \left[ 3 \frac{(\mathbf{m}_i \cdot \mathbf{r}) \mathbf{r}}{r^5} - \frac{\mathbf{m}_i}{r^3} \right], \quad (1.4)$$

$$\text{where } \mathbf{m}_i = \frac{1}{2} \int_{V_i} \mathbf{r}' \times \mathbf{j}(\mathbf{r}') d\mathbf{r}' = \int_{V_i} \mathbf{M}(\mathbf{r}') d\mathbf{r}' \quad (1.5)$$

denotes the magnetic moment of the  $i$ -th particle and  $\mathbf{B}_i(\mathbf{r})$  is the magnetic field generated by the particle at distance  $\mathbf{r}$  from its center.

Therefore, the total magnetic field at position  $\mathbf{r}$  generated by a set of particles with positions  $\mathbf{r}_i$  and magnetic moments  $\mathbf{m}_i$  ( $i = 1 \dots N$ ) is

$$\mathbf{B}(\mathbf{r}) = \sum_{i=1}^N \mathbf{B}_i(\mathbf{r} - \mathbf{r}_i) = \frac{\mu_0}{4\pi} \sum_{i=1}^N 3 \frac{(\mathbf{m}_i \cdot \Delta \mathbf{r}_i) \Delta \mathbf{r}_i}{|\Delta \mathbf{r}_i|^5} - \frac{\mathbf{m}_i}{|\Delta \mathbf{r}_i|^3} \quad (1.6)$$

with  $\Delta \mathbf{r}_i = (\mathbf{r} - \mathbf{r}_i)$  and for  $|\Delta \mathbf{r}_i| \gg \sqrt[3]{V_i}$  to allow us to confine ourselves to the dipolar term in the multipole expansion.

Finally, we derive the particle–particle interaction. The potential energy of a permanent magnetic dipole  $\mathbf{m}$  in a magnetic field  $\mathbf{B}_{tot}$  reads  $U^m = -\mathbf{m} \cdot \mathbf{B}_{tot}$  [53]. We split

the total magnetic field acting on a particle into contributions from an external field  $\mathbf{B}_0$  and from the other particles:  $\mathbf{B}_{tot} = \mathbf{B}_0 + \mathbf{B}$ , see Eq. (1.6). Then, the energy of our system composed of  $N$  dipolar particles reads

$$U^m = - \sum_{i=1}^N \mathbf{B}_0(\mathbf{r}_i) \cdot \mathbf{m}_i - \sum_{i=1}^N \mathbf{B}(\mathbf{r}_i) \cdot \mathbf{m}_i. \quad (1.7)$$

Taking care of counting the interaction of each pair of dipoles only once and avoiding self-interactions, we obtain the final expression for the magnetic energy

$$U^m = - \sum_{i=1}^N \mathbf{B}_0(\mathbf{r}_i) \cdot \mathbf{m}_i + \frac{1}{2} \sum_{\substack{i,j=1 \\ i \neq j}}^N v^{dd}(\mathbf{m}_i, \mathbf{m}_j, \mathbf{r}_{ij}), \quad (1.8)$$

$$\text{with } v^{dd}(\mathbf{m}_i, \mathbf{m}_j, \mathbf{r}_{ij}) = \frac{\mu_0}{4\pi} \left[ \frac{\mathbf{m}_i \cdot \mathbf{m}_j}{r_{ij}^3} - 3 \frac{(\mathbf{m}_i \cdot \mathbf{r}_{ij})(\mathbf{m}_j \cdot \mathbf{r}_{ij})}{r_{ij}^5} \right] \quad (1.9)$$

the dipole–dipole magnetic interaction,  $\mathbf{r}_{ij} = \mathbf{r}_j - \mathbf{r}_i$  and  $r_{ij} = |\mathbf{r}_{ij}|$ . In the following, we will often consider the case of dipoles oriented along a common direction of magnetization, e.g., by an external field,  $\mathbf{m}_i = m_i \widehat{\mathbf{m}}$  ( $i = 1, \dots, N$ ). In this case the dipole–dipole potential becomes

$$v^{dd}(\mathbf{m}_i, \mathbf{m}_j, \mathbf{r}_{ij}) = \frac{m_i m_j \mu_0}{4\pi} \left[ \frac{r_{ij}^2 - 3(\widehat{\mathbf{m}} \cdot \mathbf{r}_{ij})(\widehat{\mathbf{m}} \cdot \mathbf{r}_{ij})}{r_{ij}^5} \right] \quad (1.10)$$

and the force  $\mathbf{F}_{ij}^{dd} = -\partial_{\mathbf{r}_{ij}} v^{dd}(\mathbf{m}_i, \mathbf{m}_j, \mathbf{r}_{ij})$  acting on particle  $i$  due to particle  $j$  reads

$$\mathbf{F}_{ij}^{dd} = \frac{m_i m_j \mu_0}{4\pi} \frac{3}{r_{ij}^5} \left[ \mathbf{r}_{ij} + 2\widehat{\mathbf{m}}(\widehat{\mathbf{m}} \cdot \mathbf{r}_{ij}) - 5 \frac{\mathbf{r}_{ij}(\widehat{\mathbf{m}} \cdot \mathbf{r}_{ij})^2}{r_{ij}^2} \right]. \quad (1.11)$$

### 1.3 Polymers and Elasticity

The simplest model to describe polymers is the ideal or freely jointed chain [2, 3]. It consists of  $N$  three-dimensional, rigid segments  $\mathbf{r}_i$ ,  $i = 1 \dots N$ , of length  $b$  free to rotate in space and jointed to each the other at their ends, as shown in Fig. 1.2. The end-to-end vector  $\mathbf{R}$  is given by

$$\mathbf{R} = \sum_{i=1}^N \mathbf{r}_i. \quad (1.12)$$

Each segment can rotate independently of the others. Because of the central limit theorem [64], for large  $N$  the probability density as a function of  $\mathbf{R}$  will approach a

Gaussian distribution, which is completely determined by its first and second moments. We obtain

$$\langle \mathbf{R} \rangle = \left\langle \sum_{i=1}^N \mathbf{r}_i \right\rangle = \sum_{i=1}^N \langle \mathbf{r}_i \rangle = \mathbf{0}, \quad (1.13)$$

because each  $\mathbf{r}_i$  freely rotates with equal probability in any direction and thus its average is  $\langle \mathbf{r}_i \rangle = \mathbf{0}$ . The second moment, however, is

$$\langle \mathbf{R}^2 \rangle = \left\langle \sum_{i=1}^N \mathbf{r}_i \cdot \sum_{j=1}^N \mathbf{r}_j \right\rangle = \sum_{i,j=1}^N \langle \mathbf{r}_i \cdot \mathbf{r}_j \rangle = Nb^2 \quad (1.14)$$

because  $\langle \mathbf{r}_i \cdot \mathbf{r}_j \rangle = \delta_{ij}b^2$ , i.e., two different segments are uncorrelated and each has constant length  $b$ . Since  $\mathbf{R}^2 = \sum_{\alpha} (R^{\alpha})^2$  ( $\alpha = x, y, z$ ), the second moment of each independent Cartesian component of  $\mathbf{R}$  is  $\langle (R^{\alpha})^2 \rangle = Nb^2/3$ .

Thus, the probability distribution  $p(\mathbf{R})$  for the end-to-end vector  $\mathbf{R}$  is

$$p(\mathbf{R}) \propto \exp \left[ - \sum_{\alpha} \frac{(R^{\alpha})^2}{2Nb^2/3} \right] = \exp \left[ - \frac{3\mathbf{R}^2}{2Nb^2} \right]. \quad (1.15)$$

One can obtain the configuration entropy

$$S(\mathbf{R}) = k_B \ln [p(\mathbf{R})] \quad (1.16)$$

$$= S_0 - 3k_B \mathbf{R}^2 / 2Nb^2, \quad (1.17)$$

where  $k_B$  is the Boltzmann constant and we absorbed the normalization prefactors of  $p(\mathbf{R})$  into the constant  $S_0$ . From Eq. (1.17) one already deduces that the maximum entropy is achieved for  $\mathbf{R} = \mathbf{0}$ . Furthermore, we consider the free energy

$$F = U - TS = F_0 + \frac{3k_B T \mathbf{R}^2}{2Nb^2} = F_0 + \frac{1}{2} \frac{3Nk_B T \mathbf{R}^2}{L^2} \quad (1.18)$$

where  $L = Nb$  is the chain contour length.

The state  $\mathbf{R} = \mathbf{0}$  is the one that minimizes the free energy which, to lowest order, is a quadratic function of the end-to-end displacement. In other words, upon attempting to stretch the chain, the polymer responds with an entropic force that brings the system towards its state of maximum entropy. Such a force is linear and it can be represented by a harmonic spring of elastic constant  $3k_B T / Nb^2$ . This is the first step in a coarse-graining description, since all the microscopic degrees of freedom of the chain are taken into account by an effective description of the overall end-to-end distance.

In general, however, the state of the polymer can be described by a multi-dimensional vector  $\mathbf{X}$  of  $D$  degrees of freedom. Again, for the central limit theorem, the distribution

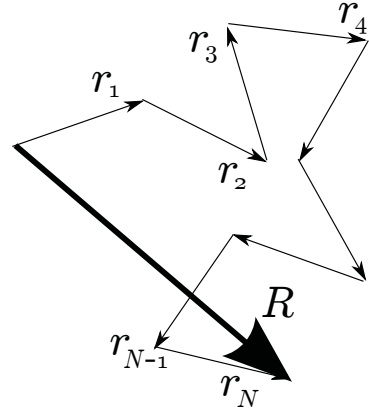


Figure 1.2: Sketch of a freely jointed chain.

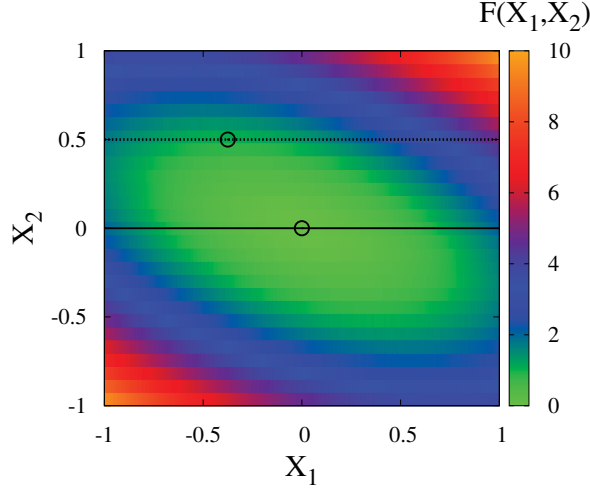


Figure 1.3: Example of free energy, suitably rescaled, as in Eq. (1.20) plotted as a function of two rescaled dimensionless variables  $X_1$  and  $X_2$  with covariance  $\Sigma_{12} = \langle (X_1 - X_{0,1})(X_2 - X_{0,2}) \rangle < 0$ . Continuous and dashed lines correspond to  $X_1 = 0$  and  $X_2 = \frac{1}{2}$ , respectively. Circles mark the minimum along each line.

must tend to a Gaussian when the number of degrees of freedom becomes very large. Following a similar derivation, given the first moments  $\langle \mathbf{X} \rangle = \mathbf{X}_0$  and the positive definite covariance matrix with components  $\Sigma_{mn} = \langle (X_m - X_{0,m})(X_n - X_{0,n}) \rangle$  ( $m, n = 1, \dots, D$ ), the limiting distribution will be a multivariate Gaussian of corresponding moments [65], i.e.,

$$p(\mathbf{X}) \propto \exp \left[ -\frac{(\mathbf{X} - \mathbf{X}_0) \cdot \bar{\bar{\Sigma}}^{-1} \cdot (\mathbf{X} - \mathbf{X}_0)}{2} \right], \quad (1.19)$$

with  $\bar{\bar{\Sigma}}^{-1}$  denoting the inverse matrix of  $\bar{\bar{\Sigma}}$ . The free energy corresponding to each overall configuration  $\mathbf{X}$  is

$$F(\mathbf{X}) = F_0 + \frac{k_B T}{2} (\mathbf{X} - \mathbf{X}_0) \cdot \bar{\bar{\Sigma}}^{-1} \cdot (\mathbf{X} - \mathbf{X}_0). \quad (1.20)$$

Fig. 1.3 depicts a simplified  $D = 2$  example of quadratic free energy  $F(\mathbf{X}) = F(X_1, X_2)$  as a function of two dimensionless variables  $X_1, X_2$  and with negative covariance  $\Sigma_{12}$ . We see that  $k_B T \bar{\bar{\Sigma}}^{-1}$  can be interpreted as a matrix containing the coefficients of harmonic effective potentials. More precisely, by expanding any free energy in a Taylor series around its minimum  $\mathbf{X}_0$  and comparing it with Eq. (1.20), one can deduce that  $\partial_{X_m} \partial_{X_n} F(\mathbf{X} = \mathbf{X}_0) = k_B T \Sigma_{mn}^{-1}$  with  $m, n = 1, \dots, D$ .

The diagonal components of  $k_B T \bar{\Sigma}^{-1}$  are interpreted as the coefficients of the harmonic interaction for each component of  $\mathbf{X}$ . In the case of  $\mathbf{X}$  being the end-to-end distance of the polymer, such a coefficient is the Young modulus of the polymer. Obviously, we may represent the corresponding behavior by introducing an effective harmonic spring. Conversely, the off-diagonal components represent mixed contributions which result in a shift of the constrained minima. For instance, following the example depicted in Fig. 1.3, for  $X_2 = 0$  the resulting free energy along the continuous black line,  $F(X_1, X_2 = 0)$ , is a quadratic function of  $X_1$  with minimum on  $X_1 = 0$  marked by the circle. However, for  $X_2 > 0$ ,  $F(X_1, X_2 = \frac{1}{2})$  (black dashed line) is still quadratic in  $X_1$  but the minimum marked by the circle shifts towards negative  $X_1$ -values. This simplified picture already accounts for a negative correlation between the two variables, i.e., when the average of one increases, the average of the other decreases and vice versa.

In summary, we have considered a simple polymer model to explain the origin of elastic behavior. In the following, we will introduce our approach in Paper I. There, we bind the ends of the polymer chain to the surface of two mesoscopic, magnetic particles. Our goal is to derive the polymer-mediated interactions between the mesoscopic particles via effective pair potentials, thus bridging the scale from the microscopic description of the polymer chain to the mesoscopic scale.

### 1.3.1 Coarse-Graining of Microscopic Simulations

In Paper I we considered two mesoscopic magnetic particles linked by a polymeric chain, see Fig. 1.4. In general, simulations of magnetic elastic composite materials will include several mesoscopic magnetic particles connected by many polymeric chains [66,67]. Here, however, we confine ourselves to a model situation as simple as possible, see Fig. 1.4, to work out the connection between a coarse-grained microscopic approach and our mesoscopic effective model description that is reduced to the coordinates of the magnetic particles.

A common approach to this problem is the adiabatic approximation [68]. It assumes that the fast-evolving degrees of freedom, here those of the linking polymer chain, relax to their equilibrium- or steady-state for every configuration of the slow-evolving ones, here those of the mesoscopic particles. As a consequence, mesoscopic and microscopic degrees of freedom can be separated to a certain degree. The Hamiltonian of the system splits and the part connected to the microscopic degrees of freedom can be integrated into an

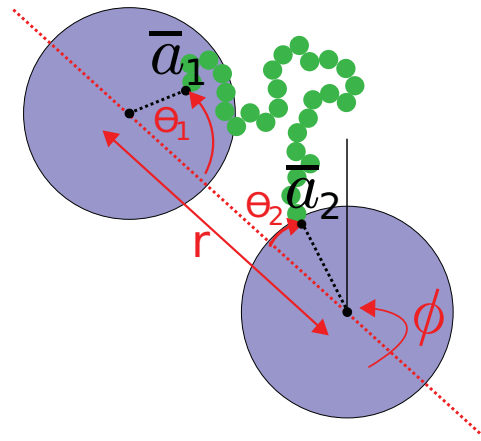


Figure 1.4: Sketch of our simplified model considered in Paper I.

“effective” mesoscopic potential [69, 70, Paper I]. In practice, this means that for every mesoscopic configuration the polymer chain explores the accessible microscopic phase space. Different mesoscopic configurations of the mesoscopic particles lead to different amounts of entropy of the polymer chain. This in turn, implies a polymer free energy that varies with the mesoscopic state and thus acts as an effective potential on the mesoscopic level.

In our reduced model, we begin with two particles of mesoscopic size connected by a polymer chain, discretized via  $N = 60$  beads of diameter  $\sigma$ , each representing a small, coarse-grained part of the polymer. The mesoscopic particles have radius  $a = 5\sigma$ . The center-to-surface vectors  $\mathbf{a}_1$  and  $\mathbf{a}_2$  identify the fixed anchoring points of the polymer chain on each spherical particle as depicted in Fig. 1.4. All the particles interact via Weeks-Chandler-Andersen (WCA) [71] core-repulsive potentials and are linked to each other by harmonic springs. After global translations and rotations are taken into account, the relative state of the two mesoscopic particles can be identified by the following parameters: center-to-center vector  $\mathbf{r}$ , angles  $\theta_1 = \arccos(\mathbf{a}_1 \cdot \mathbf{r}/|\mathbf{a}_1| |\mathbf{r}|)$  and  $\theta_2 = \arccos(\mathbf{a}_2 \cdot \mathbf{r}/|\mathbf{a}_2| |\mathbf{r}|)$ , as well as the angle  $\phi$  of relative torsion around the  $\mathbf{r}$ -axis, see Fig. 1.4..

Brownian Dynamics simulations (i.e., overdamped dynamics with a Langevin thermostat) are employed. We let the simulation run and explore the phase space of the system. Each microscopic configuration  $\mathbf{\Gamma}$  corresponds to a mesoscopic state identified by the phase-space vector  $\boldsymbol{\gamma} = (r, \theta_1, \theta_2, \phi)$ , with  $r = |\mathbf{r}|$ . The mesoscopic phase space is sampled within the following intervals  $r \in [0, 100\sigma[$ ,  $\theta_1, \theta_2 \in [0, \pi[$ , and  $\phi \in [0, 2\pi[$ . For the purpose of collecting statistics, each interval is subdivided into 100 bins of equal width. At regular intervals during the time-evolution of the simulation, each sampled microstate is counted into the corresponding mesoscopic bin. We collect a total of 34 billion sampled configurations. Division by the total number of microstates observed yields a discrete histogram  $h(r_i, \theta_{1j}, \theta_{2k}, \phi_l)$ ,  $i, j, k, l = 1, \dots, 100$ , that represents the relative occurrence of the mesoscopic configurations contained in each single  $(i, j, k, l)$  bin.

The connection with the continuous probability density  $p_c(\boldsymbol{\gamma})$  of the mesoscopic phase-space is given by comparing the normalization conditions

$$\int p_c(\boldsymbol{\gamma}) \sin(\theta_1) \sin(\theta_2) dr d\theta_1 d\theta_2 d\phi = 1 = \sum_{i,j,k,l=1}^{100} h(r_i, \theta_{1j}, \theta_{2k}, \phi_l), \quad (1.21)$$

where  $h(r_i, \theta_{1j}, \theta_{2k}, \phi_l)$  has been normalized. Then, on discrete grid points at the center of each bin, the probability distribution is evaluated as

$$p_c(\boldsymbol{\gamma}) \Big|_{\boldsymbol{\gamma}=(r_i, \theta_{1j}, \theta_{2k}, \phi_l)} = \frac{h(r_i, \theta_{1j}, \theta_{2k}, \phi_l)}{\sin(\theta_{1j}) \sin(\theta_{2k})} \quad (1.22)$$

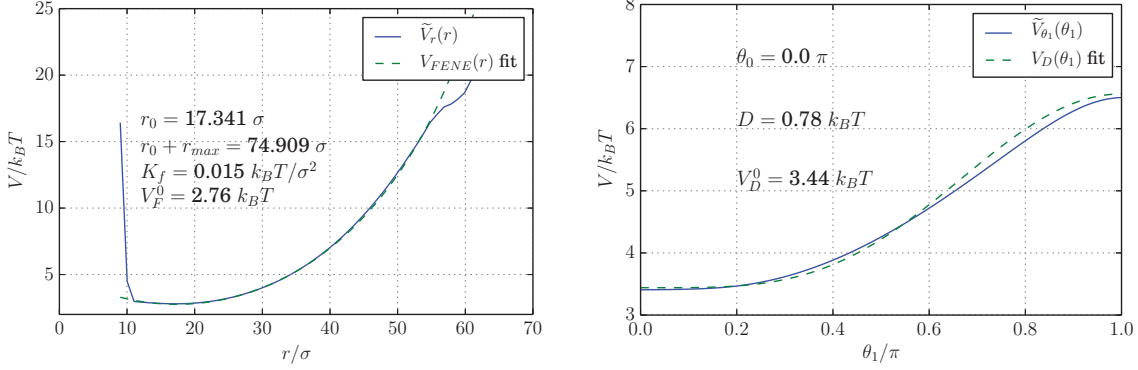


Figure 1.5: (LEFT) Effective potential  $\tilde{V}_r(r)$  and fit to a FENE [73] expression with model parameters as listed in the figure. To lowest order,  $\tilde{V}_r(r) \sim K_f(r-r_0)^2$ . (RIGHT) Effective potential  $\tilde{V}_{\theta_1}(\theta_1)$  and fit with an expression  $\sim V_D^0 - D \cos(\theta_1 - \theta_0)^4$ , with model parameters as listed in the plot. Reproduced from Ref. 75 with permission. © IOP Publishing. All rights reserved.

and its corresponding effective potential reads

$$V_c(\boldsymbol{\gamma}) = -k_B T \ln [p_c(\boldsymbol{\gamma})] \Leftrightarrow p_c(\boldsymbol{\gamma}) = \exp \left[ -\frac{V_c(\boldsymbol{\gamma})}{k_B T} \right], \quad (1.23)$$

where  $V_c(\boldsymbol{\gamma})$  can always be shifted by an appropriate, convenient constant so that  $p_c(\boldsymbol{\gamma})$  is always normalized. Finally, the mesoscopic configuration that minimizes the effective potential and maximizes the probability density was found to be  $\boldsymbol{\gamma}_0 = (20.20\sigma, 0.36\pi, 0.36\pi, 0)$ .

In obtaining the proper probability density  $p_c(\boldsymbol{\gamma})$  and thus the correct effective potential  $V_c(\boldsymbol{\gamma})$  it is crucial to normalize the frequencies obtained from the data by the sines of the angles  $\theta_1$  and  $\theta_2$  as in Eq. (1.22), see also Ref. 70. This leads to the apparent contradiction that the probability density at  $\theta_1 = 0$  and  $\theta_2 = 0$  reaches its maximum even though this very configuration almost never occurs in simulations. In contrast to that, division by  $r^2$  as one would need in polar coordinates is not necessary here because our mesoscopic distance  $r$  is not a radius vector but simply the distance between the two centers.

By selective integration, one obtains the marginal probability densities and the corresponding one-variable effective potentials, e.g., for  $r$ ,

$$\tilde{p}_r(r) = \int p_c(\boldsymbol{\gamma}) d\theta_1 d\theta_2 d\phi \Rightarrow \tilde{V}_r(r) = -k_B T \ln [\tilde{p}_r(r)]. \quad (1.24)$$

The one-variable effective potentials are excellently approximated by potentials proposed in the literature, such as the FENE pair interaction [72, 73] or those involving periodic functions for the rotational degrees of freedom [74], see Fig. 1.5. Fits of the effective potentials with such analytical expressions lead to excellent agreement.

If the mesoscopic variables are uncorrelated, one can separate them and approximate the full effective potential  $V_c(\gamma)$  as a sum of independent one-variable terms as in Eq. (1.24). However, one has to be careful if correlations between the variables are not small. We define the correlation  $\rho_{\alpha\beta} = \langle\alpha\beta\rangle/\sqrt{\langle\alpha^2\rangle\langle\beta^2\rangle}$  ( $\alpha, \beta = r, \theta_1, \theta_2, \phi$ ) and find in Paper I that the most prominent ones are  $\rho_{r, \theta_1} \simeq \rho_{r, \theta_2} \simeq -0.341$ . The relative torsion  $\phi$ , conversely, is more weakly influenced by the other parameters, as evinced by the smaller correlations  $\rho_{\phi, r} \simeq 0.083$  and  $\rho_{\phi, \theta_1} \simeq \rho_{\phi, \theta_2} \simeq -0.083$ .

In practice, this leads to a negative correlation similar to the one described in section 1.3 and depicted in Fig. 1.3. To demonstrate it, we focus on the effective potential  $V_c(\gamma)$ , for  $\theta_1 = \theta_2 = \theta$ ,  $\phi = 0$ , and as a function of  $r$ . We obtain the effective interaction  $V_c(r)$  for the interparticle distance  $r$  the minimum of which shifts to lower values of  $r$  with increasing  $\theta$ , see Fig. 1.6.

This correlation is physically interpreted as a tendency of the polymer chain to wrap around the mesoscopic particles with changing angles  $\theta_1$  and  $\theta_2$ . When the angles  $\theta_1$  and  $\theta_2$  increase the particle separation  $r$  reduces. Vice versa, even by rotating just one particle, their distance reduces. The stretched chain is  $60\sigma$  long, whereas the maximal circumference of the mesoscopic particles is  $2\pi a \simeq 30\sigma$ . Thus, the chain is long enough to, hypothetically allow for large rotations of the spheres without drawing them together. Nevertheless, as we see from simulations, rotations of  $\theta_1$  or  $\theta_2$  typically imply that particles are pulled closer together.

To take into account such correlations between the variables, one possible solution is to fit the simulation data to a Gaussian distribution with cross-coupled terms as in Eq. (1.19). That would be a viable option in case of overall smooth potentials. However, because of the steep WCA-repulsion between the two mesoscopic particles (see Fig. 1.5), such an approach would only work in an very small neighborhood of the minimum of  $V_c(\gamma)$ . Therefore, we follow a hybrid approach. We approximate  $p_c(\gamma)$  by a product of fit-obtained, one-variable marginal distributions as in Eq. (1.24) and coupled terms as in Eq. (1.19)

$$p_c(\gamma) \propto \prod_{\alpha} \tilde{p}_{\alpha}(\alpha) \times \exp [(\gamma - \xi) \cdot \mathcal{Q} \cdot (\gamma - \xi)] \quad (1.25)$$

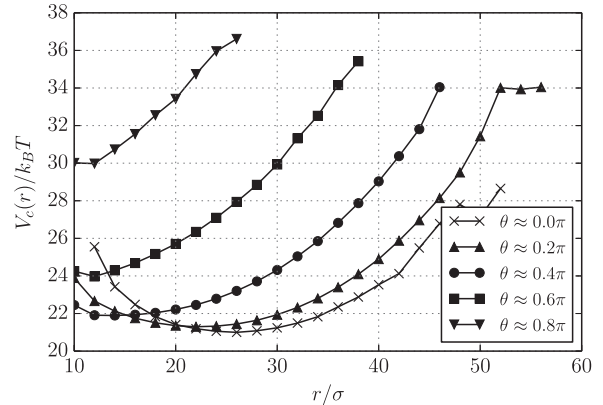


Figure 1.6: Free energy of the polymer chain for fixed torsional angle  $\phi = 0$ , varying deflections  $\theta_1 = \theta_2 = \theta$ , and as a function of distance  $r$  between the mesoscopic particles. Reproduced from Ref. 75 with permission. © IOP Publishing. All rights reserved.

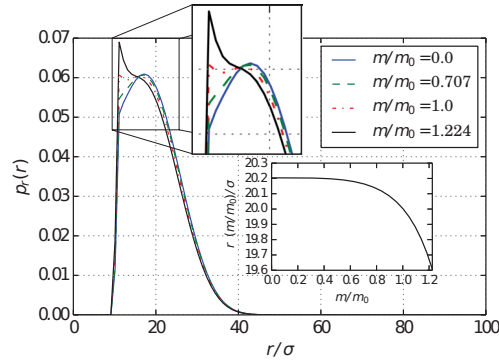


Figure 1.7: Impact of magnetic interactions on the marginal distribution  $p_r(r)$  of the two mesoscopic particles for increasing magnitude  $m$  of their magnetic moments. Obviously, the particles are pulled together by the magnetic interactions. Reproduced from Ref. 75 with permission. © IOP Publishing. All rights reserved.

with  $\alpha = r, \theta_1, \theta_2, \phi, \boldsymbol{\xi}$  and  $\mathcal{Q}$  a vector and a symmetric matrix, respectively, containing best-fit parameters to match the moments of the simulation data.

Finally, we calculate the impact of magnetic moments on the probability distributions of the system, see Fig. 1.7. The modified probability density is obtained by multiplying  $p_c(\boldsymbol{\gamma})$  in the absence of magnetic interactions by the Boltzmann factor  $\exp[-v^{dd}(\boldsymbol{\gamma})/k_B T]$ , with  $v^{dd}$  as described in Eq. (1.10). Thus, the statistical impact of the dipole–dipole interaction is additionally taken into account.

Altogether, we have outlined a way that, starting from simple ingredients such as beads and springs, describes effective entropy-driven pair potentials. Our picture, however, is far from being complete. First, not only one but usually a large number of chains is connected to and wrapped around embedded particles in a magnetoelastic material. Additionally, many magnetic particles should be included in a realistic description of magnetoelastomers. In the following section we will increase the number of particles in studying the buckling effect of chains of paramagnetic particles embedded in soft elastic gels and exposed to perpendicular magnetic fields.

## 1.4 Buckling of Paramagnetic Chains of Particles

The next step in increasing the complexity in our description of magnetoelastomers is the study of one-dimensional structures of several magnetic particles embedded in a soft elastic gel. The formation of chain-like aggregates has been widely experimentally investigated [8, 10, 54–56, 76, 77].

The case of one-dimensional chains in a polymeric matrix, albeit seemingly relatively simple, involves many complex details. Above all, the interaction of the particles with the embedding polymer matrix is complicated and not simple to model. Experiments

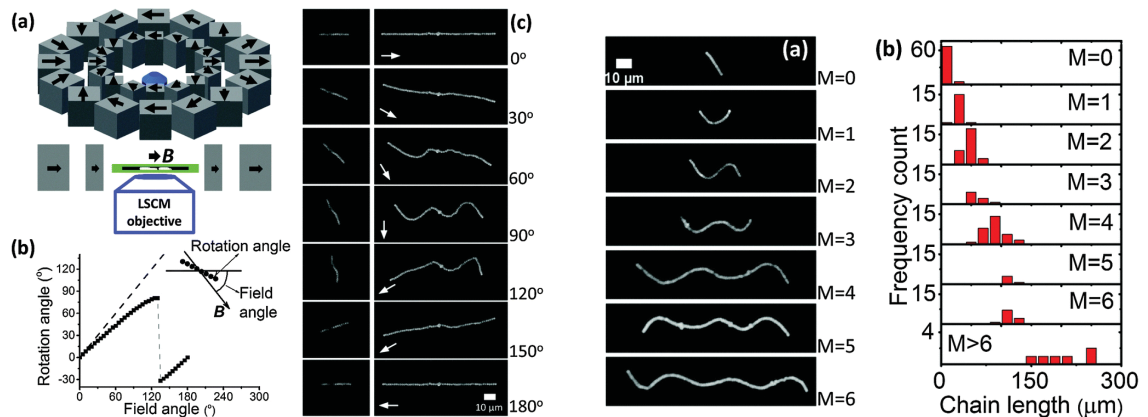


Figure 1.8: (LEFT) (a) Experimental setup and Halbach magnetic array for generating a homogeneous magnetic field. (b) Deflection angle of a short chain under a rotating external field ( $\sim 216$  mT). (c) Deformation morphologies of short and long chains under rotating magnetic field. (RIGHT) Panel (a): buckling examples of chains for perpendicular magnetic fields. Chains of varying lengths display different buckling morphologies. Panel (b): the chains are sorted according to the number of buckles  $M$  (or “half-waves”). Reproduced from Ref. 12 - Published by The Royal Society of Chemistry under a Creative Commons Attribution 3.0 Unported Licence.

to study the deformation of such chain-like aggregates were conducted, see Paper II, using an experimental setup as illustrated in Fig. 1.8. A small amount (0.09 wt%) of paramagnetic particles (iron oxide) of diameter  $d \sim 1.48 \mu\text{m}$  is dispersed in a polymer solution. Polymerization by action of a catalyst is performed under the influence of a moderate (100 mT) magnetic field. As a consequence, chains of various lengths (up to 170 particles) are formed. The chains are diluted, separated by distances larger than 30  $\mu\text{m}$ , and are therefore basically not-interacting with each other.

When a magnetic field of 100 mT is applied perpendicularly to the axes of the longer chains, they buckle, see Fig. 1.8, panel (c) for 90° and Fig. 1.8. It is evident from Fig. 1.8 that longer chains buckle with more oscillations. This is proven by panel (b) on the right-hand side, where particles are sorted according to number of buckles (“half-waves”)  $M$  and chain length. High values of  $M$  can be obtained only for long enough chains. vice versa, very short chains do not buckle at all ( $M = 0$ ) and just undergo rotations.

To describe the buckling effect, we follow a phenomenological model. The main ingredients are the dipole–dipole magnetic interactions within the chain and the chain-polymer matrix interactions. Only dipole–dipole interactions between the particles in the same chain are considered. Modeling the effect of the elastic matrix is significantly more complicated. Recently, exact solutions of the elastic interaction between magnetic particles in a soft gel have been derived by solution of the elastostatic equations [78–81]. Here, we follow a simpler phenomenological approach.

Elastic contributions are modeled as the sum of two effects: one deriving from bending the chain and one from net displacements against the surrounding matrix. Significant bending contributions probably arise from absorbed polymers on the surfaces of the particles making the chain-like aggregate stiffer than the elasticity of the base surrounding matrix would suggest. By applying a magnetic field to the particles in the sol phase [59], we find “U”- or “S”-shaped deformations even in the absence of crosslinking. This demonstrates the existence of a bending rigidity contribution of the chains themselves. [82].

Penalties of displacement energy originate from the crosslinked polymer matrix which is immovable in space and hinders translations and rotations of the embedded chain. The necessity of a displacement term is proven by the  $M = 0$  case depicted in Fig. 1.8, panel (b) on the left-hand side. There, a straight short chain (virtually no bending present) rotates under a perpendicular field. Because of the displacement resistance, however, the chain does not align completely with the field (which would correspond to the absolute minimum of the magnetic interactions), but ends up in a partially rotated configuration.

In a coarse-grained approach, we describe the chain of particles as a continuous line profile  $y(x)$ . Moreover, the chain length is constrained, i.e., the contour length of  $y(x)$  remains constant

$$\int_{x_1}^{x_2} \sqrt{1 + y'(x)^2} dx = L \quad (1.26)$$

with  $x_1$  and  $x_2$  the  $x$ -coordinates of the two ends of the chain and the  $x$ -axis aligned with the initial chain axis.

By considering interactions between two particles of equal diameter  $d$ , separated by the center-to-center length element  $(dx, y'(x)dx)$ , and taking into account only nearest-neighbor contributions, we obtain the following functional for the magnetic energy

$$E_{magn}[y] = W \int_{x_1}^{x_2} [1 + y'(x)^2]^{-1/2} dx, \quad \text{with } W = \frac{3\mu_0 \mathbf{m}^2}{4\pi d^4} \quad (1.27)$$

setting the magnetic energy per unit length of a segment tilted by  $\arctan[y'(x)]$ . Furthermore,  $\mathbf{m}$  denotes the magnetic moment of each particle, it is set identical for all of them, and  $\mu_0$  is the vacuum magnetic permeability. The elastic displacement and bending energies read, respectively,

$$E_{displ}[y] = C_d \int_{x_1}^{x_2} y(x)^2 [1 + y'(x)^2]^{3/2} dx \quad \text{and} \quad (1.28)$$

$$E_{bend}[y] = C_b \int_{x_1}^{x_2} \frac{y''(x)^2}{[1 + y'(x)^2]^{5/2}} dx. \quad (1.29)$$

The buckling deformation  $y(x)$  was found by minimizing the total energy  $E_{tot}[y] = E_{magn}[y] + E_{displ}[y] + E_{bend}[y]$  with respect to  $y(x)$ , i.e., by setting its functional derivative

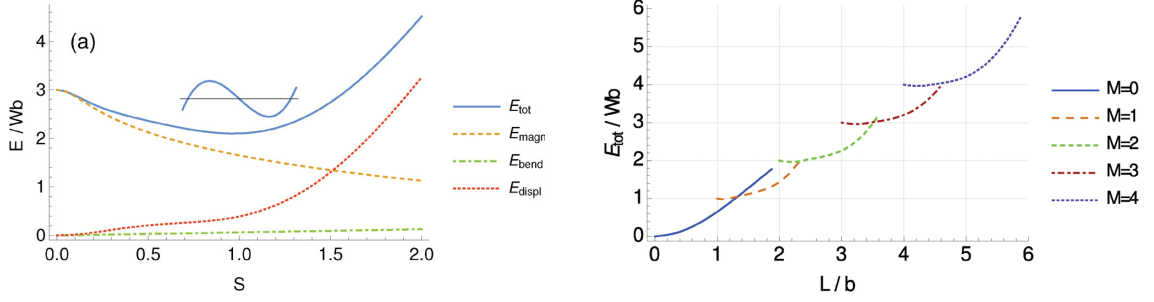


Figure 1.9: (LEFT) Variational energy as a function of deformation amplitude  $S$ . A chain of length  $L$  (here  $L = 3b$ ) is made to buckle twice ( $M = 2$ ). The amplitude  $S$  is varied. (RIGHT) For a given  $M = 0, \dots, 4$  the minimized total energy  $E_{tot}$  is depicted as a function of  $L$ . Each point represents the minimum of the energy landscape as can be extracted from the left panel. Reproduced from Ref. 12 - Published by The Royal Society of Chemistry under a Creative Commons Attribution 3.0 Unported Licence.

to zero

$$\frac{\delta E_{tot}}{\delta y(x)}[y] = 0, \quad (1.30)$$

see the supplementary information of Paper II for a complete listing.

While the parameter  $W$  was obtained from the calculation, the parameters  $C_d$  and  $C_b$  are found phenomenologically. For that purpose, we determine optimized values  $C_d$  and  $C_b$  to match the experimentally observed rotations of straight chains ( $M = 0$ ) and to match the buckling amplitudes for  $M \geq 1$ . By linearizing Eq. (1.30), we obtain the solution in the case of small-amplitude deformations, see supplementary material of Paper II. There, the solution is a plane wave of wavenumber  $q = W(1 \pm \sqrt{1 - 16C_dC_b/W^2})/4C_b$ . Thus, for  $W^2/16C_dC_b > 1$  the wavenumber is real and the solution purely oscillatory, setting the ratio  $C_dC_b/W^2$  that marks the onset of buckling deformations.

Subsequently, we proceed with making an ansatz for the  $y(x)$  deformation in the form of a polynomial of order  $M + 1$  with as many zeroes set at regular intervals  $b$  along the  $x$ -axis. This is motivated by the experimental observation that the spacing between the nodes as depicted in Fig. 1.8 seems to be constant amid the various cases. Our ansatz profile reads  $y(x) = S \prod_{m=0}^M (x - mb)$  with  $b$  fixing the “half-wave” length and  $S$  tuning the amplitude of the deformation. Thus, we obtain the energy of a chain profile  $y(x)$  for a given set of free parameters  $M$ ,  $x_1$ , and  $x_2$ . The length constraint of in Eq. (1.26) implicitly defines  $x_2$  for a given  $x_1$  and thus only two free parameters remain.

Finally, we express the total energy  $E_{tot}[y]$  as a function of the variational deformation amplitude  $S$ , with the constraint of constant contour length  $L$  and symmetry or antisymmetry of the buckling profile under inversion  $x \rightarrow -x$ . The result is depicted in Fig. 1.9 for  $M = 2$  (three nodes, i.e., two bucklings). The total energy shows a single minimum which arises from the counterbalance of magnetic and elastic interactions.

On the one hand, a configuration in which the chain is completely oriented in the

$y$ -direction ( $S \rightarrow \infty$ ,  $y'(x) \rightarrow \pm\infty$ ) is the absolute minimum of the magnetic energy. In other words, the magnetic energy favors steep slopes  $|y'(x)|$ . This can be realized either by a straight, rotated chain or by a steep sawtooth-like profile. On the other hand, the flat  $y(x) = 0$  shape is the global minimum of the elastic energy terms because it features neither displacement nor bending ( $y''(x) = 0$ ). The displacement contribution  $E_{displ}$  penalizes rotations of straight chains and net displacements, whereas the bending term  $E_{bend}$  prevents the formation of cusps with diverging second derivative.

The amplitude  $S$  that minimizes  $E_{tot}$  is obtained for varying  $L$  and increasing, integer  $M$ . The result, depicted in the right-hand panel of Fig. 1.9, are the energetic costs for increasing chain length while keeping the buckling shape (determined by  $M$ ) constant. The crossings of the curves belonging to different values of  $M$  mark transition points at which increasing the chain length induces one extra buckle rather than further increasing the deflection amplitude.

After characterizing these one-dimensional particle assemblies we now move on to describe more complex distributions. Our goal is to study the impact of the particle arrangement on the overall system properties. We employ basic dipole–spring models in 2- and 3D to build regular and disordered particle distributions. In the next sections we introduce the main concepts of elasticity and viscoelasticity that are the subject of our mesoscopic investigations. Then, we review the analytically calculated elastic properties of regular spring networks to use them as a benchmark before presenting the main results of our dipole–spring models in Paper III, Paper IV, and Paper V.

## 1.5 Static Linear Elasticity

In this section we briefly review the concepts and quantities of linear elasticity [82] that we apply to characterize the macroscopic properties of our mesoscopic model systems. Elasticity theory describes the mechanics of reversible deformations of solid bodies, which are treated as continuous media. Here, we only consider the case of homogeneous, isotropic materials.

### 1.5.1 Homogeneous Isotropic Materials

Upon deformation, a point of a three-dimensional elastic solid moves from  $\mathbf{r}$  to  $\mathbf{r}' = (\mathbb{1} + \mathcal{D}) \cdot \mathbf{r}$ , with  $\mathbb{1}$  the identity tensor,  $\mathcal{D}$  the deformation gradient tensor, and displacements  $\mathbf{u} = \mathbf{r}' - \mathbf{r} = \mathcal{D} \cdot \mathbf{r}$ . The fundamental dimensionless variable to describe the deformation of the body is the linearized  $3 \times 3$  *strain tensor*  $\bar{\bar{\varepsilon}}$ , the components of which are given by

$$\varepsilon_{\alpha\beta} = \frac{1}{2} \left( \frac{\partial u_\alpha}{\partial r_\beta} + \frac{\partial u_\beta}{\partial r_\alpha} \right) = \frac{1}{2} (\mathcal{D}_{\alpha\beta} + \mathcal{D}_{\beta\alpha}). \quad (1.31)$$

It is symmetrical and defined for every point  $\mathbf{r}$ , with  $\alpha, \beta = x, y, z$ . Furthermore, the relative local change in the infinitesimal volume element  $d\mathbf{r}$  is  $(d\mathbf{r}' - d\mathbf{r})/d\mathbf{r} = \text{Tr}(\bar{\bar{\varepsilon}}) =$

$\sum_{\alpha} \varepsilon_{\alpha\alpha}$ .

The equilibrium condition for the material is that the total forces or stresses vanish at every point. The *stress tensor*  $\bar{\sigma}$  is related to the internal density of force  $\mathbf{f}$  via [82]

$$f_{\alpha} = \sum_{\beta} \frac{\partial \sigma_{\alpha\beta}}{\partial r_{\beta}}. \quad (1.32)$$

In 3D stresses have the dimension of a pressure, and can be interpreted as  $\sigma_{\alpha\beta}$  being the  $\alpha$ -component of the force per unit area acting on the surface perpendicular to the  $\beta$ -direction. Furthermore,  $\bar{\sigma}$  must be symmetrical to avoid rotations. Therefore, in presence of an external force and distinguishing between internal stresses  $\bar{\sigma}$  and external force density  $\mathbf{f}^{ext}$ , the equilibrium condition reads  $\partial/\partial\mathbf{r} \cdot \bar{\sigma} + \mathbf{f}^{ext} = 0$ , or, in the case of an external force per area  $\mathbf{p}$  acting on the system,

$$\sum_{\beta} \sigma_{\alpha\beta} = -p_{\alpha}. \quad (1.33)$$

The work performed by an internal stress  $\bar{\sigma}$  and resulting in a small strain  $\delta\bar{\varepsilon}$  reads

$$W = \int \delta w \, d\mathbf{r} = \int \sum_{\alpha} f_{\alpha} \delta u_{\alpha} d\mathbf{r} = - \int \sum_{\alpha\beta} \sigma_{\alpha\beta} \delta \varepsilon_{\alpha\beta} \, d\mathbf{r}, \quad (1.34)$$

with  $\delta w$  the local work density (per volume).

Thus, one obtains the variation in internal energy density (per volume)  $du = Tds - dw = Tds + \sum_{\alpha\beta} \sigma_{\alpha\beta} d\varepsilon_{\alpha\beta}$ , with  $T$  denoting the temperature,  $s$  the entropy density, and the variation in free energy density  $f = u - Ts$ ,

$$df = sdT + \sum_{\alpha\beta} \sigma_{\alpha\beta} d\varepsilon_{\alpha\beta}. \quad (1.35)$$

Furthermore, Eq. (1.35) implies that

$$\sigma_{\alpha\beta} = \frac{\partial f}{\partial \varepsilon_{\alpha\beta}}. \quad (1.36)$$

The ground state of the material corresponds to vanishing stresses and strains, i.e.,  $\sigma_{\alpha\beta} = 0 = \varepsilon_{\alpha\beta}$ ,  $\alpha, \beta = x, y, z$ . In the regime of small deformations, the free energy density can be expanded in powers of the strain tensor. Therefore, Eq. (1.36) implies that the linear terms of the Taylor series vanish.

Since the free energy density is a scalar and the lowest term of the expansion is quadratic, we need to form independent scalars of second order using the components of  $\bar{\varepsilon}$  if we wish to construct a corresponding expression. One possible choice [82] is

to use the squared trace  $\text{Tr}(\bar{\varepsilon})^2 = (\sum_{\alpha} \varepsilon_{\alpha\alpha})^2$  and the sum of the squared components  $\sum_{\alpha} (\varepsilon_{\alpha\alpha})^2$ . Truncating to second order, we write

$$f = \frac{\lambda}{2} \text{Tr}(\bar{\varepsilon})^2 + \mu \sum_{\alpha\beta} (\varepsilon_{\alpha\beta})^2, \quad (1.37)$$

where  $\lambda$  and  $\mu$  are the *Lamé coefficients*. Furthermore, we can reformulate the free energy density as

$$f = \frac{K}{2} \text{Tr}(\bar{\varepsilon})^2 + \mu \sum_{\alpha\beta} \left[ \varepsilon_{\alpha\beta} - \frac{\delta_{\alpha\beta}}{3} \text{Tr}(\bar{\varepsilon}) \right]^2, \quad (1.38)$$

where  $\delta_{\alpha\beta}$  denotes the Kronecker delta. The *modulus of hydrostatic compression*, or *bulk modulus*,  $K = \lambda + 2\mu/3$  is involved in energy variations only if  $\bar{\varepsilon}$  induces a volume change ( $\text{Tr}(\bar{\varepsilon}) \neq 0$ ). The second term on the right-hand side is the sum of the squared components of  $\bar{\varepsilon} - \mathbf{1} \text{Tr}(\bar{\varepsilon})/3$ . Thus, the *shear modulus*  $\mu$  is related to a zero-trace tensor and leads to energetic changes also under volume-conserving deformations.

The stress tensor then follows via Eq. (1.36) as

$$\sigma_{\alpha\beta} = \delta_{\alpha\beta} K \text{Tr}(\bar{\varepsilon}) + 2\mu \left[ \varepsilon_{\alpha\beta} - \frac{\delta_{\alpha\beta}}{3} \text{Tr}(\bar{\varepsilon}) \right]. \quad (1.39)$$

In the case of *linear elasticity*, i.e., small deformations, the free energy expansion to second order in strain leads to  $\bar{\sigma}$  linear in  $\bar{\varepsilon}$ . Thus, in the linear regime Eq. (1.39) can be inverted, and we obtain

$$\varepsilon_{\alpha\beta} = \frac{\delta_{\alpha\beta}}{9K} \text{Tr}(\bar{\sigma}) + \frac{1}{2\mu} \left[ \sigma_{\alpha\beta} - \frac{\delta_{\alpha\beta}}{3} \text{Tr}(\bar{\sigma}) \right]. \quad (1.40)$$

## 1.5.2 Homogeneous Deformations

Here, we focus on homogeneous deformations. Strain and stress tensors are constant throughout the material and related to each other via Eqs. (1.39) and (1.40). In the simplest case of *hydrostatic compression/expansion*, the stress tensor reads  $\sigma_{\alpha\beta} = p\delta_{\alpha\beta}$  and Eq. (1.40) becomes  $\varepsilon_{\alpha\beta} = p\delta_{\alpha\beta}/3K$ . The relative change in volume is given by

$$\text{Tr}(\bar{\varepsilon}) = \frac{p}{K}, \quad (1.41)$$

and  $K$ , again, is the modulus that directly controls the amount of volume variation.

A prominent homogeneous deformation is the *axial compression/expansion*. In this case, a small external force per area  $\mathbf{p}$  acts along one direction. We set our reference system such that the external stress is compressive along the  $z$ -axis and orient our surface with outward normal unit vector  $\mathbf{n} = \hat{z}$ .  $p_{\alpha} = -p_0\delta_{\alpha z}$ . Thus, on the surface perpendicular to  $\hat{z}$  the equilibrium condition as in Eq. (1.33) reads  $\sum_{\beta} \sigma_{\alpha\beta} n_{\beta} = \sigma_{\alpha z} =$

$-p_\alpha$  and thus  $\sigma_{zz} = p_0$ . On the side surfaces ( $\mathbf{n} \perp \hat{z}$ ) there is no external force, therefore  $\sum_\beta \sigma_{\alpha\beta} n_\beta = 0$  and we obtain  $\sigma_{\alpha\beta} = 0$  for  $\alpha\beta \neq zz$ .

The axial deformations are derived from Eq. (1.40), leading to

$$\varepsilon_{xx} = \varepsilon_{yy} = -\frac{p_0}{3} \left( \frac{3K - 2\mu}{6K\mu} \right) \text{ and } \varepsilon_{zz} = \frac{p_0}{3} \left( \frac{3K + \mu}{3K\mu} \right). \quad (1.42)$$

The ratio  $p_0/\varepsilon_{zz}$ , often measured in rheological investigations [83], is the *Young modulus*

$$E = \frac{p_0}{\varepsilon_{zz}} = \frac{9K\mu}{3K + \mu}, \quad (1.43)$$

and quantifies the resistance of the material to an axial deformation in the linear elastic regime.

In this case, the sample is free to relax in the  $x$  and  $y$  directions. As a result, when the  $z$ -axis compresses/expands, the  $x$ - and  $y$ -lengths widen/contract, respectively. The relaxation hinders volume changes and can be quantified via the *Poisson ratio*

$$\nu = -\frac{\varepsilon_{xx}}{\varepsilon_{zz}} = -\frac{\varepsilon_{yy}}{\varepsilon_{zz}} = \frac{1}{2} \frac{3K - 2\mu}{3K + \mu}. \quad (1.44)$$

Since  $K$  and  $\mu$  are always positive,  $\nu \in [-1, \frac{1}{2}]$ .

### 1.5.3 Elasticity and Compliance Tensors: Voigt Notation

In the case of homogeneous but non-isotropic materials, Eq. (1.39) is generalized to

$$\sigma_{\alpha\beta} = \sum_{\mu\nu} \mathcal{C}_{\alpha\beta\mu\nu} \varepsilon_{\mu\nu} \quad (1.45)$$

with the *elasticity tensor*  $\mathcal{C}$  defined as  $\mathcal{C}_{\alpha\beta\mu\nu} = \partial\sigma_{\alpha\beta}/\partial\varepsilon_{\mu\nu}$ .

Since both the stress and strain tensors have 9 components and are symmetric, only 6 of them are independent. One can represent them in Voigt notation as vectors containing their independent components

$$\begin{aligned} \bar{\sigma} &= (\sigma_{xx}, \sigma_{yy}, \sigma_{zz}, \sigma_{yz}, \sigma_{xz}, \sigma_{xy}) \\ \bar{\varepsilon} &= (\varepsilon_{xx}, \varepsilon_{yy}, \varepsilon_{zz}, 2\varepsilon_{yz}, 2\varepsilon_{xz}, 2\varepsilon_{xy}) \end{aligned}$$

related by the  $6 \times 6$  symmetric matrix  $\mathcal{C}$ :  $\bar{\sigma} = \mathcal{C} \cdot \bar{\varepsilon}$ . In the homogeneous case treated so far in sections 1.5.1 and, 1.5.2, it reads

$$\mathcal{C} = \begin{pmatrix} K + 4\mu/3 & K - 2\mu/3 & K - 2\mu/3 & 0 & 0 & 0 \\ K - 2\mu/3 & K + 4\mu/3 & K - 2\mu/3 & 0 & 0 & 0 \\ K - 2\mu/3 & K - 2\mu/3 & K + 4\mu/3 & 0 & 0 & 0 \\ 0 & 0 & 0 & \mu & 0 & 0 \\ 0 & 0 & 0 & 0 & \mu & 0 \\ 0 & 0 & 0 & 0 & 0 & \mu \end{pmatrix} \quad (1.46)$$

with the symmetries  $\mathcal{C}_{11} = \mathcal{C}_{22} = \mathcal{C}_{33} = K + 4\mu/3$ ,  $\mathcal{C}_{12} = \mathcal{C}_{23} = \mathcal{C}_{13} = K - 2\mu/3$ ,  $\mathcal{C}_{44} = \mathcal{C}_{55} = \mathcal{C}_{66} = \mu$ , and all other vanishing.

The *compliance tensor*  $\mathcal{S}$  is the inverse of the elasticity tensor, i.e.,  $\mathcal{S} \cdot \mathcal{C} = \mathbb{1}$ , with  $\mathbb{1}$  the identity matrix. It relates the resulting strain to a prescribed stress  $\bar{\varepsilon} = \mathcal{S} \cdot \bar{\sigma}$  and reads

$$\mathcal{S} = \begin{pmatrix} 1/E & \frac{(3K-2\mu)}{18K\mu} & \frac{(3K-2\mu)}{18K\mu} & 0 & 0 & 0 \\ \frac{(3K-2\mu)}{18K\mu} & 1/E & \frac{(3K-2\mu)}{18K\mu} & 0 & 0 & 0 \\ \frac{(3K-2\mu)}{18K\mu} & \frac{(3K-2\mu)}{18K\mu} & 1/E & 0 & 0 & 0 \\ 0 & 0 & 0 & 1/\mu & 0 & 0 \\ 0 & 0 & 0 & 0 & 1/\mu & 0 \\ 0 & 0 & 0 & 0 & 0 & 1/\mu \end{pmatrix} \quad (1.47)$$

Its components are also symmetric with  $\mathcal{S}_{11} = \mathcal{S}_{22} = \mathcal{S}_{33} = 1/E$ ,  $\mathcal{S}_{12} = \mathcal{S}_{23} = \mathcal{S}_{13} = (2\mu - 3K)/18K\mu$ ,  $\mathcal{S}_{44} = \mathcal{S}_{55} = \mathcal{S}_{66} = 1/\mu$ , and all others vanishing. It is remarkable that the diagonal elements of  $\mathcal{S}$  are the inverse of the Young and shear moduli. This follows from the fact that, from this perspective, the stress is prescribed and the strain components relax, thus corresponding to the case described in section 1.5.2.

In the following, in Paper IV, and in Paper V, to describe anisotropic materials, we use the following notation for the Young and shear moduli resulting from our numerical calculations:

$$\begin{aligned} E_{xx} &= 1/\mathcal{S}_{11}, & E_{yy} &= 1/\mathcal{S}_{22}, & E_{zz} &= 1/\mathcal{S}_{33}, \\ G_{zy} &= 1/\mathcal{S}_{44}, & G_{zx} &= 1/\mathcal{S}_{55}, & G_{xy} &= 1/\mathcal{S}_{66}. \end{aligned} \quad (1.48)$$

## 1.6 Viscoelasticity

The elastic treatment so far has assumed that we are observing deformation under complete relaxation, with stresses and strains equilibrating each other. In general, however, stress and strain are related via a time-dependent relationship

$$\varepsilon(t) = \int_{t'=-\infty}^{t'=\infty} \chi(t-t') d\sigma(t') = \int_{-\infty}^{\infty} \chi(t-t') \dot{\sigma}(t') dt' \quad (1.49)$$

with  $\sigma$  and  $\varepsilon$  two elements of the stress and strain tensors and  $\chi$  the *linear response function*. Both stress  $\sigma(t)$  and strain  $\varepsilon(t)$  are time-dependent and  $\chi(t-t')$  vanishes for  $t' > t$ . We can write  $\sigma(t)$  and  $\chi(t)$  via their Fourier transform as

$$\sigma(t) = \frac{1}{\sqrt{2\pi}} \int_{-\infty}^{\infty} \sigma(\omega) e^{i\omega t} d\omega \quad \text{and} \quad \chi(t-t') = \frac{1}{\sqrt{2\pi}} \int_{-\infty}^{\infty} \chi(\omega) e^{i\omega(t-t')} d\omega. \quad (1.50)$$

Substituting  $\chi(t-t')$  from Eq. (1.50) in Eq. (1.49), we obtain

$$\varepsilon(t) = \int_{-\infty}^{\infty} i\omega \chi(\omega) \sigma(\omega) e^{i\omega t} d\omega, \quad (1.51)$$

which implies  $\varepsilon(\omega) = i\omega\sigma(\omega)\chi(\omega)$ .

We define the dynamic (complex) modulus  $E(\omega)$  as the ratio between stress and strain amplitudes in the frequency domain

$$E(\omega) = \frac{\sigma(\omega)}{\varepsilon(\omega)} = \frac{1}{i\omega \chi(\omega)}. \quad (1.52)$$

It represents the ratio of stress and strain amplitudes in the case of a single-frequency oscillating deformation and in the stationary regime. It is composed of *storage* and *loss* moduli  $E(\omega) = E'(\omega) + iE''(\omega)$  corresponding, respectively, to the real and imaginary parts. The former is related to the elastic time-dependent deformation, whereas the latter provides a dissipative contribution. The phase lag  $\delta(\omega) = \arctan[E''(\omega)/E'(\omega)]$  is the oscillation delay between driving stress and strain response in the stationary regime.

### 1.6.1 Hookean and Dashpot Elements

The basic elements to model viscoelasticity are springs and dashpots [84]. The former, stylized in panel a) of Fig. 1.10 correspond to elastic elements of Young modulus  $E$ . When the relaxation rates are much quicker than the ones over which the corresponding stress  $\sigma_E(t)$  and strain  $\varepsilon_E(t)$  vary, the Hookean model describes a one-dimensional, time-dependent stress-strain relation equivalent to Eq. (1.45)

$$\sigma_E(t) = E\varepsilon_E(t). \quad (1.53)$$

Over short timescales, instead, the dashpot model represented in panel b) of Fig. 1.10 resists a constant deformation by opposing a stress  $\sigma_\eta(t)$  proportional to the strain rate  $\dot{\varepsilon}_\eta(t)$ . Such a resistance is related to an effective viscosity  $\eta$  of the material and leads to the following stress-strain relationship:

$$\sigma_\eta(t) = \eta\dot{\varepsilon}_\eta(t). \quad (1.54)$$

Here, the dot indicates a time derivative.

### 1.6.2 Kelvin-Voigt Model

The Hookean and dashpot models describe, respectively, completely elastic or viscous material responses. More realistic macroscopic models combine these two ingredients multiple times in series or in parallel to describe viscoelastic systems [84].

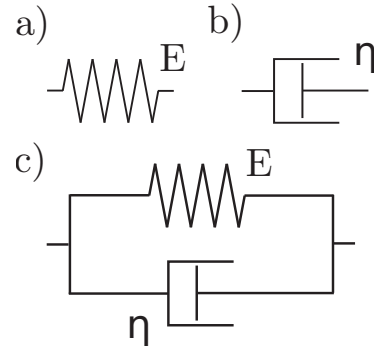


Figure 1.10: Basic rheological elements: a) elastic Hookean element of modulus  $E$ , b) dashpot of viscosity  $\eta$ , and c) Kelvin-Voigt model.

The two simplest combinations of the above described elements are obtained by setting them either in series or in parallel and are called *Maxwell* and *Kelvin-Voigt* models, respectively. For crosslinked polymeric materials, i.e., elastomers, the former describes well the short-time behavior, whereas the latter is particularly appropriate for the long-time behavior. In the following we will describe only the Kelvin-Voigt model because, as we will show, it reflects the dynamics of the normal modes in our dipole–springs systems.

The Kelvin-Voigt model is composed of an elastic and a dashpot in parallel, see panel c), Fig. 1.10. Therefore, each element adds to the total stress  $\sigma(t) = \sigma_E(t) + \sigma_\eta(t)$ . On the contrary, the strains are equal because both ends of the elements are constrained together:  $\varepsilon(t) = \varepsilon_E(t) = \varepsilon_\eta(t)$ . By using the relationships for spring and dashpot as in Eqs. (1.53) and (1.54), we obtain

$$\sigma(t) = E\varepsilon_E(t) + \eta\dot{\varepsilon}_\eta(t) = E\varepsilon(t) + \eta\dot{\varepsilon}(t) \quad (1.55)$$

Taking the Fourier transform on both sides leads us to the expression for the dynamic Kelvin-Voigt modulus

$$E(\omega) = \frac{\sigma(\omega)}{\varepsilon(\omega)} = E + i\omega\eta. \quad (1.56)$$

It describes a material which is basically a solid over the longer times (low- $\omega$  limit) and of constant viscosity. Furthermore, it predicts a crossing point between storage and loss parts of the dynamic moduli, which occurs at  $\omega_c = E/\eta$ . This is a typically accurate description of elastomers in the low- $\omega$  regime [85–87]. Finally, the complex dynamic modulus  $E(\omega)$  is typically denoted by real and imaginary parts as  $E(\omega) = E' + iE''$ , i.e., storage and loss moduli. In the Kelvin-Voigt model,  $E' = E$  and  $E'' = \eta\omega$ .

## 1.7 Elasticity of Spring Lattices

The main property of elastomers is the their elastic, reversible deformability. Since we study our systems near equilibrium, every displacement or deformation contributes, to lowest order, quadratically to the elastic energy. Therefore, it is natural to represent our material via a network of linear springs.

As a first step, we investigate the properties of regular spring networks arranged on regular lattices. The network nodes correspond to lattice sites and the springs are set onto neighbor-connecting vectors. The deformational energy and force of a linear spring connecting two network nodes via the vector  $\mathbf{r}$  read, respectively,

$$v^{el}(\mathbf{r}) = \frac{K^{spr}}{2}(r - \ell^0)^2 \quad \text{and} \quad -\frac{\partial v^{el}}{\partial r^\alpha}(\mathbf{r}) = -K^{spr}(r - \ell^0)\frac{r^\alpha}{r} \quad (1.57)$$

with  $r = |\mathbf{r}|$ ,  $K^{spr}$  the elastic constant of the spring,  $\ell^0$  its initial length, and  $\alpha = x, y, z$ . Additionally,  $K^{spr}/\ell^0$  represents the Young modulus of the spring.

When the springs are set on a network with nodes located at  $\mathbf{R}_i$  ( $i = 1 \dots N$ ), the total elastic energy and forces  $\mathbf{F}_i$  are given by the contributions of all springs

$$U^{el} = \frac{1}{2} \sum_{\substack{i,j=1 \\ j \neq i}}^N v^{el}(r_{ij}) \quad \text{and} \quad F_i^\alpha = -\frac{\partial v^{el}}{\partial R_i^\alpha}(\mathbf{R}_i) = \sum_{\substack{j=1 \\ j \neq i}}^N \frac{\partial v^{el}}{\partial r_{ij}^\alpha}(\mathbf{r}_{ij}) \quad (1.58)$$

with  $\mathbf{r}_{ij} = \mathbf{R}_j - \mathbf{R}_i$ ,  $r_{ij} = |\mathbf{r}_{ij}|$ , and as further detailed in appendices B and C of Paper IV. Finally, we give the expression for the Hessian matrix of the total energy, the elements of which read

$$\mathcal{H}_{ij}^{\alpha\beta} = \frac{\partial^2 U^{el}}{\partial R_i^\alpha \partial R_j^\beta} = \begin{cases} -\frac{\partial^2 v_{ik}^{el}}{\partial r_{ik}^\alpha \partial r_{ik}^\beta} & (i \neq k), \\ \sum_{\substack{j=1 \\ j \neq i}}^N \frac{\partial^2 v_{ij}^{el}}{\partial r_{ij}^\alpha \partial r_{ij}^\beta} & (i = k). \end{cases} \quad (1.59)$$

It involves calculation of the second derivatives of the pair harmonic interaction

$$\frac{\partial^2 v^{el}}{\partial r^\beta \partial r^\alpha} = K^{spr} \left[ \frac{r^\alpha r^\beta}{r^2} + (r - \ell^0) \frac{\delta^{\alpha\beta} r^2 - r^\alpha r^\beta}{r^3} \right]. \quad (1.60)$$

In practice, when all the degrees of freedom are arranged into a  $3N$ -dimensional vector  $|\mathbf{R}\rangle$ , the Hessian  $\mathcal{H}$  is represented by a  $3N \times 3N$  matrix.

In the following, we start by static considerations. That is, we consider systems that are given the time to undergo complete relaxation of the energy  $U$  (for a spring network and in the absence of other interactions,  $U = U^{el}$ ) given by the condition

$$\frac{\partial U^{el}}{\partial R_i^\alpha} = 0 \quad (i = 1 \dots N, \alpha = x, y, z). \quad (1.61)$$

Moreover, in our mesoscopic calculation we consider systems undergoing complete relaxation and in the absence of thermal fluctuations.

The elasticity tensor is defined, for a system in equilibrium, as [88]:

$$\mathcal{C}_{\alpha\beta\mu\nu} = \frac{1}{V} \frac{\partial^2 U^{el}}{\partial \varepsilon_{\alpha\beta} \partial \varepsilon_{\mu\nu}} \quad (1.62)$$

with  $V$  the volume of the system,  $\varepsilon_{\alpha\beta}$  the strain tensor, and  $\alpha, \beta, \mu, \nu = x, y, z$ .

If the network is deformed homogeneously and a primitive lattice cell can be defined (springs included) in a way that the whole network can be constructed by periodically repeating it, we may define the energy per lattice-cell as

$$U_c = \frac{U^{el}}{N_c} = \frac{1}{2} \sum_{n \in \mathcal{N}_0} v^{el}(\mathbf{r}_n) \quad (1.63)$$

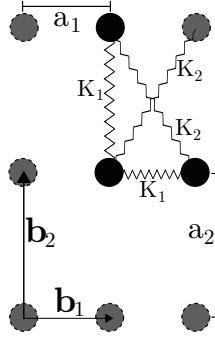


Figure 1.11: Rectangular lattice of parameters  $a_1$  and  $a_2$ . Springs of constant  $K_1$  and  $K_2$  are set along nearest- and next-nearest neighbors.

where  $N_c$  is the total number of cells,  $v^{el}$  is the pair potential, and the sum is over the set  $\mathcal{N}_0$  identifying lattice sites the connecting springs of which are included in the primitive cell.

Thus, we introduce the volume of the cell  $V_c$  such that  $V = V_c N_c$  and, as described similarly in appendix E of Paper IV, we obtain the following expression for the elasticity tensor

$$\mathcal{C}_{\alpha\beta\mu\nu} = \frac{1}{2V_c} \sum_{n \in \mathcal{N}_0} r_n^\alpha \frac{\partial^2 v^{el}(\mathbf{r}_n)}{\partial r^\beta \partial r^\mu} r_n^\nu. \quad (1.64)$$

From this point, the Young and shear moduli can be derived in two equivalent ways. One possibility, as described in appendix E of Paper IV, is to compute Eq. (1.64) with the additional conditions of complete relaxation for remaining elements of  $\bar{\varepsilon}$ . Alternatively, one can compute the compliance tensor  $\mathcal{S}$  by inversion of  $\mathcal{C}$  and then look at the reciprocal of its diagonal elements, see Eq. (1.47). The two methods are equivalent since both prescribe a stress applied along one direction and allow relaxation for the remaining ones.

### 1.7.1 Square and Rectangular Lattices

The simplest case is represented by two-dimensional square and rectangular lattices. The elastic moduli have the unit of measure of a stress, which, in turn, is defined as a force divided by the measure of the boundary on which it is applied. Thus, elastic moduli and stresses in 2D have the dimension of force over length.

The rectangular spring network is generated by the lattice vectors  $\mathbf{b}_1 = (a_1, 0)$  and  $\mathbf{b}_2 = (0, a_2)$ . Furthermore, the volume (area)  $V_c$  of the unit cell is given by  $V_c = a_1 \cdot a_2$  and we denote by  $d^2 = a_1^2 + a_2^2$  the square of the cell diagonal. We set vertical and horizontal springs of elastic constant  $K_1$  between nearest neighbors and diagonal springs of constant  $K_2$  between second-nearest neighbors (diagonally across the unit cell) as depicted in Fig. 1.11. The rectangular lattice has one lattice site per unit cell.

Furthermore, there are on average one horizontal, one vertical, and two diagonal springs per cell, see Fig. 1.11. In Voigt notation we write  $\bar{\sigma} = (\sigma_{xx}, \sigma_{yy}, \sigma_{yz})$ ,  $\bar{\varepsilon} = (\varepsilon_{xx}, \varepsilon_{yy}, 2\varepsilon_{yz})$ , and  $\bar{\sigma} = \mathcal{C} \cdot \bar{\varepsilon}$ . The elasticity tensor  $\mathcal{C}$  for a homogeneous lattice deformation is obtained from Eq. (1.64) and reads

$$\mathcal{C} = \begin{pmatrix} \frac{a_1}{a_2} K_1 + \frac{2a_1^3}{a_2 d^2} K_2 & \frac{2a_1 a_2}{d^2} K_2 & 0 \\ \frac{2a_1 a_2}{d^2} K_2 & \frac{a_2}{a_1} K_1 + \frac{2a_2^3}{a_1 d^2} K_2 & 0 \\ 0 & 0 & \frac{2a_1 a_2}{d^2} K_2 \end{pmatrix}. \quad (1.65)$$

We immediately notice that neglecting diagonal springs ( $K_2 = 0$ ) leads to  $\mathcal{C}_{33} = 0$ , which implies that the system is basically unstable under shear deformations. This soft-shear mode follows from the lack of diagonal springs. Nevertheless, such an omission is found in the literature [89].

The Young and shear moduli result from the reciprocal of the diagonal elements of the compliance tensor  $\mathcal{S} = \mathcal{C}^{-1}$ , with  $^{-1}$  indicating the inverse matrix. We find the Young and shear moduli to be, respectively,

$$E_{xx} = \frac{1}{\mathcal{S}_{11}} = \frac{a_1}{a_2} K_1 \frac{K_1 + 2K_2}{K_1 + 2\frac{a_2^2}{d^2} K_2}, \quad (1.66)$$

$$E_{yy} = \frac{1}{\mathcal{S}_{22}} = \frac{a_2}{a_1} K_1 \frac{K_1 + 2K_2}{K_1 + 2\frac{a_1^2}{d^2} K_2}, \quad (1.67)$$

$$G_{xy} = \frac{1}{\mathcal{S}_{33}} = \mathcal{C}_{33} = \frac{2a_1 a_2}{d^2} K_2. \quad (1.68)$$

A numerical evaluation of the Young moduli of rectangular spring networks was described in Paper III. There, the elastic moduli are calculated for different aspect ratios and system sizes. Moreover, two numerical schemes are implemented: affine and non-affine deformations. Affine transformations (AT) rescale distances along each direction by a fixed ratio, see Fig. 1.12 bottom left panel. Thus, in 2D, axial affine deformation can be described via two independent degrees of freedom: axial strain along the  $x$ - and axial strain along the  $y$ -direction. Non-affine transformations (NAT), instead, allow every degree of freedom (here, each lattice site) to move independently, see Fig. 1.12 top left panel and relative inset.

We prescribe the boundaries of the systems in Fig. 1.12, right panel, to undergo a small, prescribed amount of displacement in the  $x$ -direction, while the remaining degrees of freedom relax. Then, the elastic moduli follow from Eq. (3) of Paper III, which corresponds to the second derivative of the energy with respect to the boundary displacement. For comparison with our above considerations, Eqs. (3) and (4) in Paper III need to be multiplied by an additional geometrical prefactor  $a_1/a_2$ , the base/height aspect ratio in our case. This makes them scale correctly with the shape of the undeformed unit cell or of the overall undeformed network. Since NAT allow for more degrees of freedom and thus more relaxation compared to AT, the Young moduli calculated for the former

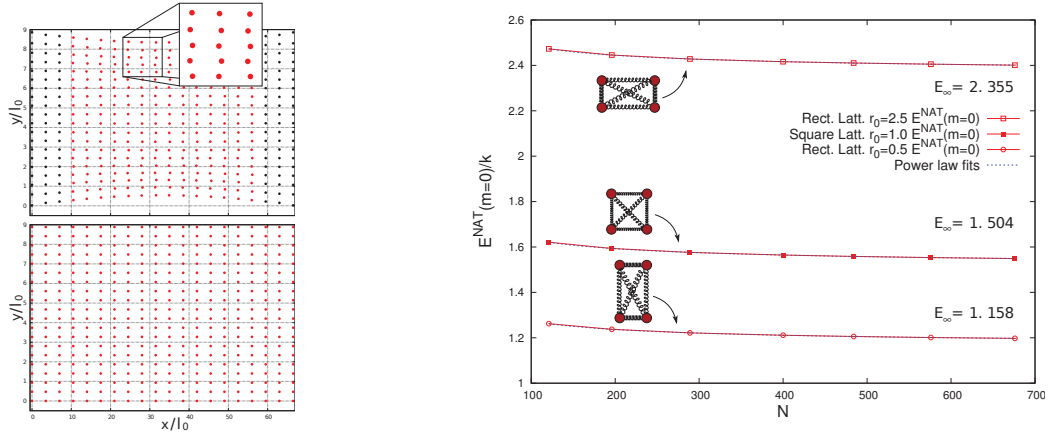


Figure 1.12: Examples of non-affine (NAT, top left panel) and affine transformations (AT, bottom left panel) for an imposed amount of strain  $\epsilon_{xx} = 1.5$  along the  $x$ -direction. The large amount of axial strain is chosen to enhance and demonstrate the non-affinity of the displacements, see inset. Right-side panel: Non-affine Young modulus  $E^{NAT}$  along the  $x$ -direction of finite-sized rectangular spring networks for different aspect ratios  $r_0 = a_1/a_2$  and with increasing number of lattice sites. Fits with a power law  $E_N/k = E_\infty + \alpha N^\beta$  and resulting  $E_\infty$  fit parameters are shown. Reproduced from Ref. 90 with permission. © AIP Publishing. All rights reserved.

( $E^{NAT}$ ) are always lower than the affine ones ( $E^{AT}$ ). Therefore, affine transformations generally result in stiffer moduli, i.e.,  $E^{AT} \geq E^{NAT}$ .

In the limit of large systems, and in the case of regular spring networks, the two methods converge to the same limit, see Tab. 1.1. From the fit of the non-affine Young moduli with increasing number of lattice sites  $N$ , we extrapolate the asymptotic value it converges to,  $E_\infty$ . Comparison between Eq. (1.66) and the fit-obtained  $E_\infty$  multiplied by the appropriate geometrical factor, see Tab. 1.1, indicates excellent agreement between our numerical methods and the analytical limit, thus confirming the validity of our numerical results.

	$E_\infty$ , Paper III	$E_{xx}$ , Eq. (1.66)		
$a_1/a_2 = 5/2$	$5.888 k$	$435 k/74$	$\simeq$	$5.878 k$
Square ( $a_1 = a_2$ )	$1.504 k$	$3 k/2$	$=$	$1.5 k$
$a_1/a_2 = 1/2$	$0.579 k$	$15 k/26$	$\simeq$	$0.577 k$

Table 1.1: Young moduli along the  $x$ -direction for rectangular lattices of different aspect ratios. Comparison with fit data in Fig. 1.12 must take into account an additional geometrical multiplicative factor  $a_1/a_2$ , in this table already included.

### 1.7.2 Cubic Lattice

The 3D cubic lattice is generated by the basis vectors  $\mathbf{b}_1 = (a, 0, 0)$ ,  $\mathbf{b}_2 = (0, a, 0)$ , and  $\mathbf{b}_3 = (0, 0, a)$ . The cubic lattice has one lattice site per unit cell, the volume of which is  $V_c = a^3$ . To each cell belong nine springs: one of initial length  $a$  for each basis vector and two diagonal ones of length  $a\sqrt{2}$  for each face of the cubic cell. Similarly to the rectangular/square 2D lattice case, we set springs of elastic constant  $K_1$  along the nearest neighbors, i.e., the three basis vectors and  $K_2$  between second-nearest neighbors along the face diagonals of the cells.

The elasticity tensor follows from Eq. (1.64). In Voigt notation it reads

$$\mathcal{C} = \frac{1}{a} \begin{pmatrix} K_1 + 2K_2 & K_2 & K_2 & 0 & 0 & 0 \\ K_2 & K_1 + 2K_2 & K_2 & 0 & 0 & 0 \\ K_2 & K_2 & K_1 + 2K_2 & 0 & 0 & 0 \\ 0 & 0 & 0 & K_2 & 0 & 0 \\ 0 & 0 & 0 & 0 & K_2 & 0 \\ 0 & 0 & 0 & 0 & 0 & K_2 \end{pmatrix}. \quad (1.69)$$

In the three-dimensional case, again, we find that neglecting second-nearest neighbor springs ( $K_2 = 0$ ) [89], leads to vanishing shear moduli and a system unstable under shear.

The Young moduli, because of the symmetries of the cubic lattice, are equivalent along the three Cartesian directions. Likewise, because of the symmetry under  $\pi/2$ -rotations, the shear moduli in the  $xy$ ,  $xz$ , and  $yz$  geometries are equal. This leads to

$$E_{xx} = E_{yy} = E_{zz} = \frac{1}{a} \frac{(K_1 + K_2)(K_1 + 4K_2)}{K_1 + 3K_2}, \quad (1.70)$$

$$G_{zy} = G_{zx} = G_{xy} = \frac{K_2}{a}. \quad (1.71)$$

In the case described in section VIII of Paper IV, we set the lattice parameter  $a = l_0$ ,  $K_1 = k/|\mathbf{b}_1| = k/l_0$  the nearest-neighbor interaction, and  $K_2 = k/|\mathbf{b}_1 + \mathbf{b}_2| = k/l_0\sqrt{2}$  the second-nearest neighbor elastic constant. This leads to  $E = (9 + 4\sqrt{2})/7 k/l_0^2 \simeq 2.094 k/l_0^2$ . The result is in good agreement with the Young modulus  $E \simeq 2.17 k/l_0^2$  calculated in Paper IV for a  $15 \times 15 \times 15$  cubic lattice, see also Fig. 1.16 below.

### 1.7.3 Face-Centered-Cubic Lattice

A three-dimensional face-centered-cubic (fcc) lattice is generated by the basis vectors  $\mathbf{b}_1 = (a, a, 0)$ ,  $\mathbf{b}_2 = (0, a, a)$ , and  $\mathbf{b}_3 = (a, 0, a)$ . Springs of constant  $K_1$  are set between nearest neighbors. Each cell contains, on average, four lattice sites, twelve springs, and has volume  $2a^3$ .

From Eq. (1.64) we write the elasticity tensor in Voigt notation

$$\mathcal{C} = \frac{1}{2a} \begin{pmatrix} 2K_1 & K_1 & K_1 & 0 & 0 & 0 \\ K_1 & 2K_1 & K_1 & 0 & 0 & 0 \\ K_1 & K_1 & 2K_1 & 0 & 0 & 0 \\ 0 & 0 & 0 & K_1 & 0 & 0 \\ 0 & 0 & 0 & 0 & K_1 & 0 \\ 0 & 0 & 0 & 0 & 0 & K_1 \end{pmatrix}. \quad (1.72)$$

Here, there is no need to introduce additional springs between others than the nearest neighbors to obtain a stable network.

Because of the fcc lattice symmetries, the three main Young and shear moduli are all equivalent and result

$$E_{xx} = E_{yy} = E_{zz} = \frac{2}{3} \frac{K_1}{a}, \quad (1.73)$$

$$G_{zy} = G_{zx} = G_{xy} = \frac{K_1}{2a}. \quad (1.74)$$

In section IX of Paper IV, we set  $K_1 = k/|\mathbf{b}_1| = k/a\sqrt{2}$  as well as  $a = 2^{-1/3}l_0$ . This leads to  $E = (2^{7/6}/3) k/l_0^2 \simeq 0.748 k/l_0^2$ . The result is in excellent agreement with the Young modulus  $E \simeq 0.75 k/l_0^2$  calculated in Paper IV for an fcc lattice of  $9 \times 9 \times 9$  cells.

### 1.7.4 Scaling of the Spring Constants

As a final remark, in Paper V we describe the polymer matrix via a randomized fcc spring network. Each spring constant scales proportionally to the initial length of the spring, i.e.,  $K^{spr} = k\ell^0$ , compare to Eq. (1.57). The stiffness of a block of elastomer, here, between two particles, depends on the ratio between cross-section and length. It is thus proportional to the typical distance between two particles. As a consequence,  $k$  sets the spring constant per unit length of each single spring as well as the natural unit of measure of the overall elastic moduli. Indeed, our numerical tests confirm that, with decreasing mesh size of the spring network, this scaling of the elastic constants yields converging elastic moduli.

This scaling, however, can be likewise deduced from Eqs. (1.69) and (1.72). Our scope is to build a spring network that mimics the polymer matrix. The embedded particles are much bigger than the polymeric mesh size and basically experience it as an elastic continuum. Therefore, the elastic moduli of the overall spring network must not depend on the mesh size of the network. Thus, in order that the elastic moduli not depend on  $a$ , the elastic constants in Eqs. (1.69) and (1.72) must scale like  $K_1, K_2 \propto a$ .

## 1.8 Ferrogels and Magnetoelastomers

Ferrogels and Magnetoelastomers [2, 30–33, 91] are hybrid materials obtained by embedding magnetic particles in a polymeric elastic matrix. They combine the elastic, reversible deformability typical of polymeric gels and rubbers [3, 92] with the characteristic responsiveness to magnetic fields of ferrofluids [21, 22]. The interest in these materials is prompted by a unique range of possible applications, e.g., soft actuators [93, 94], tunable vibration absorbers [95, 96], adjustable damping devices [97], magnetic field sensors [98, 99], electromagnetic screens [100], or acceleration detectors [51, 101].

The central feature of magneto-elastic materials is the “magneto-mechanical” coupling [36–38]. Such a coupling emerges, for instance, when a polymer solution, in which magnetic particles of mesoscopic size are dispersed, is crosslinked. After the curing process, the polymers form an interconnected three-dimensional network. The magnetic particles can be, for instance, chemically bound to the polymer network or simply trapped in it, because their size is typically much larger than the mesh spacing [36, 102, 103]. In this way, when the particles interact with an external magnetic field or with each other, they are subject to forces and torques, which are then transmitted to the matrix. The matrix, in turn, acts as a medium transmitting elastic interactions [79–81].

As a consequence, magnetic interactions directly affect strain [40–43, 104] and elastic moduli [10, 11, 44–50] of the hybrid material. Other properties, e.g., relaxation times [105], resonance frequency [51], or electrical impedance [52], can as well be tuned by applying external fields. Additional examples of characteristic behaviors are the buckling of chains of particles [12], superelasticity [106, 107], or reversal of the magnetic stiffening effect at different oscillating frequencies, see Paper IV and Paper V.

The main features of these materials, however, are the variations in shape and stiffness in response to external magnetic fields. These two aspects have often been observed and measured in experiments [10, 11, 40–50, 104] and modeled in theory. Macroscopic theory [38, 98, 108–111] usually treats both the elastomer and the magnetic particles as a homogeneous continuum. Finite-element methods [39, 112–115] also treat both elements as continua but can spatially resolve the two components. Mesoscopic models can resolve the individual magnetic particles and usually coarse-grain the polymer matrix, representing it via a homogeneous continuum [116], networks of springs [Paper III, Paper IV, Paper V], or meshes of almost-incompressible tetrahedra [106, 107]. Some models are even more detailed and resolve both magnetic particles and individual polymer chains. The latter are typically modeled by chains of beads, each representing a small, coarse-grained piece of polymer [67, 117], see also Paper I.

In the following, we describe the deformation and stiffening (or softening) effects in mesoscopic dipole–spring models. The great strength of this approach consists in allowing to resolve the particle arrangement and estimate its impact on the material properties. We set all the dipoles aligned along the same direction. This situation is representative, for instance, of paramagnetic particles in a strong external field or ferromagnetic particles in a saturating external field. The elastic polymer matrix is here

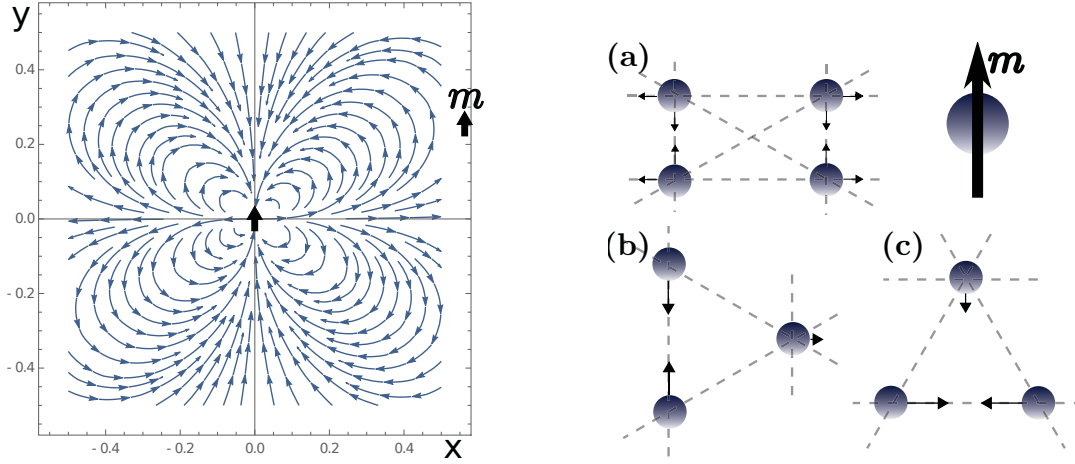


Figure 1.13: (LEFT) Lines of force resulting from the dipole–dipole interaction on one dipole at position  $(x, y)$ , see Eq. (1.11), while another dipole is centered in the origin, and are both aligned in the  $y$ -direction. (RIGHT) Initial displacement upon switching on the magnetic moment  $\mathbf{m} \parallel \hat{y}$  (color gradient) in (a) rectangular and (b, c) triangular with (b) vertical or (c) horizontal rows of dipoles on the dipole–spring lattices.

represented by a network of springs. In Paper III and Paper IV the springs directly connect the centers of the particles, whereas in Paper V we set extra network nodes homogeneously in the interparticle spaces.

### 1.8.1 2D and 3D Field-Induced Deformation

The deformation of magnetoelastomers under external magnetic fields has been observed since the very early experiments [40, 104, 118]. In the case of a homogeneous external magnetic field, the phenomenon is called “magnetostriction” [41] or “magnetodipolar striction” [39]. It can result in elongation [98, 119] or contraction [120, 121] along the field direction. Two-dimensional dipole–spring models help us understand the dipole–dipole contribution to magnetostriction in the linear elasticity regime. For simplicity we will assign identical dipole moments to all particles and set them aligned along the  $y$ -direction to represent a system with a finite net magnetization.

In the simplest, exemplary case of magnetic particles arranged on a rectangular lattice, see Fig.1.13 (a), the kind of deformation is, for small magnetic moments  $\mathbf{m}$ , determined by the nearest-neighbor orientation. When  $\mathbf{m}$  is set parallel to the nearest neighbor vector (i.e., parallel to  $\hat{y}$ ), the particles attract each other along the  $\mathbf{m}$ -direction and repel each other perpendicularly to that, see Fig. 1.13, left-side panel. This leads to a contraction of the lattice along  $\mathbf{m}$  and transversal expansion. The perpendicular extension to  $\mathbf{m}$  is caused by the elastic response of the spring network to the axial contraction as well as by the dipole–dipole direct repulsion.

The behavior of triangular lattices depends strongly on the relative orientation of lattice and magnetic moments. In the case of a triangular lattice with rows parallel to  $\mathbf{m}$ , see Fig. 1.13 (b), the direct attraction in the  $y$ -direction dominates and causes a contraction, with only a lesser impact on transversal deformation. Interestingly, the triangular lattice with rows perpendicular to  $\mathbf{m}$  shows more complex behaviors. Albeit the nearest neighbors along the  $x$ -direction repel each other, the overall tendency is to align with the neighbors along the  $y$ -direction. As a result, the lattice shrinks in *both* the  $x$ - and  $y$ -direction. The deformation in the  $x$ -direction is, however, larger than along  $y$  and as a result the overall aspect ratio stretches in the  $\mathbf{m}$ -direction. In this case the main deformation drive is the tendency of the moments to align along the  $\mathbf{m}$ -direction. This differs from the cases (a) and (b) of Fig. 1.13 because there the moments of the neighbors are already aligned and this leads directly to contraction.

The two-dimensional cases are helpful to understand the three-dimensional deformations. In 3D we conventionally set  $\mathbf{m}$  oriented along the  $z$ -direction. As expected, the cubic lattice shrinks in the  $\mathbf{m}$ -direction for  $\mathbf{m} \parallel \mathbf{b}_3$ , see section VIII of Paper IV, and expands in the perpendicular directions, analogously to a 2D rectangular lattice. Interestingly, the fcc lattice elongates along  $\mathbf{m}$ , see section IX of Paper IV, and contracts transversally. This, as in the case of the triangular lattice with horizontal rows, happens because the configuration of dipoles aligned along  $\mathbf{m}$  is energetically favored.

Finally, the more realistic case of disordered distributions was studied in both Paper IV and Paper V with similar approaches. In particular, the distributions studied in Paper V with resulting deformations showed in Fig. 1.14, are acquired from experimental measurements on samples characterized by homogeneous, isotropic particles distributions. In both cases we observe, for large enough magnetic interactions, an overall contraction of the system in all directions, see Fig. 12 of Paper IV. This deformation is promoted by the formation of hardened [74] chain-like aggregates, see Fig. 1.14, left panel, and section X A of Paper IV. It results in extensive changes in the system structure. Interestingly, for small strength of magnetic interactions, see Fig. 1.14, right panel, inset (a), the investigated isotropic sample with high volume fraction shows a trend of elongation along  $\mathbf{m}$ .

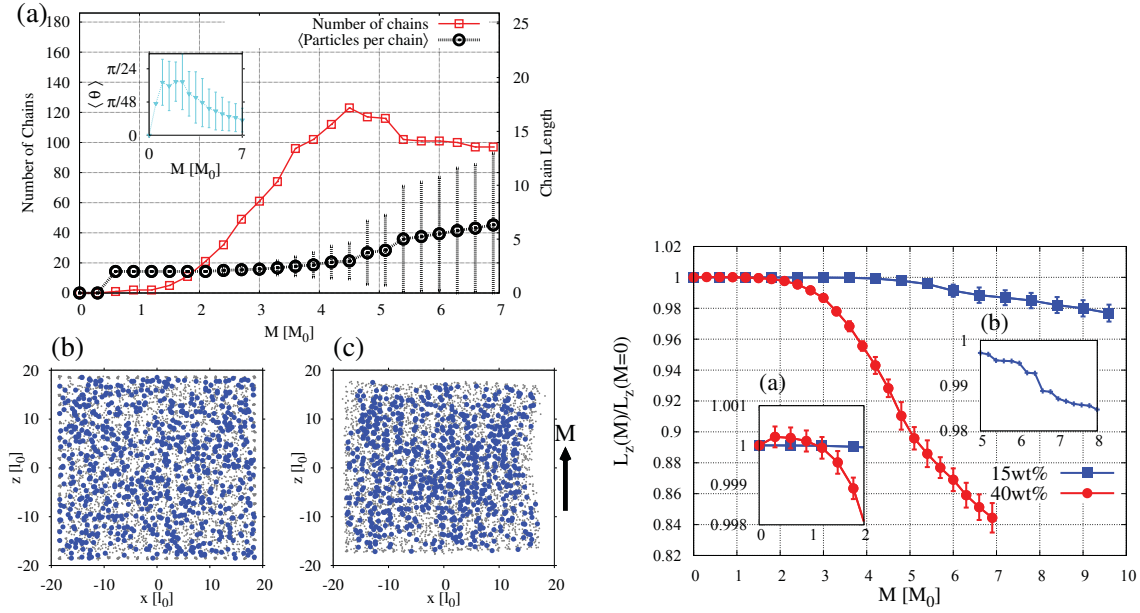


Figure 1.14: (LEFT) (a) contraction and chain formation in a homogeneous, isotropic distribution of magnetic particles in an elastic matrix under increasing magnetization  $M = |\mathbf{M}|$ , expressed in reduced units of  $M_0$ , see Paper V. The particle arrangement was extracted by X-ray micro-computed tomography from a real experimental sample of 40 wt% of magnetic particles. The number of chain-like aggregates refers to the scale on the left ordinate and their average length on the right ordinate. The inset depicts the average angle between the chains and the magnetization direction. On the panels below we show the system (b) initially and (c) under full magnetic interactions. (RIGHT) Magnetostriction of isotropic particle arrangements (see left panel) of volume fraction of 2.3% (15 wt%) and 5.6% (40 wt%). Inset (a): initial elongation for small strength of magnetic interactions. Inset (b): exemplary deformation driven by discrete events of aggregating pairs. Reproduced from Ref. 122.

### 1.8.2 Static Elastic Moduli

The case of two-dimensional arrangements of particles can be very helpful to understand the mechanisms behind the variations in stiffness effect in the presence of an external magnetic field. Here, we consider the dipolar particles and the spring network lying onto the  $x$ - $y$  plane. The Young modulus is measured for imposed deformations along the  $x$ -direction (indicated by the axis labeled by  $\varepsilon$  in Fig. 1.15). First, if the magnetic moment  $\mathbf{m}$ , identical for all particles, is set perpendicular to the plane, the Young modulus always increases, see section IV E of Paper III. When  $\mathbf{m}$  is, instead, set along the  $x$ -direction, the modulus has an increasing trend only for aspect ratios above a certain threshold ( $r_0 \gtrsim 1.9$ ), see Fig. 1.15.

This changing behavior is determined by the orientation of the nearest neighbors. In the case  $r_0 = 2.5$  of Fig. 1.15, the distance between the nearest neighbors perpendicular to  $\mathbf{m}$  ( $y$ -direction) is much smaller than along the  $\mathbf{m}$ -direction. Thus, the strongest magnetic interactions for this geometry are repulsive and here the modulus shows a clear trend of initial increase with  $m = |\mathbf{m}|$ . Contrariwise, for lower  $r_0$ , the neighboring distance in the  $\mathbf{m}$ -direction becomes smaller. In this regime, the modulus is always decreasing with  $m$ . This effect happens in a similar fashion for  $r_0 \gtrsim 1.9$  at higher  $m$ -values. There, strong magnetic attraction has deformed the initial structure and reduced the aspect ratio.

Let us consider the dipole–dipole potential as in Eq. (1.10) for two neighboring dipolar particles with  $\mathbf{m}_1 = \mathbf{m}_2 = \mathbf{m}$  separated by the vector  $\mathbf{r}$ . On the one hand, when the dipoles are parallel and arranged side-by-side,  $\mathbf{m} \cdot \mathbf{r} = 0$  and the potential reduces to  $v^{dd} = +\mu_0 m^2 / 4\pi r^3$ . On the other hand, if  $\mathbf{m} \parallel \mathbf{r}$ , the dipole–dipole attraction is stronger in magnitude by a factor 2 and reads  $v^{dd} = -2\mu_0 m^2 / 4\pi r^3$ .

The crucial point is that the second derivative  $v^{dd}{}''(r)$  of the dipole–dipole potential is positive in the repulsive case and negative in the attractive case. Thus, since the elastic moduli are essentially related to the second derivatives of the energy, see Eq. (1.62), prevailing repulsive interactions make the energy landscape around the equilibrated state more convex with increasing  $m$ . Attractive dipole–dipole interactions, instead, contribute negatively with increasing  $m$  to the overall second derivatives of the total energy, leading to decreasing elastic moduli. This is evidenced in Fig. 1.15 by the

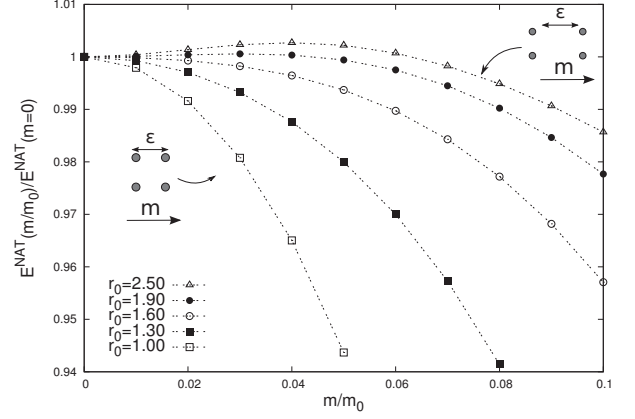


Figure 1.15: Normalized Young modulus of rectangular dipole–spring networks with varying aspect ratios  $r_0$  for increasing strength of the magnetic moments  $\mathbf{m}$ , rescaled by our reduced unit  $m_0$ . Reproduced from Ref. 90 with permission. © AIP Publishing. All rights reserved.

cases of  $r_0 \gtrsim 1.9$ , in which repulsion is dominant, and  $r_0 \lesssim 1.9$ , for which magnetic attraction is preponderant instead.

Summarizing, we have drawn a connection between the second derivatives of the interactions and the elastic moduli. The simplified, exemplary, two-dimensional case gives us the right insight to investigate 3D cases. To understand stiffening in three dimensions, it is useful to begin with the cubic lattice, which is the natural extension of the rectangular case discussed above.

The magnetic moments, equal for all particles, are set along the lattice generating vector  $\mathbf{b}_3$ , see section 1.7.2, i.e., along the  $z$ -direction. Thus, interactions along the  $z$ -axis are attractive and in the  $x$ - and  $y$ -direction repulsive. As a consequence, following the argument above, we expect the Young modulus in the  $z$ -direction to decrease. Indeed, as shown in Fig. 1.16 (a), the Young modulus  $E_{zz}(m)$ , see Fig. 1.17, decreases with increasing strength of magnetic interactions. In the transversal directions,  $E_{xx}(m)$  and  $E_{yy}(m)$  have an increasing trend, which we attribute to the dipole–dipole repulsion along the  $x$ - and  $y$ -directions.

As already observed in section 1.7.2, the agreement with the Young modulus obtained from the compliance tensor calculated in Eq. (1.64) is excellent. Furthermore, by including in Eq. (1.64) the second derivatives of the magnetic interactions (see appendix B of Paper IV) we can calculate the contribution to lowest order in  $m$  to the elastic moduli, see also appendix E of Paper IV. The result, depicted by the dashed lines in Fig. 1.16 (a), is in excellent agreement with the numerical results. Notice that the analytical curves are vertically shifted by  $\sim 0.08k/l_0^2$  for a better comparison of the initial quadratic trend.

The shear modulus that we indicate as  $G_{zy}$  corresponds to shear deformations with the shear plane containing  $\hat{\mathbf{z}}$  but the macroscopic shear forces applied perpendicular to it, see Fig. 1.17. Increasing magnetic interactions tighten the alignment of dipoles in the  $\mathbf{m}$ -direction. Therefore, shear deforma-

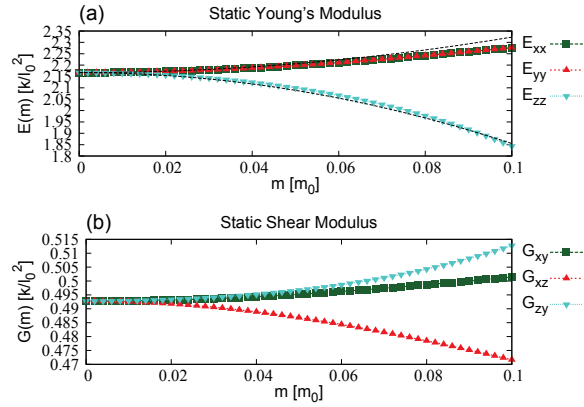


Figure 1.16: (a) Young and (b) shear moduli of a cubic dipole–spring network for increasing dipole moments  $\mathbf{m}$  of strength  $m$  and oriented in the  $z$ -direction. Reproduced from Ref. 123 with permission. © AIP Publishing. All rights reserved.

In the transversal directions,  $E_{xx}(m)$  and  $E_{yy}(m)$  have an increasing trend, which we attribute to the dipole–dipole repulsion along the  $x$ - and  $y$ -directions.

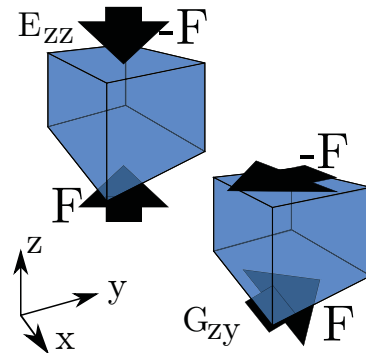


Figure 1.17: Sketch of the stress-strain geometries determining the moduli  $E_{zz}$  and  $G_{zy}$ .

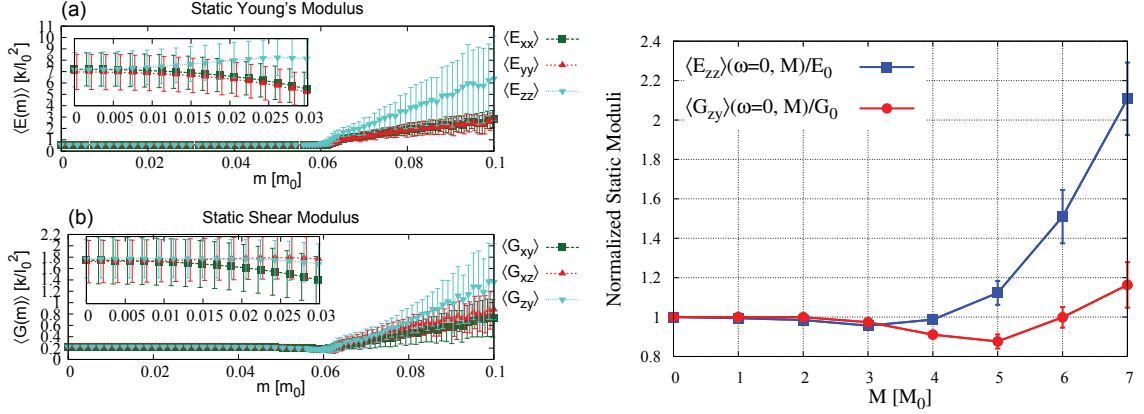


Figure 1.18: (LEFT) (a) Young and (b) shear moduli for increasing magnetic interactions of our disordered particle arrangements presented in Paper IV. Insets zoom in onto the respective low- $m$  behaviors. Reproduced from Ref. 123 with permission. © AIP Publishing. All rights reserved. (RIGHT) Young  $\langle E_{zz} \rangle$  and shear  $\langle G_{zy} \rangle$  moduli for increasing magnetic interactions in our isotropic system containing an experimentally measured particle distribution of volume fraction of 5.6% (40wt%) as presented in Paper V. Bars for  $M < 5M_0$  are smaller than the ones at  $M = 5M_0$ . Reproduced from Ref. 122.

tions as the one in Fig. 1.17 tend to de-align the dipoles. This is growingly hindered by increasing dipole–dipole attraction and thus the shear modulus  $G_{zy}$  in Fig. 1.16 increases with increasing  $m$ .

Moving on to more realistic, disordered distributions in 3D, we find a direct connection between the formation of chain-like aggregates in a “hardened” state [74] and large increases in the elastic moduli. The formation of chains-like structures, as showed in Fig. 1.14 and detailed in sections X A of Paper IV and V A of Paper V, introduces anisotropy in the system. This is reflected by a change of the material properties, in particular, the elastic moduli, see Fig. 1.18.

In both our Paper IV and Paper V we find common traits in the behavior of the elastic moduli. First, the initial behavior with increasing magnetic interactions is basically flat or even slightly decreasing, see Fig. 1.18. In the regime of  $M \lesssim 5M_0$  of Figs. 1.14 and 1.18, right panel, the formation of chain-like clusters is under way and this process appears to soften the material. Nevertheless, such particle arrangements are stable configurations of the system, as evidenced by the moduli always being positive.

After that, a “hardened” [74] regime emerges. Here, chain-like aggregates of significant size have formed ( $m \gtrsim 0.06m_0$  and  $M \gtrsim 5M_0$  in, respectively, left and right panels of Fig. 1.18). The particles in the chains are “locked-in” by the counterbalance of strong dipole–dipole attraction and strong steric repulsion. In this state, the energy landscape around the equilibrated state is extremely steep and convex as a result of the “locking”.

Intuitively, a macroscopic strain can involve deformations of these hardened chains that now span large portions of the system and include an extensive amount of the particles. Thus, in agreement with experimental observations [10, 11, 46], we find large increases in both Young and shear moduli, see Fig. 1.18 (a) and (b), signaling an overall hardening of the system. Moreover, our numerical calculations in Paper IV reveal a significantly larger increase of the Young modulus in the magnetic-field direction, compared with the transversal ones. Qualitatively, this has been observed in experiments, too [11].

### 1.8.3 Dynamic Elastic Moduli

In Paper IV we have described a method for calculating the frequency-dependent elastic moduli of finite-sized discretized particle–springs systems in the overdamped limit. This calculation directly connects the dynamic moduli with the “relaxational” (normal) modes of the network [105].

The static elastic moduli represent the vanishing-frequency limit of the dynamic moduli. They are a property of the ground state of the particle distribution. The normal modes are the eigenvectors  $|\mathbf{v}_n\rangle$  of the Hessian matrix of the total energy, see Eq. (1.59) supplemented by corresponding steric and magnetic energetic contributions, in our case. Each of the resulting  $n$  modes has a corresponding eigenvalue  $\lambda_n$ ,  $n = 1 \dots D$ , with  $D$  the number of degrees of freedom. The static moduli can be expressed as a sum containing the normal modes and their eigenvalues, via a definition equivalent to Eq. (1.62), see section V of Paper IV. A key ingredient in this derivation is the construction of a mesoscopic force field  $|\mathbf{f}\rangle$  that represents an external macroscopic stress of magnitude  $\sigma = F/S$  resulting from a force  $F$  applied on a boundary of surface  $S$ . Such a force field is applied in the preselected direction and results in neither net overall force nor torque on the system, see section V B of Paper IV. Differentiating twice with respect to the stress intensity we obtain the static modulus as

$$E = \frac{L}{S} \left[ \frac{1}{F^2} \sum_{n=1}^D \frac{(f_n)^2}{\lambda_n} \right]^{-1}, \quad (1.75)$$

where  $L$  is the distance between the boundaries on which the forces are applied and  $f_n = \langle \mathbf{f} | \mathbf{v}_n \rangle$  is the projection of the mesoscopic force field onto the  $n$ -th mode.

The final step to obtain the dynamic moduli is to write down the coupled dynamic equations of motion of the system. Because of the large dissipation typically happening on the mesoscopic scale in the polymeric network, the motion is considered to be overdamped, i.e., the inertial contribution is negligible, see section VI of Paper IV. The equation of motion can be decomposed over the normal modes. Thus, we obtain  $D$  decoupled differential equations, each describing the dynamics of a single mode. Each mode behaves as an independent Kelvin-Voigt element as in section 1.6.2, see Eq. (24) of Paper IV. The response of the system is calculated for a given frequency  $\omega$  of the

imposed force field. Finally, as detailed in section VII of Paper IV, the stress-strain ratio as in Eq. (1.56) yields the elastic moduli

$$E(\omega) = \frac{L}{S} \left[ \sum_{n=1}^D \frac{f_n^2}{\lambda_n + ic\omega} \right]^{-1}, \quad (1.76)$$

where  $L$  is the distance between the boundaries of surface  $S$  on which the forces are applied,  $f_n^u = \langle \mathbf{f} | \mathbf{v}_n \rangle / F$  is the coefficient obtained by projecting the normalized mesoscopic force field representing the external stress onto the  $n$ -th mode, and  $c$  is a parameter related to the friction associated with internal deformations in the system.

A characteristic example of dynamic moduli of a spring network at vanishing magnetization is displayed in Fig. 1.19. Comparison with typical rheological measurements suggest that our Kelvin-Voigt-based model is particularly appropriate for long timescales. In our notation that happens in the regime  $\omega \lesssim 10 \omega_0$ , with  $\omega_0$  our reduced units for frequency. Eq. (1.76) describes a material that is fundamentally a solid considering its long-time behavior. Therefore, the storage modulus at low  $\omega$  shows a plateau and the loss modulus vanishes. Stress and strain are in phase in the low- $\omega$ , quasi-static regime. Here, the stress propagates through the whole system because the bulk has time to relax completely. Such a high degree of relaxation implies that the modulus assumes the lowest value.

In the high- $\omega$  regime the behavior is the opposite. The external stress oscillates over a period much shorter than the typical relaxation time of the bulk. The system does not have time to relax and the whole response comes from the surface, the localized deformation of which leads to a high plateau of the storage moduli. Furthermore, dissipation at this frequency is much higher and so is the loss modulus.

Thus, stress and strain are out of phase and the phase lag reaches  $\pi/2$ .

In between, the connection is given by a gradual mixing of different modes. At  $\omega = 0$

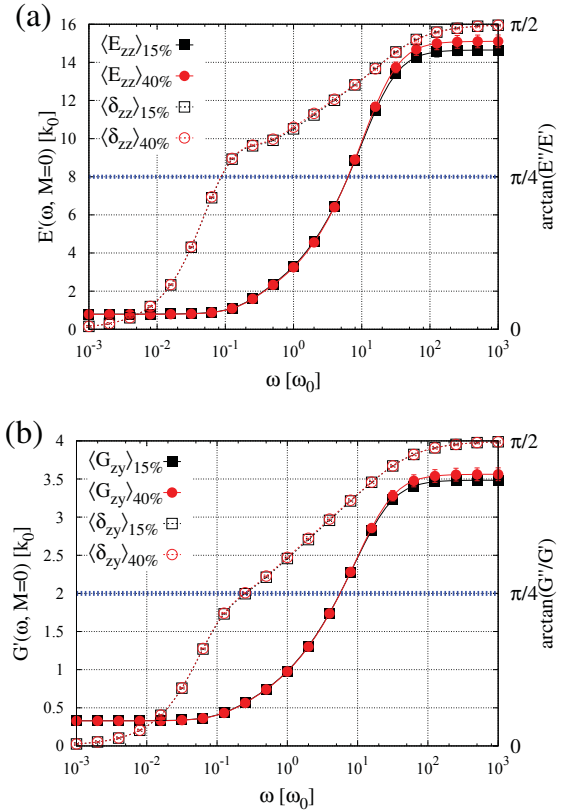


Figure 1.19: Storage (a) Young and (b) shear moduli of typical 3D spring networks extracted from measurements on real experimental samples in the absence of magnetic effects. The phase lag  $\delta = \arctan(E'/E'')$  is plotted on the right axis. Reproduced from Ref. 122.

most of the contributions stem from modes involving global, collective deformations and low eigenvalues. High- $\omega$  modes, instead, typically represent localized deformations and have high eigenvalues.

Introducing magnetic interactions can have unexpected effects on the dynamic moduli. In the simple case of a cubic lattice, see section VIII of Paper IV, the Young storage moduli over the whole frequency-range show increase or decrease with increasing  $m$  in accordance with the static case, see Fig. 1.20, left panel. Interestingly, the shear moduli can show a nonmonotonous behavior as a function of frequency when the magnetic interactions are increased. Specifically, the shear storage modulus  $G'_{zy}(\omega)$ , see Fig. 1.17, switches from increasing to decreasing with  $m$  when comparing the low- $\omega$  and the high- $\omega$  regimes. The fcc dipole-spring network (section IX of Paper IV) also features a nonmonotonous behavior. There, however, the shear modulus  $G'_{zy}(\omega)$  switches from decreasing to increasing instead. Finally, our disordered fcc system (see Fig. 16 of Paper IV) only shows increase in both Young and shear moduli over all frequencies in the hardened ( $m \gtrsim 0.06m_0$ ) regime.

Remarkably, our experimentally obtained particle distribution in Paper V also features a reversal of the stiffening effect from the low- to the intermediate- $\omega$  regime, see Fig. 1.20, right panel. As also described in section 1.8.2, the static shear modulus  $G'_{zy}(\omega = 0)$  increases at high magnetization ( $M = 7M_0$ ) as a consequence of the long chain-like structures. At intermediate ( $10^{-1}\omega_0 \lesssim \omega \lesssim 10^1\omega_0$ ) frequencies, however, the shear storage modulus decreases, before increasing again at high- $\omega$ . The Young storage modulus  $E'_{zz}(\omega)$ , similarly to the regular lattices, shows persistent (increasing) trend for increasing magnetic interactions at all frequencies.

Lastly, the increasing magnetization  $M$  has a strong impact on the stress-strain phase lag, see Fig. 1.20, right panel. This always has a decreasing impact in all cases with increasing magnetization  $M$ , especially for the Young modulus and at low- to intermediate- $\omega$ . In practical terms, this means that increasing magnetic interactions help keeping stress and strain in phase, thus effectively reducing the dissipated energy in the loading cycle.

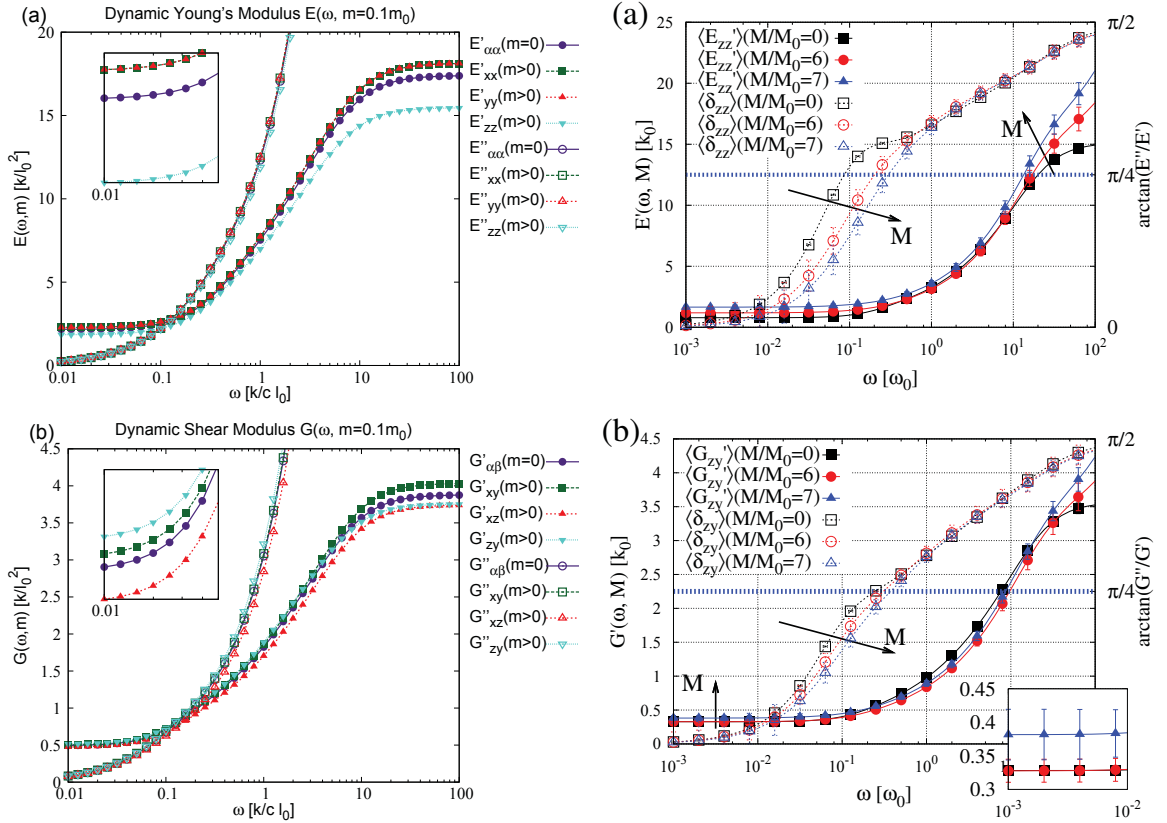


Figure 1.20: (LEFT) Dynamic (a) Young and (b) shear moduli for increasing magnetic moment  $m$  of a cubic dipole–spring network and as a function of frequency. Reproduced from Ref. 123 with permission. © AIP Publishing. All rights reserved. (RIGHT) (a) Young  $\langle E_{zz} \rangle$  and (b) shear  $\langle G_{zy} \rangle$  dynamic moduli for increasing magnetization  $M$  in our experimentally obtained system, see Paper V, with the scale given on the left ordinate. Corresponding phase lags  $\delta = \arctan(E'/E'')$  are plotted against the scale on the right ordinate. Reproduced from Ref. 122.

## 2 Publications



# Paper I Towards a scale-bridging description of ferrogels and magnetic elastomers

Reproduced from

Giorgio Pessot, Rudolf Weeber, Christian Holm, Hartmut Löwen, and  
Andreas M. Menzel,

Towards a scale-bridging description  
of ferrogels and magnetic elastomers.

*J. Phys.: Condens. Matter*, **32** 325105 (2015), IOP Publishing

with the permission of *IOP Publishing*. © IOP Publishing. All rights reserved.  
(Version of Record, Supplementary Material)

DOI: 10.1088/0953-8984/27/32/325105

## Authors' Contributions

All authors contributed to the writing of the manuscript. Rudolf Weeber performed the molecular dynamics simulations. Andreas M. Menzel, Christian Holm, and Hartmut Löwen supervised the work. I performed the numerical analysis of the data and developed the coarse-graining.

I estimate my total contribution to this work to approximately 70%.

## Copyright and Permission Informations

From IOP FAQ/Author Rights :

“[...]upon transfer of copyright, IOP Publishing and/or the copyright owner grants back to authors a number of rights. These include the right to include the Final Published Version of the article in research theses or dissertations. Please include citation details and, for online use, a link to the Version of Record.”



# Towards a scale-bridging description of ferrogels and magnetic elastomers

Giorgio Pessot<sup>1</sup>, Rudolf Weeber<sup>2</sup>, Christian Holm<sup>2</sup>, Hartmut Löwen<sup>1</sup>  
and Andreas M Menzel<sup>1</sup>

<sup>1</sup> Institut für Theoretische Physik II: Weiche Materie, Heinrich-Heine-Universität Düsseldorf, D-40225 Düsseldorf, Germany

<sup>2</sup> Institute for Computational Physics, Universität Stuttgart, 70569 Stuttgart, Germany

E-mail: [giorgpess@thphy.uni-duesseldorf.de](mailto:giorgpess@thphy.uni-duesseldorf.de), [weeber@icp.uni-stuttgart.de](mailto:weeber@icp.uni-stuttgart.de), [holm@icp.uni-stuttgart.de](mailto:holm@icp.uni-stuttgart.de), [hlowen@thphy.uni-duesseldorf.de](mailto:hlowen@thphy.uni-duesseldorf.de) and [menzel@thphy.uni-duesseldorf.de](mailto:menzel@thphy.uni-duesseldorf.de)

Received 13 February 2015, revised 9 June 2015

Accepted for publication 22 June 2015

Published 27 July 2015



## Abstract

Ferrogels and magnetic elastomers differentiate themselves from other materials by their unique capability of reversibly changing shape and mechanical properties under the influence of an external magnetic field. A crucial issue in the study of these outstanding materials is the interaction between the mesoscopic magnetic particles and the polymer matrix in which they are embedded. Here we analyze interactions between two such particles connected by a polymer chain, a situation representative for particle-crosslinked magnetic gels. To make a first step towards a scale-bridging description of the materials, effective pair potentials for mesoscopic configurational changes are specified using microscopic input obtained from simulations. Furthermore, the impact of the presence of magnetic interactions on the probability distributions and thermodynamic quantities of the system is considered. The resulting mesoscopic model pair potentials can be used to economically model the system on the particle length scales. This first coarse-graining step is important to realize simplified but realistic scale-bridging models for these promising materials.

Keywords: magnetic elastomer, ferrogel, scale-bridging, coarse-graining, statistical analysis

 Online supplementary data available from [stacks.iop.org/JPhysCM/27/325105/mmedia](http://stacks.iop.org/JPhysCM/27/325105/mmedia)

(Some figures may appear in colour only in the online journal)

## 1. Introduction

Ferrogels and magnetic elastomers are fascinating materials, born by the union of polymeric networks and ferrofluids. Their amazing properties derive from the unique combination of the elastic behavior typical for polymers and rubbers [1] on the one hand, and magnetic effects characteristic of ferrofluids and magnetorheological fluids [2–10] on the other. One of the most interesting results is that their shape and mechanical properties can be externally controlled by applying a magnetic field [11–21]. A form of tunability, distinguished by reversibility as well as non-invasiveness and based on a magneto-mechanical coupling is one of the most appealing properties of these materials. This makes them excellent candidates for use as

soft actuators [22], magnetic field detectors [23, 24], as well as tunable vibration and shock absorbers [14, 25]. Moreover, studying their heat dissipation due to hysteretic remagnetization in an alternating external magnetic field might be helpful to understand better the processes during possible applications in hyperthermal cancer treatment [26, 27].

Typically, these materials consist of cross-linked polymer networks in which magnetic particles of nano- or micrometer size are dispersed [16]. A central role in the coupling of magnetic and mechanical properties is played by the specific interactions between the embedded mesoscopic magnetic particles and the flexible polymer chains filling the space between them. These couplings are responsible for a modified macroscopic elasticity [12, 28, 29], orientational memory effects

[30, 31], and reversibility of the magnetically induced deformations [15].

Many theoretical and computational studies have been performed on the topic, using different approaches to incorporate the particle-polymer interaction. Some of them rely on a continuum-mechanical description of both the polymeric matrix and the magnetic component [23, 32, 33]. Others explicitly take into account the discrete embedded magnetic particles, but treat the polymer matrix as an elastic background continuum [34, 35]. Usually in these studies, an affine deformation of the whole sample is assumed. The limitations of such an approach for the characterization of real materials have recently been pointed out [36]. In order to include irregular distributions of particles and non-affine sample deformations, other works employ, for instance, finite-element methods [19, 37–40].

To optimize economical efficiency, a first step is the use of simplified dipole-spring models. In this case, steric repulsion and other effects like orientational memory terms can be included [30, 36, 41–44]. A step beyond the often used harmonic spring potentials can be found in [42] where non-linear springs of finite extensibility are considered.

From all the studies mentioned above it becomes clear that microscopic approaches that explicitly resolve polymer chains are rare [45, 46], and what is particularly missing is a link between such microscopic approaches and the mesoscopic models that only resolve the magnetic particles, not the single polymer chains. In particular, a microscopic foundation of the phenomenological mesoscopic expressions for the model energies should be built up.

The present work is a first step to close this gap. We consider an explicit microscopic description in a first simplified approach: a single polymer chain, discretized through multiple beads, each representing a coarse-grained small part of the polymer, connects two mesoscopic particles. The ends of the polymer chain are rigidly anchored on the surfaces of the two mesoscopic particles, which are spherical, can be magnetized, and are free to rotate and change their distance. From molecular dynamics simulations on the microscopic level, we collect the statistics of the micro-states corresponding to different configurations in the mesoscopic model. Based on these statistics we derive effective mesoscopic pair potentials, inspired by previous achievements for other polymeric systems [47, 48]. The subsequent step in scale-bridging, connecting the mesoscopic picture to the macroscopic description, has been recently addressed [49] for a special class of magnetic polymeric materials.

In the following, we first define and describe our model in section 2. Then, in section 3, we mention the details of the microscopic simulation. In section 4, we further characterize the probability distribution of the mesoscopic variables, connecting it to a wrapping effect in section 5. After that, in section 6, we determine the values of mesoscopic model parameters based on the results of our microscopic simulations. In section 7, we derive an approximated expression for the mesoscopic effective pair potential characterizing the particle configurations. In this way, we build the bridge from the explicit microscopic characterization to the mesoscopic

particle-resolved models by averaging over the microscopic details. Last, in section 8, we consider the effect of adding magnetic moments to the particles and, in section 9, the effect of increasing magnetic interaction on the thermodynamic properties, before we draw our final conclusions in section 10. Appendix A addresses the trends in the dependences of the mesoscopic model parameters on varying microscopic system parameters, while appendix B briefly comments on the separability of magnetic interactions in the mesoscopic picture and microscopic chain configurations.

## 2. The system

Our simplified system is composed of two mesoscopic and spherical particles, both of radius  $a$ , and a polymer chain explicitly resolved by  $N = 60$  beads of diameter  $\sigma$  and interconnected by harmonic springs. Here we choose the mesoscopic particle radius  $a$  to be  $5\sigma$ .

We consider steric repulsion between all described particles through a WCA potential, which represents a purely repulsive interaction. It is given by

$$V_{\text{WCA}}\left(\frac{r'}{\sigma'}\right) = \begin{cases} 4\epsilon \left[ \left(\frac{r'}{\sigma'}\right)^{-12} - \left(\frac{r'}{\sigma'}\right)^{-6} + \frac{1}{4} \right] & \text{for } r' \leq r_c \\ 0 & \text{otherwise} \end{cases} \quad (1)$$

where  $r'$  is the distance between the particle centers,  $\epsilon$  denotes the energy scale of the potential, and  $r_c = 2^{1/6}\sigma'$  is the cut-off distance. For any combination of large and small particles,  $\sigma'$  is chosen as the sum of the radii of the respective particles, which is equivalent to the mean of their respective diameters. In our simulations, we set  $\epsilon = 10k_{\text{B}}T$ , where  $k_{\text{B}}$  is the Boltzmann constant and  $T$  is the temperature of the system. Neighboring beads within the chain are bound by means of a harmonic potential

$$V_{\text{H}}(r') = \frac{1}{2}k(r' - r_0)^2, \quad (2)$$

where we choose the force constant  $k = 10k_{\text{B}}T/\sigma^2$ . The equilibrium distance  $r_0$  is set to match the cut-off distance of the WCA-potential  $r_0 = r_c = 2^{1/6}\sigma$ .

The ends of the chains are bound via the same harmonic potential to binding sites placed below the surface of the mesoscopic particles, see figure 1. These binding sites are rigidly connected to the mesoscopic particles and follow both, their translational and rotational motion. Thus, when the magnetic particle moves or rotates, the binding site of the polymer chain has to follow, and vice versa. The technical details for the virtual sites mechanism can be found in [50]. We identify the anchoring points of the polymer chain by the vectors  $\mathbf{a}_1$  and  $\mathbf{a}_2$ , respectively (see figure 1). Furthermore, the distance vector between the two mesoscopic particle centers is indicated as  $\mathbf{r}$ , with magnitude  $r$ . The angles that the vectors  $\mathbf{a}_1$  and  $\mathbf{a}_2$  adopt with respect to the connecting vectors  $\mathbf{r}$  and  $-\mathbf{r}$  are denoted as  $\theta_1$  and  $\theta_2$ , respectively.  $\theta_1$  and  $\theta_2$  are zenithal angles and they can span the interval  $[0, \pi]$ . Last,  $\phi \in [-\pi, \pi[$  is the relative

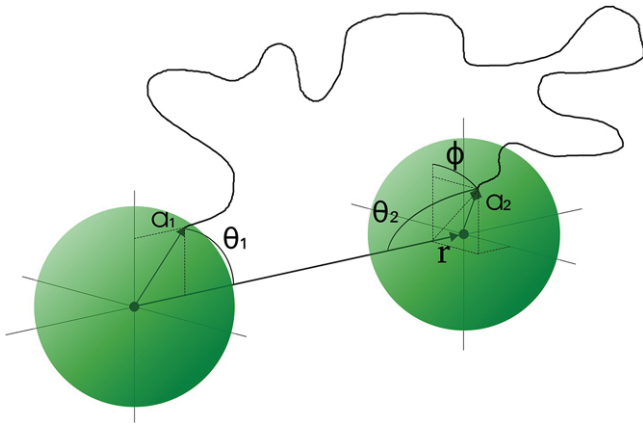


**Figure 1.** A simplified sketch of the geometry of the microscopic system.  $\mathbf{r}$  is the vector connecting the centers of the mesoscopic particles.  $\mathbf{a}_1$  and  $\mathbf{a}_2$  identify the anchoring points of the polymer chain on the surfaces of the particles.  $\theta_1$ ,  $\theta_2$ , and  $\phi$  are the angles that represent the remaining relative rotational degrees of freedom of the system.

azimuthal angle between the projections of  $\mathbf{a}_1$  and  $\mathbf{a}_2$  on a plane perpendicular to  $\mathbf{r}$ . It can be used to parametrize the relative torsion between the two particles around the  $\mathbf{r}$  axis. Let us for brevity introduce the vector  $\boldsymbol{\gamma} = (r, \theta_1, \theta_2, \phi)$ . Therefore, the  $\boldsymbol{\gamma}$ -space, where our mesoscopic vector  $\boldsymbol{\gamma}$  is defined, is given by  $[0, +\infty[ \times [0, \pi] \times [0, \pi] \times [-\pi, \pi]$ .

Through molecular dynamics simulations (thoroughly described in the next section) we find the probability density  $p_c(\boldsymbol{\gamma})$  of a certain configuration  $\boldsymbol{\gamma}$  of the two mesoscopic particles. We normalize  $p_c(\boldsymbol{\gamma})$  such that  $\int p_c(\boldsymbol{\gamma}) d\boldsymbol{\gamma} = 1$ , with  $d\boldsymbol{\gamma} = \sin(\theta_1) \sin(\theta_2) dr d\theta_1 d\theta_2 d\phi$  the  $\boldsymbol{\gamma}$ -space volume element. Moreover, we are working in the canonical ensemble.

From statistical mechanics [51], we know that the probability density  $p_c(\boldsymbol{\gamma})$  to find the system in a certain configuration  $\boldsymbol{\gamma}$  is  $p_c(\boldsymbol{\gamma}) = \exp[-\beta V_c(\boldsymbol{\gamma})]/Z_c$ , where  $\beta = 1/k_B T$  and  $Z_c$  is the partition function of the system. Shifting  $V_c(\boldsymbol{\gamma})$  by an appropriate constant, we can still reproduce  $p_c(\boldsymbol{\gamma})$  but simultaneously normalize  $Z_c = 1$ . Then, since  $\ln(Z_c) = 0$ ,

$$V_c(\boldsymbol{\gamma}) = -k_B T \ln[p_c(\boldsymbol{\gamma})] \quad (3)$$

represents an effective energy of the state  $\boldsymbol{\gamma}$  of our mesoscopic two-particle system and corresponds to an effective pair potential on the mesoscopic level, see also [47]. Through the normalization of  $Z_c$ , we set our reference free energy  $F = -k_B T \ln(Z_c)$  equal to zero.

### 3. Microscopic simulation

To obtain the probability distribution from which the mesoscopic pair potential is derived, we performed molecular dynamics simulations using the ESPResSo software [50, 52]. Because entropic effects are important to capture the behavior of the polymer, the canonical ensemble is employed. This is achieved using a Langevin thermostat, which adds random kicks as well as a velocity-dependent friction force to the particles. For the translational degrees of freedom of each particle, the equation of motion is then given by

$$m_p \dot{\mathbf{v}}(t) = -\zeta \mathbf{v}(t) + \mathbf{F}_r + \mathbf{F}, \quad (4)$$

where  $m_p$  is the mass of a particle,  $\mathbf{F}$  is the force due to the interaction with other particles,  $\mathbf{F}_r$  denotes the random thermal noise, and  $\zeta$  is the friction coefficient.

To maintain a temperature of  $T$ , according to the fluctuation-dissipation theorem, each random force component must have zero mean and variance  $2k_B T \zeta$ . Furthermore, random forces at different times are uncorrelated. In order to track the orientation of the magnetic nanoparticles, rotational degrees of freedom also have to be taken into account. This is achieved by means of a Langevin equation of motion similar to (4) where, however, mass, velocity, and force are replaced by inertial moment, angular velocity, and torque, respectively [53].

The time step for the integration using the Velocity-Verlet method [54] is  $dt = 0.01$ . To sample the probability distribution, we record the state of the simulation  $\boldsymbol{\gamma}$  every ten time steps. In order to obtain a smooth probability distribution over a wide range of parameters, 34 billion states have been sampled in total, by running many parallel instances of the simulation, summing up to about  $10^4$  core hours of CPU time.

Finally, we find the probability distribution by sorting the results of our simulations into a histogram with 100 bins for each variable ( $r$ ,  $\theta_1$ ,  $\theta_2$ , and  $\phi$ ). When a 64-bit unsigned integer is used as data type, this leads to a memory footprint of 800 Mb. Hence, the complete histogram can be held in memory on a current computer. If the resulting numerical version of the effective pair potential as defined in (3) is to be used in a simulation, a smoothing procedure should be employed, especially in parts of the configuration space with a very low probability density. One approach here might be hierarchical basis sets.

In our simulations, we chose the thermal energy  $k_B T$  as well as the mass  $m_p$ , the friction coefficient  $\zeta$ , and the corresponding rotational quantities to be unity. We measure all lengths in units of  $\sigma$  and the energies in multiples of  $k_B T$ .

### 4. Description of the probability density

We now consider some aspects of the probability density resulting from the microscopic simulation described in section 3. The entropic role of the microscopic degrees of freedom is considered by assigning to every configuration  $\boldsymbol{\gamma}$  a certain probability, given by the number of times it was encountered in the simulation divided by the total number of recorded states. As explained before,  $\boldsymbol{\gamma} = (r, \theta_1, \theta_2, \phi)$  corresponds to the set of variables that we use to describe the state of the system on the mesoscopic level.

In calculating the probability density from the microscopic simulations, we must remember the normalizing condition

$$\int p_c(\boldsymbol{\gamma}) \sin(\theta_1) \sin(\theta_2) dr d\theta_1 d\theta_2 d\phi = 1, \quad (5)$$

where  $r$  is integrated over  $[0, +\infty[$ ,  $\theta_1$  and  $\theta_2$  over  $[0, \pi]$ , and  $\phi$  over  $[-\pi, \pi]$ . Therefore, to obtain the probability density, we have to properly divide the data acquired from the simulations by the factor  $\sin(\theta_1) \sin(\theta_2)$ .

It is useful to introduce here the average of a quantity over  $p_c$ , defined as  $\langle \cdot \rangle_c = \int \cdot p_c(\boldsymbol{\gamma}) d\boldsymbol{\gamma}$ . We can therefore calculate the average value of  $\boldsymbol{\gamma}$ ,  $\bar{\boldsymbol{\gamma}} = \langle \boldsymbol{\gamma} \rangle_c$ , and the covariance matrix  $\Sigma_{\alpha\beta}^c = \langle (\alpha - \bar{\alpha})(\beta - \bar{\beta}) \rangle_c$ , for  $\alpha, \beta = r, \theta_1, \theta_2, \phi$ . We find  $\bar{\boldsymbol{\gamma}} \simeq (20.20\sigma, 0.36\pi, 0.36\pi, 0)$ . It is more practical to discuss the system in terms of correlation than in terms of covariance. Correlation is defined as  $\rho_{\alpha\beta}^c = \Sigma_{\alpha\beta}^c / \sqrt{\Sigma_{\alpha\alpha}^c \Sigma_{\beta\beta}^c}$  (no summation rule in this expression), is dimensionless, and  $\rho_{\alpha\beta}^c \in [-1, 1]$ . Here, we obtain

$$\boldsymbol{\rho}^c \simeq \begin{pmatrix} 1 & -0.341 \pm 0.028 & -0.356 \pm 0.029 & 0.083 \pm 0.022 \\ -0.341 \pm 0.028 & 1 & -0.006 \pm 0.006 & -0.083 \pm 0.010 \\ -0.356 \pm 0.029 & -0.006 \pm 0.006 & 1 & -0.083 \pm 0.011 \\ 0.083 \pm 0.022 & -0.083 \pm 0.010 & -0.083 \pm 0.011 & 1 \end{pmatrix}, \quad (6)$$

where lines and columns refer to  $r, \theta_1, \theta_2, \phi$  in this order. The diagonal elements are unity by definition, because each variable is perfectly correlated with itself. The errors follow from the unavoidable discretization during the statistical sampling procedure in the simulations, where the results have to be recorded in discretized histograms of finite bin size.

We find a strong anticorrelation between  $r$  and  $\theta_{1,2}$ , meaning that when the distance between the mesoscopic particles changes they tend to rotate. We will address in detail the background of this behavior in section 5 in the form of the wrapping of the polymer chain around the mesoscopic particles. For angles  $\theta_1$  and  $\theta_2$  different from 0 and  $\pi$  it is clear that such a wrapping and corresponding distance changes are likewise induced by modifying the relative torsion of angle  $\phi$ . These coupling effects are partly reflected by the remaining non-vanishing correlations which, however, are weaker than the correlations between  $r$  and  $\theta_1, \theta_2$  by at least a factor 4. The correlations between  $\theta_1$  and  $\theta_2$  are very weak and, within the statistical errors, may in fact even vanish. Within the statistical errors, the magnitudes of the correlations  $\rho_{r,\theta_1}^c$  and  $\rho_{r,\theta_2}^c$  as well as  $\rho_{\theta_1,\phi}^c$  and  $\rho_{\theta_2,\phi}^c$  agree well with each other, respectively, which reflects the symmetry of the system. Finally, we performed additional microscopic simulations for different sizes of mesoscopic particles and different chain lengths of the connecting polymer. As a general trend, we found that the correlations tend to decrease in magnitude for smaller mesoscopic particles and for longer polymer chains (see appendix A).

As a further step in the analysis of  $p_c$ , we can determine the marginal probability density  $\tilde{p}_\alpha(\alpha)$  for one of the four mesoscopic parameters  $\alpha = r, \theta_1, \theta_2, \phi$  integrating out the other three, for instance,  $\tilde{p}_{\theta_1}(\theta_1) = \int p_c(\boldsymbol{\gamma}) \sin(\theta_2) dr d\theta_2 d\phi$ . This is the total probability density for the variable  $\theta_1$  to assume a certain value, regardless of the others. Calculations for  $\tilde{p}_r(r)$ ,  $\tilde{p}_{\theta_2}(\theta_2)$ , and  $\tilde{p}_\phi(\phi)$  are analogously performed by integrating out all respective other variables (see figure 2). Of course,  $\tilde{p}_\alpha(\alpha)$  is still a normalized probability density since  $\int \tilde{p}_\alpha(\alpha) d\alpha = \int p_c(\boldsymbol{\gamma}) d\boldsymbol{\gamma} = 1$ , where we indicate  $d\alpha = \sin(\theta_i) d\theta_i$

for  $\alpha = \theta_i$  ( $i = 1, 2$ ) and  $d\alpha = dr, d\phi$  for  $\alpha = r, \phi$ . Following (3), we also introduce the one-variable effective pair potentials

$$\tilde{V}_\alpha(\alpha) = -k_B T \ln[\tilde{p}_\alpha(\alpha)] \quad (7)$$

that are associated with the corresponding single-variable marginal probability density.

In figure 2 most of the probability density  $\tilde{p}_r(r)$  for the interparticle distance is contained between  $r = 10\sigma$  and  $r = 50\sigma$ , with a single maximum at  $r = 17\sigma$ . Moreover, the

steep increase in  $\tilde{p}_r(r)$  at  $r = 11\sigma$  is to be attributed to the WCA steric repulsion, since at that distance the two particles are in contact. From figure 2 we find that the maximum of  $\tilde{p}_{\theta_i}(\theta_i)$  (with  $i = 1, 2$ ) is located at  $\theta_i = 0$ . The highest probability density for  $\theta_{1,2} = 0$  is obtained from the microscopic simulations by taking into account the  $\boldsymbol{\gamma}$ -space normalization following from the use of spherical coordinates in (5), see also [47]. Moreover,  $\tilde{p}_\phi(\phi)$  shows a maximum for  $\phi = 0$ , indicating that, as expected, the system does not tend to spontaneously twist around the connecting axis in the absence of further interactions. The presence of a maximum at  $\phi = 0$  confirms that  $\tilde{p}_\phi$  is an even function of  $\phi$  invariant under the transformation  $\phi \rightarrow -\phi$ , as expected from the symmetry of the set-up.

## 5. Wrapping effect

Before developing an approximate analytical expression for the effective pair potential between the mesoscopic particles, it is helpful to examine in detail the results of the molecular dynamics simulations. In a magnetic gel in which mesoscopic magnetic particles act as cross-linkers [31, 55], two driving mechanisms for a deformation in an external magnetic field are possible. First, in any magnetic gel, the magnetic interactions between the mesoscopic particles lead to attractions and repulsions between them, which directly implies deformations of the intermediate polymer chains. As we would like to examine this mechanism separately, the magnetic interaction was not included explicitly in the simulations described in section 3. Rather, it will be considered later in section 8. Second, due to the anchoring of the polymer chains on the surfaces, rotations of the mesoscopic particles are transmitted to chain deformations.

It has been shown in model II of [45] that the second mechanism on its own can lead to a deformation of such a gel in an external magnetic field: if mesoscopic magnetic particles are forced to rotate to align with the field, the polymers attached to their surfaces have to follow. The resulting wrapping of the polymer chains around the particles leads to a shrinking of

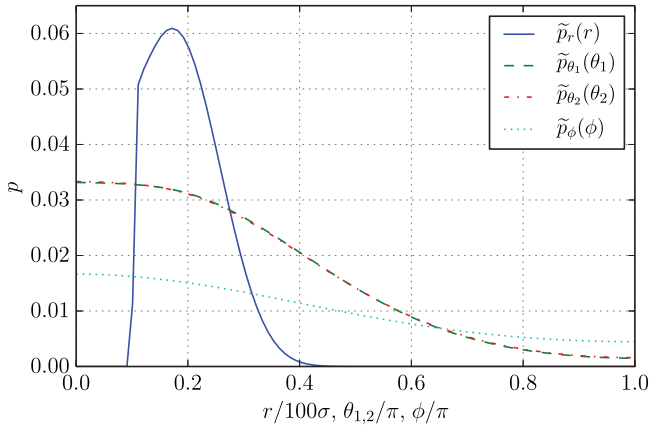


**Figure 2.** Marginal probability densities for the single variables. The abscissa has been rescaled:  $r$  ranges from 0 to  $100\sigma$ , whereas the angles range from 0 to  $\pi$ .  $\tilde{p}_{\theta_1}(\theta_1)$  and  $\tilde{p}_{\theta_2}(\theta_2)$  are practically indistinguishable due to the symmetry of the set-up. Due to the symmetry of the system under the transformation  $\phi \rightarrow -\phi$ , here we only plot  $\tilde{p}_{\phi}(\phi)$  from 0 to  $\pi$ . The maxima of the single-variable densities are located at  $r = 17\sigma$  and  $\theta_{1,2} = \phi = 0$ , respectively. The maxima of  $\tilde{p}_{\theta_1}(\theta_1)$  and  $\tilde{p}_{\theta_2}(\theta_2)$  at  $\theta_{1,2} = 0$  are found from the microscopic simulations after the  $\gamma$ -space normalization contained in (5) has been taken into account.

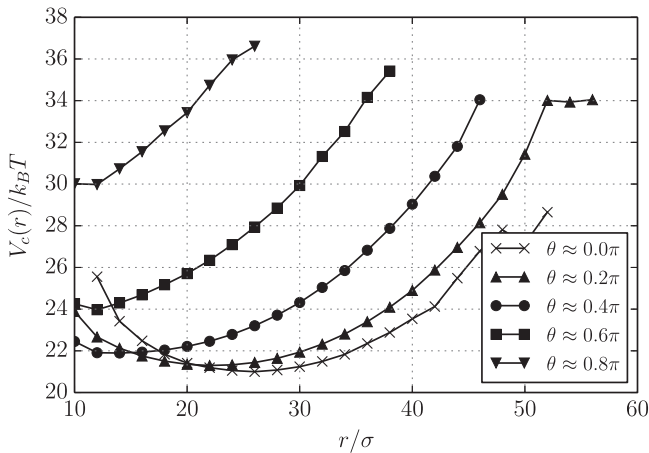


**Figure 3.** Plot of the effective mesoscopic pair potential  $V_c(r)$  for a situation in which both particles are rotated by the same amount to the angles  $\theta_1 = \theta_2 = \theta$  at a torsional angle of  $\phi = 0$ . It can be seen that the more the particles are rotated out of their equilibrium position, the closer they will approach each other because the minimum of the effective pair potential shifts to smaller separation distances  $r$ . The irregularities in the effective pair potential for high values of  $r$  are attributed to the naturally low sampling of those low-probability configurations.

the gel. Transferring this to our model system, it could imply an external magnetic field rotating the particles to a state in which the angles  $\theta_1$  and  $\theta_2$  are non-zero. The effect of induced particle rotations on the interparticle distance is illustrated in figure 3, where the effective pair potential  $V_c(r)$  is plotted for the case of  $\phi = 0$  and various values of  $\theta_1 = \theta_2 = \theta$ . I.e. both particles are rotated by the same angle  $\theta$  with respect to the connecting vector  $\pm \mathbf{r}$ , respectively. It can be seen that the more the particles are rotated, the more the minimum of the effective pair potential is shifted towards closer interparticle distances corresponding to smaller separation distances  $r$ .

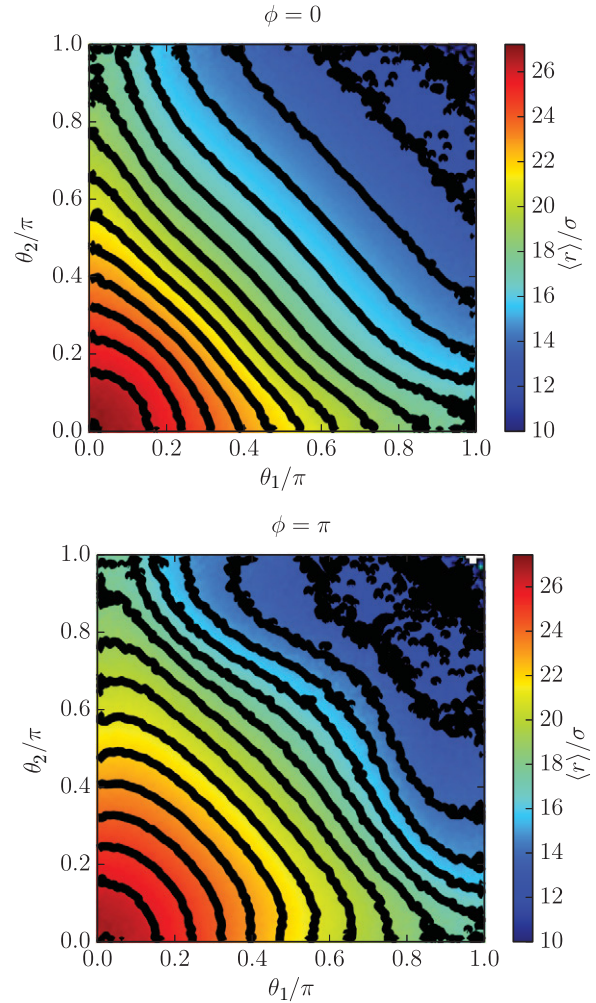


**Figure 4.** Average distance between the two mesoscopic particles versus the angles  $\theta_1$  and  $\theta_2$  shown as a color and contour map for the two cases  $\phi = 0$  (top) and  $\phi = \pi$  (bottom). It can be seen that even by rotating only one of the two particles, the average distance can be reduced considerably. However, the maximum reduction is observed when both particles are rotated. The variation of the torsion angle  $\phi$  does not change the main trend but has a moderate influence for intermediate rotations.

To get a more detailed picture, we also consider independent rotations of the two mesoscopic particles. In figure 4, the average distance between the particles is depicted in a contour plot as a function of the angles  $\theta_1$  and  $\theta_2$ . Images are shown for torsion angles of  $\phi = 0$  and  $\phi = \pi$ . It can be seen that quite a decrease in the average distance can already be achieved by rotating only one particle. However, very strong reduction in interparticle distance can only occur when both particles are rotated. The torsion angle  $\phi$  does not alter the general trend of reduction of the average distance when the particles are rotated. However, the resulting numbers vary to a certain degree.

## 6. One-variable effective pair potentials

We now introduce some mesoscopic analytical expressions to model the effective pair potentials  $\tilde{V}_\alpha(\alpha)$  introduced in (7). We will determine functional forms and parameters that can be

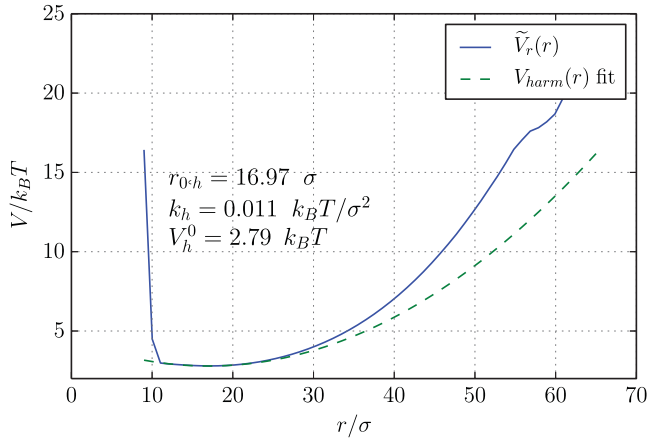


**Figure 5.** Effective pair potential  $\tilde{V}_r(r)$  obtained from the microscopic simulation data and fit using a simple expression  $V_{\text{harm}}(r)$  as in (8). The fit was made in the interval  $[11\sigma, 27\sigma]$ . In this way, the values for the mesoscopic model parameters  $r_{0,h}, k_h, V_h^0$  are determined.

used to model strain and torsion energies. Here, we use the term ‘strain’ to denote variations of  $r$ , whereas the term ‘torsion’ is used to describe changes in the angles  $\theta_1$  and  $\theta_2$  or  $\phi$ , depending on the initial orientation of the spheres and relative rotations. The quality of the analytical model expressions will be analyzed by fitting to the corresponding results from the microscopic simulations.

First, we turn to the energetic contributions arising from changes in the interparticle distance  $r$ . The corresponding effective energy  $\tilde{V}_r(r)$  obtained from the microscopic data is plotted in figure 5. It can be seen that there are essentially two regimes: up to  $r \simeq 11\sigma$  the WCA repulsion between the two mesoscopic particles dominates, whereas, for  $r > 11\sigma$ ,  $\tilde{V}_r(r)$  shows a smooth behavior and a single minimum arising from the entropic contribution of the polymer chain. Moreover, at  $r \gtrsim 55\sigma$ ,  $\tilde{V}_r(r)$  shows an irregular, non-smooth behavior. This is attributed to the low sampling rate of this extremely stretched configuration, which has a very low probability to occur in the microscopic simulations (see figure 2). As a first approximation, it is natural to reproduce  $\tilde{V}_r(r)$  by a harmonic expansion for  $r > 11\sigma$ ,

$$V_{\text{harm}}(r) = V_h^0 + \frac{k_h}{2}(r - r_{0,h})^2. \quad (8)$$

We derive the mesoscopic parameters  $V_h^0, k_h, r_{0,h}$  by fitting  $V_{\text{harm}}(r)$  in a neighborhood of the minimum to the data  $\tilde{V}_r(r)$  obtained from microscopic simulations. In figure 5 the resulting parameters and the two curves are shown.

Moreover, we have compared  $\tilde{V}_r(r)$  with the following expression for a finitely extensible non-linear elastic potential (FENE) [42, 56],

$$V_{\text{FENE}}(r) = V_F^0 - \frac{K_f r_{\text{max}}^2}{2} \ln \left[ 1 - \left( \frac{r - r_0}{r_{\text{max}}} \right)^2 \right]. \quad (9)$$

It takes into account that the chain cannot extend beyond a maximal length, since  $V_{\text{FENE}}(r)$  diverges when  $r \rightarrow r_0 + r_{\text{max}}$ .

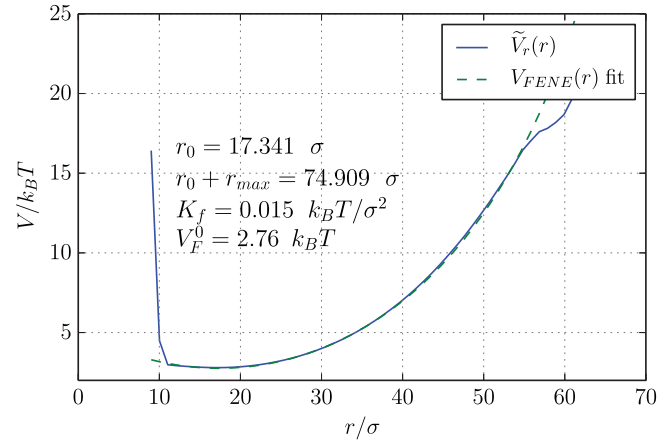


**Figure 6.** Effective pair potential  $\tilde{V}_r(r)$  obtained from the microscopic simulation data and fit using  $V_{\text{FENE}}(r)$  from (9) leading to the parameter values as listed in the plot. The fit was made in the interval  $[11\sigma, 52\sigma]$ . In this way, the values for the mesoscopic model parameters  $r^0, r_{\text{max}}, K_f, V_F^0$  are determined.

We see that  $d^2 V_{\text{FENE}}(r)/dr^2 = K_f$  for  $r = r_0$  and therefore  $K_f$  represents the elastic constant in a harmonic expansion of this non-linear potential. As for the harmonic expression, we fit  $V_{\text{FENE}}(r)$  to our microscopic data and thus derive the mesoscopic model parameters  $K_f, r_0, r_{\text{max}}$ , and  $V_F^0$  as displayed in figure 6. The agreement between the resulting expression for  $V_{\text{FENE}}(r)$  and  $\tilde{V}_r(r)$  in the regime  $r \gtrsim 11\sigma$  is excellent, especially for the branch of the curve right to the minimum. According to the fit, the maximum extension of the chain occurs for  $r = r_0 + r_{\text{max}} \simeq 75\sigma$ . In fact, since the radius of the mesoscopic particles is  $5\sigma$  and each of the 60 beads making up the polymer chain has diameter  $\sigma$ , at  $r = 70\sigma$  the polymer chain is completely stretched. A further elongation is of course possible due to the harmonic inter-bead interaction and this justifies the result of  $\sim 75\sigma$  for the maximal extension.

Last, we compare the elastic constants  $k_h$  and  $K_f$  obtained from the harmonic and FENE approximation, respectively, as listed in figures 5 and 6. The resulting values of  $0.011 k_B T / \sigma^2$  and  $0.015 k_B T / \sigma^2$  are in good agreement with each other.

To find a mesoscopic model expansion for the effective pair potential  $\tilde{V}_{\theta_1}(\theta_1)$  [ $\tilde{V}_{\theta_2}(\theta_2)$  has a very similar behavior], we compare it with the phenomenological expression,

$$V_D(\theta_1) = V_D^0 + D[\cos(\theta_1) - \cos(\theta_0)]^2 \quad (10)$$

introduced in (3) of [30]. As before, we can derive the mesoscopic parameters  $V_D^0, D$ , and  $\theta_0$  by fitting  $V_D(\theta_1)$  to the microscopic data represented by  $\tilde{V}_{\theta_1}(\theta_1)$ . The resulting parameters and the comparison between the two curves are shown in figure 7. Although (10) does not perfectly reproduce the one-variable pair potential  $\tilde{V}_{\theta_1}(\theta_1)$ , it appears as a reasonable approximation in the neighborhood of the minimum energy. Moreover, the rather flat behavior of  $\tilde{V}_{\theta_1}(\theta_1)$  for small  $\theta_1$  is well represented by  $V_D(\theta_1)$ , which is at leading order proportional to  $\theta_1^4$ .

Finally, we want to find a mesoscopic expression to reproduce the effective pair potential  $\tilde{V}_\phi(\phi)$  obtained from the

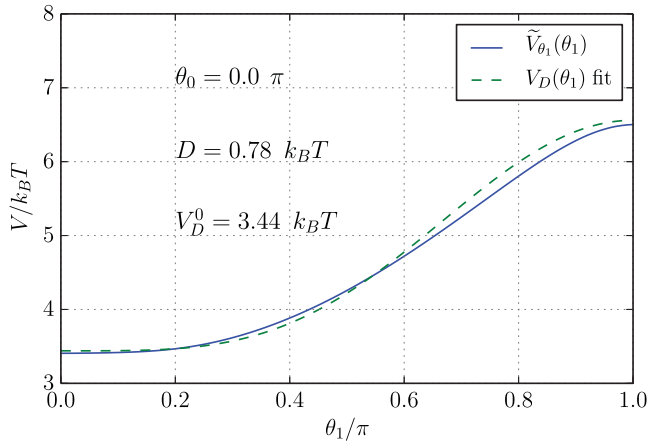


**Figure 7.** Effective pair potential  $\tilde{V}_{\theta_1}(\theta_1)$  calculated from the microscopic simulation data and fit using the phenomenological mesoscopic expression  $V_D(\theta_1)$  from (10). Resulting values for the mesoscopic model parameters are listed in the plot. The fit was made on the interval  $[0, \pi]$ .

microscopic data due to relative torsional rotations between the two particles around the connecting vector  $\mathbf{r}$ . We fit the microscopic data  $\tilde{V}_\phi(\phi)$  around the minimum with the expression

$$V_\tau(\phi) = V_\tau^0 + \tau[\cos(\phi_0) - \cos(\phi)]. \quad (11)$$

It leads to the parameters and fit depicted in figure 8 and is quadratic at lowest order in  $\phi$ ,  $V_\tau(\phi) \simeq V_\tau^0 + \tau\phi^2$ . The parameter  $\phi_0$  is redundant and can be absorbed into  $V_\tau^0$ , but we leave it for reasons of comparison to the following (12).

It is interesting to compare  $\tilde{V}_\phi(\phi)$  with the expression taken from (4) of [30],

$$V'_\tau(\phi) = V'^0_\tau + \tau'[\cos(\phi'_0) - \cos(\phi)]^2. \quad (12)$$

The discrepancy between the two curves shown in figure 9 is obvious. The reason becomes clear when we expand (12) to lowest order in  $\phi$ ,  $V'_\tau(\phi) \simeq V'^0_\tau + \tau'\phi^4$ . This expression is quartic in the torsion angle  $\phi$ , leading to the comparatively flat behavior in the region around the minimum. The last two comparisons suggest that the analytical form of the mesoscopic model pair potential as a function of the azimuthal angle, which acts as a torsion, can be optimized by using a quadratic form as in (11) instead of the quartic one implied by (12) at leading order around the minimum.

Finally, we performed additional microscopic simulations to estimate how the microscopic system parameters affect the mesoscopic model parameters. In particular, the influence of the mesoscopic particle radius  $a$  and the number of beads  $N$  of the connecting polymer chain was investigated. As a trend, we found that the single-variable potentials tend to become stiffer for shorter chains and for bigger mesoscopic particles (see appendix A). Moreover, we observe that the fit of the functional forms in expressions (9)–(11) with the simulation data further improves for increasing chain length and decreasing size of the mesoscopic particles<sup>3</sup>.

So far, we have discussed mesoscopic analytical expressions to approximate the one-variable effective pair potentials

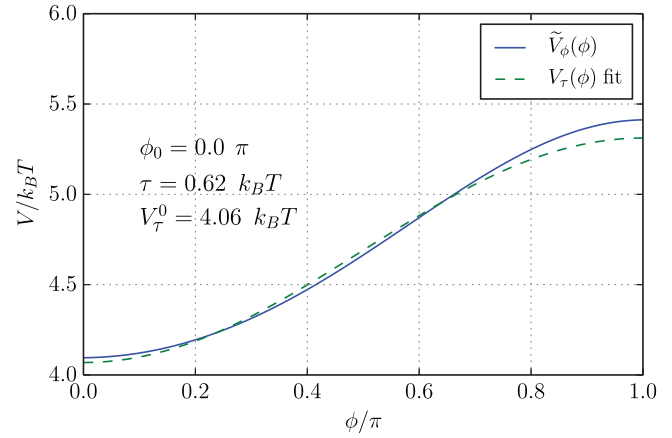


**Figure 8.** Effective pair potential  $\tilde{V}_\phi(\phi)$  calculated from the microscopic simulation data and fit using  $V_\tau(\phi)$  from (11). Resulting values for the mesoscopic model parameters are listed in the plot. The fit was made in the interval  $[0, 0.8\pi]$ .

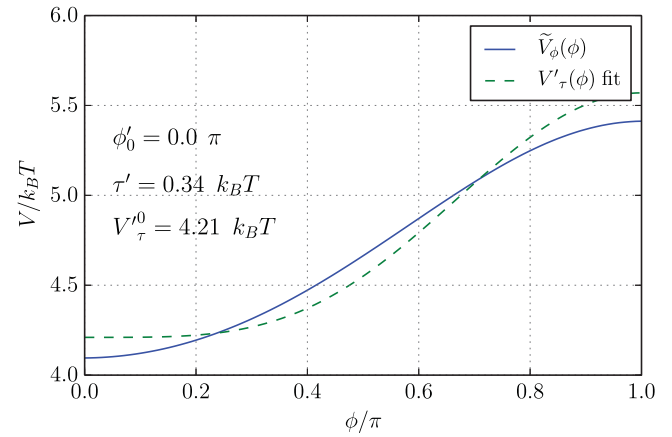


**Figure 9.** Effective pair potential  $\tilde{V}_\phi(\phi)$  calculated from the microscopic simulation data and fit using  $V'_\tau(\phi)$  from (12). Resulting values for the mesoscopic model parameters are listed in the plot. The fit was made in the interval  $[0, 0.8\pi]$ .

$\tilde{V}_\alpha(\alpha)$ . In the following section, using a numerical fitting procedure, we will determine harmonic coupling terms that take account of the correlations between the mesoscopic variables. In this way, we will further develop and improve our approximation of the probability density  $p_c(\gamma)$  from the microscopic simulations.

## 7. Building a coupled effective pair potential

Our goal is to describe the effective interaction between the two mesoscopic particles, coarse-graining the role of the connecting polymer chain. The entropic nature of the polymeric interactions provides a direct route to average out the microscopic degrees of freedom and thus build an effective scale-bridged model. A natural way to proceed would be to find an analytical approximation for  $p_c(\gamma)$  and thus derive an

<sup>3</sup> Corresponding data curves from the additional microscopic simulations and fitted mesoscopic model curves are summarized in the supplemental material ([stacks.iop.org/JPhysCM/27/325105/mmedia](http://stacks.iop.org/JPhysCM/27/325105/mmedia)).

analytical expression for the mesoscopic pair potentials in the spirit of (3).

As a first approximation we may describe  $p_c$  as the simple product of the one-variable probability densities,  $\prod_\alpha \tilde{p}_\alpha(\alpha)$ . We obtain

$$p'_{\text{app}}(\boldsymbol{\gamma}) = \exp\{-\beta[V_{\text{WCA}}(r/2a) + V_{\text{FENE}}(r) + V_D(\theta_1) + V_D(\theta_2) + V_r(\phi)]\}, \quad (13)$$

when we use (7). Analytical approximations for the pair potentials  $\tilde{V}_\alpha(\alpha)$  were derived in (9)–(11) in section 6 together with the fitting parameters listed in figures 6–8. Care must be taken for the term  $\tilde{V}_r(r)$ , which has to be substituted by  $V_{\text{WCA}}(r/2a) + V_{\text{FENE}}(r)$  to take account of the steric repulsion between the mesoscopic particles, see (1). (13) correctly describes some aspects of the system behavior. For instance, the steep variation due to the WCA potential between the mesoscopic particles is well represented in this approximation. However, this description would lead to a distribution with vanishing correlations between the mesoscopic variables. That corresponds to assuming them independent of each other, which omits some important physical aspects, see the wrapping effect in section 5.

To make a step forward and take account of correlations we multiply correction terms to the previous factorized approximation in (13), obtaining the expression

$$p_{\text{app}}(\boldsymbol{\gamma}) \propto p'_{\text{app}}(\boldsymbol{\gamma}) \times \exp[-(\boldsymbol{\gamma} - \boldsymbol{\xi}) \cdot \boldsymbol{\Xi} \cdot (\boldsymbol{\gamma} - \boldsymbol{\xi})], \quad (14)$$

where the elements of  $\boldsymbol{\xi}$ , a 4-components vector, and  $\boldsymbol{\Xi}$ , a  $4 \times 4$  symmetric matrix, are free parameters chosen to match the original data. There are at least two possible numerical approaches to find the best  $\boldsymbol{\xi}$  and  $\boldsymbol{\Xi}$  values. On the one hand, we can simply fit the original probability density (e.g. minimize the squared difference between  $p_c$  and  $p_{\text{app}}$ ). On the other hand, we can follow a moment-matching approach, looking for a  $p_{\text{app}}$  that has a correlation matrix as close as possible to the original one. We performed a mixed strategy by fitting the expression in (14) to the simulation data  $p_c(\boldsymbol{\gamma})$ , using as a criterion for best initialization of the fit an outcome that as closely as possible matches the correlations directly calculated from the simulation data  $p_c(\boldsymbol{\gamma})$ . This fit was performed by minimizing the squared difference between  $p_c(\boldsymbol{\gamma})$  and  $p_{\text{app}}(\boldsymbol{\gamma})$ , using the Nelder–Mead algorithm [57] provided by the SciPy library [58]. In this procedure, normalization of the approximated probability density as in (5) is enforced. The best set of parameters  $\boldsymbol{\xi}$  and  $\boldsymbol{\Xi}$  found is

$$\boldsymbol{\xi} \simeq \begin{pmatrix} 23.54\sigma \\ 0.321\pi \\ 0.321\pi \\ 0 \end{pmatrix}, \quad (15)$$

$$\boldsymbol{\Xi} \simeq \begin{pmatrix} 4.8 \cdot 10^{-3}/\sigma^2 & 0.19/\sigma\pi & 0.19/\sigma\pi & -1.8 \cdot 10^{-3}/\sigma\pi \\ 0.19/\sigma\pi & 1.21/\pi^2 & 1.54/\pi^2 & 1.25/\pi^2 \\ 0.19/\sigma\pi & 1.54/\pi^2 & 1.21/\pi^2 & 1.25/\pi^2 \\ -1.8 \cdot 10^{-3}/\sigma\pi & 1.25/\pi^2 & 1.25/\pi^2 & -0.32/\pi^2 \end{pmatrix}, \quad (16)$$

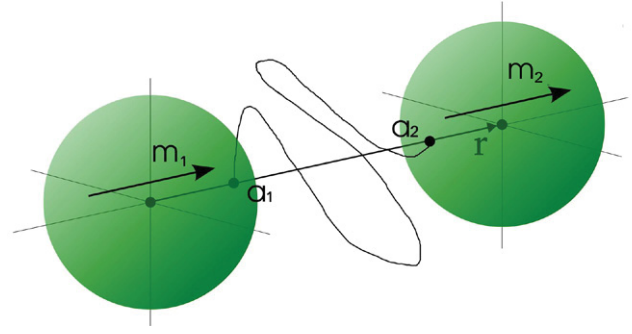


**Figure 10.** A simplified sketch of the mesoscopic configuration in which the magnetic moments are assigned to the particles. The depicted orientations  $\mathbf{a}_1$  and  $\mathbf{a}_2$ , which identify the anchoring points of the polymer chain, correspond to the  $\theta_1 = \theta_2 = 0$  and  $\phi = 0$  configuration. The distance between the centers of the mesoscopic particles here corresponds to  $r = 26\sigma$ . In this configuration, the magnetic moments  $\mathbf{m}_1$  and  $\mathbf{m}_2$  are introduced parallel to each other and pointing along the connecting vector  $\mathbf{r}$ .

resulting in the correlation matrix

$$\boldsymbol{Q}^{\text{app}} \simeq \begin{pmatrix} 1 & -0.306 & -0.306 & 0.045 \\ -0.306 & 1 & 0.027 & -0.071 \\ -0.306 & 0.027 & 1 & -0.071 \\ 0.045 & -0.071 & -0.071 & 1 \end{pmatrix}. \quad (17)$$

It would be unrealistic to try to exactly reproduce all properties of  $p_c(\boldsymbol{\gamma})$  through an analytical approximation. Nevertheless, using the resulting expressions from (14)–(16), we can take account of the strong anticorrelation  $\mathcal{Q}_{r\theta_{1,2}}$  between  $r$  and  $\theta_{1,2}$ , which is the strongest and most important one in the system; compare (6) and (17). For the other elements  $\mathcal{Q}_{r\phi}$ ,  $\mathcal{Q}_{\theta_1,2\phi}$  and  $\mathcal{Q}_{\theta_1\theta_2}$  we then obtain stronger deviations. However, those correlations are smaller than  $\mathcal{Q}_{r\theta_{1,2}}$  at least by a factor 4 and therefore carry a smaller amount of information about the overall system behavior.

As a total result and in analogy to (3), we obtain from (14) the optimized analytical expression  $V_{\text{app}}$  to model the effective interaction between the mesoscopic particles:

$$V_{\text{app}}(\boldsymbol{\gamma}) = V_{\text{WCA}}(r/2a) + V_{\text{FENE}}(r) + V_D(\theta_1) + V_D(\theta_2) + V_r(\phi) + k_B T \sum_{\alpha\beta} \Xi_{\alpha\beta}(\alpha - \xi_\alpha)(\beta - \xi_\beta). \quad (18)$$

The corresponding expressions and values for the fitting parameters are given by (1), (9)–(11), (15) and (16) as well as figures 6–8. Thus, the effective pair potential is divided into two parts: one-variable and two-variable potentials. The former are the analytical single-variable pair potentials derived in section 6, see (1) and (9)–(11), together with the diagonal  $\alpha = \beta$  terms in the double summation of (18). The latter are the off-diagonal  $\alpha \neq \beta$  terms and take account, to lowest order, of the correlations between different mesoscopic degrees of freedom. Correlations between  $r$  and  $\theta_{1,2}$  are the dominating ones, leading to such physical effects as the wrapping effect introduced in section 5.

## 8. Impact of magnetic dipole moments

We will now consider how magnetic interactions between the mesoscopic particles modify the physics of the system, in particular the probability densities and other mesoscopic quantities. For this purpose, we assign to each particle a permanent magnetic dipole moment  $\mathbf{m}_i$  ( $i = 1, 2$ ), in the present work not going into the details of how these could be generated. We introduce these magnetic moments in the state of highest probability density. At vanishing magnetic moments, this is the state of minimal effective energy of the mesoscopic system, i.e. following (3), the one that has maximum  $p_c(\boldsymbol{\gamma})$  over all the configurations  $\boldsymbol{\gamma}$ . The maximum occurs for  $(r^M, \theta_1^M, \theta_2^M, \phi^M) \simeq (26\sigma, 0.0, 0.0, 0.0)$ , and is displayed in figure 10. When the mesoscopic particles are in this configuration, we assign to them the two magnetic moments  $\mathbf{m}_1$  and  $\mathbf{m}_2$  that are parallel to each other and point along the connecting vector  $\mathbf{r}$ , i.e. in their orientation of minimal magnetic energy, as depicted in figure 10. To first order, this configuration should leave the angular orientations unchanged when increasing the magnetic interaction, but see also the discussion in section 5. This is just one of the possible orientations that the moments could assume. However, such a configuration could be achieved with a certain probability, for instance, when the sample is cross-linked in the presence of an external magnetic field that aligns the magnetic moments [59–62]. The dipole moments  $\mathbf{m}_1$  and  $\mathbf{m}_2$  are assumed to have equal magnitude  $m = |\mathbf{m}_1| = |\mathbf{m}_2|$  and are rigidly fixed with respect to each particle frame. We measure the magnetic moments in multiples of  $m_0 = \sqrt{4\pi k_B T (2a)^3 / \mu_0}$ , where  $\mu_0$  is the vacuum magnetic permeability. Then, for each  $\boldsymbol{\gamma}$ , we can calculate the magnetic dipole interaction energy between the two moments

$$\begin{aligned} V_m(\boldsymbol{\gamma}) &= \frac{\mu_0}{4\pi} \frac{\mathbf{m}_1 \cdot \mathbf{m}_2 r^2 - 3(\mathbf{m}_1 \cdot \mathbf{r})(\mathbf{m}_2 \cdot \mathbf{r})}{r^5} \\ &= \frac{\mu_0 m^2}{4\pi} \frac{-2 \cos(\theta_1^m) \cos(\theta_2^m) + \sin(\theta_1^m) \sin(\theta_2^m) \cos(\phi^m)}{r^3}. \end{aligned} \quad (19)$$

$\theta_i^m$  indicates the angle between  $\mathbf{m}_i$  and  $\mathbf{r}$ , while  $\phi^m$  is the angle between the projections of  $\mathbf{m}_1$  and  $\mathbf{m}_2$  on a plane perpendicular to  $\mathbf{r}$ . These quantities can be expressed in the  $\boldsymbol{\gamma}$  variables once the orientations of  $\mathbf{m}_1$  and  $\mathbf{m}_2$  with respect to the particle frames are set by the protocol we described above.

For non-magnetic polymer chains, the potential acting on the mesoscopic level  $V(\boldsymbol{\gamma})$  is separable into a sum of magnetic and non-magnetic interactions  $V(\boldsymbol{\gamma}) = V_c(\boldsymbol{\gamma}) + V_m(\boldsymbol{\gamma})$ . Consequently, magnetic effects do not modify the contributions of the polymer chain to  $V_c(\boldsymbol{\gamma})$ , as is further explained in appendix B.

This corresponds to a factorization of the probability densities  $p_c(\boldsymbol{\gamma})$  and  $p_m(\boldsymbol{\gamma})$ , where the latter is defined via the Boltzmann factor

$$p_m(\boldsymbol{\gamma}) = \exp[-\beta V_m(\boldsymbol{\gamma})] \quad (20)$$

in analogy to (3). Therefore the total probability density becomes

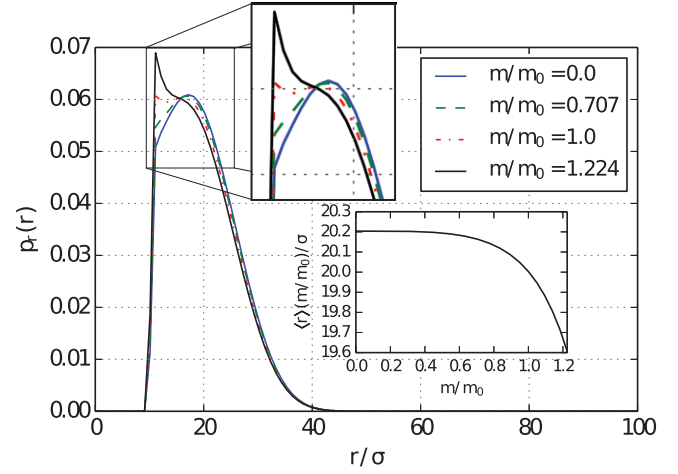


**Figure 11.** Nonvanishing permanent magnetic dipole moments of the mesoscopic particles and their impact on the system. We plot the marginal probability density  $p_r$  for the distance  $r$  between the particles for different values of the reduced magnetic moment  $m/m_0$ . Inset: average particle distance  $\langle r \rangle$  as a function of the reduced magnetic moment  $m/m_0$ .

$$p(\boldsymbol{\gamma}) = \frac{e^{-\beta[V_c(\boldsymbol{\gamma}) + V_m(\boldsymbol{\gamma})]}}{Z(m)} = \frac{p_c(\boldsymbol{\gamma})p_m(\boldsymbol{\gamma})}{Z(m)}, \quad (21)$$

where  $Z(m) = \int p_c(\boldsymbol{\gamma})p_m(\boldsymbol{\gamma})d\boldsymbol{\gamma}$  is the partition function describing the system for non-vanishing magnetic moments. We can calculate averages on the system with magnetic interactions by

$$\langle \cdot \rangle = \int \cdot p(\boldsymbol{\gamma}) d\boldsymbol{\gamma} = \frac{\int \cdot p_c(\boldsymbol{\gamma}) p_m(\boldsymbol{\gamma}) d\boldsymbol{\gamma}}{Z(m)}. \quad (22)$$

The single-variable marginal probability density  $p_\alpha(\alpha)$ ,  $\alpha = r, \theta_1, \theta_2, \phi$ , is again defined as  $p(\boldsymbol{\gamma})$  integrated over all the  $\boldsymbol{\gamma}$  variables except for  $\alpha$ . This is the same procedure as described in section 4 but substituting  $p_c(\boldsymbol{\gamma})$  with  $p(\boldsymbol{\gamma})$ . As can be seen from figure 11,  $p_r(r)$  shows an increase of the probability to find the particles close together when  $m$  is increased. A peak builds up at small  $r$  because the magnetic energy tends to  $V_m(r \rightarrow 0) \rightarrow -\infty$ . Although the magnetic spheres attract each other, a collapse is prevented by the WCA-potential, which becomes effective at  $r \lesssim 11\sigma$  and for  $r \rightarrow 0$  diverges faster to  $+\infty$  than the magnetic energy to  $-\infty$ . For  $m = m_0$ , the presence of a double peak in  $p_r(r)$  could be connected to a hardening transition of the kind described in [30]. Due to the mutual magnetic attraction between the parallel dipoles we expect the average distance  $\langle r \rangle$  to decrease with increasing  $m$ , and indeed it does so, as can be seen from the inset in figure 11.

The changes in the angular distributions for  $\theta_1$  and  $\theta_2$  due to the magnetic interaction are illustrated in figure 12. For the two angles  $\theta_1$  and  $\theta_2$  the distributions  $p_{\theta_1}(\theta_1)$  and  $p_{\theta_2}(\theta_2)$  are similar, and the behavior for varying  $m$  is approximately the same. Therefore, we only display the results for  $p_{\theta_1}(\theta_1)$ . The magnetic moments tend to align in parallel along the connecting axis  $\mathbf{r}$ , corresponding to their absolute energy minimum. Since we introduced the magnetic moments in that configuration for  $\theta_1 = \theta_2 = 0$ , for any fixed  $\theta_1$  the minimum of

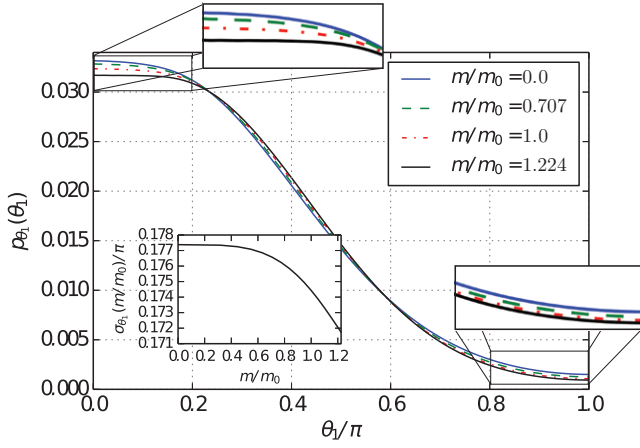


**Figure 12.** Marginal probability density  $p_{\theta_1}$  for the angle  $\theta_1$  (very similar for  $\theta_2$ ) for increasing reduced magnetic moment  $m/m_0$ . Inset: standard deviation of  $\theta_1$ ,  $\sigma_{\theta_1} = \sqrt{\langle(\theta_1 - \langle\theta_1\rangle)^2\rangle}$  (very similar for  $\theta_2$ ) as a function of  $m/m_0$ .

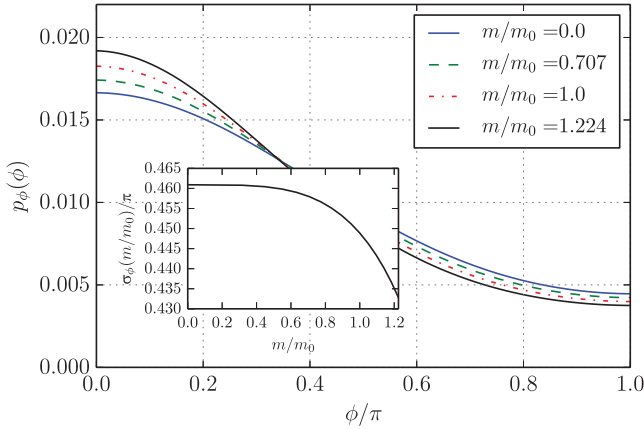


**Figure 13.** Marginal probability density  $p_{\phi}$  for the angle  $\phi$  describing the relative torsion between the particles, for increasing reduced magnetic moment  $m/m_0$ . Inset: standard deviation of  $\phi$ ,  $\sigma_{\phi} = \sqrt{\langle(\phi - \langle\phi\rangle)^2\rangle}$  as a function of  $m/m_0$ .

$V_m$ , and therefore the maximum of  $p_m$ , is located at  $\theta_2 = \theta_1$  and vice versa. As a consequence, the  $\theta_1 = \theta_2 = 0$  configuration leads to the same magnetic interaction energy as  $\theta_1 = \theta_2 = \pi$ . Concerning only magnetic interactions, both configurations show the same probability  $p_m$ . Integrating out  $r$ ,  $\theta_2$ , and  $\phi$  from  $p_m(\gamma)$ , the shape of the resulting magnetic probability density for  $\theta_1$  is symmetric around  $\theta_1 = \pi/2$  with one peak at  $\theta_1 = 0$  and one at  $\theta_1 = \pi$ . Therefore, coupling magnetic ( $p_m$ ) and non-magnetic ( $p_c$ ) contributions, we find that some probability shifts to higher values of  $\theta_1$  due to the magnetic interactions. However, we find the standard deviation of  $p_{\theta_1}(\theta_1)$  to decrease with increasing  $m$  (see the inset of figure 12), meaning that the particles become less likely to rotate along the  $\theta_1$  (or likewise  $\theta_2$ ) direction.

The same calculation for  $p_{\phi}(\phi)$  shows that the particles also become less likely to rotate around the connecting vector  $\mathbf{r}$ . The probability density of  $\phi \simeq 0$  rises and sharpens, as we can see in figure 13, and the standard deviation (see the inset of

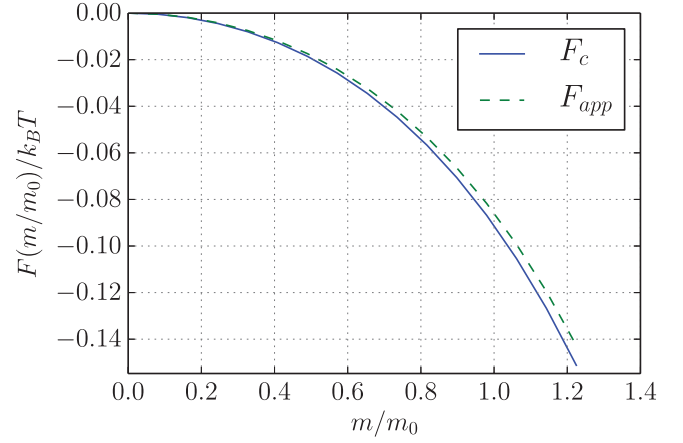


**Figure 14.** Free energy  $F(m) = -k_B T \ln[Z(m)]$  as a function of the reduced magnetic moment  $m/m_0$ . The partition function  $Z(m)$  is calculated once using  $p_c(\gamma)$  and once using  $p_{app}(\gamma)$ . The result from the microscopic simulation is labeled with ‘ $F_c$ ’ and the one from the analytical approximation with ‘ $F_{app}$ ’. Note that for  $m = 0$  the free energies are equal.

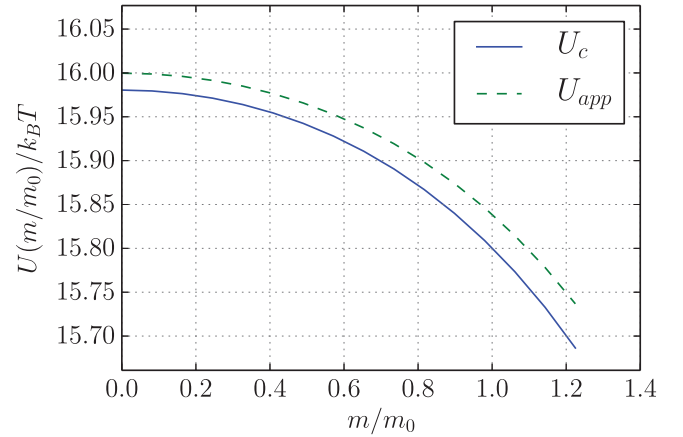


**Figure 15.** Internal energy  $U(m)$  as a function of the reduced magnetic moment  $m/m_0$ , calculated according to (23). The curve labeled with ‘ $U_c$ ’ shows the result from the microscopic data using (23), whereas in the one labeled with ‘ $U_{app}$ ’  $p_c(\gamma)$  has been replaced by  $p_{app}(\gamma)$ .

figure 13) decreases, confirming quantitatively the sharpening of  $p_{\phi}(\phi)$ .

## 9. Thermodynamic properties

Finally, we provide the connection to the thermodynamics of our canonical system and demonstrate the influence of the magnetic interactions. With the partition function  $Z(m)$  as in (21), we can calculate the overall free energy as  $F(m) = -k_B T \ln[Z(m)]$ , the internal energy of the system as

$$U(m) = \langle V \rangle(m) = \frac{\int V(\gamma) p_c(\gamma) p_m(\gamma) d\gamma}{Z(m)} \quad (23)$$

with  $V(\gamma)$  defined before (20), and the entropy as  $S(m) = [U(m) - F(m)]/T$ .

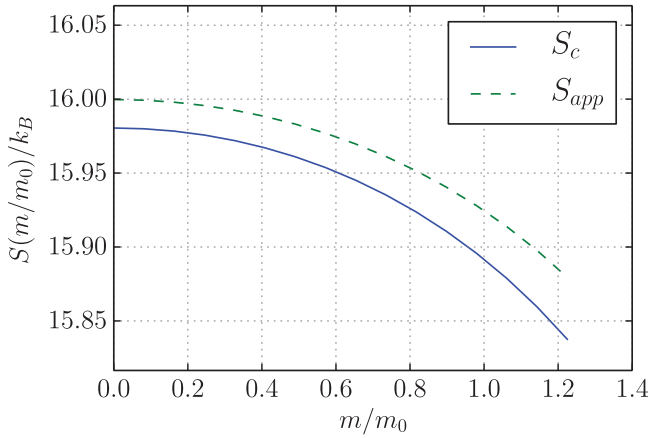


**Figure 16.** Entropy  $S(m) = [U(m) - F(m)]/T$  as a function of the reduced magnetic moment  $m/m_0$  calculated once using  $p_c(\gamma)$  from the microscopic simulation (labeled with ‘ $S_c$ ’), and once replacing  $p_c(\gamma)$  by  $p_{app}(\gamma)$  (labeled with ‘ $S_{app}$ ’).

To test the validity of our effective potential scheme using the coupling approximation described in section 7, we calculate the thermodynamic quantities using both probability densities  $p_c(\gamma)$  and  $p_{app}(\gamma)$  and compare the results. At vanishing magnetic moment, the free energy of the system is the same for both probability densities. This is expected, because it is a direct consequence of the normalization condition:  $Z(m=0) = Z_c = \int p_c(\gamma) d\gamma = \int p_{app}(\gamma) d\gamma = 1$  by construction of  $p_{app}(\gamma)$ . For non-vanishing magnetic moments, the partition functions obtained from the two probability densities (and thus the corresponding free energies) start to deviate from each other because the integral  $\int p_c(\gamma) p_m(\gamma) d\gamma$  is, in general, different from  $\int p_{app}(\gamma) p_m(\gamma) d\gamma$ . With increasing magnetic interaction, the difference between  $p_c(\gamma)$  and  $p_{app}(\gamma)$  becomes more important and, as shown in figure 14, leads to a slightly increasing deviation in the free energies  $F(m)$  calculated in both ways: at  $m \simeq 1.224m_0$  they already differ by  $\sim 5.6\%$ . Analogously, we can compare the internal energies of the system, shown in figure 15: at  $m = 0$  the error due to the probability density approximation is  $\sim 0.12\%$  of the exact value, rising up to  $\sim 0.32\%$  at  $m \simeq 1.224m_0$ . A similar deviation follows for the entropy, see figure 16, where, however, the error at  $m \simeq 1.224m_0$  increases to  $\sim 0.26\%$  of the exact value. Overall, however, the relative errors remain small, which confirms the validity and viability of our coarse-grained effective model potential in (18).

To summarize the effect of the magnetic dipoles on the system, we may conclude that the particles are driven towards each other. In other words, the average distance between them decreases (see figure 11) and the distributions for the particle separation and for the angular degrees of freedom sharpen (see figures 11–13). This reflects a decrease in entropy, which becomes possible due to the gain in magnetic interaction energy. Indeed, the calculated entropy decreases with increasing magnetic interactions (see figure 16), which is achieved by the decreasing free energy and internal energy (see figures 14 and 15, respectively).

## 10. Conclusions

Most of the previous studies on ferrogels describe the polymer matrix as a continuous material [23, 32, 34, 35] or represent it by springs connecting the particles [30, 36, 41–44], but only a few resolve explicitly the polymeric chains [45, 46]. In particular, a link between such microscopic chain-resolved calculations and the expressions for the investigated mesoscopic model energies has so far been missing. We have outlined in the present work a way to connect detailed microscopic simulations to a coarse-grained mesoscopic model.

This manifests a step into the direction of bridging the scales in material modeling. Starting from microscopic simulations considering explicitly an individual polymer chain connecting two mesoscopic particles, we specified effective mesoscopic pair potentials by fitting analytical model expressions. In this way, we were able to optimize a coarse-grained mesoscopic model description on the basis of the input from the explicit microscopic simulation details. Furthermore, we have shown that correlations between the mesoscopic degrees of freedom must be taken into account to provide a complete picture of the physics of the system. Moreover, we have examined the effect of a magnetic interaction, finding a tightening of the system by reducing the average distance between the magnetic particles and by reducing the rotational fluctuations around the configuration of highest probability density.

Our system consisted of only two mesoscopic particles, for which we derived the corresponding effective pair interaction potential. However, using this pair potential in a first approximation, two- and three-dimensional structures can be built up, similarly to elastic network structures generated using pairwise harmonic spring interactions between the particles [36, 43]. Including as a first approach magnetic interactions between neighboring particles only, the different angles between the magnetic moment of a particle and the anchoring points of the polymer chain to its different neighbors must be taken into account. Yet, using the reduced picture of pairwise mesoscopic interactions, it should be possible to reproduce for example previously observed deformational behavior in external magnetic fields for two- and three-dimensional systems [45, 46].

The scope of our approach is a first attempt of scale-bridging in modeling ferrogels and magnetic elastomers. Naturally, the procedure can be improved in many different ways. For example, we would like to study a system with multiple chains connecting the magnetic particles, with anchoring points randomly distributed over the surfaces of the particles. Such a development would eliminate artificial symmetries in the model and be another step towards the description of real systems. Furthermore, to study more realistic systems, interactions between more than two mesoscopic particles would need to be considered. Likewise, also the effect of interactions between next-nearest neighbors connected by polymer chains could be included. The last two points imply a step beyond the reduced picture of considering only effective pairwise interactions between the mesoscopic particles. Finally, via subsequent procedures of scale-bridging from the mesoscopic to the macroscopic level [49], a connection between

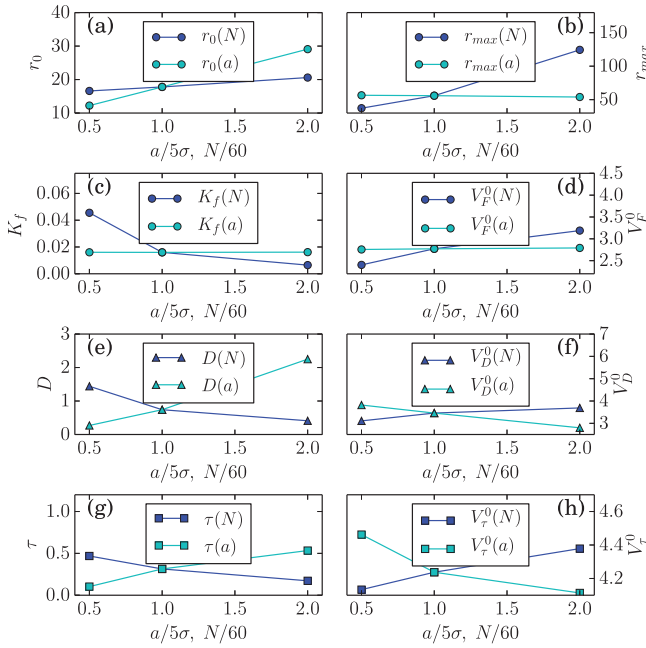


**Figure A1.** Effect of varying microscopic system parameters on the resulting mesoscopic model parameters. In the microscopic simulations, we varied the mesoscopic particle radius  $a$  and the number of beads  $N$  forming the connecting polymer chain. Fits of the single-variable mesoscopic model potentials (9)–(11) to the microscopic simulation data lead to the presented mesoscopic parameter values. ((a)–(d),  $\circ$ ) Model parameters for the FENE potential (9); ((e), (f),  $\triangle$ ) model parameters for the angular  $\theta_1$ - and  $\theta_2$ -potential (10); ((g), (h),  $\square$ ) model parameters for the torsional  $\phi$ -potential (11). Values for  $\theta_0$  and  $\phi_0$  vanished in all cases and are not shown. The data points for  $a/5\sigma = 1$  and  $N/60 = 1$  correspond to the results presented in figures 6–8.

microscopic details and macroscopic material behavior may become attainable for magnetic gels.

### Acknowledgments

The authors thank the Deutsche Forschungsgemeinschaft for support of this work through the priority program SPP 1681. RW and CH acknowledge further funding through the cluster of excellence EXC 310, SimTech, and are grateful for the access to the computer facilities of the HLRS and BW-University in Stuttgart.

### Appendix A. Dependence on microscopic system parameters

In sections 6 and 7 we derived an analytical approximation for the effective mesoscopic model potential describing our system. Here, we test how the mesoscopic model parameters depend on the microscopic system parameters. In particular, we performed additional microscopic simulations with varied radius  $a$  of the mesoscopic particles and varied number  $N$  of beads forming the connecting polymer chain.

In each case, we repeated the analysis of sections 4, 6 and 7 by fitting the mesoscopic single-variable model potentials (9)–(11) to the microscopic simulation data. This reveals the trends

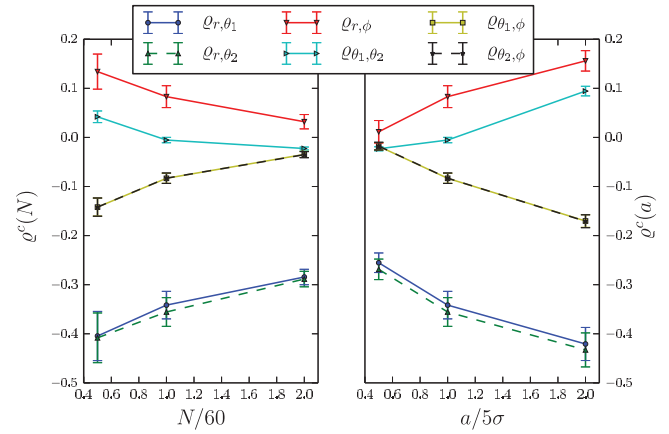


**Figure A2.** Elements of the correlation matrix  $\rho$  for different values of  $a$  and  $N$ . The data points for  $a/5\sigma = 1$  and  $N/60 = 1$  correspond to the results presented in (6).

in the dependences of the coefficients in the mesoscopic model potentials on the parameters  $a$  and  $N$ , as depicted in figure A1. From the trend of the resulting model parameters  $K_f$ ,  $D$ , and  $\tau$  in figures A1(c), (e) and (g) we conclude that the potentials tend to become stiffer as the chain becomes shorter or—at least for the rotational degrees of freedom—the mesoscopic particles become larger (see<sup>4</sup> for corresponding fitting curves).

Moreover, we have calculated the trend in the correlations between the mesoscopic degrees of freedom for varying values of  $a$  and  $N$ , see figure A2. We find that the magnitude of the correlations decreases with increasing  $N$  or decreasing  $a$ . Thus, quite intuitively, the coupling between the  $\gamma$  variables tends to decrease with longer chains or smaller mesoscopic particle sizes.

### Appendix B. Separability of the Hamiltonian and consequences for coarse-graining

In section 8 we have included the magnetic interactions analytically on the mesoscopic level. They had not been included in the microscopic simulations. This procedure is possible due to a separability of the magnetic and non-magnetic effects, which as a consequence implies a factorization of the corresponding probability. Thus the contribution of the polymer chain needs to be simulated explicitly. The contribution of any interaction acting solely on the mesoscopic particles can be exactly taken into account separately afterwards.

This argument relies on the separability of the Hamiltonian into a sum of mesoscopic and microscopic parts, as well as on the fact that magnetic interactions affect the mesoscopic part only. We write down the Hamiltonian of the system as

$$\mathcal{H}(\gamma, \Gamma) = \mathcal{T}_{\text{meso}}(\gamma) + V_m^{A,B}(\gamma) + V_{\text{WCA}}^{A,B}(\gamma) \quad (\text{B.1})$$

$$+ \mathcal{T}_{\text{micro}}(\Gamma) + \sum_{n=1}^N [V_{\text{WCA}}^{A,n}(\gamma, \Gamma) + V_{\text{WCA}}^{n,B}(\gamma, \Gamma)] + \sum_{n < n'}^N V_{\text{WCA}}^{n,n'}(\Gamma) \quad (\text{B.2})$$

<sup>4</sup> Corresponding data curves from the additional microscopic simulations and fitted mesoscopic model curves are summarized in the supplemental material ([stacks.iop.org/JPhysCM/27/325105/mmedia](http://stacks.iop.org/JPhysCM/27/325105/mmedia)).

$$+V_H^{A,1}(\boldsymbol{\gamma}, \boldsymbol{\Gamma}) + V_H^{N,B}(\boldsymbol{\gamma}, \boldsymbol{\Gamma}) + \sum_{n=1}^{N-1} V_H^{n,(n+1)}(\boldsymbol{\Gamma}). \quad (\text{B.3})$$

Similarly to the main text, let us here indicate with  $\boldsymbol{\gamma}$  the degrees of freedom (now velocities included) of the mesoscopic particles and with  $\boldsymbol{\Gamma}$  the ones of the microscopic particles that build up the chain. For brevity we here label the mesoscopic particles by  $A$  and  $B$  and the microscopic ones by the discrete indices  $n, n' = 1, \dots, N$ . Moreover, we denote by  $V_{ij}^{p,q}(\boldsymbol{\gamma}, \boldsymbol{\Gamma})$  the corresponding interaction between particles  $p$  and  $q$ , where the explicit expressions of  $V_{WCA}$ ,  $V_H$ , and  $V_m$  are as described in (1), (2) and (19).  $\mathcal{T}_{\text{meso}}(\boldsymbol{\gamma})$  and  $\mathcal{T}_{\text{micro}}(\boldsymbol{\Gamma})$  indicate, respectively, the kinetic energies of the mesoscopic and microscopic particles. Therefore,  $\mathcal{H}(\boldsymbol{\gamma}, \boldsymbol{\Gamma})$  is separable into

$$\mathcal{H}(\boldsymbol{\gamma}, \boldsymbol{\Gamma}) = \mathcal{H}_{\text{meso}}(\boldsymbol{\gamma}) + \mathcal{H}_{\text{micro}}(\boldsymbol{\gamma}, \boldsymbol{\Gamma}), \quad (\text{B.4})$$

where  $\mathcal{H}_{\text{meso}}(\boldsymbol{\gamma})$  contains the terms in line (B.1) and  $\mathcal{H}_{\text{micro}}(\boldsymbol{\gamma}, \boldsymbol{\Gamma})$  is composed of the terms in lines (B.2) and (B.3).

Since we work in the canonical ensemble, the physics of the system derives from the partition function

$$\begin{aligned} \mathcal{Z}(m) &= \int e^{-\beta\mathcal{H}(\boldsymbol{\gamma}, \boldsymbol{\Gamma})} d\boldsymbol{\gamma} d\boldsymbol{\Gamma} \\ &= \int e^{-\beta\mathcal{H}_{\text{meso}}(\boldsymbol{\gamma})} e^{-\beta\mathcal{H}_{\text{micro}}(\boldsymbol{\gamma}, \boldsymbol{\Gamma})} d\boldsymbol{\gamma} d\boldsymbol{\Gamma}, \end{aligned} \quad (\text{B.5})$$

with  $\beta = 1/k_B T$ . Coarse-graining means to integrate out the microscopic degrees of freedom  $\boldsymbol{\Gamma}$ , so we rearrange

$$\begin{aligned} \mathcal{Z}(m) &= \int e^{-\beta\mathcal{H}_{\text{meso}}(\boldsymbol{\gamma})} \left[ \int e^{-\beta\mathcal{H}_{\text{micro}}(\boldsymbol{\gamma}, \boldsymbol{\Gamma})} d\boldsymbol{\Gamma} \right] d\boldsymbol{\gamma} \\ &= \int e^{-\beta\mathcal{H}_{\text{meso}}(\boldsymbol{\gamma})} \mathcal{Z}_{\text{micro}}(\boldsymbol{\gamma}) d\boldsymbol{\gamma} \\ &= \int e^{-\beta V_m^{A,B}(\boldsymbol{\gamma})} e^{-\beta[\mathcal{T}_{\text{meso}}(\boldsymbol{\gamma}) + V_{WCA}^{A,B}(\boldsymbol{\gamma})]} \mathcal{Z}_{\text{micro}}(\boldsymbol{\gamma}) d\boldsymbol{\gamma}. \end{aligned} \quad (\text{B.6})$$

The connection to the probability density  $p_c(\boldsymbol{\gamma})$  is given by

$$p_c(\boldsymbol{\gamma}) = \frac{\mathcal{Z}_{\text{micro}}(\boldsymbol{\gamma}) e^{-\beta[\mathcal{T}_{\text{meso}}(\boldsymbol{\gamma}) + V_{WCA}^{A,B}(\boldsymbol{\gamma})]}}{\mathcal{Z}(m=0)}. \quad (\text{B.7})$$

Since the magnetic interactions only affect the mesoscopic particles, see line (B.1), it is solely contained in  $\mathcal{H}_{\text{meso}}(\boldsymbol{\gamma})$ . Therefore, the microscopic Hamiltonian  $\mathcal{H}_{\text{micro}}(\boldsymbol{\gamma}, \boldsymbol{\Gamma})$  for a specific fixed configuration  $\boldsymbol{\gamma}$  of the mesoscopic particles does not explicitly depend on the magnetic moments. The magnetic effects do not modify the physics of the polymer chain for a given configuration of the mesoscopic particles. The underlying physical reason is that the polymer chain does not contain magnetic components.

As we can see, the magnetic interactions only appear on the mesoscopic level of the final partition function  $\mathcal{Z}$ . The magnetic interactions are simply included by multiplying on the mesoscopic level with the additional probability factor  $\exp[-\beta V_m^{A,B}(\boldsymbol{\gamma})]$ . The remaining part of the integrand that contains the information drawn from the MD simulations, is not affected.

Explicitly introducing the magnetic moments in the microscopic simulation would therefore not affect the final outcome.

Thus, it is sufficient to determine the effects of the polymer chain through MD simulations and add the magnetic interactions analytically in a subsequent step.

## References

- [1] Strobl G 2007 *The Physics of Polymers* (Berlin: Springer)
- [2] Klapp S H L 2005 Dipolar fluids under external perturbations *J. Phys.: Condens. Matter* **17** R525
- [3] Huke B and Lücke M 2004 Magnetic properties of colloidal suspensions of interacting magnetic particles *Rep. Prog. Phys.* **67** 1731
- [4] Rosenzweig R E 1985 *Ferrohydrodynamics* (Cambridge: Cambridge University Press)
- [5] Odenbach S 2003 Ferrofluids—magnetically controlled suspensions *Colloid Surf.* **217** 171–8
- [6] Odenbach S 2003 *Magnetoviscous Effects in Ferrofluids* (Berlin: Springer)
- [7] Odenbach S 2004 Recent progress in magnetic fluid research *J. Phys.: Condens. Matter* **16** R1135–50
- [8] Ilg P, Kröger M and Hess S 2005 Structure and rheology of model-ferrofluids under shear flow *J. Magn. Magn. Mater.* **289** 325–7
- [9] Ilg P, Coquelle E and Hess S 2006 Structure and rheology of ferrofluids: simulation results and kinetic models *J. Phys.: Condens. Matter* **18** S2757–70
- [10] Holm C and Weis J-J 2005 The structure of ferrofluids: a status report *Curr. Opin. Colloid Interface Sci.* **10** 133–40
- [11] Menzel A M 2014 Tuned, driven, and active soft matter *Phys. Rep.* **554** 1–45
- [12] Jarkova E, Pleiner H, Müller H-W and Brand H R 2003 Hydrodynamics of isotropic ferrogels *Phys. Rev. E* **68** 041706
- [13] Zrínyi M, Barsi L and Büki A 1996 Deformation of ferrogels induced by nonuniform magnetic fields *J. Chem. Phys.* **104** 8750–6
- [14] Deng H-X, Gong X-L and Wang L-H 2006 Development of an adaptive tuned vibration absorber with magnetorheological elastomer *Smart Mater. Struct.* **15** N111–6
- [15] Stepanov G V, Abramchuk S S, Grishin D A, Nikitin L V, Kramarenko E Y and Khokhlov A R 2007 Effect of a homogeneous magnetic field on the viscoelastic behavior of magnetic elastomers *Polymer* **48** 488–95
- [16] Filipcsei G, Csetneki I, Szilágyi A and Zrínyi M 2007 Magnetic field-responsive smart polymer composites *Adv. Polym. Sci.* **206** 137–89
- [17] Guan X, Dong X and Ou J 2008 Magnetostrictive effect of magnetorheological elastomer *J. Magn. Magn. Mater.* **320** 158–63
- [18] Böse H and Röder R 2009 Magnetorheological elastomers with high variability of their mechanical properties *J. Phys.: Conf. Ser.* **149** 012090
- [19] Gong X, Liao G and Xuan S 2012 Full-field deformation of magnetorheological elastomer under uniform magnetic field *Appl. Phys. Lett.* **100** 211909
- [20] Evans B A, Fiser B L, Prins W J, Rapp D J, Shields A R, Glass D R and Superfine R 2012 A highly tunable silicone-based magnetic elastomer with nanoscale homogeneity *J. Magn. Magn. Mater.* **324** 501–7
- [21] Borin D Y, Stepanov G V and Odenbach S 2013 Tuning the tensile modulus of magnetorheological elastomers with magnetically hard powder *J. Phys.: Conf. Ser.* **412** 012040
- [22] Zimmermann K, Naletova V A, Zeidis I, Böhm V and Kolev E 2006 Modelling of locomotion systems using deformable magnetizable media *J. Phys.: Condens. Matter* **18** S2973–83

- [23] Szabó D, Szeghy G and Zrínyi M 1998 Shape transition of magnetic field sensitive polymer gels *Macromolecules* **31** 6541–8
- [24] Ramanujan R V and Lao L L 2006 The mechanical behavior of smart magnet-hydrogel composites *Smart Mater. Struct.* **15** 952–6
- [25] Sun T L, Gong X L, Jiang W Q, Li J F, Xu Z B and Li W H 2008 Study on the damping properties of magnetorheological elastomers based on *cis*-polybutadiene rubber *Polym. Test.* **27** 520–6
- [26] Babincová M, Leszczynska D, Sourivong P, Čičmanec P and Babinec P 2001 Superparamagnetic gel as a novel material for electromagnetically induced hyperthermia *J. Magn. Magn. Mater.* **225** 109–12
- [27] Lao L L and Ramanujan R V 2004 Magnetic and hydrogel composite materials for hyperthermia applications *J. Mater. Sci.: Mater. Med.* **15** 1061–4
- [28] Landau L D and Lifshitz E M 1975 *Elasticity Theory* (Oxford: Pergamon)
- [29] Bohlius S, Brand H R and Pleiner H 2004 Macroscopic dynamics of uniaxial magnetic gels *Phys. Rev. E* **70** 061411
- [30] Annunziata M A, Menzel A M and Löwen H 2013 Hardening transition in a one-dimensional model for ferrogels *J. Chem. Phys.* **138** 204906
- [31] Messing R, Frickel N, Belkoura L, Strey R, Rahn H, Odenbach S and Schmidt A M 2011 Cobalt ferrite nanoparticles as multifunctional cross-linkers in PAAm ferrohydrogels *Macromolecules* **44** 2990–9
- [32] Zubarev A Y 2012 On the theory of the magnetic deformation of ferrogels *Soft Matter* **8** 3174–9
- [33] Brand H R and Pleiner H 2014 Macroscopic behavior of ferronematic gels and elastomers *Eur. Phys. J. E* **37** 122
- [34] Ivaneyko D, Toshchevikov V, Saphiannikova M and Heinrich G 2012 Effects of particle distribution on mechanical properties of magneto-sensitive elastomers in a homogeneous magnetic field *Condens. Matter Phys.* **15** 33601
- [35] Wood D S and Camp P J 2011 Modeling the properties of ferrogels in uniform magnetic fields *Phys. Rev. E* **83** 011402
- [36] Pessot G, Cremer P, Borin D Y, Odenbach S, Löwen H and Menzel A M 2014 Structural control of elastic moduli in ferrogels and the importance of non-affine deformations *J. Chem. Phys.* **141** 124904
- [37] Raikher Y L, Stolbov O V and Stepanov G V 2008 Shape instability of a magnetic elastomer membrane *J. Phys. D* **41** 152002
- [38] Stolbov O V, Raikher Y L and Balasoiu M 2011 Modelling of magnetodipolar striction in soft magnetic elastomers *Soft Matter* **7** 8484–7
- [39] Han Y, Hong W and Faidley L E 2013 Field-stiffening effect of magneto-rheological elastomers *Int. J. Solids Struct.* **50** 2281–8
- [40] Spieler C, Kästner M, Goldmann J, Brummund J and Ulbricht V 2013 XFEM modeling and homogenization of magnetoactive composites *Acta Mech.* **224** 2453–69
- [41] Dudek M R, Grabiec B and Wojciechowski K W 2007 Molecular dynamics simulations of auxetic ferrogel *Rev. Adv. Mater. Sci.* **14** 167–73
- [42] Sánchez P A, Cerdà J J, Sintes T and Holm C 2013 Effects of the dipolar interaction on the equilibrium morphologies of a single supramolecular magnetic filament in bulk *J. Chem. Phys.* **139** 044904
- [43] Tarama M, Cremer P, Borin D Y, Odenbach S, Löwen H and Menzel A M 2014 Tunable dynamic response of magnetic gels: impact of structural properties and magnetic fields *Phys. Rev. E* **90** 042311
- [44] Cerdà J J, Sánchez P A, Holm C and Sintes T 2013 Phase diagram for a single flexible Stockmayer polymer at zero field *Soft Matter* **9** 7185
- [45] Weeber R, Kantorovich S and Holm C 2012 Deformation mechanisms in 2d magnetic gels studied by computer simulations *Soft Matter* **8** 9923–32
- [46] Weeber R, Kantorovich S and Holm C 2015 Ferrogels cross-linked by magnetic nanoparticles—deformation mechanisms in two and three dimensions studied by means of computer simulations *J. Magn. Magn. Mater.* **383** 262–6
- [47] Harmandaris V A, Reith D, van der Vegt N F A and Kremer K 2007 Comparison between coarse-graining models for polymer systems: two mapping schemes for polystyrene *Macromol. Chem. Phys.* **208** 2109–20
- [48] Mulder T, Harmandaris V A, Lyulin A V, van der Vegt N F A, Vorseelaars B and Michels M A J 2008 Equilibration and deformation of amorphous polystyrene: scale-jumping simulational approach *Macromol. Theory Simul.* **17** 290–300
- [49] Menzel A M 2015 Bridging from particle to macroscopic scales in uniaxial magnetic gels *J. Chem. Phys.* **141** 194907
- [50] Arnold A, Lenz O, Kesselheim S, Weeber R, Fahrenberger F, Röhm D, Košován P and Holm C 2013 Espresso 3.1: molecular dynamics software for coarse-grained models *Meshfree Methods for Partial Differential Equations VI* (Lecture Notes in Computational Science and Engineering vol 89) ed M Griebel and M A Schweitzer (Berlin: Springer) pp 1–23
- [51] Hansen J P and Löwen H 2002 Effective interactions for large-scale simulations of complex fluids *Bridging Time Scales: Molecular Simulations for the Next Decade* (Lecture Notes in Physics vol 605) ed P Nielaba *et al* (Berlin: Springer) pp 167–96
- [52] Limbach H J, Arnold A, Mann B A and Holm C 2006 ESPResSo—an extensible simulation package for research on soft matter systems *Comput. Phys. Commun.* **174** 704–27
- [53] Wang Z, Holm C and Müller H W 2002 Molecular dynamics study on the equilibrium magnetization properties and structure of ferrofluids *Phys. Rev. E* **66** 021405
- [54] Frenkel D and Smit B 2002 *Understanding Molecular Simulation* 2nd edn (San Diego, CA: Academic)
- [55] Frickel N, Messing R and Schmidt A M 2011 Magneto-mechanical coupling in CoFe<sub>2</sub>O<sub>4</sub>-linked PAAm ferrohydrogels *J. Mater. Chem.* **21** 8466–74
- [56] Warner H R 1972 Kinetic theory and rheology of dilute suspensions of finitely extensible dumbbells *Ind. Eng. Chem. Fundam.* **11** 379–87
- [57] Nelder J A and Mead R 1965 A simplex method for function minimization *Comput. J.* **7** 308–13
- [58] Jones E, Oliphant T and Peterson P 2001 SciPy: open source scientific tools for Python
- [59] Günther D, Borin D Y, Günther S and Odenbach S 2012 X-ray micro-tomographic characterization of field-structured magnetorheological elastomers *Smart Mater. Struct.* **21** 015005
- [60] Collin D, Auernhammer G K, Gavati O, Martinoty P and Brand H R 2003 Frozen-in magnetic order in uniaxial magnetic gels: preparation and physical properties *Macromol. Rapid Commun.* **24** 737–41
- [61] Varga Z, Fehér J, Filipcsei G and Zr M 2003 Smart nanocomposite polymer gels *Macromol. Symp.* **200** 93–100
- [62] Borbáth T, Günther S, Borin D Y, Gundermann T and Odenbach S 2012 X $\mu$ CT analysis of magnetic field-induced phase transitions in magnetorheological elastomers *Smart Mater. Struct.* **21** 105018

## SUPPLEMENTARY MATERIAL

### Towards a scale-bridging description of ferrogels and magnetic elastomers

Giorgio Pessot,<sup>1,\*</sup> Rudolf Weeber,<sup>2,†</sup> Christian Holm,<sup>2,‡</sup> Hartmut Löwen,<sup>1,§</sup> and Andreas M. Menzel<sup>1,¶</sup>

<sup>1</sup>*Institut für Theoretische Physik II: Weiche Materie,*

*Heinrich-Heine-Universität Düsseldorf, D-40225 Düsseldorf, Germany*

<sup>2</sup>*Institute for Computational Physics, Universität Stuttgart, 70569 Stuttgart, Germany*

#### Fit of the single-variable mesoscopic model potentials for different microscopic system parameters

In the present supplementary material we include the plots of the single-variable effective mesoscopic model potentials for different system parameters of the microscopic simulations. That is, we vary the radius  $a$  of the mesoscopic particles and the number of beads  $N$  forming the connecting polymer chain. We show the curves obtained from fitting the mesoscopic model potentials (9)–(12) of section VI in the main text to the microscopic simulation results.

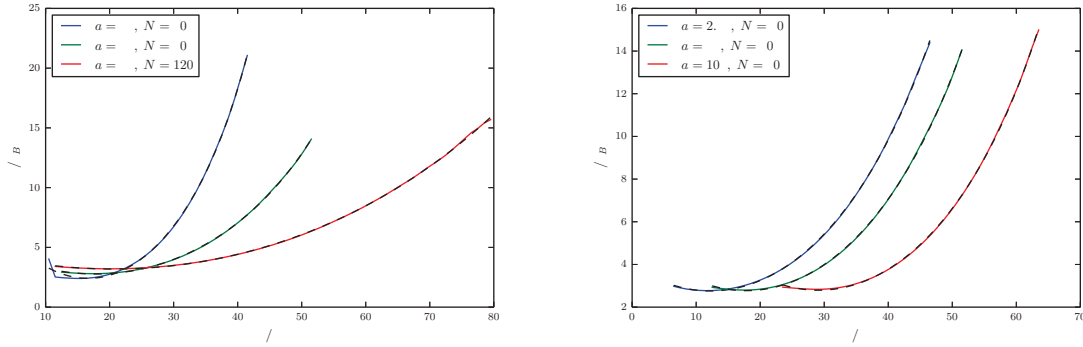


Figure 1: Solid lines: effective potentials  $\tilde{V}_r(r)$  for different combinations of parameters  $a$  and  $N$ . Dashed lines: fit of the  $V_{FENE}(r)$  potential (9) of the main text; see appendix A for the resulting mesoscopic model parameters.

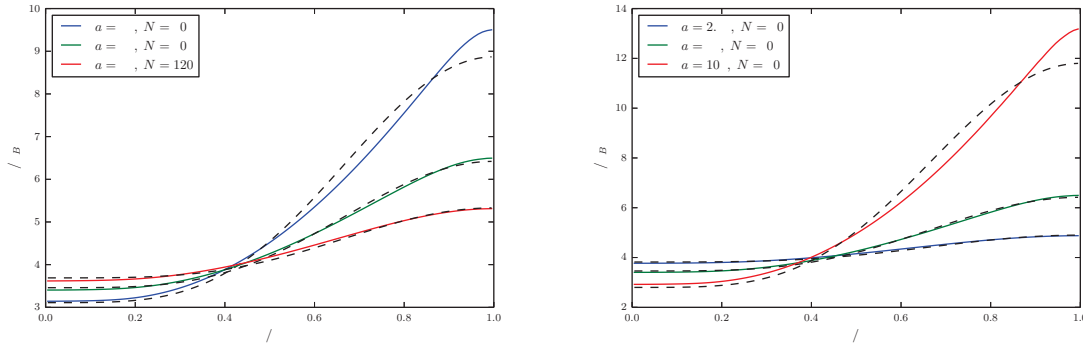


Figure 2: Solid lines: effective potentials  $\tilde{V}_\theta(\theta)$  for different combinations of parameters  $a$  and  $N$ . Dashed lines: fit of the  $V_D(\theta)$  potential (10) of the main text; see appendix A for the resulting mesoscopic model parameters.

\*Electronic address: [giorgpess@thphy.uni-duesseldorf.de](mailto:giorgpess@thphy.uni-duesseldorf.de)

†Electronic address: [weeber@icp.uni-stuttgart.de](mailto:weeber@icp.uni-stuttgart.de)

‡Electronic address: [holm@icp.uni-stuttgart.de](mailto:holm@icp.uni-stuttgart.de)

§Electronic address: [hlowen@thphy.uni-duesseldorf.de](mailto:hlowen@thphy.uni-duesseldorf.de)

¶Electronic address: [menzel@thphy.uni-duesseldorf.de](mailto:menzel@thphy.uni-duesseldorf.de)

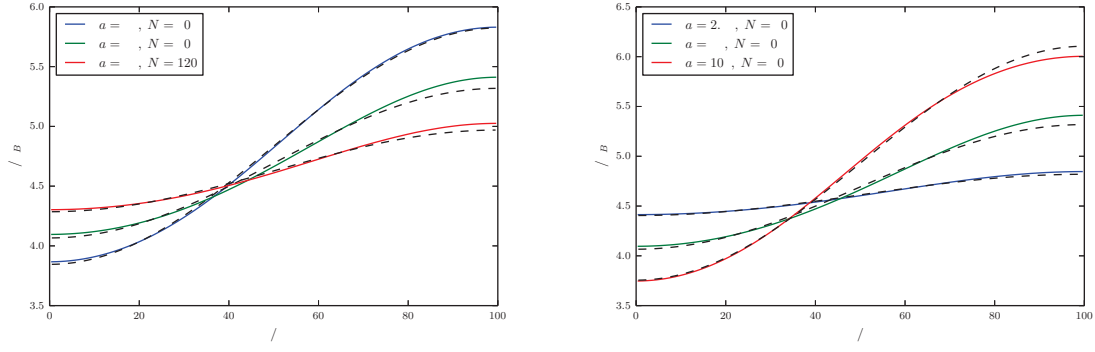


Figure 3: Solid lines: effective potentials  $\tilde{V}_\phi(\phi)$  for different combinations of parameters  $a$  and  $N$ . Dashed lines: fit of the  $V_\tau(\phi)$  potential (11) of the main text; see appendix A for the resulting mesoscopic model parameters.

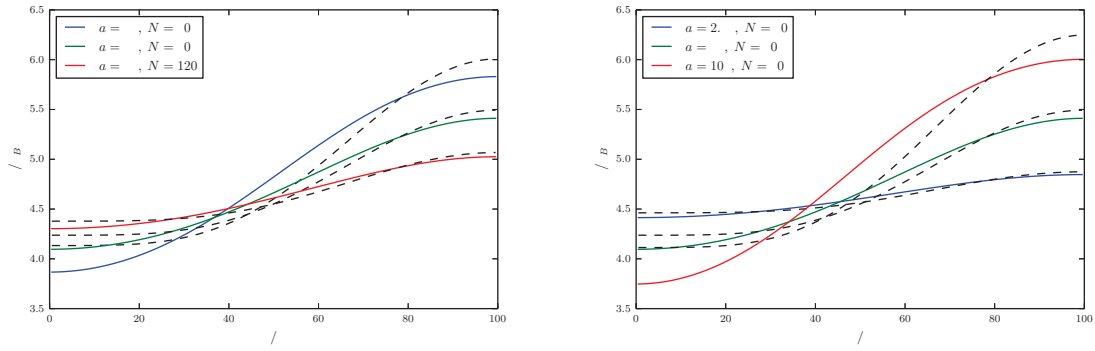


Figure 4: Solid lines: effective potentials  $\tilde{V}_\phi(\phi)$  for different combinations of parameters  $a$  and  $N$ . Dashed lines: fit of the  $V'_\tau(\phi)$  potential (12) of the main text.

## Paper II Buckling of paramagnetic chains in soft gels

Reproduced from

Shilin Huang, Giorgio Pessot, Peet Cremer, Rudolf Weeber, Christian Holm, Johannes Nowak, Stefan Odenbach, Andreas M. Menzel, and Günter K. Auernhammer, **Buckling of paramagnetic chains in soft gels**. *Soft Matter*, **12** 228 (2016), The Royal Society of Chemistry,

published by *The Royal Society of Chemistry* under a Creative Commons Attribution 3.0 Unported Licence.

(Version of Record, Supplementary Material)

DOI: 10.1039/C5SM01814E

### Authors' Contributions

All authors contributed to the writing of the manuscript. Christian Holm, Stefan Odenbach, Andreas M. Menzel, and Günter K. Auernhammer supervised the work in the respective groups. Shilin Huang performed the main experimental contribution. Johannes Nowak measured the magnetization curves. I performed the numerical calculations based on the phenomenological model devised together with Andreas M. Menzel. Rudolf Weeber carried out the particle-resolved simulations. I estimate my total contribution to this work to approximately 25%.

### Copyright and Permission Informations

From Publication Details/ Open Access :

This article, published by *The Royal Society of Chemistry*, is licensed under a Creative Commons Attribution 3.0 Unported Licence. Material from this article can be used in other publications provided that the correct acknowledgment is given with the reproduced material.





Cite this: *Soft Matter*, 2016, 12, 228

## Buckling of paramagnetic chains in soft gels†

Shilin Huang,<sup>a</sup> Giorgio Pessot,<sup>b</sup> Peet Cremer,<sup>b</sup> Rudolf Weeber,<sup>c</sup> Christian Holm,<sup>c</sup> Johannes Nowak,<sup>d</sup> Stefan Odenbach,<sup>d</sup> Andreas M. Menzel<sup>b</sup> and Günter K. Auernhammer<sup>\*a</sup>

We study the magneto-elastic coupling behavior of paramagnetic chains in soft polymer gels exposed to external magnetic fields. To this end, a laser scanning confocal microscope is used to observe the morphology of the paramagnetic chains together with the deformation field of the surrounding gel network. The paramagnetic chains in soft polymer gels show rich morphological shape changes under oblique magnetic fields, in particular a pronounced buckling deformation. The details of the resulting morphological shapes depend on the length of the chain, the strength of the external magnetic field, and the modulus of the gel. Based on the observation that the magnetic chains are strongly coupled to the surrounding polymer network, a simplified model is developed to describe their buckling behavior. A coarse-grained molecular dynamics simulation model featuring an increased matrix stiffness on the surfaces of the particles leads to morphologies in agreement with the experimentally observed buckling effects.

Received 22nd July 2015,  
Accepted 8th October 2015

DOI: 10.1039/c5sm01814e

[www.rsc.org/softmatter](http://www.rsc.org/softmatter)

## 1 Introduction

Magneto-responsive hybrid gels (MRGs) have been attracting great attention due to their tunable elasticity, swelling properties and shape that can be remotely controlled by a magnetic field. They have potential applications as soft actuators, artificial muscles, as well as sensors<sup>1–3</sup> and can serve as model systems to study the heat transfer in hyperthermal cancer treatment.<sup>4</sup> Compared to other stimuli-responsive gels, MRGs have the advantage of fast response, controlled mechanical properties and reversible deformabilities.<sup>5–7</sup> A typical MRG consists of a chemically cross-linked polymer network, swollen in a good solvent, and embedded magnetic particles.<sup>5,8</sup> The size of the magnetic particles can range from ~10 nm to several  $\mu\text{m}$ .<sup>7</sup>

The origin of the magneto-responsive behavior of MRGs is the magnetic interaction between the magnetic filler particles as well as their interaction with external magnetic fields.<sup>9,10</sup> In a uniform magnetic field, paramagnetic particles can be polarized

and act as approximate magnetic dipoles. Depending on their mutual azimuthal configuration, the dipolar interactions can be either attractive or repulsive. In a liquid carrier, the dipolar interaction drives the magnetic particles to form chains and columns<sup>11–14</sup> aligning in the direction of the magnetic field. However, in a polymer gel, the particles cannot change their position freely. Instead, relative displacements of the particles, induced *e.g.* by changes in the magnetic interactions, lead to opposing deformations of the polymer network. As a result, the magnetic interactions can induce changes in the modulus of the gel.<sup>7,15</sup> This magneto-elastic effect is well known to be related to the spatial distribution of the magnetic particles.<sup>16–21</sup> For example, the modulus of anisotropic materials that contain aligned chain-like aggregates of magnetic filler particles<sup>15,22–24</sup> can be significantly enhanced when an external magnetic field is applied along the chain direction.<sup>7</sup> The anisotropic arrangement of particles also dominates the anisotropic magnetostriction effects.<sup>25–27</sup>

Different theoretical routes have been pursued to investigate the magneto-elastic effects of MRGs: macroscopic continuum mechanics approaches,<sup>28,29</sup> mesoscopic modeling,<sup>16–19</sup> and more microscopic approaches<sup>30–32</sup> that resolve individual polymer chains. Theoretical routes to connect and unify these different levels of description have recently been proposed.<sup>33–35</sup> The authors of ref. 34 show how the interplay between the mesoscopic particle distribution and the macroscopic shape of the sample affects the magneto-elastic effect. In addition to these factors, recent experiments and computer simulations also point out that a direct coupling between the magnetic particles and attached polymer chains can play another important role.<sup>1,30,31,36–39</sup>

<sup>a</sup> Max Planck Institute for Polymer Research, Ackermannweg 10, 55128 Mainz, Germany. E-mail: [auhammer@mpip-mainz.mpg.de](mailto:auhammer@mpip-mainz.mpg.de); Fax: +49 6131 379 100; Tel: +49 6131 379 113

<sup>b</sup> Institut für Theoretische Physik II: Weiche Materie, Heinrich-Heine-Universität Düsseldorf, 40225 Düsseldorf, Germany

<sup>c</sup> Institute for Computational Physics, Universität Stuttgart, 70569 Stuttgart, Germany

<sup>d</sup> Chair of Magneto-fluidynamics, Measuring and Automation Technology, Institute of Fluid Mechanics, Technische Universität Dresden, 01069 Dresden, Germany

† Electronic supplementary information (ESI) available. See DOI: 10.1039/c5sm01814e



An experimental model system showing a well-defined particle distribution and a measurable magneto-elastic effect can help to understand the magneto-elastic behavior of MRGs at different length scales. Projected into a two-dimensional plane, the distribution of magnetic particles in thin diluted MRGs can be detected using optical microscopy or light scattering methods.<sup>15,40</sup> By combining these techniques with magnetic or mechanical devices, it is possible to observe the particle rearrangement when the MRG sample is exposed to a magnetic field or mechanical stimuli.<sup>15,41</sup> For three-dimensional (3D) characterization, X-ray micro-tomography has been used.<sup>23</sup> Here we introduce another 3D imaging technique – laser scanning confocal microscopy (LSCM). Compared to normal optical microscopy, LSCM is able to observe 3D structures and it has a better resolution.<sup>42</sup> Compared to X-ray micro-tomography, LSCM is faster in obtaining a 3D image and easier to combine with other techniques for real-time investigation.<sup>43,44</sup>

We use LSCM to study the magneto-elastic effects of paramagnetic chains in soft gels. As a result, we find that the paramagnetic chains in soft gels (elastic modulus < 2 Pa) under an oblique magnetic field show rich morphologies. Depending on the length of the chain, modulus of the gel and strength of an external magnetic field, the chains can rotate, bend, and buckle. The deformation field in the polymer network around the deformed paramagnetic chains can also be tracked. The result confirms that the chains are strongly coupled to the polymer network. A simplified model is developed to understand the magnetically induced buckling behavior of the paramagnetic chains in soft gels. In addition to serving as a model experimental system for studying the magneto-elastic effect of MRGs, our approach may also provide a new microrheological technique to probe the mechanical property of a soft gel.<sup>45</sup> Furthermore, our results may be interesting to biological scientists who study how magnetosome chains interact with the surrounding cytoskeletal network in magnetotactic bacteria.<sup>46</sup>

## 2 Materials and methods

The elastic network was obtained by hydrosilation of a difunctional vinyl-terminated polydimethylsiloxane (vinyl-terminated PDMS, DMS-V25, Gelest Inc.) prepolymer with a SiH-containing cross-linker (PDMS, HMS-151, Gelest Inc.). Platinum(0)-1,3-divinyl-1,1,3,3-tetramethyldisiloxane complex (Alfa Aesar) was used as a catalyst. A low-molecular-weight trimethylsiloxy-terminated PDMS (770 g mol<sup>-1</sup>, Alfa Aesar GmbH & Co. KG, in the following “PDMS 770”) served as a solvent that carried the polymer network and the paramagnetic particles. The paramagnetic particles were purchased from microParticles GmbH. They were labeled with fluorophores (visible in LSCM). The materials consist of porous polystyrene spheres. Within the pores, nanoparticulate iron oxide was distributed rendering the particles superparamagnetic. To prevent iron oxide leaching, the particles had a polymeric sealing that also held the fluorophores. The particles had a diameter of  $1.48 \pm 0.13 \mu\text{m}$  (ESI,† Fig. S1a). We measured the magnetization curve (ESI,† Fig. S1b) of the paramagnetic particles by a vibrating sample magnetometer

(VSM, Lake Shore 7407). We found about 20% deviations in the magnetic properties of the magnetic particles (*e.g.*, magnetic moment, see ESI,† Fig. S2). In order to observe the deformation field in the polymer network, we used fluorescently labeled silica particles as tracers. They had a diameter of  $830 \pm 50 \text{ nm}$  and the surface was modified with *N,N*-dimethyl-*N*-octadecyl-3-amino-propyltrimethoxysilylchloride.

After drying under vacuum at room temperature overnight, the paramagnetic particles were dispersed into PDMS 770. In some samples, tracer particles (3 wt%) were also dispersed into PDMS 770 in this step. The prepolymer mixture was prepared with 9.1 wt% vinyl-terminated PDMS and 90.9 wt% SiH-containing cross-linker. The prepolymer mixture (2.86 wt%) was dissolved in PDMS 770, which contained the paramagnetic particles. Finally, by adding PDMS 770, which carried the catalyst, the concentration of the prepolymer mixture in the sol solution was carefully adjusted in the range from 2.74 wt% to 2.78 wt%. This concentration range guaranteed the formation of soft gels with an elastic modulus lower than 10 Pa (see ESI,† Fig. S3). In the sol solution, the catalyst concentration was 0.17 wt%, and the concentration of magnetic particles was 0.09 wt%. The sol solution was agitated at 2500 rpm with a Reax Control (Heidolph, Schwabach, Germany) for 2 min for homogenization, followed by ultrasonication (2 min, Transsonic 460/H, Elma) to disperse the magnetic particles. Then the sol solution was introduced into a thin sample cell ( $\sim 160 \mu\text{m}$  thick and  $\sim 1 \text{ cm}$  wide) by capillary forces. The sample cells consisted of two No. 1 standard coverslips, separated by  $\sim 160 \mu\text{m}$  spacers. After sealing with two-component glue, the cells that contained the sol were exposed to a  $100.8 \pm 0.5 \text{ mT}$  magnetic field. The paramagnetic particles aligned into chains along the direction of the applied magnetic field while the prepolymer was crosslinking. A visible reaction of the prepolymer occurred within 10 min, and the rheological measurements showed that it took about 40 min to form a gel. Due to the low concentration of magnetic particles, the magnetic chains in the gel were well separated ( $> 30 \mu\text{m}$ ). The length of the chains varied from a single particle up to about 170 particles. We stored the samples at ambient temperature for at least two weeks before testing. The modulus of the gels in the sample cells was characterized using microrheological techniques (see ESI,† Fig. S4).<sup>47</sup>

A home-built LSCM setup was used to observe the chain structure in the gel.<sup>43,44</sup> We were able to analyze a sample of thickness of about  $150 \mu\text{m}$ . A homogeneous magnetic field was attained by building Halbach magnetic arrays near the sample stage of the LSCM.<sup>48</sup> A 32-magnet array (Fig. 1a) was used to change the field direction while keeping the field strength constant ( $216.4 \pm 1.1 \text{ mT}$ , see ESI,† Fig. S5). Another 4-magnet Halbach array (see ESI,† Fig. S6) was used to change the field strength (up to  $100.8 \pm 0.5 \text{ mT}$ ). The magnetic field was measured by a Lake Shore Model 425 Gaussmeter with a transverse probe.

To study the deformation of the PDMS gel around the magnetic chain, the magnetic field strength was increased from 0 mT to  $60.2 \pm 0.3 \text{ mT}$  in 8 steps ( $\sim 30 \text{ min}$  per step). 3D images of the sample with randomly distributed tracer particles were recorded in every step. One isolated magnetic chain was chosen for further analysis. Thus, from the 3D images we extracted a



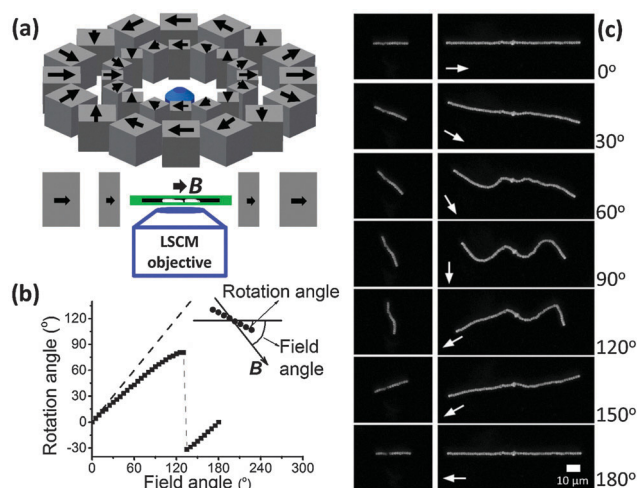


Fig. 1 (a) Laser scanning confocal microscopy (LSCM) was used to observe the morphologies of the paramagnetic chains in the soft gels. The Halbach magnetic array provided a homogeneous magnetic field (here  $B = 216.4 \pm 1.1$  mT). This array could be rotated to change the orientation of the magnetic field. (b) The orientation of the magnetic field  $B$  was successively increased from  $0^\circ$  to  $180^\circ$  in 36 steps (square points). A magnetic chain of 15 particles rotated to follow the magnetic field, but the rotation angle was smaller than the orientation angle of  $B$  (dashed line). (c) Morphologies of magnetic chains in a soft gel changed when the orientation angle of  $B$  increased. The scale bar is  $10 \mu\text{m}$ . The gel in (b) and (c) had an elastic modulus  $G'$  of  $0.25 \pm 0.06$  Pa.

time series of 2D images that focused on this magnetic chain. From these 2D images, the trajectories of the embedded tracer particles were determined using the particle tracker plug-in developed on ImageJ software.<sup>49</sup> The corresponding displacements of the tracers were deduced from the trajectories. Naturally, the tracer particles were stochastically distributed over the sample. We divided the images into a grid of small rectangles ( $7.0 \times 5.5 \mu\text{m}^2$ , containing, on average  $\sim 3.5$  tracer particles) and determined the average displacement in each cell.

### 3 Results

In the absence of a magnetic field, the paramagnetic chains in a soft gel kept the aligned morphologies (ESI,† Section S1, Movie S1). When a magnetic field ( $216.4 \pm 1.1$  mT) was applied in the direction parallel to the chains (Fig. 1c, images for  $0^\circ$ ), the paramagnetic chains still aligned with the original chain direction (horizontal). We changed the direction of the magnetic field step-by-step ( $5^\circ$  steps) in the clockwise direction ( $\sim 1$  min between steps, quasi-static). We also define the orientation of the magnetic field  $B$  as the angle included between the magnetic field and the initial chain direction (see Fig. 1b). The left images of Fig. 1c show a short chain with 15 particles in a gel of elastic modulus  $G'$  of  $0.25 \pm 0.06$  Pa. The chain rotated to follow the magnetic field. However, the rotation angle of the chain was smaller than the orientation angle of the magnetic field (Fig. 1b). This difference increased until the orientation of  $B$  reached  $135^\circ$ , where the chain flipped backward and had a negative angle. The chain again became parallel to the field when the orientation of

$B$  increased to  $180^\circ$ . The morphology of the chain was the same at orientations of the magnetic field of  $0^\circ$  and  $180^\circ$  because of the superparamagnetic nature of the particles. Note that the chain was not straight at the intermediate angles (e.g., images for  $60^\circ$ ,  $90^\circ$  and  $120^\circ$ ). Instead it bended.

The images on the right-hand side of Fig. 1c show a longer chain with 59 particles in the same gel. When the orientation of  $B$  was  $30^\circ$ , the chain rotated and bended, with its two ends tending to point in the direction of the magnetic field. When the orientation of  $B$  was  $60^\circ$ , the chain wrinkled and started to buckle. A sinusoidal-shape buckling morphology was observed when the magnetic field was perpendicular to the original chain (orientation of the magnetic field of  $90^\circ$ , see ESI,† Section S1, Movie S2). When the orientation of  $B$  increased from  $90^\circ$  to  $120^\circ$ , the left part of the chain flipped downward in order to follow the magnetic field. The right part flipped upward when the orientation of  $B$  increased from  $120^\circ$  to  $150^\circ$ . Finally, when the field direction was again parallel to the original chain direction (orientation of the magnetic field of  $180^\circ$ ), the chain became straight. The same rotation/buckling morphologies as in Fig. 1c could be observed when increasing the orientation of  $B$  from  $180^\circ$  to  $360^\circ$ .

We also directly applied a perpendicular magnetic field to the paramagnetic chains in the soft gels. The paramagnetic chains showed different buckling morphologies (Fig. 2a) depending on the chain length. Fig. 2b gives frequency counts of the different morphologies in the same sample ( $G' = 0.25 \pm 0.06$  Pa) under a magnetic field of  $100.8 \pm 0.5$  mT. In total 180 chains were observed. Longer chains tended to buckle with a higher number of half waves. Moreover, the distributions overlapped, implying that paramagnetic chains of identical length could have different morphologies under the perpendicular magnetic field.

These buckling morphologies are reminiscent of the buckling of paramagnetic chains in a liquid medium under a perpendicular magnetic field.<sup>50,51</sup> The most stable morphology in the latter system

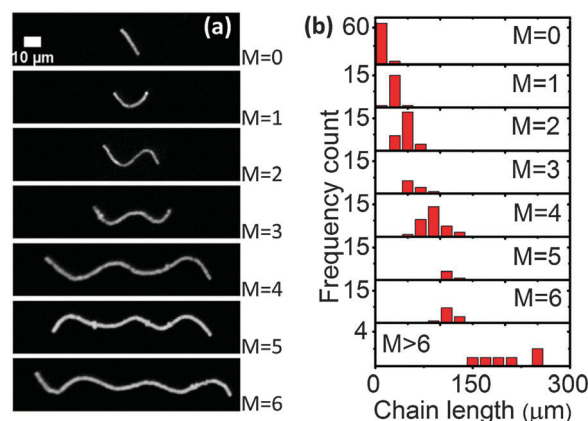
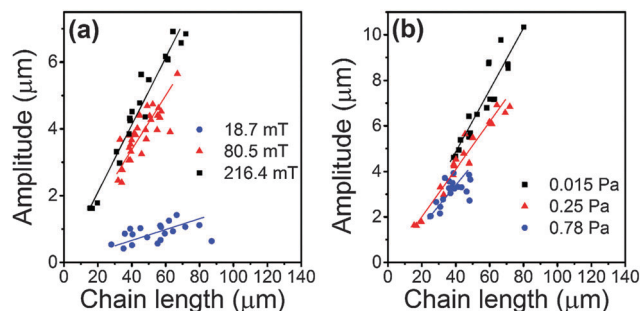


Fig. 2 (a) Different morphologies of paramagnetic chains in a soft gel ( $G' = 0.25 \pm 0.06$  Pa) under a perpendicular magnetic field ( $100.8 \pm 0.5$  mT). The original chain direction was horizontal, and the applied magnetic field was vertical. The scale bar is  $10 \mu\text{m}$ . (b) Frequency count of different buckling morphologies in the same sample.  $M$  is the number of half waves.





**Fig. 3** Influence of chain length, strength of magnetic field and elastic modulus of the gel matrix on the amplitude of the S-shaped chains, observed when the magnetic field is applied perpendicularly to the initial chain orientation. (a) The elastic modulus of the gel was  $0.25 \pm 0.06$  Pa, and the magnetic field strengths were  $216.4 \pm 1.1$  mT (black squares),  $80.5 \pm 0.4$  mT (red triangles), and  $18.7 \pm 0.1$  mT (blue circles), respectively. (b) The magnetic field strength was  $216.4 \pm 1.1$  mT and the elastic modulus of the gel were  $0.015 \pm 0.005$  Pa (black squares),  $0.25 \pm 0.06$  Pa (red triangles), and  $0.78 \pm 0.22$  Pa (blue circles), respectively. The solid lines are guides to the eye.

was a straight chain aligning along the magnetic field direction. However, in our system this morphology was not observed. Even the short chains showed a rotation angle smaller than the orientation of the magnetic field (e.g., Fig. 1b). The major difference between our experiments and ref. 50 and 51 was the nature of the surrounding medium. In our system, the polymer network around the paramagnetic chains impeded the rotation of the chains into the magnetic field direction (a more detailed discussion will be given below).

We used ImageJ software (NIH<sup>52</sup>) to extract the skeletons of the chains that have 2 half waves (S-shaped). The amplitude of deflection or deformation of different chains was quantified by the square root of the mean square displacement, *i.e.* amplitude =  $(\langle y^2 \rangle - \langle y \rangle^2)^{1/2}$ , where  $y$  measures the particle displacement along the field direction. The results are shown in Fig. 3. The amplitude increased with increasing chain length. At the same chain length, the amplitude tends to increase with increasing magnetic field strength (Fig. 3a; an example is also given in Fig. 4a) or with decreasing gel modulus (Fig. 3b).

The modulus dependence of the amplitude demonstrated that the polymer network around the paramagnetic chains impeded the chain deformations. Therefore, the deformation field within the polymer network plays an important role to understand the buckling of the chains. We thus added tracer particles into the gel matrix, and used their trajectories to record the deformation field around the paramagnetic chains. As shown in Fig. 4a, a linear paramagnetic chain buckled and formed an S shape in a perpendicular magnetic field. The amplitude increased with increasing field strength, while the contour length of the chain remained constant. The chain extension decreased along the original chain direction (horizontal direction) and increased along the perpendicular direction. Simultaneously, the polymer network around the chain followed the deformation (Fig. 4b) of the paramagnetic chain, both in the transverse and longitudinal directions. This confirmed that the paramagnetic chain is strongly coupled to the polymer network. Within our experimental

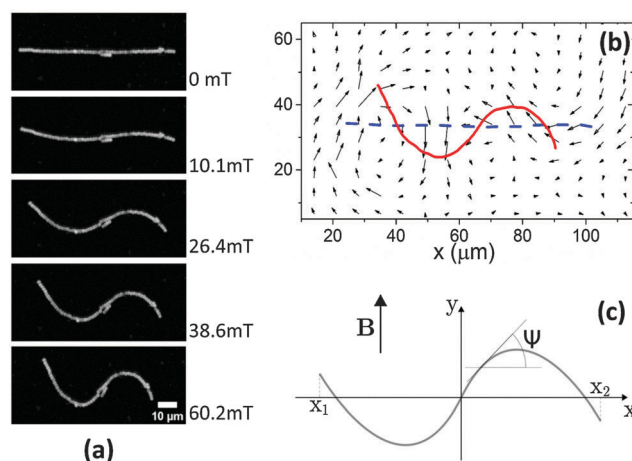


**Fig. 4** (a) Influence of the magnetic field strength on a buckling chain. From top to bottom, the magnetic field strengths were 0 mT,  $10.1 \pm 0.1$  mT,  $26.4 \pm 0.1$  mT,  $38.6 \pm 0.2$  mT and  $60.2 \pm 0.3$  mT, respectively. The modulus of this gel was about 0.01 Pa. (b) Tracer particles were inserted into the gel matrix of the sample. Tracking these embedded tracer particles, the deformation field in the gel matrix was determined. The red solid line represents the skeleton of the magnetic chain shown in (a) for a field strength of  $60.2 \pm 0.3$  mT, and the dashed blue line indicates the original chain shape. (c) We modeled the paramagnetic chain in the elastic gel as a continuous object uniformly carrying dipolar magnetic moments. Without the magnetic field, the straight chain was oriented along the  $x$ -axis. Under a perpendicular magnetic field  $\mathbf{B}$  (oriented along the  $y$ -axis), the magnetic chain deformed. The surrounding polymer network impeded the chain deformation.

resolution, the chain seemed to have a rigid non-slip contact to the surrounding network.

## 4 Modeling

We now turn to a qualitative description of the situation in the framework of a reduced minimal model. Theoretically capturing in its full breadth the problem of displacing rigid magnetic inclusions in an elastic matrix is a task of high complexity and enormous computational effort.<sup>53</sup> We do not pursue this route in the following. Instead, we reduce our characterization to a phenomenological description in terms of the shape of the magnetic chain only. This is possible if the dominant modes of deformation of the surrounding matrix are reflected by the deformational modes of the magnetic chain.

Below, we assume that the chain is composed of identical spherical particles. In its undeformed state, the straight chain is located on the  $x$ -axis of our coordinate frame. The contour line of the deformed chain running through the particle centers is parameterized as  $y(x)$ , see Fig. 4c.

### 4.1 Magnetic energy

First, concerning the magnetic energy along the chain, we assume dipolar magnetic interactions between the particles. In the perpendicular geometry (Fig. 4c), the external magnetic field approximately aligns all dipoles along the  $y$ -axis. For simplicity, we only include nearest-neighbor magnetic interactions. In an



infinite straight chain, this would result in an error given by a factor of  $\zeta(3) \approx 1.2$ , where  $\zeta$  is the Riemann zeta function.<sup>33,54,55</sup> Within our qualitative approach this represents a tolerable error. Replacing the magnetic interaction energy between the discrete magnetic particles by a continuous line integral and shifting the path of integration from the contour line of the chain to the  $x$ -axis, we obtain the magnetic interaction energy (see ESI,<sup>†</sup> Section S3.1)

$$E_{\text{magn}} = W \int_{x_1}^{x_2} \frac{1}{\sqrt{1 + y'(x)^2}} dx, \quad (1)$$

where  $x_1$  and  $x_2$  label the end points of the chain. The prefactor  $W$  has the dimension of energy per unit length and is given by (see ESI,<sup>†</sup> Section S3.1)

$$W \approx \frac{3\mu_0 m^2}{4\pi d^4}, \quad (2)$$

where  $\mu_0$  is the vacuum magnetic permeability,  $m$  the magnetic moment of a single particle, and  $d$  its diameter.

#### 4.2 Elastic bending energy

Next, we need to include terms that provide a measure for the magnitude of the elastic deformation energy. To estimate the importance of different modes of the elastic matrix deformation, we analyze the experimentally determined displacement field around the distorted chain shown in Fig. 4b. For this purpose, we model the continuous matrix by a discretized spring network.<sup>19,56</sup> Network nodes are set at the positions where the displacement field was tracked experimentally. The nodes are then connected by elastic springs. After that, we determine the normal modes of deformation of this network.<sup>56</sup> Finally, we can decompose the experimentally observed deformation field in Fig. 4b into these normal modes. Occupation numbers  $\phi_n$  give the contribution of the  $n$ th mode to the overall deformation.

The four most occupied modes are shown in Fig. 5. We find a major contribution of “oscillatory” modes, *i.e.* alternating up and down displacements along the central horizontal axis. Such oscillatory displacements of the matrix are connected to corresponding oscillatory displacements of the chain, see Fig. 4b. A bending term of the form (see ESI,<sup>†</sup> Section S3.2)

$$E_{\text{bend}} = C_b \int_{x_1}^{x_2} \frac{[y''(x)]^2}{[1 + y'(x)^2]^{5/2}} dx \quad (3)$$

becomes nonzero when such deformational modes occur and is therefore taken as a measure for their energetic contribution. In addition to that, we have experimental evidence that the chain itself shows a certain amount of bending rigidity (see ESI,<sup>†</sup> Fig. S7), possibly due to the adsorption of polymer chains on the surfaces of the magnetic particles. Similar indication follows from two-dimensional model simulations, see below.

#### 4.3 Elastic displacement energy

The bending term does not energetically penalize rotations of a straight chain, see Fig. 2a for  $M = 0$ . Yet, such rotations cost energy. Boundaries of the block of material are fixed, therefore any displacement of an inclusion induces a distortion of the

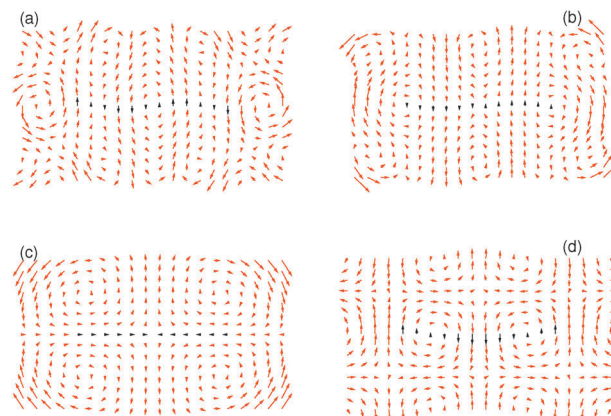


Fig. 5 The four most occupied normal modes of the deformation field in Fig. 4b after projection to an elastic spring network, ordered by decreasing magnitude of contribution to the overall deformation. The normal modes (a), (b) and (d) are of an “oscillatory” type, whereas mode (c) represents a longitudinal contraction. Corresponding relative weights of the modes are  $\phi_{(a)}^2 = 0.095$ ,  $\phi_{(b)}^2 = 0.057$ ,  $\phi_{(c)}^2 = 0.055$ , and  $\phi_{(d)}^2 = 0.051$ , where we normalized the sum of the weights over all modes to unity. For better visualization, the overall amplitudes are rescaled as against the actual weights. The matrix region in close vicinity of the chain is indicated by black arrows.

surrounding gel matrix. We model this effect by a contribution (see ESI,<sup>†</sup> Section S3.3)

$$E_{\text{displ}} = C_d \int_{x_1}^{x_2} [y(x)]^2 [1 + y'(x)^2]^{3/2} dx. \quad (4)$$

This term increasingly disfavors the rotations of longer straight chains, which reflects the experimental observations (see ESI,<sup>†</sup> Fig. S9).

Moreover, in Fig. 5c the third dominating mode of the matrix deformation corresponds to a contraction along the chain direction and an expansion perpendicular to it. We conjecture that this should be the dominating mode in the deformational far-field, yet this hypothesis needs further investigation. It is induced by chain deflections in  $y$ -direction, which imply a matrix contraction in  $x$ -direction (experimentally we observe that the chain length is conserved under deformations and that the individual magnetic particles remain in close contact). We simultaneously use  $E_{\text{displ}}$  to represent the energetic contribution of this type of underlying matrix deformation.

#### 4.4 Energetic evaluation

We now consider the resulting phenomenological model energy  $E_{\text{tot}} = E_{\text{magn}} + E_{\text{bend}} + E_{\text{displ}}$ . A standard procedure would consist of minimizing  $E_{\text{tot}}$  with respect to the functional form of  $y(x)$ . Corresponding calculations and results are listed in the ESI,<sup>†</sup> Section S3.4. There are, however, severe limitations to this route in the present case. In contrast to several previous approaches in different contexts,<sup>57–61</sup> our magnetic chains are of finite length and show significant displacements at their end points, see Fig. 2. Detailed knowledge of the boundary conditions of the deflection  $y(x)$  and its derivatives at the end points of the chain would be necessary to determine the chain shape.



Indeed the solutions become very sensitive to additional conditions (see ESI,† Section S3.4). In our case, the necessary additional boundary conditions depend on the interaction with the matrix. They are not accessible in the present reduced framework.

Therefore, we proceed in a different way. We use as an input for our calculations the experimental observations. The experimentally found chain shapes can to good approximation be represented by a polynomial form

$$y(x) = S \prod_{m=0}^{M-1} (x - mb) \quad \text{for } x_1 \leq x \leq x_2, \quad (5)$$

where  $M$  is again the number of half-waves, the prefactor  $S$  sets the strength or amount of chain deformation and deflection,  $b$  is the spacing between the nodes, and the interval  $[x_1, x_2]$  follows from the experimental result of preserved chain length  $L$ ,

$$\int_{x_1}^{x_2} \sqrt{1 + [y'(x)]^2} dx = L. \quad (6)$$

We prefer the polynomial form of eqn (5) to, for instance, a sinusoidal ansatz because it better reproduces the deformations of our finite-sized chain objects. In particular, the pronounced displacements of the chain ends, see *e.g.* Fig. 2a, are well captured by polynomial forms. Likewise, an experimentally observed tendency to smaller oscillation amplitudes inside longer chains is covered. Furthermore, rotations of short straight chains are readily included in this way.

Next, we insert eqn (5) into the above expressions for the energy and minimize with respect to  $S$ ,  $x_1$ , and  $x_2$  for a given  $M$ , with the constraint of constant length  $L$ , see eqn (6). The minimization was performed using Wolfram Mathematica minimization routines.<sup>62</sup> Parameter values of the coefficients  $C_b$  and  $C_d$  are found by matching the resulting shapes to the corresponding experimental profiles (chain deformations for  $G' = 0.25$  Pa and magnetic field  $B = 100.8$  mT as in Fig. 2a,  $M = 2$ , are used for this purpose). We obtain  $C_b \approx 0.01Wb^2$  and  $C_d \approx 2W/b^2$ .

To illustrate how the energetic contributions vary under increasing preset deformation, we plot in Fig. 6 the energies for increasing  $S$  for two fixed combinations of  $M$  and  $L$ . The total energy  $E_{\text{tot}}$  shows a global minimum in both panels, which we always observed for symmetric chain deformations. As expected, with increasing  $S$  the magnetic energy decreases, whereas the deformation energies increase.

Next, we determine the minimal total energy as a function of chain length  $L$  for different numbers of half-oscillations  $M$ , see Fig. 7. With increasing chain length  $L$  the shapes that minimize the energy show an increasing number of half-waves  $M$  in good agreement with the experimental data in Fig. 2b.

Moreover, we quantify the amplitude of the chain deflection or deformation by

$$\text{Amplitude} = \sqrt{\langle y^2 \rangle - \langle y \rangle^2}, \quad \langle \cdot \rangle = \frac{\int_{x_1}^{x_2} \cdot dx}{x_2 - x_1}. \quad (7)$$

Resulting values are plotted in Fig. 8. As mentioned above, we optimized the model parameters with respect to the experimental

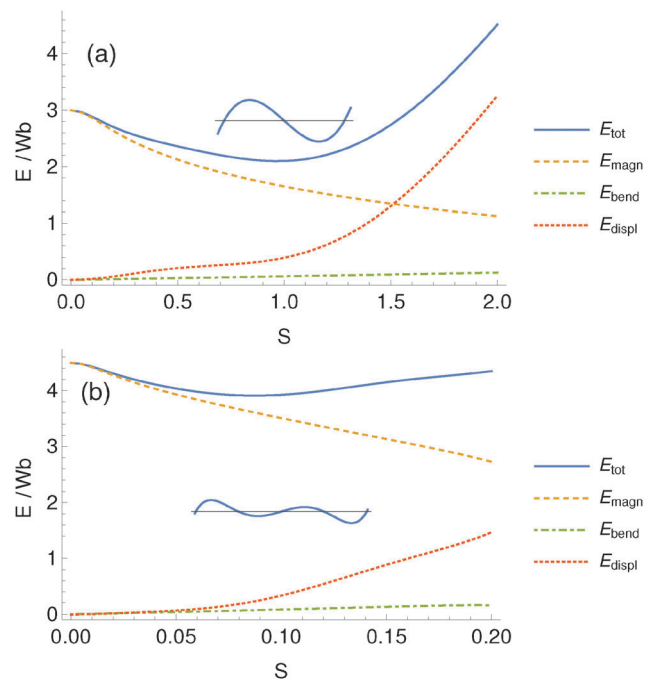


Fig. 6 Contributions to the total energy as a function of the amount  $S$  of deformation and minimized with respect to  $x_1$  and  $x_2$  for a chain of the shape given by eqn (5). Here we show the cases (a)  $M = 2$ ,  $L = 3b$  and (b)  $M = 4$ ,  $L = 4.5b$ . The total energy  $E_{\text{tot}}$  has a global minimum as a function of  $S$ , which corresponds to the most stable chain shape. We always observed the global minimum for symmetric shapes.

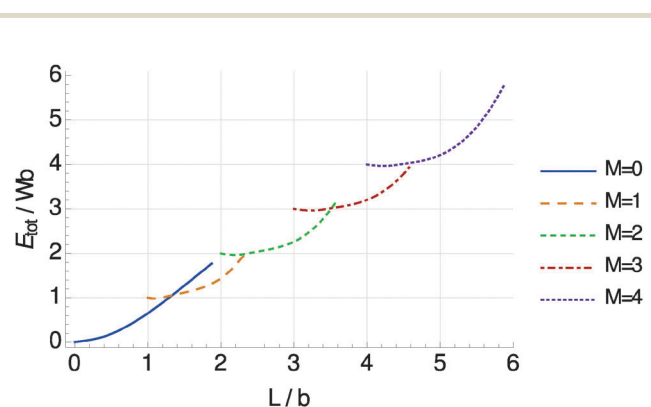


Fig. 7 Energies  $E_{\text{tot}}$  of chain deformations of the shape given by eqn (5), minimized with respect to  $S$ ,  $x_1$ , and  $x_2$ , as a function of chain length  $L$  and number of half-oscillations  $M$ . Each curve describes a shape of  $M$  half-waves with a minimum total length of  $(M - 1)b$ . The resulting curves show crossing points from where the total energy for an increasing  $L$  is lowered by bending one extra time (jumping to a higher  $M$ ) rather than conserving the same shape.

data for a magnetic field intensity of  $B = 100.8$  mT. We demonstrate in Fig. 8 that moderate variations of the magnetic field intensity only slightly affect our results: the brighter curves are obtained when multiplying the magnetic energy scale  $W$  by a factor  $\sim 1.42$ , corresponding to an increased magnetic field intensity of approximately  $B \sim 216$  mT (see ESI,† Fig. S1b). This is in agreement with the experimental observations. We include in Fig. 8 the experimentally determined values for  $B = 80.5$  mT and  $B = 216.4$  mT. Only a slight trend of increasing deflection amplitudes is found for this increase of magnetic field intensity.



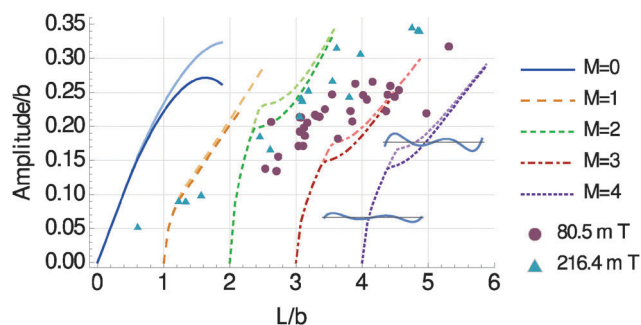


Fig. 8 Resulting deflection amplitudes of the chain deformation, calculated according to eqn (7). Darker curves represent the model parameters optimized with respect to the experimental shapes for a magnetic field intensity  $B = 100.8$  mT. Brighter curves were obtained by increasing the magnetic energy scale  $W$  by a factor  $\sim 1.42$ , which corresponds to an increased magnetic field intensity of  $B \sim 216$  mT (see ESI,† Fig. S1b), comparable with the triangular experimental data points. Both, model curves and included experimental data points, demonstrate that moderate variations of the magnetic field intensities only slightly affect the observed deflection and deformation amplitudes. The value of  $b$  necessary to perform the analysis was determined from the  $M = 2$  experimental data as  $b = 12.6$   $\mu\text{m}$ . For  $M \geq 2$  “kinks” appear in the curves, which arise from a change in the type of solution as illustrated by the insets: for each  $M \geq 2$  curve, left of the kink the chain deformation shows nodes at the end points of the chain, *i.e.*  $y(x_1) \approx y(x_2) \approx 0$  (lower left inset); right from the kink, these outer nodes are shifted to the inside of the chain (upper right inset). As seen from Fig. 7, the solutions left of the kinks are not energetically preferred.

Together, although the curves for  $M = 2$  in Fig. 8 slightly overshoot the data points, Fig. 7 and 8 are in good agreement with the experimental results. The amplitude of deflection and deformation is not observed to unboundedly increase with chain length  $L$  in the experiments. Likewise, our model predicts that longer chains prefer to bend one extra time (switching to higher- $M$  shape) rather than to show too large deflection amplitudes.

## 5 Coarse-grained molecular dynamics simulation

We also studied the buckling of the chain using two-dimensional coarse-grained molecular dynamics simulations by means of the ESPResSo software.<sup>63,64</sup> A simple model was developed that allowed us to analyze the influence of particular interactions and material properties on the buckling effect. Here, we focus on the elasticity of the polymer matrix in the immediate vicinity of the magnetic particles.

By choosing the coarse-grained scale for our model, we ignore any chemical details but rather describe the system in terms of the magnetic particles as well as small pieces of polymer gel. As the buckling effect appears to be two-dimensional, and as the ground states for systems of dipolar particles have also been found to be two-dimensional,<sup>55</sup> we use this dimensionality for our simulations. We study a chain of 100 magnetic particles with a significant amount of surrounding elastic matrix.

As in the analytical approach, the gel matrix is modeled by a network of springs. Here, however, we use a regular hexagonal mesh as a basis. To mimic the non-linear elastic behavior of

polymers, we use a finitely extensible non-linear elastic spring potential (FENE-potential<sup>65</sup>) for the springs along the edges of the mesh. As a simple implementation of the finite compressibility, we introduce FENE-like angular potentials on the angles at the mesh points, with a divergence at  $0^\circ$  and  $180^\circ$  (see ESI,† Section S4.2). The magnetic particles are modeled as rigid spheres interacting by a truncated, purely repulsive Lennard-Jones potential, the so-called Weeks-Chandler-Andersen potential (see ESI,† Section S4.1).<sup>66</sup> Their magnetic moment is assumed to be determined purely by the external magnetic field and to be constant throughout the simulation, *i.e.* we assume that the external field is significantly stronger than the field created by the particles. The magnetic moments are taken parallel to the external field and with a magnitude given by the experimentally observed magnetization curve. The coupling between the particles and the mesh is introduced in such a way, that under the volume occupied by a particle, the mesh does not deform, but rigidly follows the translational and rotational motion of the particle (see ESI,† Section S4.3). A local shear strain on the matrix can rotate a magnetic particle, but not its magnetic moment.

An important point is the elasticity of the polymer matrix in the immediate vicinity of the magnetic particles and, in particular, between two magnetic particles. We study two situations here, the first one including a stiffer region in the immediate vicinity of the particles, the second one without such a stiffer layer and directly jumping to the bulk elasticity. The stiffer layer, if imposed, is created using a spring constant larger by three orders of magnitude on those springs which originate from mesh sites within the particle volumes (see ESI,† Section S4.3). The angular potentials are unchanged.

A comparison between the cases with and without a stiffer layer of gel around the magnetic particles can be seen in Fig. 9. The images show a small part of the resulting configuration of magnetic particles and the surrounding mesh for a field applied perpendicular to the initial chain direction. Thus the magnetic moments of the particles are oriented perpendicular to the undistorted chain direction. This results in an energetically unfavorable parallel side-by-side configuration for the dipole moments. The energy can be reduced either by increasing the distance between the dipoles along the initial chain direction, or by moving dipoles perpendicularly to the initial chain direction so that they approach the energetically most favorable head-to-tail configuration. If the matrix is made stiffer immediately around the particles, and thus the contour length of the chain cannot change significantly, the re-positioning towards the head-to-tail configuration causes the buckling effect observed in the experiments (Fig. 9). When one assumes the matrix immediately around the magnetic particles to be as soft as in the bulk of the material, neighboring particles can move apart and the chain breaks up into individual particles or small columns perpendicular to the original chain direction. Additionally, a layer of increased stiffness also introduces a bending rigidity of the chain. In Fig. 10, the full chain and the surrounding matrix is shown for an external field of magnitude 216 mT, which from the experimental magnetization measurements corresponds to a magnetic moment of about  $4.5 \times 10^{-14}$  A m<sup>2</sup> (see ESI,† Fig. S1b). Due to the different



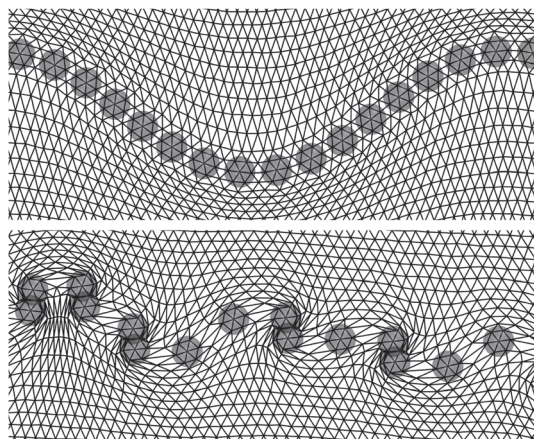


**Fig. 9** Detailed view of the local deformations in the polymer mesh around the magnetic particles with a layer of increased stiffness (top) and without one (bottom) in the immediate vicinity of the particle surfaces. The external magnetic field of strength 216 mT is applied in the vertical direction. When the boundary layer is assumed to be stiffer than the bulk (top), the buckling effect, as observed in the experiments, occurs. When the layer around the particles is soft (bottom), neighboring particles either form tight columns parallel to the field, or separate in the direction perpendicular to the field.

dimensionalities, the elastic modulus of the surrounding matrix could not be directly matched to the experimental system.

Actually, the amplitude of the chain oscillation increases when the external field is higher and induces larger dipole moments in the particles. This increases the tendency of the magnetic moments to approach the head-to-tail configuration, which in turn leads to a stronger deformation of the matrix. We note that the relative amplitude of the buckling along the chain is similar in the simulations (Fig. 9) and experiments (Fig. 2). The matrix surrounding the chain follows the chain oscillation with an amplitude that decreases over distance from the chain. Deviations may be expected from the deformational far-field in the experimental system due to the different dimensionalities of the systems.

In the ESI† (Fig. S7) we show an experimental evidence for the existence of a stiff polymer layer around the magnetic particles. The sample was prepared at a concentration of prepolymer mixture well below the percolation threshold, *i.e.*, some cross-linking of the polymer took place in the sample but no macroscopic gel was formed. When this cross-linking was done under an applied magnetic field, the particle chains stayed intact even after removal of the magnetic field (Fig. S7a, ESI†). Hairpin or “S”-shape morphologies were observed when these chains were exposed to a magnetic field (Fig. S7b, ESI†), indicating that they have a bending rigidity.<sup>50,51</sup> Our interpretation of this behavior is that a stiff gel layer connects the particles and stabilizes the particle chains, even though no bulk gel is formed. As the magnetic particles have a good affinity for PDMS (*e.g.*, the magnetic particles can be easily dispersed into PDMS), we conjecture that there is an adsorbed layer of polymer (*i.e.*, PDMS prepolymer or cross-linker) on the surface of the magnetic particles.<sup>57</sup> Therefore, the gel layer on the particles is denser and thus stiffer than in the bulk. Further study of the

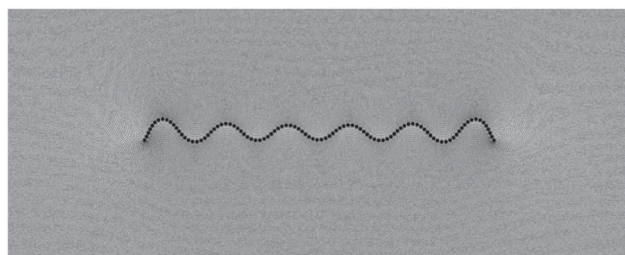


**Fig. 10** Buckling chain of magnetic particles and the surrounding polymer mesh for an external field of magnitude 216 mT pointing along the vertical direction. In this image, roughly one quarter of the full simulation area is shown. The surrounding matrix follows the chain oscillation with an amplitude that decreases over distance from the chain.

stiff polymer layer and its effect on the buckling behavior is under way.

Moreover, in Fig. S8 (ESI†) we show that the buckling behavior of the magnetic chains can still be observed in the gel when we increase the elastic modulus to 170 Pa (for this purpose, carbonyl iron particles are used as magnetic filler particles). Our studies on that stiffer sample provide further evidence that the interaction between the magnetic particles and the polymer matrix in their close vicinity can play an important role in the magneto-elastic response of soft MRGs.

## 6 Conclusions

We have shown that paramagnetic chains in a soft polymer gel can buckle in a perpendicular magnetic field. The buckling morphology depends on the length of the chain, the strength of the magnetic field and the modulus of the gel. Longer chains form buckling structures with a higher number of half waves. Higher strengths of the magnetic field and a lower modulus of the gel matrix can lead to higher deformation amplitudes. The deformation field in the surrounding gel matrix confirms that the embedding polymer network is strongly coupled to the paramagnetic chain. A minimal magneto-elastic coupling model is developed to describe the morphological behavior of the paramagnetic chains in the soft gel under a perpendicular magnetic field. It shows that the chains deform in order to decrease the magnetic energy. This is hindered by the simultaneous deformation of the gel matrix, which costs elastic energy. Additionally, we have introduced a coarse-grained molecular dynamics simulation model, which covers both, the magnetic particles and the surrounding polymer mesh. In this model, the buckling of the chains can only be observed when the surface layer around the particles is assumed to be stiffer than the bulk of the gel. This prevents the chains from breaking up into columns oriented perpendicular to the initial chain direction or into isolated particles. These findings support the picture that the embedded magnetic chains themselves feature a certain bending rigidity, possibly due to the existence of a stiff polymer layer on the particle surfaces.

Since the magneto-elastic effect demonstrated and analyzed in this paper is pronounced, reversible, and controllable, it may



be useful for designing micro-devices, e.g. micro-valves and pumps for microfluidic control.<sup>68</sup> As the morphologies of the buckling paramagnetic chains are correlated with the modulus of the gel matrix, we may use them as mechanical probes for soft gels (similarly to active microrheology techniques).<sup>45</sup> Moreover, our study may help to understand the physical interactions between the magnetic chains and the surrounding cytoskeleton network in magnetotactic bacteria.<sup>46</sup> In our future study we will focus on how the interfacial coupling between the magnetic particles and the polymer network influences the local magneto-elastic coupling effect.

## Acknowledgements

The authors acknowledge support by the Deutsche Forschungsgemeinschaft (DFG) through the SPP 1681 (SH and GKA acknowledge the project AU321/3-1; GP, PC and AMM acknowledge the project LO418/16-1; RW and CH acknowledge the project HO 1108/23-1; JN and SO acknowledge the project OD18/21). RW and CH acknowledge funding through the cluster of excellence EXC 310, SimTech at the University of Stuttgart. We thank Dr Peter Blümmler for inspiring discussions on designing the Halbach magnetic arrays.

## References

- 1 P. Ilg, *Soft Matter*, 2013, **9**, 3465–3468.
- 2 R. L. Snyder, V. Q. Nguyen and R. V. Ramanujan, *Smart Mater. Struct.*, 2010, **19**, 055017.
- 3 K. Zimmermann, V. A. Naletova, I. Zeidis, V. Böhm and E. Kolev, *J. Phys.: Condens. Matter*, 2006, **18**, S2973–S2983.
- 4 R. Hergt, S. Dutz, R. Müller and M. Zeisberger, *J. Phys.: Condens. Matter*, 2006, **18**, S2919–S2934.
- 5 D. Szabó, G. Szeghy and M. Zrínyi, *Macromolecules*, 1998, **31**, 6541–6548.
- 6 S. S. Abramchuk, D. A. Grishin, E. Y. Kramarenko, G. V. Stepanov and A. R. Khokhlov, *Polym. Sci., Ser. A*, 2006, **48**, 138–145.
- 7 G. Filipcsei, I. Csetneki, A. Szilágyi and M. Zrínyi, *Adv. Polym. Sci.*, 2007, **206**, 137–189.
- 8 D. Collin, G. K. Auernhammer, O. Gavot, P. Martinoty and H. R. Brand, *Macromol. Rapid Commun.*, 2003, **24**, 737–741.
- 9 J. Farauo, J. S. Andreu and J. Camacho, *Soft Matter*, 2013, **9**, 6654–6664.
- 10 D. J. Griffiths, *Introduction to Electrodynamics*, Prentice-Hall, Upper Saddle River, NJ, 3rd edn, 1999, p. 282.
- 11 S. H. L. Klapp and M. Schoen, *J. Chem. Phys.*, 2002, **117**, 8050–8062.
- 12 S. H. L. Klapp, *J. Phys.: Condens. Matter*, 2005, **17**, R525–R550.
- 13 G. P. Gajula, M. T. Neves-Petersen and S. B. Petersen, *Appl. Phys. Lett.*, 2010, **97**, 103103.
- 14 J. de Vicente, D. J. Klingenberg and R. Hidalgo-Alvarez, *Soft Matter*, 2011, **7**, 3701–3710.
- 15 G. K. Auernhammer, D. Collin and P. Martinoty, *J. Chem. Phys.*, 2006, **124**, 204907.
- 16 D. S. Wood and P. J. Camp, *Phys. Rev. E: Stat., Nonlinear, Soft Matter Phys.*, 2011, **83**, 011402.
- 17 D. Ivaneyko, V. Toshchevnikov, M. Saphiannikova and G. Heinrich, *Condens. Matter Phys.*, 2012, **15**, 33601.
- 18 Y. Han, W. Hong and L. E. Faidley, *Int. J. Solids Struct.*, 2013, **50**, 2281–2288.
- 19 G. Pessot, P. Cremer, D. Y. Borin, S. Odenbach, H. Löwen and A. M. Menzel, *J. Chem. Phys.*, 2014, **141**, 124904.
- 20 A. M. Menzel, *Phys. Rep.*, 2015, **554**, 1–46.
- 21 O. V. Stolbov, Y. L. Raikher and M. Balasoiu, *Soft Matter*, 2011, **7**, 8484–8487.
- 22 G. Filipcsei, I. Csetneki, A. Szilágyi and M. Zrínyi, *Magnetic Field-Responsive Smart Polymer Composites*, Springer, Berlin, Heidelberg, 2007, vol. 206, pp. 137–189.
- 23 D. Günther, D. Y. Borin, S. Günther and S. Odenbach, *Smart Mater. Struct.*, 2012, **21**, 015005.
- 24 T. Borbáth, S. Günther, D. Y. Borin, T. Gundermann and S. Odenbach, *Smart Mater. Struct.*, 2012, **21**, 105018.
- 25 X. C. Guan, X. F. Dong and J. P. Ou, *J. Magn. Magn. Mater.*, 2008, **320**, 158–163.
- 26 K. Danas, S. V. Kankanala and N. Triantafyllidis, *J. Mech. Phys. Solids*, 2012, **60**, 120–138.
- 27 A. Y. Zubarev, *Soft Matter*, 2013, **9**, 4985–4992.
- 28 E. Jarkova, H. Pleiner, H. W. Müller and H. R. Brand, *Phys. Rev. E: Stat., Nonlinear, Soft Matter Phys.*, 2003, **68**, 041706.
- 29 S. Bohlius, H. R. Brand and H. Pleiner, *Phys. Rev. E: Stat., Nonlinear, Soft Matter Phys.*, 2004, **70**, 061411.
- 30 R. Weeber, S. Kantorovich and C. Holm, *Soft Matter*, 2012, **8**, 9923–9932.
- 31 R. Weeber, S. Kantorovich and C. Holm, *J. Magn. Magn. Mater.*, 2015, **383**, 262.
- 32 A. V. Ryzhkov, P. V. Melenev, C. Holm and Y. L. Raikher, *J. Magn. Magn. Mater.*, 2015, **383**, 277.
- 33 A. M. Menzel, *J. Chem. Phys.*, 2014, **141**, 194907.
- 34 D. Ivaneyko, V. Toshchevnikov, M. Saphiannikova and G. Heinrich, *Soft Matter*, 2014, **10**, 2213–2225.
- 35 G. Pessot, R. Weeber, C. Holm, H. Löwen and A. M. Menzel, *J. Phys.: Condens. Matter*, 2015, **27**, 325105.
- 36 L. Roeder, M. Reckenthäler, L. Belkoura, S. Roitsch, R. Strey and A. M. Schmidt, *Macromolecules*, 2014, **47**, 7200–7207.
- 37 N. Frickel, R. Messing, T. Gelbrich and A. M. Schmidt, *Langmuir*, 2009, **26**, 2839–2846.
- 38 N. Frickel, R. Messing and A. M. Schmidt, *J. Mater. Chem.*, 2011, **21**, 8466–8474.
- 39 R. Messing, N. Frickel, L. Belkoura, R. Strey, H. Rahn, S. Odenbach and A. M. Schmidt, *Macromolecules*, 2011, **44**, 2990–2999.
- 40 I. Csetneki, G. Filipcsei and M. Zrínyi, *Macromolecules*, 2006, **39**, 1939–1942.
- 41 H. N. An, J. Groenewold, S. J. Picken and E. Mendes, *Soft Matter*, 2014, **10**, 997–1005.
- 42 M. Minsky, *Scanning*, 1988, **10**, 128–138.
- 43 M. Roth, M. Franzmann, M. D'Acunzi, M. Kreiter and G. K. Auernhammer, 2011, arXiv preprint, arXiv:1106.3623.
- 44 M. Roth, C. Schilde, P. Lellig, A. Kwade and G. K. Auernhammer, *Eur. Phys. J. E: Soft Matter Biol. Phys.*, 2012, **35**, 124.



- 45 C. Wilhelm, *Phys. Rev. Lett.*, 2008, **101**, 028101.
- 46 A. Körnig, J. Dong, M. Bennet, M. Widdrat, J. Andert, F. D. Müller, D. Schüler, S. Klumpp and D. Faivre, *Nano Lett.*, 2014, **14**, 4653–4659.
- 47 T. G. Mason, T. Gisler, K. Kroy, E. Frey and D. A. Weitz, *J. Rheol.*, 2000, **44**, 917–928.
- 48 H. Raich and P. Blümler, *Concepts Magn. Reson., Part B*, 2004, **23**, 16–25.
- 49 I. F. Sbalzarini and P. Koumoutsakos, *J. Struct. Biol.*, 2005, **151**, 182–195.
- 50 C. Goubault, P. Jop, M. Fermigier, J. Baudry, E. Bertrand and J. Bibette, *Phys. Rev. Lett.*, 2003, **91**, 260802.
- 51 V. P. Shcherbakov and M. Winklhofer, *Phys. Rev. E: Stat., Nonlinear, Soft Matter Phys.*, 2004, **70**, 061803.
- 52 <http://imagej.nih.gov/ij/>.
- 53 C. Spieler, M. Kästner, J. Goldmann, J. Brummund and V. Ulbricht, *Acta Mech.*, 2013, **224**, 2453–2469.
- 54 M. A. Annunziata, A. M. Menzel and H. Löwen, *J. Chem. Phys.*, 2013, **138**, 204906.
- 55 T. Prokopiya, V. Danilov, S. Kantorovich and C. Holm, *Phys. Rev. E: Stat., Nonlinear, Soft Matter Phys.*, 2009, **80**, 031404.
- 56 M. Tarama, P. Cremer, D. Y. Borin, S. Odenbach, H. Löwen and A. M. Menzel, *Phys. Rev. E: Stat., Nonlinear, Soft Matter Phys.*, 2014, **90**, 042311.
- 57 I. Gelfand and S. Fomin, *Calculus of variations*, Prentice-Hall Inc., Englewood Cliffs, NJ, 1963.
- 58 G. W. Hunt, M. Wade and N. Shiacolas, *J. Appl. Mech.*, 1993, **60**, 1033–1038.
- 59 B. Audoly, *Phys. Rev. E: Stat., Nonlinear, Soft Matter Phys.*, 2011, **84**, 011605.
- 60 H. Diamant and T. A. Witten, 2010, arXiv preprint arXiv:1009.2487.
- 61 H. Diamant and T. A. Witten, *Phys. Rev. Lett.*, 2011, **107**, 164302.
- 62 Wolfram Research, *Mathematica 10.0*, 2014.
- 63 H. J. Limbach, A. Arnold, B. A. Mann and C. Holm, *Comput. Phys. Commun.*, 2006, **174**, 704–727.
- 64 A. Arnold, O. Lenz, S. Kesselheim, R. Weeber, F. Fahrenberger, D. Röhm, P. Košovan and C. Holm, *Meshfree Methods for Partial Differential Equations VI*, 2013, pp. 1–23.
- 65 H. R. Warner, *Ind. Eng. Chem. Fundam.*, 1972, **11**, 379–387.
- 66 J. D. Weeks, D. Chandler and H. C. Andersen, *J. Chem. Phys.*, 1971, **54**, 5237.
- 67 L. Cohen-Tannoudji, E. Bertrand, L. Bressy, C. Goubault, J. Baudry, J. Klein, J.-F. Joanny and J. Bibette, *Phys. Rev. Lett.*, 2005, **94**, 038301.
- 68 E. K. Fleischmann, H. L. Liang, N. Kapernaum, F. Giesselmann, J. Lagerwall and R. Zentel, *Nat. Commun.*, 2012, **3**, 1178.



## Supplementary Information

### Buckling of paramagnetic chains in soft gels

Shilin Huang,<sup>a</sup> Giorgio Pessot,<sup>b</sup> Peet Cremer,<sup>b</sup> Rudolf Weeber,<sup>c</sup>  
Christian Holm,<sup>c</sup> Johannes Nowak,<sup>d</sup> Stefan Odenbach,<sup>d</sup>  
Andreas M. Menzel,<sup>b</sup> Günter K. Auernhammer<sup>a</sup>

<sup>a</sup> Max Planck Institute for Polymer Research, Ackermannweg 10, 55128 Mainz, Germany.

<sup>b</sup> Institut für Theoretische Physik II: Weiche Materie, Heinrich-Heine-Universität Düsseldorf, D-40225 Düsseldorf, Germany.

<sup>c</sup> Institute for Computational Physics, Universität Stuttgart, 70569 Stuttgart Germany.

<sup>d</sup> Chair of Magnetofluidynamics, Measuring and Automation Technology, Institute of Fluid Mechanics, Technische Universität Dresden, 01069 Dresden, Germany.

## 1 Supplementary movies

**Movie S1** Typical 3D morphology of paramagnetic chains in a soft gel in the absence of a magnetic field. The elastic modulus of the gel is  $0.78 \pm 0.22$  Pa and the scale bar is  $300 \mu\text{m}$ .

**Movie S2** Typical 3D morphology of paramagnetic chains in a soft gel under a perpendicular magnetic field ( $B = 216.4 \pm 1.1$  mT). The elastic modulus of the gel is  $0.78 \pm 0.22$  Pa and the scale bar is  $300 \mu\text{m}$ .

## 2 Supplementary information for experiments

### 2.1 Paramagnetic particles

According to the manufacturer (microParticles GmbH), the paramagnetic particles were fabricated based on porous polystyrene particles. Within the pores of the polystyrene particles, nanoparticulate iron oxide was distributed, rendering the particles superparamagnetic. To prevent iron oxide leaching, the paramagnetic particles were covered with thin polymer layers which also held the fluorophores. The diameter of the paramagnetic particles from the scanning electron microscopy (SEM) images (see Fig. S1a) is  $1.4 \pm 0.2 \mu\text{m}$ . We also measured the length of linear particle chains in polydimethylsiloxane using laser scanning confocal microscopy (LSCM). Dividing the length of the chains by the number of particles in the chains we got a diameter of  $1.48 \pm 0.13 \mu\text{m}$  (average for 20 chains). We used the latter value for calibration and calculation in this paper.

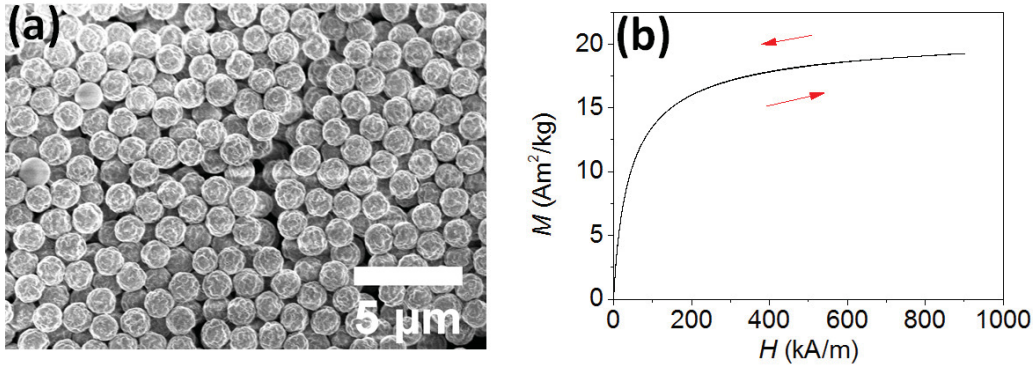


**Figure S1** (a) Scanning electron microscopy (SEM) image of the paramagnetic particles. The scale bar is  $5 \mu\text{m}$ . (b) Magnetization curve of the paramagnetic particles. The magnetic field  $H$  was increased from 0  $\text{kA/m}$  to 900  $\text{kA/m}$  and then decreased to 0  $\text{kA/m}$ , and the magnetization  $M$  showed no hysteresis, as indicated by the red arrows.

The magnetization curve of the paramagnetic particles was measured by a vibrating sample magnetometer (VSM, Lake Shore 7407). The magnetization of the particles showed no hysteresis when the external magnetic field was increased and decreased, demonstrating the superparamagnetic property (Fig. S1b).

### 2.2 Calibrating the magnetic properties of the paramagnetic particles

A spherical colloidal particle moving in a viscous fluid with a relative velocity  $\mathbf{v}$  is subject to a frictional force (Stokes' drag)

$$\mathbf{F}_d = -6\pi\eta R\mathbf{v}, \quad (\text{S1})$$

where  $R$  is the radius of the particle and  $\eta$  is the dynamic viscosity of the fluid.

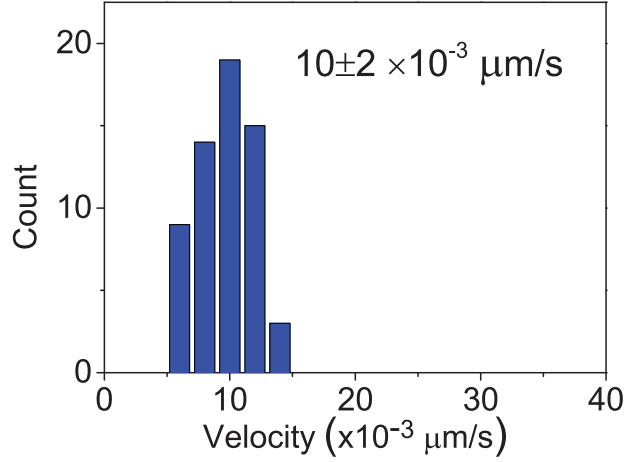


**Figure S2** Histogram of velocity of paramagnetic particles moving in a viscous liquid. The viscosity of the liquid is  $0.61 \pm 0.02$  Pas. The magnetic field strength is  $32.7 \pm 0.2$  mT and the magnetic gradient is  $3.63 \pm 0.02 \times 10^{-5}$  mT/ $\mu\text{m}$ . Using a density of  $1.7$  g/cm<sup>3</sup>, the movement of the particles, the magnetic gradient, and the magnetization curve can be correlated.<sup>S1,S2</sup>

Under a magnetic field  $\mathbf{B}$ , the magnetic particles move along the magnetic field gradient. The magnetic force  $\mathbf{F}_m$  acting on a paramagnetic particle is<sup>S1,S2</sup>

$$\mathbf{F}_m = \mathbf{m} \cdot \nabla \mathbf{B}, \quad (\text{S2})$$

where  $\mathbf{m}$  is the induced magnetic dipole moment of the paramagnetic particle. In the steady state, the magnetic force is balanced by Stokes' drag, thus

$$6\pi\eta R\mathbf{v} = \mathbf{m} \cdot \nabla \mathbf{B}. \quad (\text{S3})$$

From experiments, the left-hand side of Eq. (S3) and  $\nabla \mathbf{B}$  can be measured directly. We dispersed the paramagnetic particles into a viscous liquid with a viscosity of  $0.61 \pm 0.02$  Pas. The dispersion was added into a sample cell with a thickness of  $160$   $\mu\text{m}$ . Then the sample cell was carefully sealed in order to avoid drift due to large-scale flow of the liquid. We used a magnetic field of  $32.7 \pm 0.2$  mT with a gradient of  $3.63 \pm 0.02 \times 10^{-5}$  mT/ $\mu\text{m}$  to induce flow of the paramagnetic particles. The magnetic field was measured by a Lake Shore Model 425 Gaussmeter with a transverse probe. The movement of the particles (far from the walls of the sample cell) was recorded using LSCM. The magnitude of the magnetic moment  $m$  can be calculated via  $m = 4\pi R^3 \rho M/3$ , where  $M$  can be obtained from the magnetization curve (Fig. S1b) and  $\rho$  is the density of the paramagnetic particles. Using  $\rho = 1.7$  g/cm<sup>3</sup>, we find that Eq. (S3) is satisfied. This density value is in agreement with the one provided by the manufacturer ( $1.5\text{--}2$  g/cm<sup>3</sup>).

In our study the paramagnetic particles are not ideally monodispersed and the induced magnetic moment is not ideally identical for every particle. For example, the velocity of the paramagnetic particles moving in a viscous liquid under a magnetic gradient has a distribution with  $\sim 20\%$  deviation (Fig. S2). According to Eq. (S3), the magnetic moment of the particles should have a similar distribution. For simplification, we do not consider this distribution in the modeling and simulation.

### 2.3 Determining the elastic modulus of the soft gels

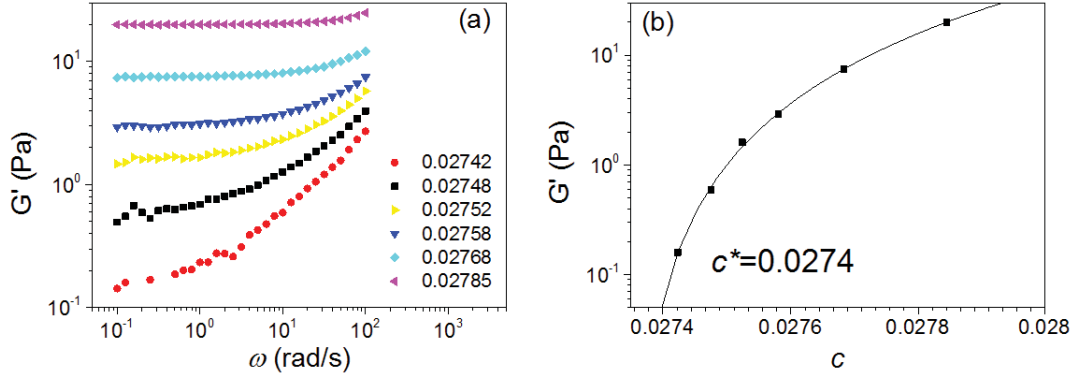


**Figure S3** (a) Shear elastic modulus ( $G'$ ) of the gels as a function of angular frequency. The gels were fabricated with different concentrations ( $c$ ) of the prepolymer mixture as indicated for the different sets of data points. (b) The low-frequency  $G'$  of the gels plotted as a function of  $c$ . The solid curve is the best fit of Eq. (S4) to the experimental data.

The rheological experiments were performed in a strain-controlled rheometer (ARES-LS, Rheometric Scientific Inc., Piscataway, NJ, USA) equipped with a Couette cell at room temperature. The elastic modulus ( $G'$ ) shows a plateau at low frequencies for the soft gels (Fig. S3a), reflecting the formation of a percolating network. The plateau modulus increases with increasing concentration of the prepolymer mixture ( $c$ ) following a power law<sup>S3</sup>

$$G' = G'_0(c - c^*)^t, \quad (\text{S4})$$

where  $G'_0$  is a prefactor,  $t$  is the critical exponent, and  $c^*$  is the percolation concentration. From this power law it is evident that the elastic modulus of the soft gels becomes very sensitive to the concentration of the prepolymer mixture when the concentration of the prepolymer mixture is close to  $c^*$ .

As a result, we cannot directly use the elastic modulus obtained from macroscopic rheological measurements to characterize our soft gels in the sample cells ( $\sim 160 \mu\text{m}$  thick), because a little change of the concentration of the prepolymer mixture during preparation of the gels can lead to a significant difference of the elastic modulus. In experiment, the concentration of the prepolymer mixture in the sample cells is difficult to control precisely, because the concentration can change slightly if some prepolymer molecules are adsorbed to the walls of the cell, to the pipette tips, or to the paramagnetic particles.

In order to solve this problem, we measured the elastic modulus of the soft gels directly in the sample cells (containing the paramagnetic chains) by passive microrheology (i.e., particle tracking). About 15 single particles were used as the mechanical probes, and a fast camera (Photron, FASTCAM SA1) and a microscope (Leica DMI6000B) were used to detect the thermal fluctuations of the particles.<sup>S4,S5</sup> Fig. S4a shows the mean-square displacement (MSD) of the particles in the gels as a function of lag time. At long lag times the MSD levels off, indicating that the particles are confined in a network. The moduli of the gels can be calculated from the MSD of the particles based on the generalized

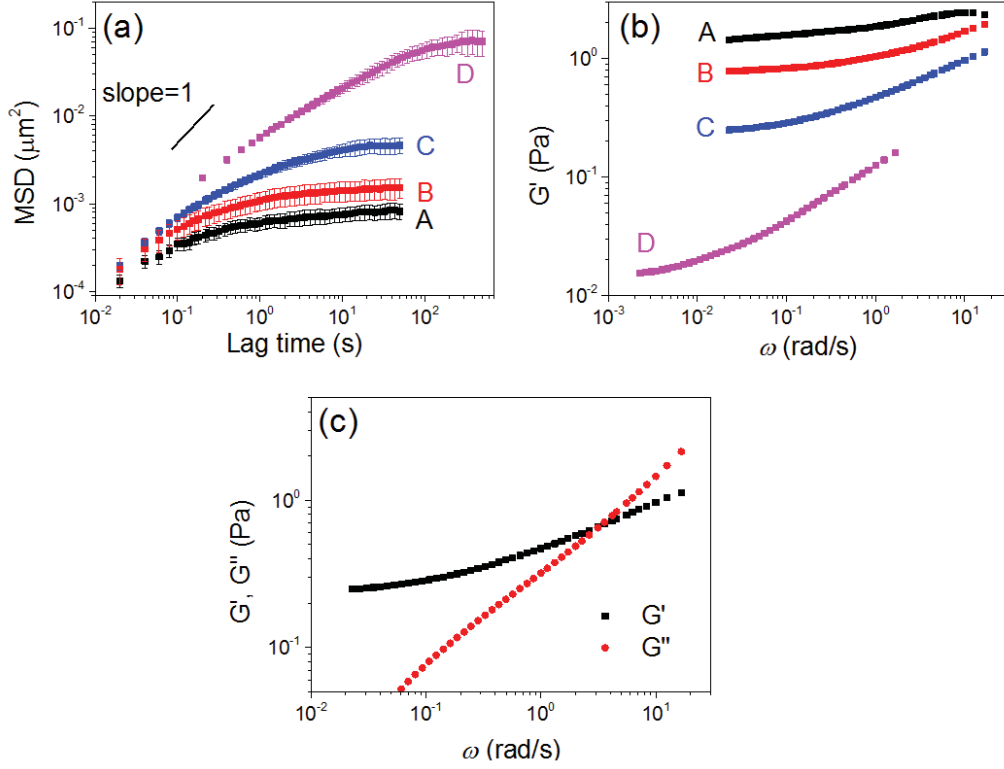


**Figure S4** Probing the viscoelastic properties of the gels in the sample cells (containing the paramagnetic chains). (a) Mean-square displacement (MSD) of the particles in the gels as a function of lag time. The concentrations of the prepolymer mixture for the four samples A–D are 2.78 wt%, 2.77 wt%, 2.76 wt%, and 2.76 wt%, respectively. The slight changes of concentration can lead to significant differences in the MSD, because the concentration used here is close to the percolation threshold ( $c^* = 2.74\%$ , see Fig. S3b).<sup>S3</sup> It is the method of passive microrheology that makes it possible to measure the viscoelastic properties of the soft gels (containing the paramagnetic chains) directly within the sample cells. (b) Elastic modulus ( $G'$ ) calculated from the MSD. (c) Elastic modulus ( $G'$ ) and loss modulus ( $G''$ ) plotted as functions of angular frequency ( $\omega$ ) for sample C. At low frequencies, the elastic character dominates.

Stokes-Einstein relation (GSER)<sup>S4,S6</sup>

$$G^*(\omega) = \frac{k_B T}{\pi R(i\omega) \mathcal{F}_u\{MSD(t)\}}, \quad (\text{S5})$$

where  $G^*(\omega)$  is the complex shear modulus and  $\mathcal{F}_u\{MSD(t)\}$  is the unilateral Fourier transform ( $\mathcal{F}\{f(t)\} = \int_0^\infty e^{-i\omega\tau} f(\tau) d\tau$ ). Using the algorithm from Crocker and Weeks,<sup>S4,S5</sup> we calculated the shear moduli (Fig. S4b). Fig. S4c shows that at low frequencies (corresponding to long time scales) the gel is mainly elastic. In the main article we use the elastic modulus of the gels obtained from passive microrheology to characterize the gels.

## 2.4 Magnetic field of the Halbach magnetic array

We used permanent magnets to provide a homogeneous magnetic field.<sup>S7</sup> The NdFeB permanent magnets were purchased from AR.ON GmbH. According to the manufacturer they have a remanence of 1.32 T. The magnets were arranged as shown in Fig. 1a. The magnets had dimensions of  $8 \times 8 \times 15 \text{ mm}^3$  and  $14 \times 14 \times 15 \text{ mm}^3$  for the inner and outer rings, respectively. The magnetic field at the center of this magnetic array was homogeneous (Fig. S5). This magnetic array was built around the objective of our home-built LSCM and it could be rotated by a motor. We put the samples in the middle of this array and used LSCM to observe the samples under the magnetic field. The typical observation area was in the central  $2 \text{ mm}^2$ , where the homogeneity of the magnetic field was  $\sim 2000 \text{ ppm}$  (Fig. S5b).

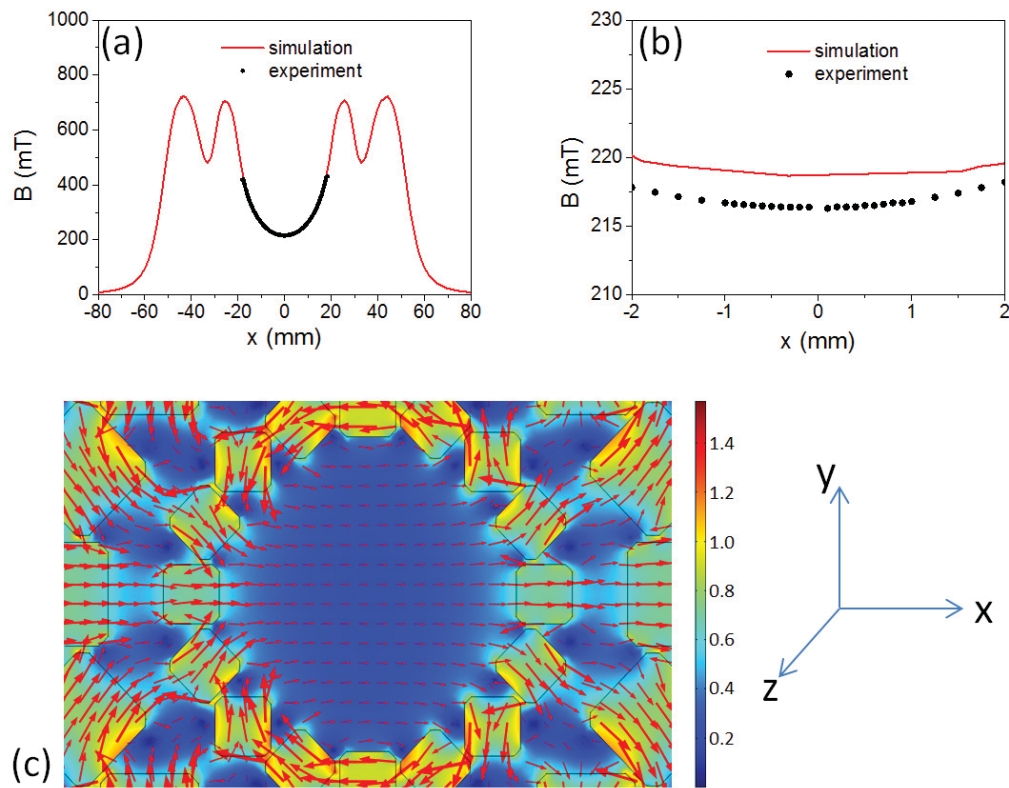


**Figure S5** Comparison of measured and simulated magnetic flux density in the Halbach magnetic array. The arrangement of the 32 permanent magnets is shown in Fig. 1a. (a) Magnitude  $B$  of the magnetic flux density along the  $x$ -axis. The red solid curve shows simulation results using Comsol software. The solid black points are experimental data (measured by a Lake Shore Model 425 Gaussmeter with a transverse probe). The data for  $x$  around 0 are shown in (b). The homogeneity in the central  $2 \text{ mm}^2$  is  $\sim 2000 \text{ ppm}$ . (c) Simulated magnetic field in the magnetic array. The magnetic flux density is shown by color map and the direction of the magnetic field is shown by red arrows.

The magnetic field of this magnetic array was simulated in Comsol Multiphysics (<http://www.comsol.com>). The parameters for the simulation were the same as in the experiments, such as the positions, the dimensions, and the remanence (1.32 T) of the magnets. The permanent magnets were modeled using Ampère's law. The influence of

the housing (made of Aluminum) of the magnets was not considered. A detailed description of the simulation can be found in the model library of Comsol Multiphysics, “Static Field Modeling of a Halbach Rotor”.

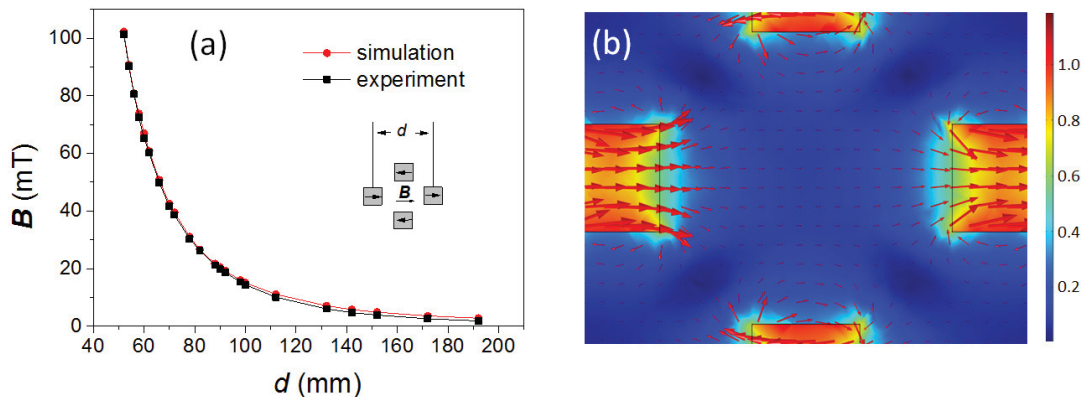


**Figure S6** Magnetic field of the four-magnet Halbach array. (a) By changing the separation between the 4 magnets, the magnetic flux density at the center of the magnetic array can be changed. The red circle points are obtained from simulation using Comsol software, and the black square points are measured by a Lake Shore Model 425 Gaussmeter with a transverse probe. The homogeneity in the central  $2 \text{ mm}^2$  is  $\sim 4000$  ppm. (b) Simulated magnetic field in the four-magnet array. The magnetic flux density is shown by color map and the direction of the magnetic field is shown by red arrows.

In some experiments we needed to change the magnetic field strength. This was realized by using a four-magnet Halbach array (Fig. S6, the magnets had dimensions of  $14 \times 14 \times 15 \text{ mm}^3$ ). By changing the distance between the magnets, the magnetic flux density in the center of this array could be changed from 0 mT to 101 mT. The homogeneity of this array in the central  $2 \text{ mm}^2$  was  $\sim 4000$  ppm.

## 2.5 Bending rigidity of the paramagnetic particle chains

Here we provide experimental evidence that the paramagnetic particle chains already by themselves (i.e. without the embedding polymer matrix) feature a bending rigidity. For this purpose, instead of preparing a percolating polymer network (gel), we prepared a sol. We decreased the concentration of the prepolymer mixture to  $c^*/2$  ( $c^*$  is the critical concentration at which a percolating network can be formed, see Fig. S3b). The prepolymer mixture reacted and formed a sol after the catalyst was added. During the reaction a magnetic field of 100.8 mT was applied, thus the magnetic particles in the sol aligned into chains. If the particles had not been connected by the polymer, the linear particle chains would not have survived after the magnetic field was removed because of thermal agitation. However, we found that the linear particle chains were stable in the sol even for several days (Fig. S7a). Once more applying a magnetic field (18.7 mT) most of the permanent paramagnetic chains in the sol aligned along the magnetic field direction (Fig. S7b). However, some of the chains bent and showed hairpin or “S”-shape morphologies (marked by the red arrows in Fig. S7b), indicating that the chains had a bending rigidity.<sup>S8</sup>

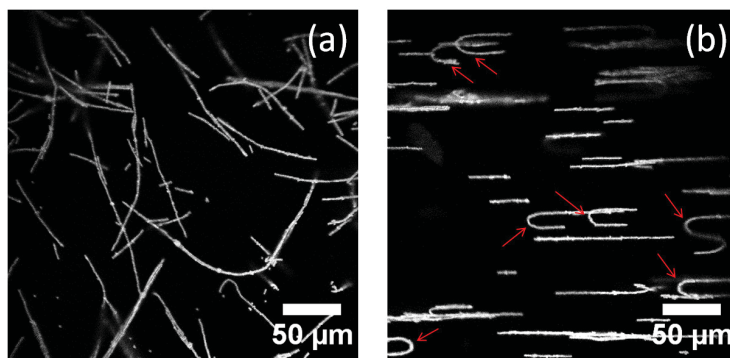


**Figure S7** Typical chain morphologies in the sol (a) in the absence of a magnetic field and (b) under a magnetic field. The magnetic field of 18.7 mT was applied horizontally. Under the magnetic field most of the paramagnetic chains aligned along the magnetic field direction. Some of the chains bent and showed hairpin or “S”-shape morphologies (marked by the red arrows), indicating that they have a bending rigidity.<sup>S8</sup> The scale bars are 50  $\mu\text{m}$ .

We conjecture that some prepolymer molecules in the solution were adsorbed onto the surfaces of the paramagnetic particles. When the prepolymer cross-linked, a polymer layer on the surfaces of the particles was formed and connected the particles. This polymer layer contributed to the bending rigidity. Only when the concentration of the prepolymer mixture is higher than  $c^*$ , a gel can be formed in the bulk. Apparently, already below this concentration, a connecting polymer layer can be formed on the surfaces of the paramagnetic particles. This suggests that a thin layer of polymer with a higher modulus compared to the bulk should be considered to understand the buckling behavior of the paramagnetic chains in the soft gels.

## 2.6 Buckling of magnetic particles in a “stiff” gel

In the main article, very soft gels ( $<1.5$  Pa) were used as a matrix. If a stiffer gel was used, the paramagnetic particle chains could not deform the gel significantly under the magnetic field of 216 mT (maximum field in our set-up). Here we used carbonyl iron (CI, CC grade, BASF, Germany,  $d_{50}$  value= $3.8\text{-}5.3$   $\mu\text{m}$ ) as magnetic particles in order to increase the magnetic force between the magnetic particles. First, the saturation of magnetization of CI ( $\sim 250$   $\text{Am}^2/\text{kg}$ ) is significantly larger than that of our otherwise used paramagnetic particles ( $\sim 20$   $\text{Am}^2/\text{kg}$ ); second, the density of CI ( $\sim 8 \times 10^3$   $\text{kg}/\text{m}^3$ ) is higher than that of our paramagnetic particles ( $\sim 1.7 \times 10^3$   $\text{kg}/\text{m}^3$ ); last, the size of CI is about 3 times larger. According to  $m = 4\pi R^3 \rho M/3$  (see Section 2.2), the magnetic moment can be  $10^3$  times larger compared to our paramagnetic case in the main article. As a result, even in a relatively “stiff” gel, the CI magnetic chains can deform the gel significantly. As shown in Fig. S8, in the gel with an elastic modulus of 170 Pa, the CI chains can buckle when a magnetic field of 100.8 mT is applied.

However, promoted by the polydispersity of the CI particles, the CI chains are not as smooth as the chains formed by the monodisperse paramagnetic particles (see Figs. 1 and 2 in the main article for comparison). In addition, we also observed fractures in some CI chains (Fig. S8c) probably due to the polydispersity of the particles. However, the chains

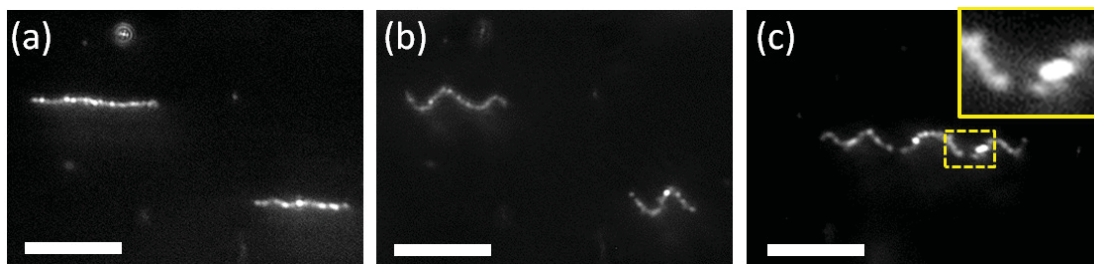


**Figure S8** Magnetic chains formed by carbonyl iron particles in a gel with an elastic modulus of 170 Pa. (a) Without magnetic field, (b, c) under a magnetic field of 100.8 mT along the vertical direction. The inset in (c) shows an enlarged image of the fracture of the magnetic chain. The scale bars are 50  $\mu\text{m}$ . These images were obtained using a 10 $\times$  objective (NA=0.28, M Plan Apo) which collected the reflection light from the carbonyl iron particles.

do not break up into structures as shown in Fig. 9 of the main article (lower image), suggesting that there is still a relatively stiff polymer layer around the CI particles.

### 3 Supplementary information concerning the modeling

#### 3.1 Magnetic interactions within the chain

In the following, we derive Eqs. (1) and (2) of the main article. We start from two neighboring particles on the chain. According to the assumptions made in the main article, each of them carries a magnetic moment  $\mathbf{m}$  oriented in  $y$ -direction. They interact via the dipole-dipole magnetic interaction given by

$$V_{dd} = \frac{\mu_0}{4\pi} \left[ \frac{\mathbf{m} \cdot \mathbf{m}}{r^3} - \frac{3(\mathbf{m} \cdot \mathbf{r})(\mathbf{m} \cdot \mathbf{r})}{r^5} \right], \quad (\text{S6})$$

where  $\mathbf{r}$  is the vector joining the centers of the particles,  $r = |\mathbf{r}|$ , and  $\mu_0$  is the vacuum magnetic permeability. Since the particles on the chain are experimentally observed to remain in contact, we have  $r = d$ , with  $d$  the particle diameter. Furthermore, we ignore the first term in the square brackets because it is constant under the given assumptions. Indicating by  $\alpha$  the angle between  $\mathbf{r}$  and  $\mathbf{m}$ , we obtain

$$V_{dd} \sim -\frac{3\mu_0 m^2}{4\pi d^3} \cos^2 \alpha. \quad (\text{S7})$$

Since  $\mathbf{m}$  is oriented in the  $y$ -direction,  $\psi = \pi/2 - \alpha$  is the angle between  $\mathbf{r}$  and the  $x$ -axis. Skipping another constant term resulting from  $\cos^2 \alpha = 1 - \sin^2 \alpha$ , the non-constant part of the dipole-dipole interaction can thus be rewritten as

$$V_{dd} \sim \varepsilon_m \sin^2(\psi - \pi/2), \quad \text{with } \varepsilon_m = \frac{3\mu_0 m^2}{4\pi d^3}. \quad (\text{S8})$$

For an undeformed infinite straight chain oriented along the  $x$ -axis in the above set-up, the resulting expression for the total dipolar magnetic interaction energy per particle along the whole chain then reads

$$V_{dd}^{chain} \sim \varepsilon_m \sum_{n=1}^{\infty} \frac{1}{n^3} = \varepsilon_m \zeta(3), \quad (\text{S9})$$

where  $\zeta$  is the Riemann Zeta function and  $\zeta(3) \simeq 1.202$ . Here,  $\varepsilon_m$  sets the scale of the nearest-neighbor dipolar interaction. In our minimal model the correction described by the factor  $\zeta(3) \simeq 1.202$  due to higher-order neighbors is negligible. Since the contour lines of the magnetic chains preserve a smooth shape under the observed deformations, without any kinks, and as the chains do not fold back onto themselves, we thus confine ourselves to nearest-neighbor interactions.

For a large number of particles, the quantity  $\varepsilon_m$  sets the magnetic interaction energy per particle. Moreover, the total magnetic interaction energy scales approximately linearly with the number of particles and chain length.

We now switch to a continuum picture by specifying the line energy density along the magnetic chain. In our coordinate system, the angle  $\psi$  that the connecting vector  $\mathbf{r}$  between two neighboring particles forms with the  $x$ -axis is locally given by  $\psi \sim$

$\arctan[y'(x)]$ , where  $y'(x) = dy/dx$ . To obtain the resulting magnetic energy of the whole magnetic chain, we need to integrate the energy line density along the contour line. For simplicity, we transform this line integral to an integration along the  $x$ -axis. If we parameterize the contour line by the parameter  $s$ , the line element  $ds$  along the chain can be expressed as  $ds = \sqrt{1 + y'(x)^2} dx$ . Therefore, the magnetic energy becomes

$$\begin{aligned} E_{magn}[y] &= W \int_{x_1}^{x_2} \sin^2 \left\{ \arctan [y'(x)] - \frac{\pi}{2} \right\} \sqrt{1 + y'(x)^2} dx \\ &= W \int_{x_1}^{x_2} \frac{1}{\sqrt{1 + y'(x)^2}} dx, \end{aligned} \quad (\text{S10})$$

where

$$W = \frac{\epsilon_m}{d} = \frac{3\mu_0 m^2}{4\pi d^4} \quad (\text{S11})$$

is the magnetic energy per unit length and  $x_1, x_2$  are the  $x$ -coordinates of the end points of the chain.

### 3.2 Elastic bending energy

Next, we briefly sketch the derivation of the elastic bending energy in Eq. (3) of the main article. For this purpose, we consider a parameterization  $\mathbf{R}(s)$  of the contour line of the magnetic chain, where the positions  $\mathbf{R}$  mark the points on the contour line and  $s \in [s_1, s_2]$  with  $s_1$  and  $s_2$  labeling the end points of the chain. On this basis, the elastic bending energy is defined as<sup>S9</sup>

$$E_{bend} = C_b \int_{s_1}^{s_2} \left| \frac{d^2 \mathbf{R}(s)}{ds^2} \right|^2 ds. \quad (\text{S12})$$

Using the parameterization  $\mathbf{R} = (x, y(x))$  and  $ds = \sqrt{1 + y'(x)^2} dx$ , we obtain

$$\frac{d\mathbf{R}}{ds} = \left(1 + y'(x)^2\right)^{-\frac{1}{2}} \begin{pmatrix} 1 \\ y'(x) \end{pmatrix} \quad (\text{S13})$$

and

$$\frac{d^2 \mathbf{R}}{ds^2} = y''(x) \left(1 + y'(x)^2\right)^{-2} \begin{pmatrix} -y'(x) \\ 1 \end{pmatrix}. \quad (\text{S14})$$

From this last expression, we obtain Eq. (3) in the main article when we again transform the line element  $ds$  to Cartesian coordinates,  $ds = \sqrt{1 + y'(x)^2} dx$ .

### 3.3 Elastic displacement energy

Finally, we motivate the expression for the elastic displacement energy in Eq. (4) of the main article. The part  $[y(x)]^2$  corresponds to a lowest order term in the displacement  $y(x)$ . We weight each of the two displacement factors  $y(x)$  by the amount of chain material displaced per integration interval  $dx$ , given by the length of the chain per integration

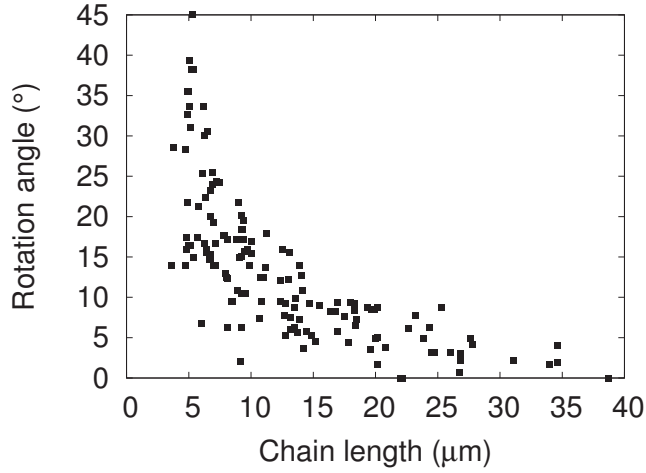


**Figure S9** Experimentally observed rotation angles of magnetic chains in a gel of shear modulus  $G' = 0.25$  Pa under a perpendicular magnetic field of magnitude  $B = 18.7$  mT. To first approximation, a rigid rotation of straight chains occurs at small enough rotation angles. This is depicted, for instance, in Fig. 1c of the main article for small angles of the magnetic field.

interval  $dx$ , i.e.  $ds/dx = \sqrt{1 + y'(x)^2}$ . This leads to  $[y(x)]^2 [1 + y'(x)^2]$ . In addition to that, we have another factor  $\sqrt{1 + y'(x)^2}$ , again from transforming the line element  $ds$  of the integration to Cartesian coordinates,  $ds = \sqrt{1 + y'(x)^2} dx$ . In total, we obtain the expression in Eq. (4) of the main article.

We explain in the following why the experimental observations suggest this form as a lowest order term. In particular, we note that the experimental investigations suggest the form  $[y(x)]^2$  rather than one containing the first derivative  $[y'(x)]^2$ . For this purpose, we consider the case of straight chains ( $M = 0$ ) undergoing small rotations in a perpendicular magnetic field. This situation can be simply parameterized by  $y(x) = Sx$ , where  $S = \tan \psi$  and  $\psi$  as introduced above giving the rotation angle. Furthermore  $E_{bend} = 0$ .

For  $y(x) = Sx$ ,  $E_{magn}$  scales linearly with the chain length  $L$ . The same would apply for an energetic contribution  $\sim \int_{x_1}^{x_2} [y'(x)]^2 [1 + y'(x)^2]^{3/2} dx$ . Therefore, the latter expression inevitably leads to a rotation angle  $\psi$  that is independent of the chain length  $L$ . However, this contradicts the experimental results. In Fig. S9 we plot the rotation angle  $\psi$  as a function of chain length  $L$  measured in a gel of shear modulus  $G' = 0.25$  Pa exposed to a perpendicular magnetic field of magnitude  $B = 18.7$  mT. There is a clear dependency of the rotation angle on the chain length  $L$ . The energetic expression  $E_{displ}$  in Eq. (4) of the main article for rotations of straight chains  $y(x) = Sx$  scales as  $E_{displ} \sim L^3$  and thus leads to disproportionately higher energetic penalties for longer chains, reflecting the experimentally observed smaller rotation angles.

### 3.4 Discussion of resulting chain shapes

Now that our total model energy  $E_{tot}$  is set as the sum of Eqs. (1), (3), and (4) in the main article, a standard route to determine the shape  $y(x)$  of the chain would be to find the extrema of the functional  $E_{tot}[y(x)]$  with respect to the function  $y(x)$ . For this purpose,

one calculates the functional derivative of  $E_{tot}[y(x)]$  with respect to  $y(x)$  and equates it with zero. The procedure is well known from the famous brachistochrone problem.<sup>S10</sup> There one wishes to find the shape of a curve linking two end points such that a body moving between them under gravity passes the distance in the least possible amount of time.

However, there is a fundamental difference compared to the brachistochrone problem. While calculating the functional derivative, boundary terms appear that explicitly include contributions from the end points of the chain or trajectory  $y(x)$ . Technically, they result from partial integration. In the brachistochrone problem, one has sufficient information to handle these boundary terms: by construction of the problem, one knows that the end points are fixed. Similarly, in other problems of infinitely extended elastic struts of periodic, periodically modulated, or localized deformations,<sup>S11–S14</sup> one can use the periodicity or localization to argue in favor of an evanescent influence of the boundary terms. This is very different from our present case, where the deflection encompasses the whole finite chain and in particular its end points. Unfortunately, acquiring sufficient knowledge of the associated boundary conditions would imply solving the whole complex three-dimensional nonlinear elasticity and magnetization problem, which is beyond the present scope and in fact was the reason to project to our reduced minimal model.

For completeness, however, we perform some additional variational analysis of our energy functional. We concentrate on possible solutions in the bulk that could be observed if boundary effects were absent (which is not the case for our experimentally investigated finitely-sized objects). Then, neglecting the boundary terms, the functional derivatives of Eqs. (1), (3), and (4) are calculated as follows (the dependencies of  $y(x)$  and its derivatives on  $x$  is omitted for brevity on the right-hand sides):

$$\frac{\delta E_{magn}}{\delta y(x)} = W y'' (1 - 2y'^2) (1 + y'^2)^{-\frac{5}{2}}, \quad (\text{S15})$$

$$\frac{\delta E_{bend}}{\delta y(x)} = C_b \left[ 5y'^3 (6y'^2 - 1) - 20y'y''y''' (1 + y'^2) + 2y'''' (1 + y'^2)^2 \right] (1 + y'^2)^{-\frac{9}{2}}, \quad (\text{S16})$$

and

$$\frac{\delta E_{displ}}{\delta y(x)} = C_d \left[ 2y - 2yy'^2 - 4yy'^4 - 3y^2y'' - 6y^2y'^2y'' \right] (1 + y'^2)^{-\frac{1}{2}}. \quad (\text{S17})$$

Together, we obtain a nonlinear fourth-order differential equation for  $y(x)$ :

$$\begin{aligned} \frac{\delta E_{tot}}{\delta y(x)} = & (1 + y'^2)^{-\frac{9}{2}} \left[ - (1 + y'^2) y'' (W (-1 + y'^2 + 2y'^4) + 20C_b y' y''') \right. \\ & - 3C_d y^2 (1 + y'^2)^4 (1 + 2y'^2) y'' + 5C_b (-1 + 6y'^2) y''^3 \\ & \left. - 2C_d y (1 + y'^2)^5 (-1 + 2y'^2) + 2C_b (1 + y'^2)^2 y'''' \right] = 0. \quad (\text{S18}) \end{aligned}$$

Eq. (S18) can in principle be solved numerically by integrating it outward from the center of the chain at  $x = 0$ . For this purpose, a sufficient amount of “initial conditions”

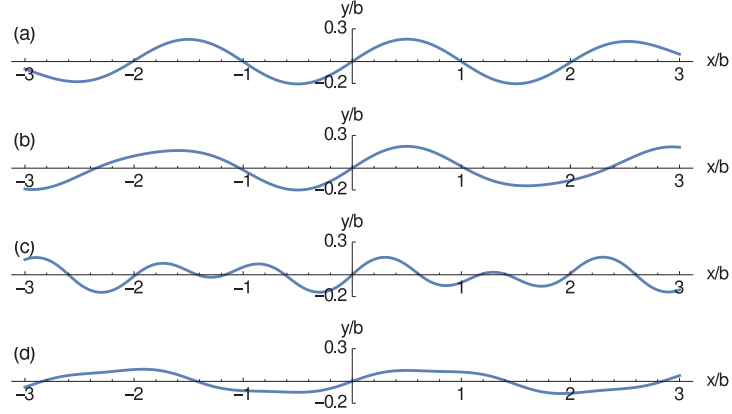


**Figure S10** Numerical solutions of Eq. (S18) for different imposed input conditions. In all cases we concentrate on uneven centro-symmetric solutions and thus prescribe  $y(0) = y''(0) = 0$ . As remaining necessary conditions, we specify the position of the first maximum: **(a)**  $y'(0.5) = 0$ ,  $y(0.5) = 0.205$ ; **(b)**  $y'(0.5) = 0$ ,  $y(0.5) = 0.2$ ; **(c)**  $y'(0.3) = 0$ ,  $y(0.3) = 0.16$ ; **(d)**  $y'(0.5) = 0$ ,  $y(0.5) = 0.1$ .

(four in our case) for  $y(x)$  and its derivatives needs to be provided. We concentrate on uneven centro-symmetric solutions, which directly prescribes two conditions:  $y(0) = 0$  and  $y''(0) = 0$ . As was found before in a different context,<sup>S11</sup> the solution is extremely sensitive to the two remaining imposed conditions. For illustration, we depict four examples in Fig. S10. There, we provide slightly varying positions of the first maximum [ $y'(x) = 0$ ] as the remaining two necessary conditions. Numerical integration shows that little variations in these conditions lead to qualitatively different oscillatory solutions.<sup>S15</sup>

Altogether, we may conclude that the solutions resulting from Eq. (S18) sensitively depend on the input conditions. As noted above, we do not have access to the appropriate conditions applying at the significantly displaced end points of the embedded chain. The strategy that we resorted to is therefore to use as an input directly the shapes of the chains suggested by the experiments. We found good representations of the experimental observations using the polynomial form suggested by Eq. (5) in the main article. In particular, with regard to the pronounced displacements of the chain ends, this choice is preferred to, for instance, a sinusoidal ansatz. Then, instead of solving Eq. (S18) explicitly, we minimize the energy functional  $E_{tot}[y(x)]$  with respect to the remaining degrees of freedom of the chain deformation ( $M$ ,  $S$ ,  $x_1$  and  $x_2$  in the main article). Thus, even if we have used an ansatz for the chain deformation, this remains a nonlinear approach as we evaluate the nonlinear contributions to the energy functional  $E_{tot}[y(x)]$ .

### 3.5 Oscillatory solutions in the linear regime

In the previous part, we have demonstrated that various complex solutions can result from the nonlinear nature of Eq. (S18). Here, we restrict ourselves to the situation in the inside of the magnetic chains for small amounts of deformation, i.e. at the onset of deformation. For this purpose, a linear stability analysis is performed by considering a linearized version of Eq. (S18). As a result, we obtain a condition describing the onset of

a linear deformational instability

$$Wy''(x) + 2C_b y''''(x) + 2C_d y(x) = 0. \quad (\text{S19})$$

This equation has solutions of the kind  $y(x) \sim \exp(\pm iqx)$ , with wavenumber

$$q^2 = \frac{W \pm \sqrt{W^2 - 16C_b C_d}}{4C_b}. \quad (\text{S20})$$

The condition for the solutions to be purely oscillatory is  $W^2/16C_b C_d > 1$  and defines an onset for this kind of deformation. It sets a threshold magnitude for the strength of the external magnetic field. Thus, for a perfectly oriented chain of identical particles in a spatially homogeneous elastic matrix, this linear stability analysis predicts a critical magnetic field amplitude above which an undulatory instability would arise in the inside of the chain. Our results are in agreement with the experimental observation of the wrinkles at onset in Fig. 1c and the final oscillatory shape in the inner part of the longer chains in Fig. 2a of the main article.

## 4 Technical description of the coarse-grained molecular dynamics simulations

### 4.1 Magnetic particles

In the molecular dynamics simulations, the centers of the magnetic particles and the nodes of the polymer mesh are treated as point particles in two-dimensional space. The magnetic particles additionally have one rotational degree of freedom, namely around the axis perpendicular to the model plane. As each magnetic particle is superparamagnetic, its magnetic moment is not affected by a rotation of the particle. Rather, the magnetic moment is determined by the magnetic field. Hence, we place the magnetic moment not on the rotating center of the particle, but rather on a separate virtual site which does not rotate. It is placed at the same location as the center of the magnetic particle. Virtual sites are particles, whose position is not determined by integrating an equation of motion, rather their position is calculated from the position and orientation of other particles. In this way, they allow us to introduce rigid extended bodies into a molecular dynamics simulation.<sup>S16</sup> Forces acting on any constituent of such a rigid body are transferred back to its center of mass, and thus included in the equation of motion of the rigid body.

Pairs of magnetic particles interact by the dipole-dipole interaction, Eq. (S6). The dipole moment of the particles is assumed to be determined entirely by the external magnetic field, and its magnitude is deduced from the experimental magnetization curve (Fig. S1b). This assumption is valid as long as the external field is much stronger than the field created by the other magnetic particles. In other cases, a self-consistent approach has to be used to determine the local magnetic fields. In addition to the dipole-dipole interaction, the magnetic particles interact via a truncated and shifted, purely repulsive Lennard-Jones potential mimicking a rigid-sphere interaction. We use the Weeks-Chandler-Andersen potential<sup>S17</sup> in the form

$$V_{WCA}\left(\frac{r}{\sigma}\right) = \begin{cases} 4\epsilon \left[ \left(\frac{r}{\sigma}\right)^{-12} - \left(\frac{r}{\sigma}\right)^{-6} + \frac{1}{4} \right] & \text{for } r \leq r_c, \\ 0 & \text{otherwise,} \end{cases} \quad (\text{S21})$$

where  $r$  is the distance between the particle centers,  $\epsilon = 1000$  denotes the energy scale of the potential, and  $r_c = 2^{1/6}\sigma$  is the cut-off distance, for which we use the experimental diameter of  $1.48 \mu\text{m}$ . The parameter  $\sigma$  denotes the root of the non-shifted potential and is used in the visualizations in Figs. 9 and 10.

### 4.2 Polymer mesh

The polymer matrix is modeled as a bead-spring network based on a hexagonal lattice. We use a lattice constant  $a$  of one third of the experimentally observed particle diameter, i.e.,  $a \approx 0.49 \mu\text{m}$ . Along the initial chain direction, we use 601 mesh points, along the perpendicular direction 301. The mesh points on the boundary of the system are fixed, all other mesh points can move in the  $x$ - and  $y$ -directions. Adjacent mesh points interact via a non-linear elastic spring based on the FENE-potential.<sup>S18</sup> Here, we use a variant with

different cut-off values for compression and expansion. It is given by

$$\begin{aligned} V(r) &= -\frac{1}{2}K(r_0 - r_{\min})^2 \ln \left[ 1 - \left( \frac{r-r_0}{r_0-r_{\min}} \right)^2 \right] \quad \text{for } r < r_0, \\ V(r) &= -\frac{1}{2}K(r_{\max} - r_0)^2 \ln \left[ 1 - \left( \frac{r-r_0}{r_{\max}-r_0} \right)^2 \right] \quad \text{for } r > r_0. \end{aligned} \quad (\text{S22})$$

In these expressions,  $K = 45$  controls the scale of the potential, the equilibrium distance  $r_0 = a$  is equal to the lattice constant, while the minimum and maximum elongations, at which the potential diverges, are  $r_{\min} = 0.1a$  and  $r_{\max} = 3a$ , respectively. The potential, as well as its second derivative, are continuous at the equilibrium extension  $r = r_0$ . In order to prevent any volume element from shrinking to zero, angular potentials are used on all pairs of neighboring springs attached to the same mesh site, encompassing an angle of  $60^\circ$  in the unstrained mesh. The potential has the same functional form as the distance-based potential in Eq. (S22), but with the values  $K = 100$ ,  $r_0 = \pi/3$ ,  $r_{\min} = 0$ , and  $r_{\max} = \pi$ . In the simulations both potentials are tabulated at 100000 equally spaced intervals between the minimum and maximum extensions. Between those points, linear interpolation is used.

### 4.3 Particle-mesh coupling and boundary layer

The mesh spans the entire simulation area, including the area covered by the magnetic particles. In order to couple the polymer mesh to both, the translational and rotational motion of a magnetic particle, the seven mesh sites within the area of each magnetic particle are treated as virtual sites, rigidly following the motion of the magnetic particle. In other words, the mesh sites within the particle and the center of the magnetic particle form a rigid body. This additionally prevents a distortion of the gel matrix in the area occupied by the magnetic particles. Two variants of gel boundary layer around the particles are studied (Fig. 9 in the main article). In the case of a soft boundary layer, the mesh springs emerging from the mesh sites rigidly connected to the particle, are modeled as in Eq. (S22) with the same parameters as for the bulk. In the case of a stiff boundary layer, a potential is used which is stiffer by three orders of magnitude. The following parameters are used in this case:  $K = 45000$ ,  $r_{\min} = -2a$ , and  $r_{\max} = 4a$ .

### 4.4 Equation of motion and integration

The simulations are performed in the canonical ensemble at a temperature of 300 K. All particles except for the virtual sites are propagated according to a Langevin equation. For any component in a Cartesian coordinate system, it is given by

$$m_p \dot{v}(t) = -\gamma v(t) + F + F_r, \quad (\text{S23})$$

where  $m_p$  denotes the mass of the particle,  $v$  its velocity,  $F$  is the force due to the interaction with other particles,  $F_r$  denotes the random thermal noise, and  $\gamma$  is the friction coefficient. To maintain a temperature  $T$ , the thermal noise has to have a mean of zero and a variance of

$$\langle F_r^2 \rangle = 2k_B T \gamma, \quad (\text{S24})$$

where  $k_B T$  denotes the thermal energy. For the rotational degree of freedom of each magnetic particle, the same equation of motion is used, but mass, velocity, and forces are replaced by moment of inertia, angular velocity, and torques, respectively. The friction coefficient, the thermal energy, and the mass of the mesh sites are all chosen to be unity, whereas the mass and rotational inertia of the centers of the magnetic particles are both 100. This slows down the relaxation time of the magnetic particles versus that of the polymer mesh and is helpful in stabilizing the simulation. The Langevin equation is integrated using a Velocity Verlet integrator. For the simulations with a stiff boundary layer, the time step is  $dt = 0.001$ , for a soft boundary layer it is  $dt = 0.00004$ . The simulations take approximately 100000 time steps to converge.

## References

- [S1] F. Ziemann, J. Rädler and E. Sackmann, *Biophys. J.*, 1994, **66**, 2210–2216.
- [S2] A. R. Bausch, W. Möller and E. Sackmann, *Biophys. J.*, 1999, **76**, 573–579.
- [S3] P. Tordjeman, C. Fargette and P. H. Mutin, *J. Rheol.*, 2001, **45**, 995–1006.
- [S4] T. G. Mason, T. Gisler, K. Kroy, E. Frey and D. A. Weitz, *J. Rheol.*, 2000, **44**, 917–928.
- [S5] <http://www.physics.emory.edu/faculty/weeks/idl/index.html>.
- [S6] T. G. Mason and D. Weitz, *Phys. Rev. Lett.*, 1995, **74**, 1250–1253.
- [S7] H. Raich and P. Blümler, *Concept. Magn. Reson. B*, 2004, **23B**, 16–25.
- [S8] C. Goubault, P. Jop, M. Fermigier, J. Baudry, E. Bertrand and J. Bibette, *Phys. Rev. Lett.*, 2003, **91**, 260802.
- [S9] L. Landau and E. Lifshitz, *Elasticity theory*, Pergamon Press, 1975.
- [S10] I. Gelfand and S. Fomin, *Calculus of variations*, Prentice-Hall Inc., Englewood Cliffs, NJ, 1963.
- [S11] G. W. Hunt, M. Wadee and N. Shiacolas, *J. Appl. Mech.*, 1993, **60**, 1033–1038.
- [S12] B. Audoly, *Phys. Rev. E*, 2011, **84**, 011605.
- [S13] H. Diamant and T. A. Witten, *arXiv preprint arXiv:1009.2487*, 2010.
- [S14] H. Diamant and T. A. Witten, *Phys. Rev. Lett.*, 2011, **107**, 164302.
- [S15] Wolfram Research, *Mathematica 10.0*, 2014.
- [S16] A. Arnold, O. Lenz, S. Kesselheim, R. Weeber, F. Fahrenberger, D. Röhm, P. Košovan and C. Holm, *Meshfree Methods for Partial Differential Equations VI*, 2013, pp. 1–23.
- [S17] J. D. Weeks, D. Chandler and H. C. Andersen, *J. Chem. Phys.*, 1971, **54**, 5237–5247.
- [S18] H. R. Warner Jr., *Ind. Eng. Chem. Fundam.*, 1972, **11**, 379–387.



# Paper III Structural control of elastic moduli in ferrogels and the importance of non-affine deformations

Reproduced from

Giorgio Pessot, Peet Cremer, Dmitry Y. Borin, Stefan Odenbach, Hartmut Löwen, and  
Andreas M. Menzel,

Structural control of elastic moduli in ferrogels  
and the importance of non-affine deformations.  
*J. Chem. Phys.*, **141** 124904 (2014), AIP Publishing

with the permission of *AIP Publishing*. © AIP Publishing. All rights reserved.

(Version of Record)

DOI: 10.1063/1.4896147

## Authors' Contributions

All authors contributed to the writing of the manuscript. Andreas M. Menzel and Hartmut Löwen devised the dipole–spring approach and supervised the whole work. Dmitry Y. Borin and Stefan Odenbach provided the input experimental data. Peet Cremer contributed to the numerical analysis of the experimental data. I personally wrote the numerical code and performed the analytical calculations.

I estimate my total contribution to this work to approximately 75%.

## Copyright and Permission Informations

From <https://publishing.aip.org/authors/copyright-reuse> :

“AIP Publishing permits authors to include their published articles in a thesis or dissertation.

It is understood that the thesis or dissertation may be published in print and/or electronic form and offered for sale on demand, as well as included in a university’s repository. Formal permission from AIP Publishing is not needed.”



## Structural control of elastic moduli in ferrogels and the importance of non-affine deformations

Giorgio Pessot,<sup>1</sup> Peet Cremer,<sup>1</sup> Dmitry Y. Borin,<sup>2</sup> Stefan Odenbach,<sup>2</sup> Hartmut Löwen,<sup>1</sup> and Andreas M. Menzel<sup>1, a)</sup>

<sup>1</sup>*Institut für Theoretische Physik II: Weiche Materie, Heinrich-Heine-Universität Düsseldorf, D-40225 Düsseldorf, Germany*

<sup>2</sup>*Technische Universität Dresden, Institute of Fluid Mechanics, D-01062 Dresden, Germany*

(Received 1 July 2014; accepted 9 September 2014; published online 25 September 2014)

One of the central appealing properties of magnetic gels and elastomers is that their elastic moduli can reversibly be adjusted from outside by applying magnetic fields. The impact of the internal magnetic particle distribution on this effect has been outlined and analyzed theoretically. In most cases, however, affine sample deformations are studied and often regular particle arrangements are considered. Here we challenge these two major simplifications by a systematic approach using a minimal dipole-spring model. Starting from different regular lattices, we take into account increasingly randomized structures, until we finally investigate an irregular texture taken from a real experimental sample. On the one hand, we find that the elastic tunability qualitatively depends on the structural properties, here in two spatial dimensions. On the other hand, we demonstrate that the assumption of affine deformations leads to increasingly erroneous results the more realistic the particle distribution becomes. Understanding the consequences of the assumptions made in the modeling process is important on our way to support an improved design of these fascinating materials. © 2014 AIP Publishing LLC. [<http://dx.doi.org/10.1063/1.4896147>]

### I. INTRODUCTION

In the search of new materials of outstanding novel properties, one route is to combine the features of different compounds into one composite substance.<sup>1–5</sup> Ferrogels and magnetic elastomers provide an excellent example for this approach. They consist of superparamagnetic or ferromagnetic particles of nano- or micrometer size embedded in a crosslinked polymer matrix.<sup>6</sup> In this way, they combine the properties of ferrofluids and magnetorheological fluids<sup>7–16</sup> with those of conventional polymers and rubbers:<sup>17</sup> we obtain elastic solids, the shape and mechanical properties of which can be changed reversibly from outside by applying external magnetic fields.<sup>6, 18–25</sup>

This magneto-mechanical coupling opens the door to a multitude of applications. Deformations induced by external magnetic fields suggest a use of the materials as soft actuators<sup>26</sup> or as sensors to detect magnetic fields and field gradients.<sup>27, 28</sup> The non-invasive tunability of the mechanical properties by external magnetic fields makes them candidates for the development of novel damping devices<sup>29</sup> and vibration absorbers<sup>19</sup> that adjust to changed environmental conditions. Finally, local heating due to hysteretic remagnetization losses in an alternating external magnetic field can be achieved. This effect can be exploited in hyperthermal cancer treatment.<sup>30, 31</sup>

In recent years, several theoretical studies were performed to elucidate the role of the spatial magnetic particle distribution on these phenomena.<sup>23, 32–42</sup> It turns out that the particle arrangement has an even qualitative impact on the effect that external magnetic fields have on ferrogels. That

is, the particle distribution within the samples determines whether the systems elongate or shrink along an external magnetic field, or whether an elastic modulus increases or decreases when a magnetic field is applied. As a first step, many of the theoretical investigations focused on regular lattice structures of the magnetic particle arrangement.<sup>32, 36, 42</sup> Meanwhile, it has been pointed out that a touching or clustering of the magnetic particles and spatial inhomogeneities in the particle distributions can have a major influence.<sup>23, 35, 39–41, 43</sup> More randomized or “frozen-in” gas-like distributions were investigated.<sup>23, 33–35, 38, 40</sup> Yet, typically in these studies an affine deformation of the whole sample is assumed, i.e., the overall macroscopic deformation of the sample is mapped uniformly to all distances in the system. An exception is given by microscopic<sup>37</sup> and finite-element studies,<sup>23, 35, 41</sup> but the possible implication of the assumption of an affine deformation for non-aggregated particles remains unclear from these investigations.

Here, we systematically challenge these issues using the example of the compressive elastic modulus under varying external magnetic fields. We start from regular lattice structures that are more and more randomized. In each case, the results for affine and non-affine deformations are compared. Finally, we consider a particle distribution that has been extracted from the investigation of a real experimental sample. It turns out that the assumption of affine deformations growingly leads to erroneous results with increasingly randomized particle arrangements and is highly problematic for realistic particle distributions.

In the following, we first introduce our minimal dipole-spring model used for our investigations. We then consider

<sup>a)</sup>Electronic mail: menzel@thphy.uni-duesseldorf.de

different lattice structures: rectangular, hexagonal, and honeycomb, all of them with increasing randomization. Different directions of magnetization are taken into account. Finally, an irregular particle distribution extracted from a real experimental sample is considered, before we summarize our conclusions.

## II. DIPOLE-SPRING MINIMAL MODEL

For reasons of illustration and computational economics, we will work with point-like particles confined in a two-dimensional plane with open boundary conditions. On the one hand, we will study regular lattices, for which simple analytical arguments can be given to predict whether the elastic modulus will increase or decrease with increasing magnetic interaction. These lattices will also be investigated after randomly introducing positional irregularities. Such structures could reflect the properties of more realistic systems, for example, those of thin regularly patterned magnetic block-copolymer films.<sup>44,45</sup>

On the other hand, irregular particle distributions in a plane to some extent reflect the situation in three dimensional anisotropic magnetic gels and elastomers.<sup>47–52</sup> In fact, our example of irregular particle distribution is extracted from a real anisotropic experimental sample. These anisotropic materials are manufactured under the presence of a strong homogeneous external magnetic field. It can lead to the formation of chain-like particle aggregates that are then “locked-in” during the final crosslinking procedure. These chains lie parallel to each other along the field direction and can span the whole sample.<sup>50</sup> To some extent, the properties in the plane perpendicular to the anisotropy direction may be represented by considering the two-dimensional cross-sectional layers on which, in this work, we will focus our attention.

Our system is made of  $N = N_x \times N_y$  point-like particles with positions  $\mathbf{R}_i$ ,  $i = 1 \dots N$ , each carrying an identical magnetic moment  $\mathbf{m}$ . That is, we consider an equal magnetic moment induced for instance by an external magnetic field in the case of paramagnetic particles, or an equal magnetic moment of ferromagnetic particles aligned along one common direction. We assume materials in which the magnetic particles are confined in pockets of the polymer mesh. They cannot be displaced with respect to the enclosing polymer matrix, i.e., out of their pocket locations. Neighboring particles are coupled by springs of different unstrained length  $l_{ij}^0$  according to the selected initial particle distribution. All springs have the same elastic constant  $k$ . The polymer matrix, represented by the springs, is assumed to have a vanishing magnetic susceptibility. Therefore, it does not directly interact with magnetic fields. (The reaction of composite bilayered elastomers of non-vanishing magnetic susceptibility to external magnetic fields was investigated recently in a different study<sup>46</sup>).

The total energy  $U$  of the system is the sum of elastic and magnetic energies<sup>43,53,54</sup>  $U_{el}$  and  $U_m$  defined by

$$U_{el} = \frac{k}{2} \sum_{(ij)} (r_{ij} - l_{ij}^0)^2, \quad (1)$$

where  $\langle ij \rangle$  means sum over all the couples connected by springs,  $\mathbf{r}_{ij} = \mathbf{R}_j - \mathbf{R}_i$ ,  $r_{ij} = |\mathbf{r}_{ij}|$  and

$$U_m = \frac{\mu_0 m^2}{4\pi} \sum_{i < j} \frac{r_{ij}^2 - 3(\hat{\mathbf{m}} \cdot \mathbf{r}_{ij})^2}{r_{ij}^5}, \quad (2)$$

where  $i < j$  means sum over all different couples of particles, and  $\hat{\mathbf{m}} = \mathbf{m}/m$  is the unit vector along the direction of  $\mathbf{m}$ . In our reduced units, we measure lengths in multiples of  $l_0$  and energies in multiples of  $kl_0^2$ ; here we define  $l_0 = 1/\sqrt{\rho}$ , where  $\rho$  is the particle area density. To allow a comparison between the different lattices we choose the initial density always the same in each case. Furthermore, our magnetic moment is measured in multiples of  $m_0 = \sqrt{4\pi k^2 l_0^5 / \mu_0}$ .

Estimative calculations show that the magnetic moments obtainable in real systems are 4–5 orders of magnitude smaller than our reduced unit for the magnetic moment, so only the behavior for the rescaled  $|\mathbf{m}|/m_0 = m/m_0 \ll 1$  would need to be considered. Here, we run our calculations for  $m$  as big as possible, until the magnetic forces become so strong as to cause the lattice to collapse, which typically occurs beyond realistic values of  $m$ . After rescaling, the magnetic moment  $\mathbf{m}$  is the only remaining parameter in our equations which can be used to tune the system for a given particle distribution.

## III. ELASTIC MODULUS FROM AFFINE AND NON-AFFINE TRANSFORMATIONS

We are interested in the elastic modulus  $E$  for dilative and compressive deformations of the system, as a function of varying magnetic moment and lattices of different orientations and particle arrangements. For a fixed geometry and magnetic moment  $\mathbf{m}$ , once we have found the equilibrium state of minimum energy of the system, we calculate  $E$  as the second derivative of total energy with respect to a small expansion/shrinking of the system, here in  $x$ -direction:

$$E = \frac{d^2 U}{d\delta_x^2} \simeq \frac{U(-\delta_x) + U(\delta_x) - 2U(0)}{\delta_x^2}. \quad (3)$$

$\delta_x$  is a small imposed variation of the sample length along  $\hat{x}$ . In order to remain in the linear elasticity regime,  $\delta_x$  must imply an elongation of every single spring by a quantity small compared to its unstrained length. In our calculations, we chose a total length change of the sample of  $\delta_x = L_x/100\sqrt{N} \simeq l_0/100$  throughout, where  $L_x$  is the equilibrium length of the sample along  $\hat{x}$ . Thus, on average, each spring is strained along  $\hat{x}$  by less than 1%. To indicate the direction of the induced strain, we use the letter  $\varepsilon$  in the figures below. The magnitude of the strain follows as  $|\varepsilon| = \delta_x/L_x \simeq 10^{-4} - 10^{-3}$ . Strains of such magnitude were for example applied experimentally using a piezo-rheometer.<sup>47</sup> A natural unit to measure the elastic modulus  $E$  in Eq. (3) is given by the elastic spring constant  $k$ .

There are different ways of deforming the lattices in order to find the equilibrium configuration of the system and calculate the elastic modulus. We will demonstrate that considering non-affine instead of affine transformations can lead

to serious differences in the results, especially for randomized and realistic particle distributions.

An affine transformation (AT) conserves parallelism between lines and in each direction modifies all distances by a certain ratio. In our case of a given strain in  $x$ -direction, in AT we obtain the equilibrium state by minimizing the energy over the ratio of compression/expansion in  $y$ -direction.

In a non-affine transformation (NAT), instead, most of the particles are free to adjust their positions independently of each other in 2D. Only the particles on the two opposing edges of the sample are “clamped” and forced to move in a prescribed way along  $x$ -direction, but they are free to adjust in  $y$ -direction. All clamped particles in the NAT are forced to be expanded in the  $x$ -direction in the same way as in the corresponding AT to allow better comparison (see Fig. 1 for an illustration of the two kinds of deformation). To perform NAT minimization, we have implemented the conjugated gradients algorithm<sup>55,56</sup> using analytical expressions of the gradient and Hessian of the total energy. Numerical thresholds were set such that the resulting error bars in the figures below are significantly smaller than the symbol size.

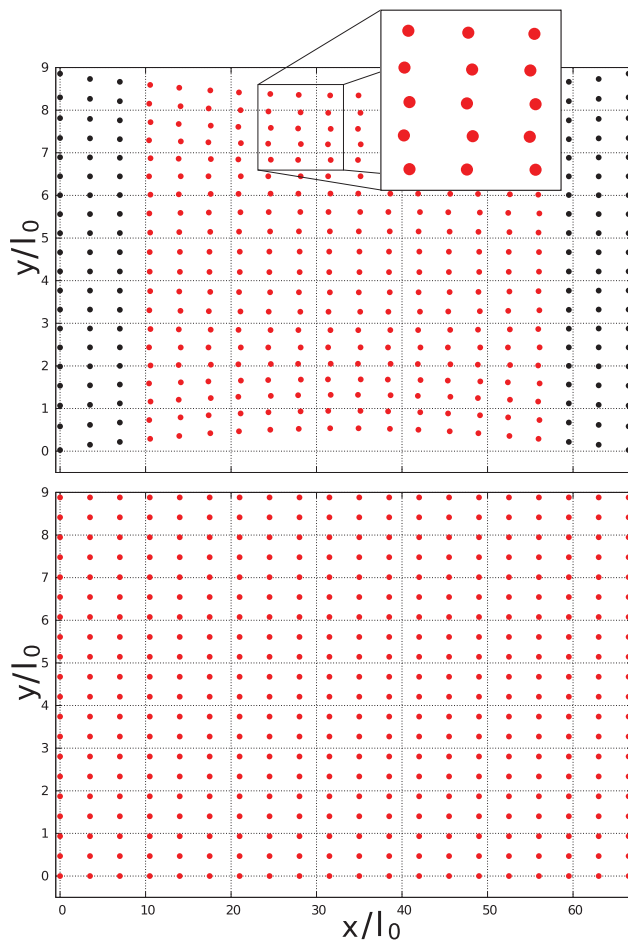


FIG. 1. An initial square lattice undergoing the same total amount of horizontal strain at vanishing magnetic moment and relaxed through NAT (top) and AT (bottom). Clamped particles are colored in black in the NAT case. The depicted deformations are much larger than the ones used in the following to determine the elastic moduli (here the sample was expanded in  $x$ -direction by a factor of 2.5).

As a consequence, NAT minimizes energy over  $\simeq 2N$  degrees of freedom. Since the NAT has many more degrees of freedom for the minimization than AT, we expect the former to always find a lower energetic minimum compared to the latter. Thus, for the elastic modulus, we obtain  $E^{\text{AT}} \geq E^{\text{NAT}}$ . Figure 1 shows how NAT and AT minimizations yield different ground states for the same total amount of strain along  $\hat{x}$ .

To compute the elastic modulus, we first find the equilibrium state through NAT for prescribed  $m$ . Next, using AT, we impose a small shrinking/expansion and after the described AT minimization obtain  $E^{\text{AT}}$  via Eq. (3). Then, starting from the NAT ground state again, we perform the same procedure using the NAT minimization and thus determine  $E^{\text{NAT}}$ .

## IV. RESULTS

In the following, we will briefly discuss the behavior of the elastic modulus in the limit of large systems. Then, on the one hand, we will demonstrate that introducing a randomization in the lattices dramatically affects the performance of affine calculations. On the other hand, we will investigate how in each case structure and relative orientation of the nearest neighbors determine the trend of  $E(m)$ .

### A. Elastic modulus for large systems

We run our simulations for lattices of  $N_x = N_y$ . It is known that the total elastic modulus of two identical springs in series halves, whereas, if they are in parallel doubles, compared to the elastic modulus of a single spring. In our case of determining the elastic modulus in  $x$ -direction, the total elastic modulus  $E$  will be proportional to  $N_y/N_x$ . Thus, with our choice of  $N_x = N_y$ , it should not depend on  $N$ . We will investigate the exemplary case of a rectangular or square lattice for  $m = 0$  to estimate the impact of finite size effects on our results, since a simple analytical model can be used to predict the value of  $E$ .

Our rectangular lattice is made of vertical and horizontal springs coupling nearest neighbors and diagonal springs connecting next-nearest neighbors. The diagonal springs are necessary to avoid an unphysical soft-mode shear instability of the bulk rectangular crystal. In the large- $N$  limit, there are on average one horizontal, one vertical, and two diagonal springs per particle. The deformation of a corresponding “unit spring cell” is depicted in Fig. 2.  $b_0$  and  $h_0$  are, respectively, the length of the horizontal and vertical spring of the unit cell in the undeformed state, whereas  $b$  and  $h$  are the respective

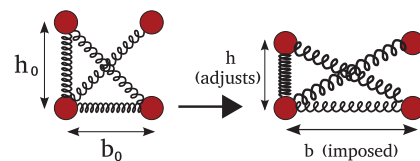


FIG. 2. Minimal rectangular model consisting of one  $x$ -oriented, one  $y$ -oriented, and two diagonal springs.  $b_0$  and  $h_0$  are the base and height of the rectangular cell in the unstrained state. Under strain,  $b_0 \rightarrow b$  and the height is free to adjust in order to minimize the elastic energy,  $h_0 \rightarrow h$ .

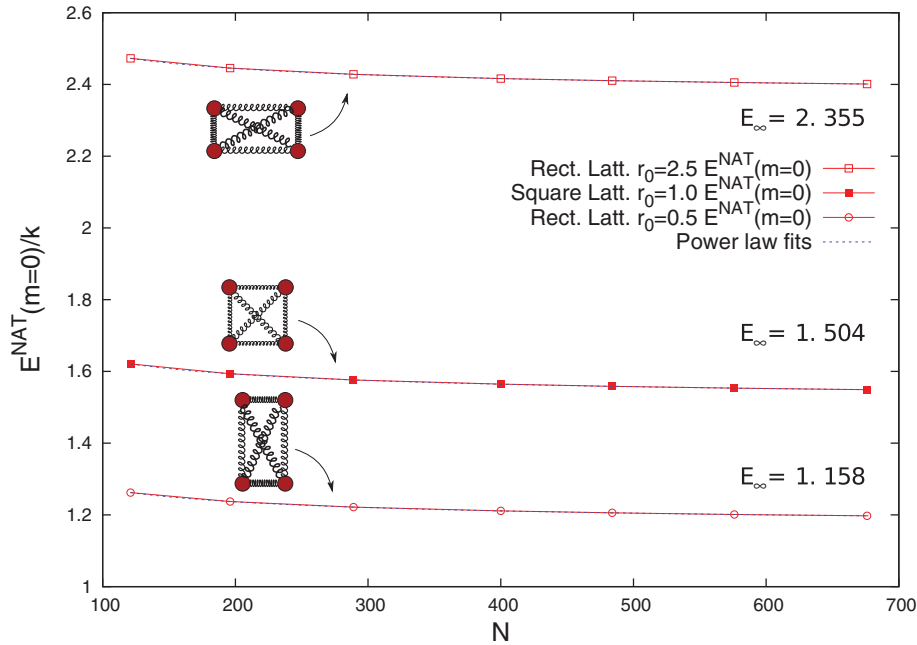


FIG. 3.  $E^{\text{NAT}}(m=0)/k$  for different rectangular lattices increasing the number of particles  $N$ . Fits with a power law of the form  $E_N/k = E_\infty + \alpha N^\beta$  show a convergence towards the finite values indicated in the figure, while the values predicted by Eq. (4) are, (bottom to top curve) 1.154, 1.500, and 2.351. The values of  $\beta$  resulting from the fit are (bottom to top curve)  $-0.56$ ,  $-0.55$ , and  $-0.54$ .  $E^{\text{NAT}}(m \neq 0)/k$  show the same convergence behavior for any  $m$ .

quantities in the deformed state.  $b$  is fixed by the imposed strain, whereas  $h$  adjusts to minimize the energy,  $\partial U/\partial h = 0$ . This model describes, basically, the deformation of a cell in the bulk within an AT framework.

If magnetic effects are neglected, we find that the linear elastic modulus of such a system is

$$E(m=0) \simeq \left. \frac{d^2 U_{el}}{db^2} \right|_{b=b_0} = k \left( 1 + \frac{2r_0^2}{3+r_0^2} \right). \quad (4)$$

Here  $r_0 = b_0/h_0$  is the base-height ratio of the unstrained lattice. Furthermore, we have linearized the  $h(b)$  deformation around  $b = b_0$ .

In the limit of large  $N$ , the elastic modulus determined by NAT should be dominated by bulk behavior. For regular rectangular lattices stretched along the outer edges of the lattice cell, the deformation in the bulk becomes indistinguishable from an affine deformation. We therefore can use our analytical calculation to test whether our systems are large enough to correctly reproduce the elastic modulus of the bulk. For this regular lattice structure, it should correspond to the modulus following from Eq. (4). We calculated numerically  $E^{\text{NAT}}(m=0)$  for different rectangular lattices as a function of  $N$  and plot the results in Fig. 3. Indeed, for large  $N$ , we find the convergence as expected.

From Fig. 3, we observe that the modulus has mostly converged to its large- $N$  limit at  $N = 400$ , therefore most of our calculations are performed for  $N = 400$  particles. We have checked numerically that a similar convergence holds for any investigated choice of  $m$  and lattice structure. For any  $m \neq 0$  that we checked, we found a similar convergence behavior as the one depicted for  $m = 0$  in Fig. 3.

## B. Impact of lattice randomization on AT calculations

We have seen how, in the large- $N$  limit, AT analytical models and NAT numerical calculations converge to the same result in the case of regular rectangular lattices. In fact, we expect AT to be a reasonable approximation in this regular lattice case, since it conserves the initial shape of the lattice. For symmetry reasons, this behavior may be expected also for NAT at small degrees of deformation. But how does AT perform in more realistic and disordered cases where the initial particle distribution can be irregular? To answer this question we will consider the difference  $E^{\text{AT}} - E^{\text{NAT}}$ , the elastic modulus numerically calculated with AT and NAT, at  $m = 0$ , for different and increasingly randomized lattices.

We have considered a rectangular lattice with diagonal springs, a hexagonal lattice with horizontal rows of nearest neighbor springs, one with vertical rows, and a honeycomb lattice with springs beyond nearest neighbors (as depicted in Fig. 4).

To obtain the randomized lattices, we start from their regular counterparts and randomly move each particle within a square box of edge length  $\bar{\eta}$  and centered in the regular lattice site. We call  $\bar{\eta}$  the randomization parameter used to quantify the degree of randomization. In our numerical calculations, we increased  $\bar{\eta}$  up to  $\bar{\eta} = 0.375l_0$ . This is an appreciable degree of randomization considering that at  $\bar{\eta} = l_0$  two nearest neighbors in a square lattice may end up at the same location. To average over different realizations of the randomized lattices, we have performed 100 numerical runs for every initial regular lattice and every chosen value of  $\bar{\eta}$ . In Fig. 4, we plot the relative difference between  $E^{\text{AT}}$  and  $E^{\text{NAT}}$ .

Already for the regular lattices of vanishing randomization  $\bar{\eta} = 0$ , we find a relative deviation of  $E^{\text{AT}}$  from  $E^{\text{NAT}}$  in

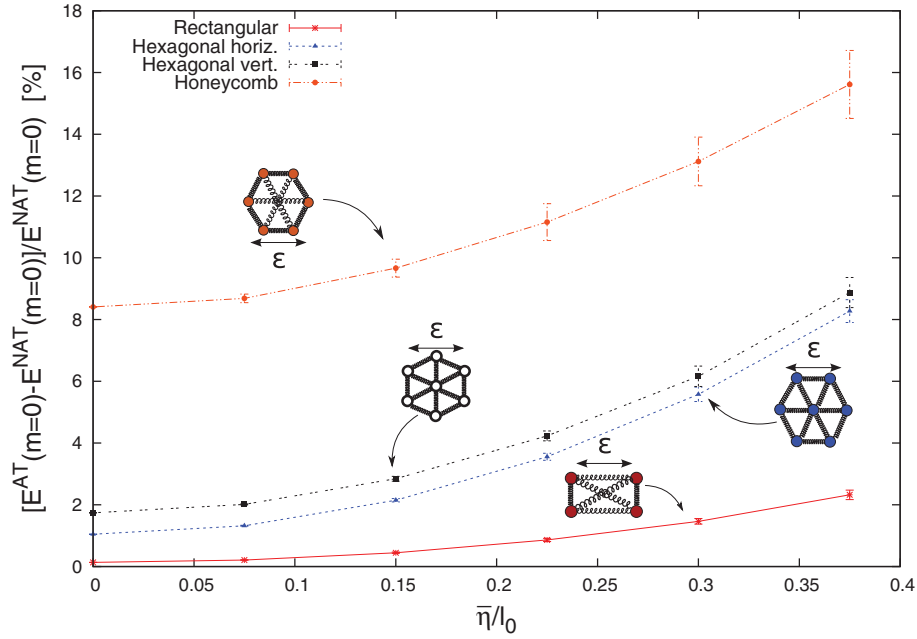


FIG. 4. Different lattices for  $m = 0$  with the initial unstrained state randomized by displacing each particle by  $(\eta_1, \eta_2)$ , where  $\eta_1, \eta_2$  are stochastic variables uniformly distributed in  $[-\bar{\eta}/2, \bar{\eta}/2]$ . Each point in this figure is obtained averaging over 100 different realizations of random distributions generated from the same starting regular lattice. Error bars were obtained from the resulting standard deviation. We indicate the direction of the applied strain by the double arrow marked by  $\epsilon$ . The difference in  $E(m = 0)$  calculated on the one hand by AT and on the other hand by NAT is plotted in % of  $E^{\text{NAT}}(m = 0)$  as a function of an increasing randomization parameter  $\bar{\eta}$ .

the one-digit per-cent regime. This deviation is smallest for the regular rectangular lattice, where the principal stretching directions are parallel to the nearest-neighbor bond vectors. The deviation for  $\bar{\eta} = 0$  increases when we consider instead the hexagonal and honeycomb lattices. Obviously, and this is our main point here, the relative difference between  $E^{\text{AT}}$  and  $E^{\text{NAT}}$  increases for each lattice that we investigated with the degree of randomization  $\bar{\eta}$ . Therefore NAT finds much lower equilibrium states with increasing randomization, and AT leads to erroneous results. So far, however, we could not yet establish a simple rigid criterion that would quantitatively predict the observed differences between AT and NAT.

### C. The case $m \parallel \hat{x}$

We will now consider a non-vanishing magnetic moment  $m \parallel \hat{x}$ . This is parallel to the direction in which we apply the strain in order to measure the elastic modulus. As we will see below, the behavior of the elastic modulus as a function of the magnetic moment  $E(m)$  strongly depends on the orientation of  $m$  and on the lattice structure. The kind of magnetic interaction between nearest neighbors is fundamental for its impact on the elastic modulus. On the one hand, when the magnetic coupling between two particles in  $U_m$  [see Eq. (2)] is solely repulsive, i.e.,  $m \perp r_{ij}$ , its second derivative is positive and therefore gives a positive contribution to the elastic modulus. On the other hand, when  $m \parallel r_{ij}$  the interaction is attractive and the second derivative of  $U_m$  gives a negative contribution to the elastic modulus.

When  $m$  is parallel to the strain direction  $\hat{x}$ , the magnetic interaction along  $\hat{x}$  is attractive and, for  $m$  large enough,

will cause the lattice to shrink and the elastic modulus to decrease. For some cases, though,  $E(m)$  shows an initial increasing trend. This happens when in the unstrained lattice the particles are much closer in  $\hat{y}$  than in  $\hat{x}$ . Then, for small deformations, magnetic repulsion is prevalent and the magnetic contribution to  $E$  is positive, as can be seen for the rectangular case from Fig. 5.

The total energy of the system is the sum of elastic and magnetic energies. Since the derivative is a linear operator, the elastic modulus can be decomposed in elastic and magnetic components:  $E = E_{el} + E_m$ . The analytical calculation for the minimal rectangular system described in Subsection IV A applied to this configuration and considering magnetic interaction up to nearest neighbors only predicts that

$$E_m \simeq \left. \frac{d^2 U_m}{db^2} \right|_{b=b_0} = \frac{12m^2}{b_0^5} \left( -2 + \frac{4r_0^7}{(3+r_0^2)^2} \right) \quad (5)$$

in the rectangular case.

From Eq. (5), we expect a magnetic contribution to the total elastic modulus increasing with  $m$  for  $r_0 \geq 1.175$  and decreasing with  $m$  for  $r_0 \leq 1.175$ . Qualitatively we observe this trend for  $m/m_0 \ll 1$  in Fig. 5. However, it seems that the initial trend for  $E(m)$ , i.e., close to the unstrained state, switches from increasing to decreasing around  $r_0 \simeq 1.60$ , higher than we expected. Although the minimal analytical model can predict the existence of a threshold value for  $r_0$  it would need the magnetic contribution of more than only nearest neighbor particles to be more accurate, since the magnetic interaction is long ranged (whereas the elastic interaction acts only on nearest neighbors).

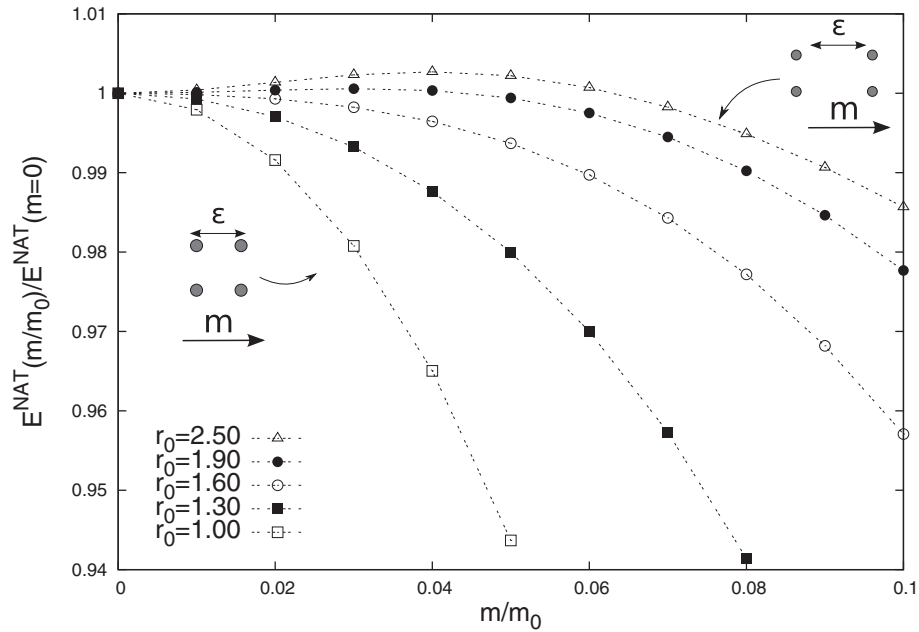


FIG. 5. Rectangular lattice with  $m \parallel \hat{x}$ . Different trends of  $E^{\text{NAT}}(m/m_0)$  are shown for different unstrained lattice shapes using the undeformed base-height ratio  $r_0$  as shape parameter. We indicate the direction of the applied strain by  $\varepsilon$ . To compare and enhance the different trends,  $E^{\text{NAT}}(m/m_0)$  is rescaled by  $E^{\text{NAT}}(m=0)$ .

#### D. The case $m \parallel \hat{y}$

In this orientation of the magnetic moment, the hexagonal lattice case is exemplary, because it shows very well the orientational structural dependence of  $E(m)$ .

On the one hand, for the hexagonal lattice “horizontally” oriented (see the bottom inset in Fig. 6) there are no nearest neighbors in the attractive direction  $\hat{y}$ ; there are instead two along  $\hat{x}$  whose interaction is purely repulsive, therefore the

second derivative of their interaction  $U_m$  is positive. On the other hand, for the same lattice rotated by  $\pi/2$  (see the top inset in Fig. 6) there are two nearest neighbors in the direction of  $m$  and their interaction is strongly attractive; therefore, the second derivative of their interaction  $U_m$  is negative.

The result, as can be seen in Fig. 6, is that in the former case the elastic modulus is increasing and in the latter is decreasing.

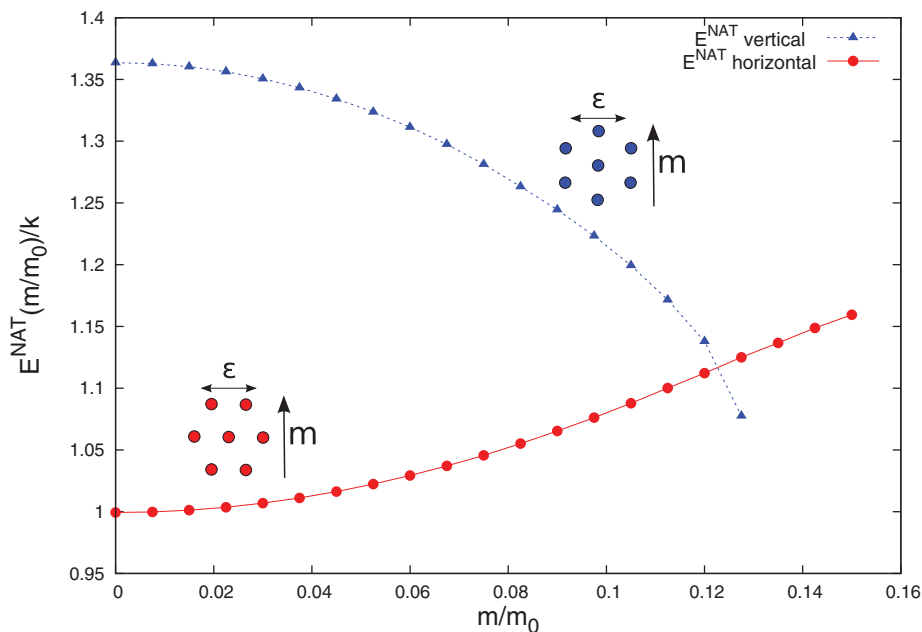


FIG. 6. Hexagonal lattice with  $m \parallel \hat{y}$  for a hexagonal lattice with horizontal rows (bottom inset, where two nearest neighbors are oriented along  $\hat{x}$ ) and for one with vertical rows (top inset, where two nearest neighbors are oriented along  $\hat{y}$ ). We indicate the direction of the applied strain by  $\varepsilon$ . It is remarkable how the magnetic interaction between nearest neighbors and the  $E^{\text{NAT}}(m)$  behavior change when the lattice is rotated by  $\pi/2$ .

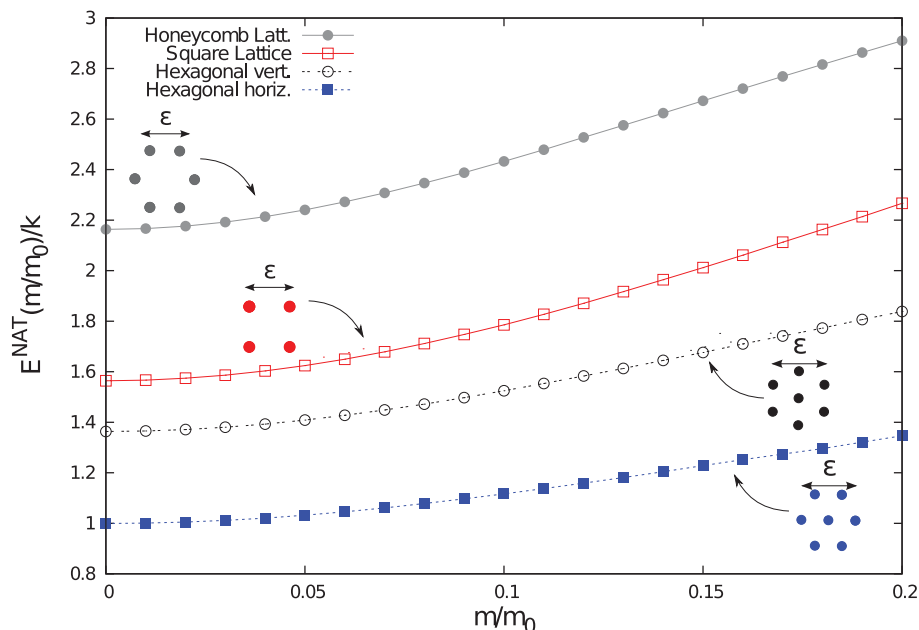


FIG. 7. Elastic modulus  $E(m/m_0)/k$  calculated with NAT for  $m \parallel \hat{z}$  for the different lattices shown. We indicate the direction of the applied strain by  $\epsilon$ . The magnetic interaction is purely repulsive and strengthens the elastic modulus in this configuration.

### E. The case $m \parallel \hat{z}$

In this configuration, the magnetic interactions between our particles are all repulsive and have the form  $m^2/r_{ij}^3$ . The second derivative of the magnetic interparticle energy is always positive along the direction connecting the particles. Therefore, we expect the elastic modulus to be enhanced with increasing  $m$ , and  $E(m)$  to be a monotonically increasing function. As can be seen from Fig. 7, this is true for all the different lattices we have considered.

We have already seen in Fig. 4 how the randomization of the lattice seriously affects the difference between AT and NAT. For the  $m \parallel \hat{z}$  case, we have also considered a real particle distribution taken from an experimental sample.<sup>50</sup> The real sample was of cylindrical shape with a diameter of about 3 cm. It had the magnetic particles arranged in chain-like aggregates parallel to the cylinder axis and spanning the whole sample. The positions of the particles were obtained through X-ray micro-tomography and subsequent image analysis. We extracted the data from a circular cross-section taken approximately at half height of the cylinder and shown in Fig. 8. In this way we consider by our model the physics of one cross-sectional plane of the cylindrical sample.

The extracted lattice was used as an input for our dipole-spring model. We placed a magnetic particle at the center of each identified spot in the tomographic image, see Fig. 8. Guided by the situation in the real sample, the magnetic moments of the particles are chosen perpendicular to the plane (i.e., “along the cylinder axis”). The springs in the resulting lattice are set using Delaunay triangulation<sup>51,57,58</sup> with the particles at the vertices of the triangles and the springs placed at their edges. Then, we cut a square block from the center of the sample containing the desired number of particles. The clamped particles are chosen in such a way that they cover about 10% of the total area (see left inset in Fig. 9).

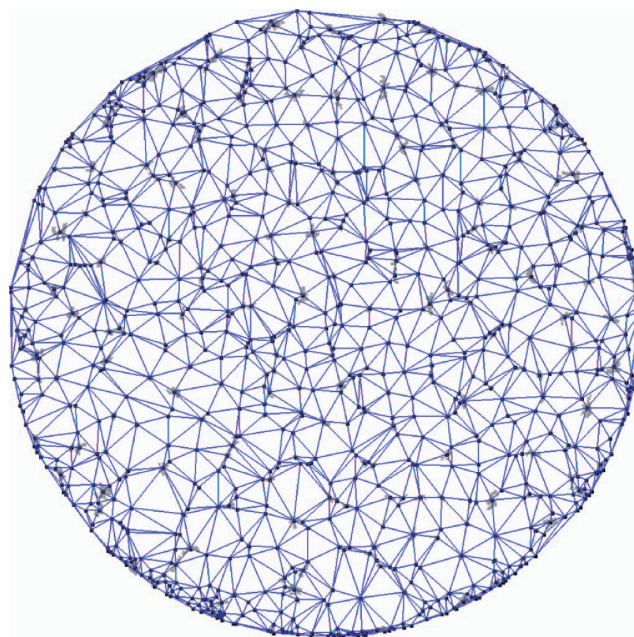


FIG. 8. Realistic lattice used to determine the elastic modulus as a function of the magnetic interactions in the case  $m \parallel \hat{z}$ . The lattice was determined from an X-ray micro-tomographic image of a real experimental sample<sup>50</sup> in the following way. The sample was of cylindrical shape with a diameter of approximately 3 cm. We show a cross-sectional cut through the sample at intermediate height. Inside the sample, the magnetic particles formed chains parallel to the cylinder axis, i.e., perpendicular to the depicted plane. The average size of the particles was around  $35 \mu\text{m}$ . Gray areas correspond to the tomographic spots generated by the magnetic particles in the sample and were identified by image analysis. In our model, we then used the centers of these spots, marked by the black boxes, as lattice sites. One magnetic particle was placed on each lattice site. Then the whole plane was tessellated by Delaunay triangulation with the particle positions at the vertices of the resulting triangles. Elastic springs were set along the edges of the triangles. The micro-tomography data (see Fig. 5 ( $H=3 \text{ mm}$ ) in Ref. 50) are reproduced with permission from Gunther *et al.*, Smart Mater. Struct. **21**, 015005 (2012). Copyright 2012 by IOP Publishing.

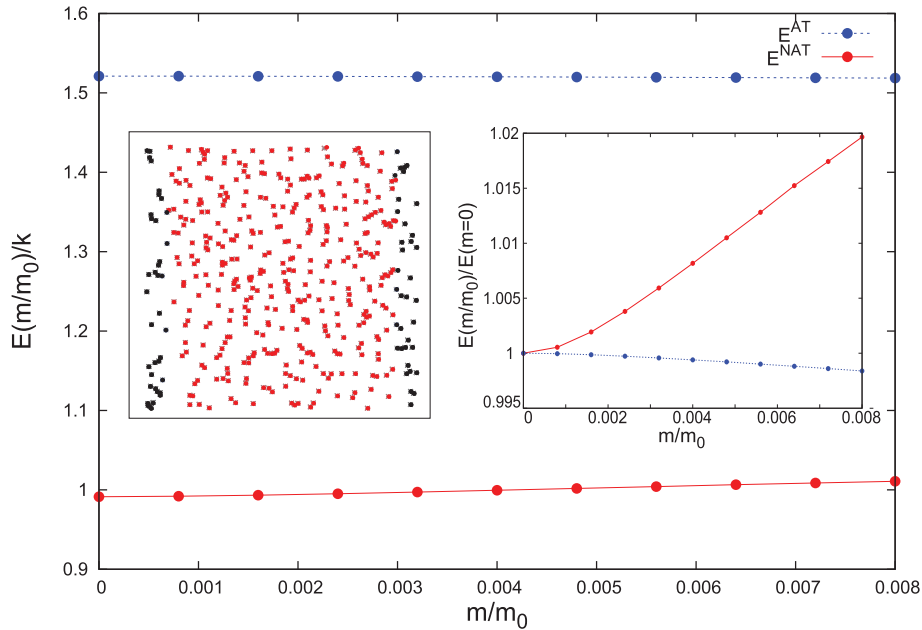


FIG. 9. Elastic modulus  $E(m/m_0)/k$  calculated for  $\mathbf{m} \parallel \hat{z}$  with NAT and AT techniques for the experimental lattice drawn in the left inset. Black dots represent clamped particles. Besides considerably overestimating the elastic modulus,  $E^{\text{AT}}(m/m_0)/k$  shows a flat/decreasing behavior, whereas  $E^{\text{NAT}}(m/m_0)/k$  is correctly increasing. In the right inset, we rescaled  $E(m/m_0)$  by  $E(m=0)$  to better show the two different trends. The numerical error bars are much smaller than the symbol size.

Again we numerically investigate two-dimensional deformations within the resulting two-dimensional layer. If, in the future, this is to be compared to the case of a real sample, the deformations of this sample in the third direction, i.e., the anisotropy direction, have to be suppressed. For instance, the sample could be confined at the base and cover surfaces and compressed along one of the sides. Then it can only extend

along the other side. Thus, within each cross-sectional plane, an overall two-dimensional deformation occurs, with macroscopic deformations suppressed in the anisotropy direction.

As we can see from Fig. 9, in our numerical calculations for this case, AT leads to a serious overestimation of the elastic modulus compared to the one obtained for NAT. Moreover, as can be seen in the right inset of Fig. 9, the former

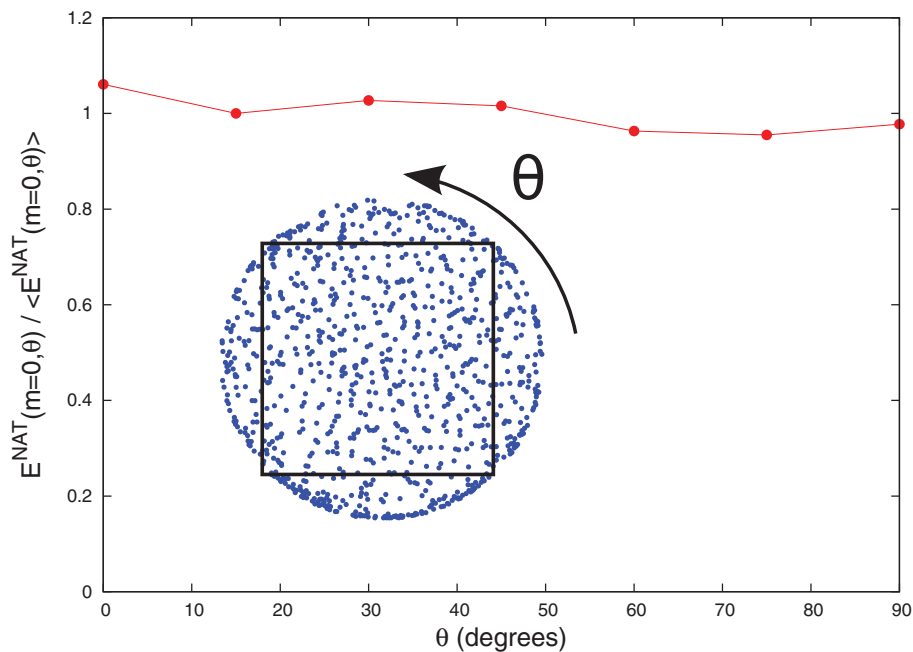


FIG. 10. Zero-field elastic modulus  $E^{\text{NAT}}(m=0)$  calculated with NAT for the experimental lattice drawn in the inset picture varying the rotation angle  $\theta$ . To illustrate the effective isotropy we plot the elastic modulus rescaled by the average of  $E^{\text{NAT}}(m=0)$  over  $\theta$ . The black square in the inset contains the block of particles extracted from the experimental data after the rotation and used in our calculation.

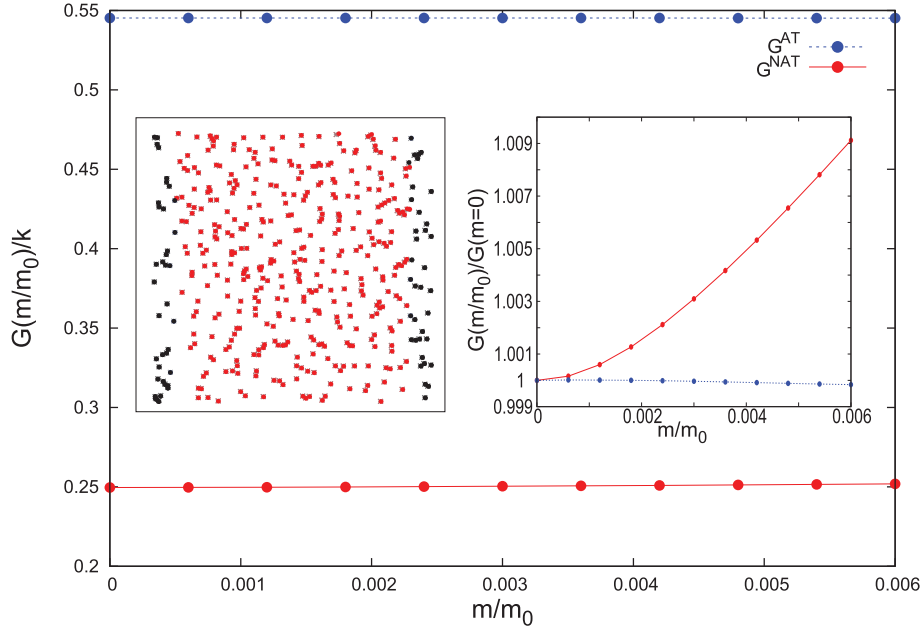


FIG. 11. Shear modulus  $G(m/m_0)/k$  calculated for  $\mathbf{m} \parallel \hat{z}$  with NAT and AT techniques for the experimental lattice drawn in the left inset. Black dots represent clamped particles. Here again, besides considerably overestimating the elastic modulus,  $G^{\text{AT}}(m/m_0)/k$  shows a flat/decreasing behavior, whereas  $G^{\text{NAT}}(m/m_0)/k$  is correctly increasing. In the right inset, we rescaled  $G(m/m_0)$  by  $G(m=0)$  to better show the two different trends. The numerical error bars are much smaller than the symbol size.

predicts an erroneous flat/decreasing trend for  $E(m)$ , whereas the latter shows instead a correct increasing behavior. This result can be interpreted considering that in AT all the particles must move in a prescribed way along each direction. When the particle arrangement is irregular, some couples are very close and some are very distant. The erroneous trend in AT is mainly attributed to the very close particle pairs. AT can force them to still move closer together despite the magnetic repulsion, whereas NAT allows them to avoid such unphysical approaches. Therefore, in order to properly minimize the energy, each particle must be free to adjust position individually with respect to its local environment. As a consequence, for such realistic lattices AT provide erroneous results both quantitatively and qualitatively, making NAT mandatory in most practical cases.

Since within the analyzed two-dimensional cross-sectional layer the particle distribution appears to be rather isotropic, we expect the elastic modulus to be approximately the same in any direction in the plane. To demonstrate this fact, we rotate the configuration in the plane with respect to the stretching direction by different angles  $\theta$  between 0 and  $\pi/2$ . As we can see from Fig. 10, the zero-field elastic modulus  $E(m=0)$  shows only small deviations for the different orientations. The origin of such deviations is ascribed to the square-cutting procedure which, after a rotation by an angle  $\theta$ , produces samples containing different sets of particles, each with different local inhomogeneities in particle distribution and spring orientation. For samples large enough to significantly average over all these different local inhomogeneities, the angular dependence of  $E(m=0)$  should further decrease. We found that for any rotation angle  $\theta$ , the behavior of  $E(m)$  is similar to the one in Fig. 9 corresponding to  $\theta = 0$ , supporting our statement about the erroneous AT result.

## F. Shear modulus

For the set-up described in Subsection IV E (see the left inset of Fig. 9 with  $\mathbf{m} \parallel \hat{z}$ ), we have also calculated the shear modulus  $G(m)$  as a function of the magnetic moment, for both AT and NAT. The shear modulus is defined as the second derivative of the total energy  $U$  with respect to a small displacement  $\delta_y$  of the clamps in  $y$ -direction:

$$G = \frac{d^2U}{d\delta_y^2} \simeq \frac{U(-\delta_y) + U(\delta_y) - 2U(0)}{\delta_y^2}. \quad (6)$$

In this calculation, to allow for the comparison between the results from AT and NAT, all particles within the clamped regions are forced to move in a prescribed (affine) way.

It turns out that the behavior of the shear modulus is qualitatively the same as for the compressive and dilative elastic modulus (see Fig. 11). Again, an incorrect decreasing behavior for the AT calculation is obtained. In numbers, the relative difference between the AT and NAT results is larger than for the compressive and dilative elastic modulus. Here we set  $\delta_y$  as one percent of the dimension of the sample. In Fig. 11, this choice produces numerical error bars much smaller than the symbol size.

## V. CONCLUSIONS

We have shown how the induction of aligned magnetic moments can weaken or strengthen the elastic modulus of a ferrogel or magnetic elastomer according to lattice structure and nearest-neighbor orientations. The orientation of nearest neighbors plays a central role. If the vector connecting two nearest neighbors lies parallel to the magnetic moment, they attract each other, the second derivative of their magnetic interaction is negative, and the corresponding contribution to

the total elastic modulus is negative, too. If, instead, the nearest neighbors lie on a direction perpendicular to the magnetic moment, the second derivative of their magnetic interaction is positive and it tends to increase the total elastic modulus. This effect can be seen modifying the nearest-neighbor structure, for instance tuning the shape of a rectangular lattice or rotating a hexagonal lattice. We have also seen how the performance of affine transformations worsens for randomized and more realistic particle distributions, making non-affine transformation calculations mandatory when working with data extracted from experiments.

In the present case, we scaled out the typical particle separation and the elastic constant from the equations to keep the description general. Both quantities are available when real samples are considered. The mean particle distance follows from the average density, while the elastic constant could be connected to the elastic modulus of the polymer matrix.

The dipole-spring system we have considered is a minimal model. We look forward to improving it in different directions. First, we would like to go beyond linear elastic interactions using nonlinear springs, perhaps deriving a realistic interaction potential from experiments or more microscopic simulations. Second, the use of periodic boundary conditions may improve the efficiency of our calculations and give us new insight into the system behavior (although we demonstrated by our study of asymptotic behavior that border effects are negligible in the present set-up). Furthermore, we may include a constant volume constraint, since volume conservation is not rigidly enforced in the present model. To isolate the effects of different lattice structures and the assumption of affine deformations, we here assumed that all magnetic moments are rigidly anchored along one given direction. In a subsequent step, this constraint could be weakened by explicitly implementing the interaction with an external magnetic field or an orientational memory. Finally, to build the bridge to real system modeling, an extension of our calculations to three dimensions is mandatory in most practical cases.

## ACKNOWLEDGMENTS

The authors thank the Deutsche Forschungsgemeinschaft for support of this work through the priority program SPP 1681.

- <sup>1</sup>E. Jarkova, H. Pleiner, H.-W. Müller, and H. R. Brand, *Phys. Rev. E* **68**, 041706 (2003).
- <sup>2</sup>P. M. Ajayan, L. S. Schadler, C. Giannaris, and A. Rubio, *Adv. Mater.* **12**, 750 (2000).
- <sup>3</sup>S. Stankovich, D. A. Dikin, G. H. B. Dommett, K. M. Kohlhaas, E. J. Zimmerman, E. A. Stach, R. D. Piner, S. T. Nguyen, and R. S. Ruoff, *Nature (London)* **442**, 282 (2006).
- <sup>4</sup>S. C. Glotzer and M. J. Solomon, *Nat. Mater.* **6**, 557 (2007).
- <sup>5</sup>J. Yuan, Y. Xu, and A. H. E. Müller, *Chem. Soc. Rev.* **40**, 640 (2011).
- <sup>6</sup>G. Filipcsei, I. Csetneki, A. Szilágyi, and M. Zrínyi, *Adv. Polym. Sci.* **206**, 137 (2007).
- <sup>7</sup>S. H. L. Klapp, *J. Phys.: Condens. Matter* **17**, R525 (2005).
- <sup>8</sup>R. E. Rosensweig, *Ferrohydrodynamics* (Cambridge University Press, Cambridge, 1985).
- <sup>9</sup>S. Odenbach, *Colloid Surf., A* **217**, 171 (2003).
- <sup>10</sup>S. Odenbach, *Magnetoviscous Effects in Ferrofluids* (Springer, Berlin/Heidelberg, 2003).
- <sup>11</sup>B. Huke and M. Lücke, *Rep. Prog. Phys.* **67**, 1731 (2004).
- <sup>12</sup>S. Odenbach, *J. Phys.: Condens. Matter* **16**, R1135 (2004).
- <sup>13</sup>P. Ilg, M. Kröger, and S. Hess, *J. Magn. Magn. Mater.* **289**, 325 (2005).
- <sup>14</sup>J. P. Embs, S. May, C. Wagner, A. V. Kityk, A. Leschhorn, and M. Lücke, *Phys. Rev. E* **73**, 036302 (2006).
- <sup>15</sup>P. Ilg, E. Coquelle, and S. Hess, *J. Phys.: Condens. Matter* **18**, S2757 (2006).
- <sup>16</sup>C. Gollwitzer, G. Matthies, R. Richter, I. Rehberg, and L. Tobiska, *J. Fluid Mech.* **571**, 455 (2007).
- <sup>17</sup>G. Strobl, *The Physics of Polymers* (Springer, Berlin/Heidelberg, 2007).
- <sup>18</sup>M. Zrínyi, L. Barsi, and A. Büki, *J. Chem. Phys.* **104**, 8750 (1996).
- <sup>19</sup>H.-X. Deng, X.-L. Gong, and L.-H. Wang, *Smart Mater. Struct.* **15**, N111 (2006).
- <sup>20</sup>G. V. Stepanov, S. S. Abramchuk, D. A. Grishin, L. V. Nikitin, E. Y. Kramarenko, and A. R. Khokhlov, *Polymer* **48**, 488 (2007).
- <sup>21</sup>X. Guan, X. Dong, and J. Ou, *J. Magn. Magn. Mater.* **320**, 158 (2008).
- <sup>22</sup>H. Böse and R. Röder, *J. Phys.: Conf. Ser.* **149**, 012090 (2009).
- <sup>23</sup>X. Gong, G. Liao, and S. Xuan, *Appl. Phys. Lett.* **100**, 211909 (2012).
- <sup>24</sup>B. A. Evans, B. L. Fiser, W. J. Prins, D. J. Rapp, A. R. Shields, D. R. Glass, and R. Superfine, *J. Magn. Magn. Mater.* **324**, 501 (2012).
- <sup>25</sup>D. Y. Borin, G. V. Stepanov, and S. Odenbach, *J. Phys.: Conf. Ser.* **412**, 012040 (2013).
- <sup>26</sup>K. Zimmermann, V. A. Naletova, I. Zeidis, V. Böhm, and E. Kolev, *J. Phys.: Condens. Matter* **18**, S2973 (2006).
- <sup>27</sup>D. Szabó, G. Szeghy, and M. Zrínyi, *Macromolecules* **31**, 6541 (1998).
- <sup>28</sup>R. V. Ramanujan and L. L. Lao, *Smart Mater. Struct.* **15**, 952 (2006).
- <sup>29</sup>T. L. Sun, X. L. Gong, W. Q. Jiang, J. F. Li, Z. B. Xu, and W. Li, *Polym. Test.* **27**, 520 (2008).
- <sup>30</sup>M. Babincová, D. Leszczynska, P. Sourivong, P. Čičmanec, and P. Babinec, *J. Magn. Magn. Mater.* **225**, 109 (2001).
- <sup>31</sup>L. L. Lao and R. V. Ramanujan, *J. Mater. Sci.: Mater. Med.* **15**, 1061 (2004).
- <sup>32</sup>D. Ivaneiko, V. P. Toshchevikov, M. Saphiannikova, and G. Heinrich, *Macromol. Theor. Simul.* **20**, 411 (2011).
- <sup>33</sup>D. S. Wood and P. J. Camp, *Phys. Rev. E* **83**, 011402 (2011).
- <sup>34</sup>P. J. Camp, *Magnetohydrodynamics* **47**, 123 (2011).
- <sup>35</sup>O. V. Stolbov, Y. L. Raikher, and M. Balasoiu, *Soft Matter* **7**, 8484 (2011).
- <sup>36</sup>D. Ivaneiko, V. Toshchevikov, M. Saphiannikova, and G. Heinrich, *Condens. Matter Phys.* **15**, 33601 (2012).
- <sup>37</sup>R. Weeber, S. Kantorovich, and C. Holm, *Soft Matter* **8**, 9923 (2012).
- <sup>38</sup>A. Y. Zubarev, *Soft Matter* **8**, 3174 (2012).
- <sup>39</sup>A. Y. Zubarev, *Soft Matter* **9**, 4985 (2013).
- <sup>40</sup>A. Zubarev, *Physica A* **392**, 4824 (2013).
- <sup>41</sup>Y. Han, W. Hong, and L. E. Faidley, *Int. J. Solids Struct.* **50**, 2281 (2013).
- <sup>42</sup>D. Ivaneiko, V. Toshchevikov, M. Saphiannikova, and G. Heinrich, *Soft Matter* **10**, 2213 (2014).
- <sup>43</sup>M. A. Annunziata, A. M. Menzel, and H. Löwen, *J. Chem. Phys.* **138**, 204906 (2013).
- <sup>44</sup>C. Garcia, Y. Zhang, F. DiSalvo, and U. Wiesner, *Angew. Chem., Int. Ed.* **42**, 1526 (2003).
- <sup>45</sup>J. Kao, K. Thorckelsson, P. Bai, B. J. Rancatore, and T. Xu, *Chem. Soc. Rev.* **42**, 2654 (2013).
- <sup>46</sup>E. Allahyarov, A. M. Menzel, L. Zhu, and H. Löwen, "Magnetomechanical response of bilayered magnetic elastomers," *Smart Mater. Struct.* (to be published); preprint [arXiv:1406.6412](https://arxiv.org/abs/1406.6412) (2014).
- <sup>47</sup>D. Collin, G. K. Auernhammer, O. Gavot, P. Martinoty, and H. R. Brand, *Macromol. Rapid Commun.* **24**, 737 (2003).
- <sup>48</sup>Z. Varga, J. Fehér, G. Filipcsei, and M. Zrínyi, *Macromol. Symp.* **200**, 93 (2003).
- <sup>49</sup>S. Bohlius, H. R. Brand, and H. Pleiner, *Phys. Rev. E* **70**, 061411 (2004).
- <sup>50</sup>D. Günther, D. Y. Borin, S. Günther, and S. Odenbach, *Smart Mater. Struct.* **21**, 015005 (2012).
- <sup>51</sup>T. Borbáth, S. Günther, D. Y. Borin, T. Gundermann, and S. Odenbach, *Smart Mater. Struct.* **21**, 105018 (2012).
- <sup>52</sup>T. Gundermann, S. Günther, D. Borin, and S. Odenbach, *J. Phys.: Conf. Ser.* **412**, 012027 (2013).
- <sup>53</sup>J. J. Cerdà, P. A. Sánchez, C. Holm, and T. Sintes, *Soft Matter* **9**, 7185 (2013).
- <sup>54</sup>P. A. Sánchez, J. J. Cerdà, T. Sintes, and C. Holm, *J. Chem. Phys.* **139**, 044904 (2013).
- <sup>55</sup>M. R. Hestensens and E. Stiefel, *J. Res. Natl. Bur. Stand.* **49**, 409 (1952).
- <sup>56</sup>J. R. Shewchuk, "An introduction to the conjugate gradient method without the agonizing pain," 1994, see <http://www.cs.cmu.edu/~quake-papers/painless-conjugate-gradient.pdf>.
- <sup>57</sup>B. Delaunay, *Bull. Acad. Sci. URSS. Cl. Sci. Math. Nat.* **6**, 793 (1934).
- <sup>58</sup>S. Pion and M. Teillaud, in *CGAL User and Reference Manual*, 4th ed. (CGAL Editorial Board, 2014), see <http://doc.cgal.org/4.4/Manual/packages.html#PkgTriangulation3Summary>.

# Paper IV Dynamic elastic moduli in magnetic gels: Normal modes and linear response

Reproduced from

Giorgio Pessot, Hartmut Löwen, and Andreas M. Menzel,  
Dynamic elastic moduli in magnetic gels:  
Normal modes and linear response.  
*J. Chem. Phys.*, **145** 104904 (2016), AIP Publishing.

with the permission of *AIP Publishing*. © AIP Publishing. All rights reserved.  
(Version of Record)  
DOI: 10.1063/1.4962365

## Authors' Contributions

All authors contributed to the writing of the manuscript. Hartmut Löwen and Andreas M. Menzel supervised the work. I and Andreas M. Menzel devised the semi-analytical method which I implemented numerically. I estimate my total contribution to this work to approximately 80%.

## Copyright and Permission Informations

From <https://publishing.aip.org/authors/copyright-reuse> :

“AIP Publishing permits authors to include their published articles in a thesis or dissertation.

It is understood that the thesis or dissertation may be published in print and/or electronic form and offered for sale on demand, as well as included in a university's repository. Formal permission from AIP Publishing is not needed.”



# Dynamic elastic moduli in magnetic gels: Normal modes and linear response

Giorgio Pessot,<sup>a)</sup> Hartmut Löwen,<sup>b)</sup> and Andreas M. Menzel<sup>c)</sup>

*Institut für Theoretische Physik II: Weiche Materie, Heinrich-Heine-Universität Düsseldorf,  
D-40225 Düsseldorf, Germany*

(Received 28 June 2016; accepted 26 August 2016; published online 14 September 2016)

In the perspective of developing smart hybrid materials with customized features, ferrogels and magnetorheological elastomers allow a synergy of elasticity and magnetism. The interplay between elastic and magnetic properties gives rise to a unique reversible control of the material behavior by applying an external magnetic field. Albeit few works have been performed on the time-dependent properties so far, understanding the dynamic behavior is the key to model many practical situations, e.g., applications as vibration absorbers. Here we present a way to calculate the frequency-dependent elastic moduli based on the decomposition of the linear response to an external stress in normal modes. We use a minimal three-dimensional dipole-spring model to theoretically describe the magnetic and elastic interactions on the mesoscopic level. Specifically, the magnetic particles carry permanent magnetic dipole moments and are spatially arranged in a prescribed way, before they are linked by elastic springs. An external magnetic field aligns the magnetic moments. On the one hand, we study regular lattice-like particle arrangements to compare with previous results in the literature. On the other hand, we calculate the dynamic elastic moduli for irregular, more realistic particle distributions. Our approach measures the tunability of the linear dynamic response as a function of the particle arrangement, the system orientation with respect to the external magnetic field, as well as the magnitude of the magnetic interaction between the particles. The strength of the present approach is that it explicitly connects the relaxational modes of the system with the rheological properties as well as with the internal rearrangement of the particles in the sample, providing new insight into the dynamics of these remarkable materials. *Published by AIP Publishing.* [<http://dx.doi.org/10.1063/1.4962365>]

## I. INTRODUCTION

The class of smart hybrid materials encompassing ferrogels and magnetorheological elastomers stands out for its unique capability of combining magnetic properties with huge elastic deformability.<sup>1–4</sup> They typically consist of a permanently crosslinked polymer matrix in which magnetic colloidal particles are embedded. The matrix is responsible for the elastic behavior typical of rubbers, while the particles magnetically interact with each other and with external magnetic fields. These materials distinguish themselves by the fascinating ability of reversible on-demand tunability of shape and stiffness under the influence of external magnetic fields,<sup>1,2,4–12</sup> similarly to the tunability of viscosity in ferrofluids.<sup>13–23</sup> This makes them ideal candidates for applications such as soft actuators,<sup>24</sup> vibration absorbers,<sup>25,26</sup> magnetic field detectors,<sup>27,28</sup> and even as model systems to study aspects of hyperthermal cancer treatment.<sup>29,30</sup>

The core feature of these materials is their magneto-mechanical coupling,<sup>31–33</sup> i.e., the way magnetic effects such as the response to an external magnetic field couple

to the overall mechanical properties (e.g., strain or elastic moduli) and vice versa. As was recently shown, such coupling is responsible for surprising properties such as superelasticity,<sup>34</sup> a characteristic buckling of chains of particles under a perpendicular external magnetic field,<sup>35</sup> qualitative reversal of the strain response,<sup>32</sup> volume changes due to mesoscopic wrapping effects,<sup>36</sup> or tunability of the electrical resistance.<sup>37</sup> There are several key factors that can influence the magneto-mechanical coupling: the magnetic particle concentration,<sup>1,38,39</sup> the stiffness of the gel,<sup>40</sup> or whether the magnetic moments of the particles can freely reorient or must instead rotate synchronously with the whole particle.<sup>2,41</sup> The particles can be chemically bound to the polymer network<sup>31,42,43</sup> or be confined inside pockets of the matrix.<sup>44,45</sup> Moreover, the magnetic material itself can either be ferro-<sup>43</sup> or (super)paramagnetic.<sup>46</sup>

Because of the variety of factors and parameters that can characterize ferrogels and magnetic elastomers, it is no surprise that they are receiving increasing attention from the modeling side. In fact, gaining insight into the mechanisms underlying the magneto-mechanical coupling can be the key to devise smarter and more efficient materials. Macroscopic theories rely on a continuum-mechanical description of both the polymeric matrix and the magnetic component,<sup>5,27,32,47–50</sup> whereas mesoscopic approaches can take into account the granularity and discreteness of the magnetic particles.<sup>34,51–53</sup>

<sup>a)</sup>Electronic address: [giorgpess@thphy.uni-duesseldorf.de](mailto:giorgpess@thphy.uni-duesseldorf.de)

<sup>b)</sup>Electronic address: [hlowen@thphy.uni-duesseldorf.de](mailto:hlowen@thphy.uni-duesseldorf.de)

<sup>c)</sup>Electronic address: [menzel@thphy.uni-duesseldorf.de](mailto:menzel@thphy.uni-duesseldorf.de)

On this mesoscopic level, simplified dipole-spring models represent a convenient approach to address effects originating on the magnetic particle level. More precisely, in such models the particles carry a dipole magnetic moment and are linked with each other by a network of elastic springs. Additionally, steric repulsion and other effects like orientational memory terms can be included.<sup>54–59</sup> Finite-element descriptions are likewise employed to address mesoscopic particle-based effects,<sup>10,33,60–63</sup> and some works even resolve the individual polymers on the microscopic scale.<sup>41,64</sup> Moreover, in a coarse-graining perspective, some routes have been outlined to connect the different length scales listed above.<sup>65,66</sup>

Often in material science, one aims at determining the material parameters that characterize the system. Fundamental quantities to describe the time-dependent mechanical behavior are the dynamic elastic moduli. They, for instance, contain the information on the frequency-dependent stress response to imposed time-periodic deformations. In the case of ferrogels and magnetic elastomers only few theoretical studies have so far addressed the dynamic properties in special cases.<sup>56,59,67</sup> In the present work we aim at calculating the dynamic (i.e., frequency-dependent) elastic moduli of ferrogels. We use a minimal three-dimensional (3D) dipole-spring model with short-ranged steric repulsion between the magnetic particles. Moreover, we consider the system around its equilibrium state of minimum total energy. Overdamped motion of the particles is assumed, which is in general a reasonable assumption for colloidal polymeric systems. We focus on regular and more disordered particle arrangements of finite size with open boundary conditions (obc). In our particle-based approach this simply refers to a detached finite assembly of particles. This system is bounded in all three directions of space, in contrast to periodic boundary conditions (pbc). We describe a semi-analytical approach using a simple, direct connection between the normal modes of the system and the linear response to an oscillating external stress.

The paper is structured as follows. First, in Section II we present our minimal dipole-spring model including steric repulsion. To find the equilibrium configurations under magnetic interactions, we use the methods as described in Section III. Then, in Section IV, we determine the normal modes and in Section V we connect them to the static linear elastic response of the system. After that, in Section VI, we address the dynamic behavior of our system and show how to decompose it into the normal modes. In Section VII, we extend the elastic moduli expressions obtained in Section V to the dynamical case and show the corresponding numerical results in Sections VIII, IX, and X before drawing our final conclusions in Section XI. Appendix A lists the specific expressions used in modeling the steric repulsion, whereas Appendices B and C list in detail the employed expressions for gradients and Hessian matrices. Appendix D describes in detail our procedure of obtaining a torque-free force field. In Appendix E we analytically estimate the Young moduli of regular lattices for comparison with our numerical results. Last, in Appendix F we present further data on the loss components of the dynamic moduli, supporting our results in the main text.

## II. DIPOLE-SPRING MODEL

For simplicity we here work with a minimal 3D dipole-spring model. On the one hand, as a first approximation, we represent the magnetic moments by permanent point dipoles of constant magnitude. Possible magnetic contributions due to the finite extension of the magnetic particles are not considered. This is a valid approach for interparticle distances larger than the particle size (i.e., at low densities).<sup>68</sup> In a simplified manner, spatial variations in dipole orientations and magnitudes due to their mutual feedback could be included in a subsequent step, see Ref. 69. On the other hand, the interaction between the mesoscopic particles mediated by the polymeric matrix is, in general, non-linear.<sup>66</sup> However, since we are mainly interested in the linear elastic moduli for small displacements around the equilibrium positions of the particles, we confine ourselves to harmonic interactions in the present study.

Our system is made of  $N$  identical spherical magnetic particles with positions  $\mathbf{R}_i = (R_i^x, R_i^y, R_i^z)$ ,  $i = 1 \dots N$ . To model the overdamped dynamics of the system, we consider viscous drag forces  $-c\dot{\mathbf{R}}_i$  during particle displacements, where the dot indicates the time derivative. Each particle carries an identical magnetic dipole moment  $\mathbf{m}$  of magnitude  $m = |\mathbf{m}|$ . This situation reflects, for instance, the case of ferromagnetic or superparamagnetic particles under strong external magnetic fields. Neighboring particles  $i$  and  $j$  are coupled by harmonic springs attached to the particle centers for simplicity. The unstrained spring length  $\ell_{ij}^0$  is set in the initial ground state particle configuration in the absence of any magnetic interactions, while the spring constants are given by  $k/\ell_{ij}^0$ . Thus,  $k$  is related to the overall elastic modulus of the system and long springs are weakened when compared to short ones. We assume the polymeric matrix—here represented by the network of springs—to have vanishing magnetic susceptibility and therefore not to directly interact with magnetic fields. If magnetic particles come too close to each other, they interact sterically.

The total energy  $U$  of the system is the sum of elastic  $U^{el}$ , steric  $U^s$ , and magnetic  $U^m$  energies.<sup>54,55,57,58</sup> Elastic interactions are given by

$$U^{el} = \frac{1}{2} \sum_{i \neq j} \frac{k_{ij}}{2} (r_{ij} - \ell_{ij}^0)^2, \quad (1)$$

where the sum runs over all particles  $i$  and  $j \neq i$ . Moreover,  $k_{ij} = k/\ell_{ij}^0$  if particles  $i$  and  $j$  are connected by a spring and vanishes otherwise. Furthermore,  $\mathbf{r}_{ij} = \mathbf{R}_j - \mathbf{R}_i$  and  $r_{ij} = |\mathbf{r}_{ij}|$ .

We model the steric interactions using a repulsive potential inspired by the Weeks-Chandler-Andersen form<sup>70</sup> but with different exponents. For instance, possibly absorbed polymer chains on the surfaces of the particles<sup>35</sup> could result in a softer repulsion. Our steric potential reads

$$U^s = \frac{1}{2} \sum_{i \neq j} v^s(r_{ij}), \quad (2)$$

where

$$v^s(r) = \varepsilon^s \left[ \left( \frac{r}{\sigma^s} \right)^{-4} - \left( \frac{r}{\sigma^s} \right)^{-2} - \left( \frac{r_c}{\sigma^s} \right)^{-4} + \left( \frac{r_c}{\sigma^s} \right)^{-2} + c^s \frac{(r - r_c)^2}{2} \right] \quad (3)$$

for  $r \leq r_c$  and zero otherwise. Here,  $\varepsilon^s$  sets the strength of the steric repulsion,  $\sigma^s$  characterizes the range of steric repulsion, and  $r_c = \sigma^s 2^{1/2}$  is a cutoff distance. The parameter  $c^s$  is chosen such that altogether we have  $v^s(r_c) = 0$ ,  $v^{s'}(r_c) = 0$ , and  $v^{s''}(r_c) = 0$  (see Appendix A).

Finally, the magnetic energy is given by the dipole–dipole interaction

$$U^m = \frac{\mu_0 m^2}{4\pi} \frac{1}{2} \sum_{i \neq j} \frac{r_{ij}^2 - 3(\hat{\mathbf{m}} \cdot \mathbf{r}_{ij})^2}{r_{ij}^5}, \quad (4)$$

where  $\hat{\mathbf{m}} = \mathbf{m}/m$  and  $\mu_0$  is the magnetic permeability of vacuum. In the present work, we use reduced units as follows: lengths are given in multiples of  $l_0$ , energies in multiples of  $kl_0$ . The length  $l_0$  is defined as  $l_0 = \sqrt[3]{1/\rho}$  where  $\rho$  is the number density of the particles. Furthermore, we measure magnetic moments, velocities, and frequencies in multiples of  $m_0 = \sqrt{4\pi k l_0^4 / \mu_0}$ ,  $k/c$ , and  $k/cl_0$ , respectively, with  $c$  setting the viscous friction coefficient of each particle. (There is a typo in the definition of  $m_0$  in Ref. 55: it should read  $m_0 = \sqrt{4\pi k l_0^5 / \mu_0}$  instead of  $m_0 = \sqrt{4\pi k^2 l_0^5 / \mu_0}$ .) For our purposes, we assume  $\sigma^s = 0.2l_0$  and  $\varepsilon^s = kl_0$ .

For reasons that will become clear in Section V, it is useful to explicitly define and indicate the boundaries of our system. We here consider samples of cubelike shape with faces perpendicular to  $\hat{\mathbf{x}}$ ,  $\hat{\mathbf{y}}$ , and  $\hat{\mathbf{z}}$ , the unit vectors defining our Cartesian coordinate system. We can define “left” and “right,” “front” and “rear,” as well as “bottom” and “top” boundaries, namely the faces oriented by  $\mp\hat{\mathbf{x}}$ ,  $\mp\hat{\mathbf{y}}$ , and  $\mp\hat{\mathbf{z}}$ , respectively. The criteria to identify which particles belong to the boundaries will be detailed later according to the specific particle distribution. Subsequently, we indicate by  $L_x$ ,  $L_y$ , and  $L_z$  the extension of the sample in the  $x$ -,  $y$ -, and  $z$ -direction, respectively. In the case of cubelike shape and uniform density,  $L_\alpha$  ( $\alpha = x, y, z$ ) will be proportional to  $N^{1/3}l_0$ . Otherwise, an additional geometry-dependent prefactor can be included. Then the scaling of cross-sectional areas (i.e.,  $S_x = L_y L_z$ ) and the volume  $V = L_x L_y L_z$  follow straightforwardly as  $N^{2/3}l_0^2$  and  $Nl_0^3$ , respectively.

### III. EQUILIBRIUM STATE

First, we need to find the equilibrium state of our system, i.e., the one that minimizes the total energy  $U = U^{el} + U^s + U^m$  with respect to all degrees of freedom. In our case the degrees of freedom are given by the positions  $\mathbf{R}_i$ , which requires

$$\partial_{\mathbf{R}_i} U = \mathbf{0}, \quad \forall i = 1 \dots N \quad (5)$$

in equilibrium. From Eqs. (1)–(4) it is straightforward to calculate the resulting gradients (see Appendix B). The second derivatives of the energy  $U$  form the corresponding Hessian matrix, see below. Analytical expressions are listed in Appendices B and C.

We seek the minimum total energy  $U$  of a sample composed of  $N$  particles arranged according to a prescribed distribution, each carrying a prescribed magnetic dipole moment  $\mathbf{m}$ . Consequently, the equilibrium state is obtained as a function of  $\mathbf{m}$ . To ease the convergence of the minimization

techniques, we gradually increase the magnitude of the magnetic moments from  $m = 0$  (ground state) to the required maximum value of  $m$  while minimizing the total energy for each intermediate value of  $m$ . Because of the large number of degrees of freedom, the only practical way to find the equilibrium state is to perform a numerical minimization of the energy. In the present work we implemented a conjugated gradient algorithm with guaranteed descent.<sup>71</sup>

We wish to study the dynamic response of our systems for different orientations while holding  $\mathbf{m}$  fixed in space. However, once the orientation of the magnetic moments is fixed from outside, the system as a whole may start to rigidly rotate to minimize its overall energy. In real samples, such rotations are for instance suppressed by macroscopic frictional and gravitational forces. Moreover, in our previous investigation, this macroscopic rotation was hindered by a “clamping” protocol of the boundaries.<sup>55</sup> Here instead, we develop a new protocol to keep the system in the desired orientation. This is achieved by subtracting from the force field acting on the boundaries those parts corresponding to rigid rotations (see below and Appendix D). This way, three constraints are applied in the form of the suppressed rigid rotations and we otherwise allow a complete internal relaxation of the sample.

### IV. NORMAL MODES

Next, we describe a generic normal mode formalism and explain how it can be employed to characterize the linear response of our systems to a small external perturbation. We do not assume regular, periodic particle distributions. Instead, our formalism can likewise be applied to irregular particle arrangements, see, e.g., Refs. 72–74.

In the following, we indicate with a bra-ket notation  $|\mathbf{X}\rangle$ , the  $D$ -component vector containing all the  $D$  degrees of freedom of the system. In our case,  $D = 3N$  as we only consider translational degrees of freedom, but in principle  $|\mathbf{X}\rangle$  could also include, for instance, particle rotations.

Once we write down the total energy  $U(|\mathbf{X}\rangle)$ , the equilibrium state  $|\mathbf{X}\rangle^{eq}$  is given by the condition

$$\partial_{\mathbf{X}} U(|\mathbf{X}\rangle^{eq}) = \mathbf{0}. \quad (6)$$

It is more convenient to discuss the problem in terms of displacement from equilibrium,  $|\mathbf{u}\rangle = |\mathbf{X}\rangle - |\mathbf{X}\rangle^{eq}$ . Furthermore, it is always possible to shift the energy by a constant so that  $U(|\mathbf{X}\rangle^{eq}) = 0$ . Around its minimum, we can expand  $U(|\mathbf{X}\rangle)$  to lowest order in the displacement  $|\mathbf{u}\rangle$ ,

$$U(|\mathbf{u}\rangle) \simeq \frac{1}{2} \langle \mathbf{u} | \mathcal{H} | \mathbf{u} \rangle, \quad \text{with } \mathcal{H}_{ij} = \partial_{u_i} \partial_{u_j} U. \quad (7)$$

Here,  $\mathcal{H}$  is the Hessian matrix composed of the second derivatives of  $U$  with respect to  $|\mathbf{u}\rangle$  (see Appendices B and C). If  $U(|\mathbf{X}\rangle)$  has continuous second partial derivatives, then  $\mathcal{H}$  is symmetric. Moreover, being in a minimum of  $U(|\mathbf{X}\rangle)$  implies that  $\mathcal{H}$  is positive-semidefinite. All its eigenvalues are positive, except for the modes representing rigid translations and rotations, which cost no energy and have vanishing eigenvalues.

We obtain the linearized gradient around the minimum from Eq. (7) as

$$\partial_{\mathbf{u}}U(|\mathbf{u}\rangle) \simeq \mathcal{H}|\mathbf{u}\rangle. \quad (8)$$

When a small external force  $|\mathbf{f}\rangle$  is applied, the system reacts to neutralize it and re-equilibrates

$$-\partial_{\mathbf{u}}U(|\mathbf{u}\rangle) + |\mathbf{f}\rangle = 0 \Rightarrow \mathcal{H}|\mathbf{u}\rangle \simeq |\mathbf{f}\rangle. \quad (9)$$

In Eq. (9) we have used Eq. (8), which is justified for small  $|\mathbf{f}\rangle$ . We diagonalize  $\mathcal{H}$  and introduce its eigenvalues  $\lambda_n$  and eigenvectors, i.e., the normal modes  $|\mathbf{v}_n\rangle$  with  $n = 1 \dots D$  and  $D$  the number of degrees of freedom, such that

$$\mathcal{H}|\mathbf{v}_n\rangle = \lambda_n|\mathbf{v}_n\rangle, \text{ and } \langle\mathbf{v}_m|\mathbf{v}_n\rangle = \delta_{mn}, \quad (10)$$

where  $\delta_{mn}$  is the Kronecker delta. Since the  $|\mathbf{v}_n\rangle$  form a complete basis, we can expand displacements and forces as

$$|\mathbf{u}\rangle = \sum_{n=1}^D u_n |\mathbf{v}_n\rangle \text{ and } |\mathbf{f}\rangle = \sum_{n=1}^D f_n |\mathbf{v}_n\rangle. \quad (11)$$

Here,  $u_n = \langle\mathbf{u}|\mathbf{v}_n\rangle$  and  $f_n = \langle\mathbf{f}|\mathbf{v}_n\rangle$ . Then, using these expansions and the orthonormality of the eigenvectors, Eq. (9) simply reduces to

$$\lambda_n u_n = f_n. \quad (12)$$

This relation clearly shows that, under the influence of an external force  $|\mathbf{f}\rangle$  exciting the  $n$ th normal mode, the amplitude  $u_n$  of the response is linearly related to the intensity  $f_n$  of the force. In this perspective, the Hessian eigenvalue  $\lambda_n$  quantifies the magnitude of the static linear response of the system within the  $n$ th mode to the external force.  $\lambda_n$  is therefore a sort of elastic constant. Thus, the energy of the system around its minimum can be written, using Eqs. (7) and (11), and (12), as

$$U = \frac{1}{2} \sum_{n=1}^D \lambda_n u_n^2 = \frac{1}{2} \sum_{n=1}^D \frac{f_n^2}{\lambda_n}. \quad (13)$$

## V. STATIC ELASTIC MODULI FROM NORMAL MODES

In numerical calculations there are two main ways to obtain elastic moduli in the zero-frequency limit, i.e., in the static case. On the one hand, one can perform a finite but small (linear-regime) strain of the whole system, both for pbc<sup>36,75,76</sup> and obc.<sup>55</sup> The system is equilibrated under the prescribed amount of strain. In this way, the moduli are measured from the slope of the resulting stress-strain curve or, equivalently, from the second derivatives of the free energy. On the other hand, when employing pbc and working in thermodynamic equilibrium, one can differentiate the free energy with respect to a macroscopic strain.<sup>75,77,78</sup> As a special case, and in the low-temperature limit, the elastic moduli of a pbc glassy system have recently been examined,<sup>79</sup> whereas the case of regular lattices was discussed under the assumption of affinity in the deformation.<sup>51</sup> However, it is important to remark that affinely mapping the macroscopic strain down to all scales in the system does not allow for internal relaxation<sup>80</sup> and can even lead to qualitatively incorrect results<sup>55</sup> in presence of non-affinity sources.

In the present work we consider the case of a finite system in the ground state neglecting thermal fluctuations

of the mesoscopic particles. The semi-analytical approach that we use to calculate elastic moduli in the linear regime does not require finite macroscopic displacements nor does it assume affinity of the deformation. This method relies on the decomposition of the linear response over the eigenvectors of the Hessian matrix  $\mathcal{H}$ . It reduces the calculation to a problem of linear algebra and gives access to dynamic properties as well, see Sections VI and VII. Physically, our procedure involves using stress instead of strain as an independent variable.

## A. Macroscopic stresses and strains

Below we will focus on Young's modulus  $E$  and the shear modulus  $G$ . They can be defined via the stress-strain relationships

$$\sigma_{\alpha\alpha} = E_{\alpha\alpha} \varepsilon_{\alpha\alpha}, \quad \sigma_{\alpha\beta} = G_{\alpha\beta} \varepsilon_{\alpha\beta}, \quad (14)$$

where  $\sigma_{\alpha\beta}$  ( $\alpha, \beta = x, y, z$ ) denotes the force per area applied in the  $\beta$ -direction acting on the boundary with the surface normal oriented in the  $\alpha$ -direction.  $\varepsilon_{\alpha\beta}$  indicates the corresponding strain deformation, i.e., the total displacement of the boundary in the  $\beta$  direction divided by the distance between the boundaries in the  $\alpha$ -direction. Here, there is no summation over  $\alpha$  and  $\beta$ . In the first formula,  $\alpha$  defines the direction of imposed stretching or compression, along which we evaluate  $E_{\alpha\alpha}$ . In the second formula, the  $\alpha\beta$  plane sets the shear plane within which we evaluate  $G$ , with the shear displacement on the boundaries introduced along the  $\beta$ -direction. Thus, only the faces of the system perpendicular to the  $\alpha$ -direction need to be explicitly addressed to impose our boundary stresses, while the rest of the system is free to relax. This configuration conceptually reproduces an experimental situation in which the sample would be enclosed between the plates of a rheometer with the plates perpendicular to the  $\alpha$ -direction.<sup>81</sup>

Applying during shear only forces oriented tangential to the surface planes typically induces rotations. In experiments, these are hindered by the confining plates. Accordingly, we here suppress such global rotations by subtracting them from the overall response of the system (see below and Appendix D). In this way, we maintain the definition of  $\sigma_{\alpha\beta}$  as above close to the experimental situation and avoid symmetrization typically performed in the context of classical elasticity theory<sup>82</sup> (for a related discussion on anisotropic systems see also Ref. 65).

In the following derivation, we focus on the Young modulus  $E_{\alpha\alpha}$  and drop the  $\alpha\alpha$  subscripts. The calculation for the shear modulus  $G_{\alpha\beta}$  is analogous. Here, stresses and strains in Eq. (14) are interpreted as macroscopic quantities characterizing the overall deformation of the system. We measure them and accordingly define the elastic moduli of the system solely by the stresses on and the displacements of the boundaries perpendicular to  $\hat{\alpha}$ , respectively. The stress is calculated from the ratio between the external force and the surface over which it is applied. Similarly, the strain is obtained by measuring the displacement of the boundaries and dividing by their initial distance.

The energy of a strain deformation is given by the work performed by the stress in the whole volume, i.e., using Eq. (14),

$$U = V \int \sigma \, d\varepsilon = V \frac{E\varepsilon^2}{2} = V \frac{\sigma^2}{2E}. \quad (15)$$

Therefore, the elastic modulus can be derived by differentiating the previous equation,

$$E = \frac{1}{V} \frac{d^2U}{d\varepsilon^2} = V \left[ \frac{d^2U}{d\sigma^2} \right]^{-1}. \quad (16)$$

## B. Mesoscopic stress

Our goal is to connect these macroscopic relations to the mesoscopic level. On the mesoscopic scale, within our linear response framework, it is impractical to use the strain as a variable to impose an external perturbation of the system. Imposing a certain amount of strain by displacing the boundary particles in a prescribed way does not provide any information on the displacement of the bulk particles because the internal relaxation of the system is not known *a priori*. Actually, the rearrangement of the bulk particles mainly determines the reaction of the system and contributes the most to the elastic response. In contrast to that, it is more convenient to use the stress as a variable to impose the external perturbation when we connect the macroscopic to the mesoscopic level. As a matter of fact, we know that an externally imposed mechanical stress leads to nonvanishing external forces on the boundary particles only.

We here describe the macroscopic mechanical stress  $\sigma$  in terms of sets of discretized forces acting directly on the mesoscopic particles. We denote the number of particles on the “left” and “right” boundaries (see Section II) as  $N_l$  and  $N_r$ , respectively. If we indicate by  $S$  the cross-section over which a total external force  $F$  is applied, then we have  $F = \sigma S$ . The corresponding externally imposed discretized mesoscopic force field  $|f\rangle$  acting directly on the particles can then be constructed using the following protocol:

- $|f\rangle$  is non-vanishing only on the boundaries and has components oriented in the stress-direction, see Fig. 1(a).
- The total force  $F$  acting on one boundary must be equal in magnitude to the total force acting on the other boundary. First, we assume all individual forces acting on individual particles on the same boundary to be equal in magnitude. We indicate by  $f_l$  and  $f_r$  those forces acting on a single individual particle on the left or right boundary, respectively. Then the condition reads  $F = N_l f_l = N_r f_r$ , see Fig. 1(b).
- The torque exerted by  $|f\rangle$  on the boundaries must vanish [see Fig. 1(c)]. This can be achieved using the method described in Appendix D. The condition is applied separately to each boundary.
- Finally, we must rescale all forces acting onto one boundary by a common factor so that the forces acting in the stress direction sum up to  $F = \sigma S$  [see Fig. 1(d)]. Again, this condition is applied separately to each boundary.

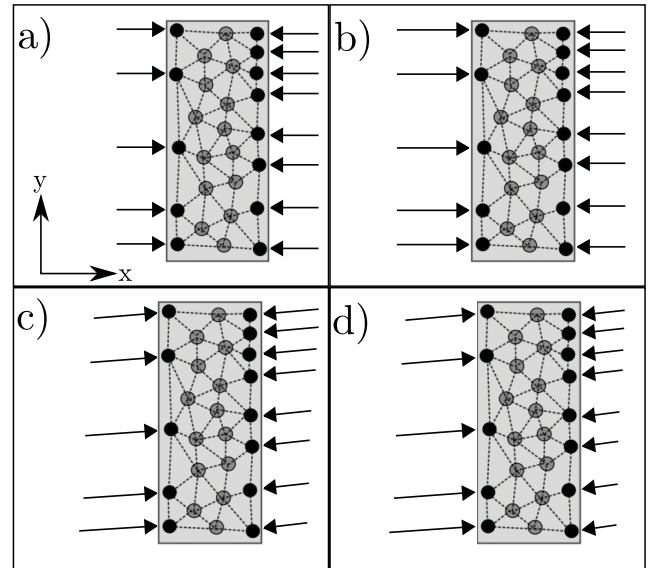


FIG. 1. Protocol to connect a macroscopic stress ( $\sigma_{xx}$ ) acting on the system boundaries to a discretized mesoscopic force field acting on the boundary particles. For simplicity, the case of an irregular two-dimensional (2D) system is shown here. Particles on the boundaries are colored in black and springs are represented by dotted lines. This figure is for illustrative purposes only, therefore lengths and vectors are scaled in a qualitative way. Our procedure is as follows: (a) First, individual discrete forces of equal magnitude are introduced on each individual boundary particle, pointing into the stress-direction (here the  $x$ -direction). (b) The forces are rescaled to balance total forces on the left- and right-hand sides. (c) An appropriate rotatory component is introduced to make the torques vanish on each boundary (separately). (d) All forces on each boundary are rescaled by a common factor so that their sum in the stress-direction is normalized correctly.

These steps serve as a protocol when generating the discretized boundary force field  $|f\rangle$  in numerical calculations. In the following, we factor out  $F$  and write  $|f\rangle = \sigma S |f^u\rangle$ , where  $|f^u\rangle$  is a force field satisfying our requirements and representing a macroscopic force of unitary magnitude ( $F = 1$ ).

## C. Calculation of static elastic moduli

We now have all the ingredients available to formulate the connection between the macroscopic elastic modulus and our discretized mesoscopic normal modes. Following the definition of particle-resolved stress  $\sigma S |f^u\rangle$  that we introduced above, we write the energy in Eq. (13) as an explicit function of  $\sigma$ ,

$$U = \frac{\sigma^2 S^2}{2} \sum_{n=1}^D \frac{f_n^{u2}}{\lambda_n}, \quad \text{with } f_n^u = \langle f^u | v_n \rangle. \quad (17)$$

Combining it with Eq. (16), we obtain

$$E = \frac{L}{S} \left[ \sum_{n=1}^D \frac{f_n^{u2}}{\lambda_n} \right]^{-1}. \quad (18)$$

Here, again,  $S$  is the surface area of the boundary on which the stress acts, while  $L$  is the distance between the two boundaries so that  $LS = V$ .  $\lambda_n$  is the  $n$ th eigenvalue of the Hessian matrix, and  $f_n^u$  is given by Eq. (17). In general,  $S$  and  $L$  will be proportional to  $N^{(d-1)/d} l_0^{d-1}$

and  $N^{1/d}l_0$ , respectively, with  $d$  the spatial dimensionality of the system. Therefore, for 3D particle arrangements of cubelike shape we obtain  $L/S \sim 1/\sqrt[3]{N}l_0$ . In other cases a prefactor must be added, taking into account the shape of the sample or the unit cell structure in the case of regular lattices.

In the following numerical calculations we used the LAPACK diagonalization routines<sup>83</sup> to find eigenvalues and eigenvectors of  $\mathcal{H}$ . Special care must be taken to avoid the zero-energy modes when computing Eq. (18). We here simply ignore contributions from the lowest 3 and 6 eigenvalues when dealing with 2D and 3D systems, respectively. They correspond to rigid translations and rotations of the system.

Overall, we have described a self-standing procedure to calculate elastic moduli in obc systems. The system is required to be in a stable equilibrium state, where the Hessian matrix of the total energy is positive semi-definite. Since the elastic moduli are properties of the ground state, they can be directly obtained via the eigenvalues and eigenvectors calculated in this configuration, see Eq. (18), for a specified force field, see Section V B. Therefore, it is not necessary to actually perform a finite deformation and drive the sample out of equilibrium as, e.g., in Refs. 36, 55, and 76. In Sec. V D we compare the results of our described method with those obtained by explicitly taking a system out of equilibrium via actual boundary displacement.

#### D. Comparison with 2D calculations

The calculation we outlined in Section V C has the advantage of requiring knowledge of only the ground state to obtain all (linear) elastic moduli. Conversely, as we just mentioned, the previously taken path to determine the elastic moduli is to drive the system out of the ground state by prescribing a small amount of strain, determining its deformation, and thereby tracking the total energy variations, see, e.g., Refs. 34, 36, and 55. To test the validity of the present approach, we compare the method described above with the numerical results obtained previously for the 2D case via explicit boundary displacements.<sup>55</sup>

We briefly sum up the technique applied in our former work, see Ref. 55. In that case, a 2D dipole-spring model, similar to the present one but without steric repulsion, is considered. The left and right boundaries of the system are set perpendicular to the  $x$ -direction and undergo a “clamping” protocol, i.e., all the particles in the boundary are constrained to move along  $\hat{x}$  or  $\hat{y}$  in a prescribed way and therefore the whole system undergoes a determined amount of strain  $\varepsilon_{xx}$  or  $\varepsilon_{xy}$ . For every prescribed position of the boundaries, the bulk of the system is free to relax [see Figs. 2(b), 2(d), and 2(f)]. Then, the static Young’s modulus is obtained from the second derivative of the total energy with respect to a small strain in the linear elasticity regime.

Contrarily to the present case, in Ref. 55 we considered springs of identical elastic constant, regardless of the spring length. To allow a better comparison with our former results we will—solely in this subsection—assign an equal elastic constant to all springs, i.e.,  $k_{ij} = k \forall i, j$ . Moreover, for the

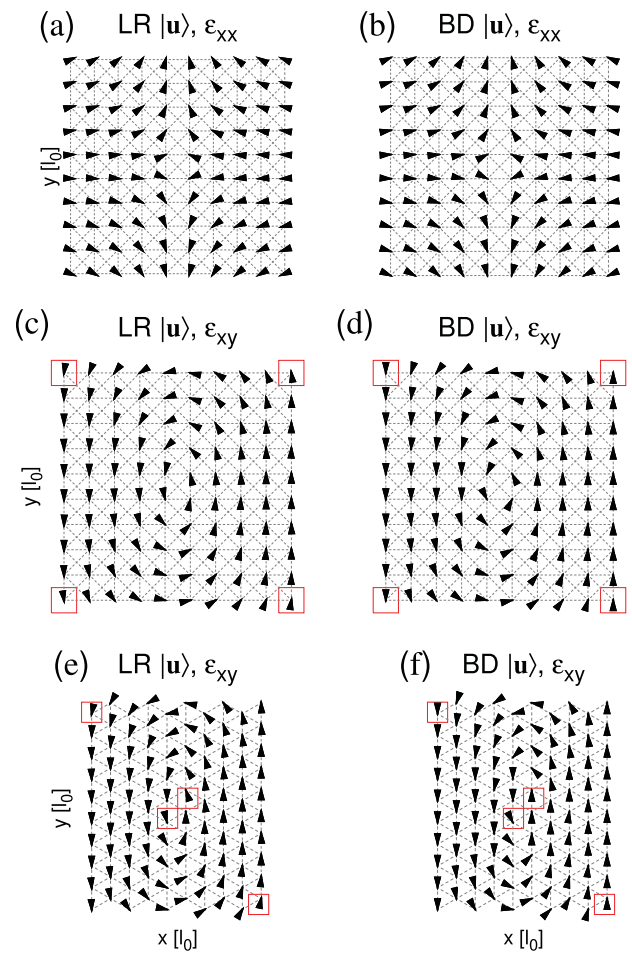


FIG. 2. Non-affine displacement field  $|\mathbf{u}\rangle$  of exemplary square and triangular lattices composed of 100 particles (springs indicated by dashed lines) for  $m=0$  obtained with LR and BD methods [panels (a), (c), (e) and (b), (d), (f), respectively] for stretching/compression  $\varepsilon_{xx}$  and simple shear  $\varepsilon_{xy}$  deformations [panels (a), (b) and (c), (d), (e), (f), respectively]. This simple, exemplary case shows how the responses obtained from the two methods are both non-affine and similar, but can yet present small differences (compare e.g., particles highlighted by red squares), explaining small deviations in the elastic moduli resulting from the two methods, see Fig. 3. Panels (b), (d), (f) were obtained by imposing small (linear-elasticity regime) strains of  $\varepsilon_{xx} = 0.03$  and  $\varepsilon_{xy} = 0.001$ , respectively.

present 2D setup, the elastic moduli will be measured in multiples of  $k$ . In the following, we will address the previous calculations of Ref. 55 as “Boundary Displacement” (BD) and those in the framework of linear response theory of the present work as “Linear Response” (LR).

We first consider the case of a 2D square spring lattice with nonmagnetized ( $m=0$ ) particles on the vertices. On the one hand, and in the BD case, we can apply a prescribed, small amount of strain  $\varepsilon_{xx}$  or  $\varepsilon_{xy}$  and, after full internal energetic relaxation, observe the resulting displacement field  $\text{BD } |\mathbf{u}\rangle$ , see Figs. 2(b), 2(d), and 2(f). On the other hand, and in the present LR scheme, we start from the small mesoscopic force field  $|\mathbf{f}\rangle$  as constructed via the protocol described in Section V B. The corresponding coefficients  $f_n$  are obtained from Eq. (11). Then, using the eigenvalues of the Hessian matrix  $\lambda_n$  as well as Eq. (12), we obtain the response of the modes, i.e., the coefficients  $u_n$ . Finally, using the coefficients  $u_n$ , we obtain via Eq. (11) the particle-resolved displacement  $\text{LR } |\mathbf{u}\rangle$ , which

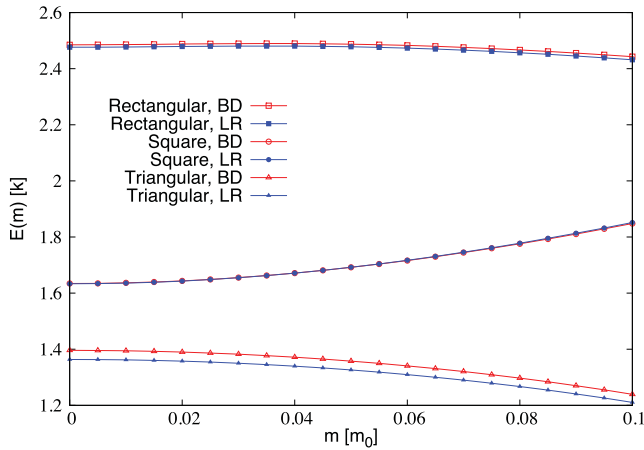


FIG. 3. Young's modulus  $E$  as a function of  $m$  calculated for comparison with BD and LR techniques. Three cases are presented (top to bottom): rectangular lattice of base-height ratio  $b/h=2.5$ , square lattice ( $b/h=1$ ), and triangular lattice [see panels (e) and (f) of Fig. 2] with  $m$  oriented in the  $x$ -,  $z$ -, and  $y$ -direction, respectively. The number of particles in all of the three examples is  $N=400$ . The triangular lattice case shows a comparatively larger difference, which, however, does not depend on  $m$ . We mostly attribute such deviations to the structure of the boundary, as detailed in Figs. 2(e) and 2(f).

is the linear response of the system to the small applied force  $|\mathbf{f}\rangle$ , see Figs. 2(a), 2(c), and 2(e).

The comparison between the resulting displacement fields is helpful to understand where small deviations between the elastic moduli obtained via the two different methods may arise from, see Fig. 3. Overall, the differences remain small, especially in the case of stretching and compression [see Figs. 2(a) and 2(b)]. For shear deformations [see Figs. 2(c) and 2(d)], such discrepancies are visible and reflect small deviations in the resulting moduli. This effect seems to be stressed when the positions of boundary particles are not mirror symmetric with respect to the direction of the calculated modulus, as in the case of the triangular lattice in Figs. 2(e) and 2(f) for Young's modulus in  $x$ -direction. In total, however, we may conclude that our protocol to construct the force field, see Section V B, works well and reproduces the mesoscopic displacement fields previously obtained via BD.

To further test the performance of the present method, we now consider magnetic particles ( $m \neq 0$ ). We compare some of the elastic moduli obtained in Figs. 5–7 of Ref. 55 as functions of  $m$  for a few exemplary cases of regular lattice structures. As shown in Fig. 3, we find the same behavior for  $E(m)$  depending on lattice structure and neighbor orientation. Depending on the particle arrangement, small discrepancies can appear, as explained above. These deviations also seem to depend on the specific shape of the boundaries and are more evident for the case of the triangular lattice in Figs. 2(e) and 2(f). From now on, we will turn back to the more general 3D case.

## VI. DYNAMICS

Because of their often highly viscous character on the mesoscale, soft matter systems in motion typically undergo large dissipation and their dynamics is studied in the

overdamped regime.<sup>36,56,59,84</sup> In the following we describe the time-evolution of our systems, starting from the overdamped equation of motion. Then, a way to decouple the full equation of motion in the normal modes is presented and the general solution for a single mode is shown.

To keep the derivation general, we here take up the notation introduced in Section IV with the difference that now  $|\mathbf{u}\rangle(t)$  and  $|\mathbf{f}\rangle(t)$  depend on time. The full, coupled equation of motion for the overdamped dynamics of the system can be written as

$$C |\dot{\mathbf{u}}\rangle(t) + \mathcal{H} |\mathbf{u}\rangle(t) = |\mathbf{f}\rangle(t), \quad (19)$$

where the dot represents time differentiation, the matrix  $C$  contains the (viscous) friction coefficients, and we have used the linearized version of the gradient  $\mathcal{H} |\mathbf{u}\rangle$  as in Eq. (8). Here, for simplicity and as a first step, we consider the case of mesoscopically isotropic building blocks under negligible long-ranged dynamic coupling, i.e.,  $C = c\mathbb{I}$ , with  $\mathbb{I}$  the  $D \times D$  identity matrix and  $c$  the viscous friction coefficient for one isotropic particle.

As a consequence, the matrices  $C$  and  $\mathcal{H}$  commute and can be simultaneously diagonalized, i.e., they have a common base of eigenvectors, namely the  $|\mathbf{v}_n\rangle$  in Eq. (10). Then, using the normal modes, Eq. (19) of  $D$  variables can be decoupled into  $D$  independent single-variable equations

$$c\dot{u}_n(t) + \lambda_n u_n(t) = f_n(t), \quad (20)$$

with  $n = 1 \dots D$ . If the external force  $|\mathbf{f}\rangle(t)$  is periodic, i.e.,  $|\mathbf{f}\rangle(t) = |\mathbf{f}^0\rangle \exp(i\omega t)$ , its projections onto the Hessian eigenvectors  $|\mathbf{v}_n\rangle$  will be equally periodic,

$$f_n(t) = f_n^0 \exp(i\omega t), \quad (21)$$

with  $f_n^0 = \langle \mathbf{f}^0 | \mathbf{v}_n \rangle$ . Thus, the solution  $u_n(t)$  of Eq. (20) after all transients have decayed must be periodic as well, i.e.,

$$u_n(t) = u_n^0 \exp(i\omega t). \quad (22)$$

Substituting the last equations into Eq. (20), we obtain

$$u_n^0 = f_n^0 / \kappa_n(\omega) \quad (23)$$

with

$$\begin{aligned} \kappa_n(\omega) &= \lambda_n + i c \omega \\ &= e^{i\delta_n(\omega)} \lambda_n \sqrt{1 + \tau_n^2 \omega^2}, \end{aligned} \quad (24)$$

where  $\delta_n(\omega) = \arctan(\tau_n \omega)$ .

In these expressions we introduced by  $\tau_n = c/\lambda_n$  the relaxation time and by  $1/\kappa_n(\omega)$  the dynamic linear response function of the  $n$ th mode.

As described above, we focus on the overdamped dynamics and do not include inertial terms in Eq. (19). If an inertial term had been considered, it would have resulted in a  $(\lambda_n - \bar{m}\omega^2)^2$  term inside the square root of Eq. (24), with  $\bar{m}$  the mass of one particle. Such a contribution would have showed up as a resonance frequency  $\tilde{\omega}_n = \sqrt{\lambda_n/\bar{m}}$  for the  $n$ -th mode. As a consequence, when the frequency of the driving force  $\omega$  coincides with  $\tilde{\omega}_n$ , large displacements can be induced by small external perturbations. Such an effect would result in a significant drop of the elastic moduli at frequencies close

to the resonances of those modes that contribute most to the linear response. This behavior, however, is not obvious from experimental reports,<sup>85–88</sup> thus supporting the overdamped approach. Eq. (24) implies that the displacement  $u_n(t)$ , i.e., the response, chases the driving force  $f_n(t)$  with identical frequency. However, because of viscous friction, it follows with a phase lag  $\delta_n(\omega)$ , which vanishes in the case of frictionless motion. Such a phase lag implies an imaginary component of  $\kappa_n(\omega)$  corresponding to a loss component of the elastic moduli, see below.

## VII. DYNAMIC ELASTIC MODULI

We aim at extending the normal modes treatment that we carried out for Eq. (9) and transfer it to the dynamic situation described by Eq. (19). The final goal will be to generalize Eq. (18) for the macroscopic overall elastic moduli to the case of periodically oscillating external stresses and thus obtain the dynamic elastic macroscopic moduli. We here consider the case of a Young modulus  $E(\omega) = E_{\alpha\alpha}(\omega)$  for direction  $\alpha \in \{x, y, z\}$ . The discussion of a shear modulus  $G_{\alpha\beta}(\omega)$  is entirely analogous, provided that the protocol prescribed in Section V B is followed.

We now start with a macroscopic, periodic, and single-frequency stress

$$\sigma(t) = \sigma^0 e^{i\omega t} \quad (25)$$

applied to the sample, with  $\sigma^0$  a real amplitude. The resulting macroscopic strain  $\varepsilon(t)$  varies with the same frequency. Thus we write

$$\varepsilon(t) = \varepsilon^0(\omega) e^{i\omega t}, \quad (26)$$

where  $\varepsilon^0(\omega)$  is, in general, a complex amplitude. Using these expressions in the single-frequency case, the frequency-dependent dynamic modulus  $E(\omega)$  follows via

$$\sigma(t) = E(\omega)\varepsilon(t) \Leftrightarrow E(\omega) = \frac{\sigma^0}{\varepsilon^0(\omega)}. \quad (27)$$

Thus,  $E(\omega) = E'(\omega) + iE''(\omega)$  has an imaginary part whenever  $\sigma(t)$  and  $\varepsilon(t)$  are not completely in phase and can be divided into storage ( $E'$ ) and loss ( $E''$ ) components.

Now we take up again the formalism of Sections IV and V. On the mesoscopic level—see Section VI—the time-dependent response  $|\mathbf{u}^0\rangle \exp(i\omega t)$  of the system, after all transients have decayed, is related to a small driving force  $|\mathbf{f}^0\rangle \exp(i\omega t)$  by

$$|\mathbf{u}^0\rangle e^{i\omega t} = \sum_{n=1}^D u_n^0 |\mathbf{v}_n\rangle e^{i\omega t} = \sum_{n=1}^D \frac{f_n^0}{\kappa_n(\omega)} |\mathbf{v}_n\rangle e^{i\omega t}, \quad (28)$$

where, again,  $D$  is the number of degrees of freedom,  $f_n^0 = \langle \mathbf{f}^0 | \mathbf{v}_n \rangle$ ,  $u_n^0 = \langle \mathbf{u}^0 | \mathbf{v}_n \rangle$ , and we used Eq. (11).

The macroscopic dynamic stress is given by  $\sigma(t) = F \exp(i\omega t)/S$ , with  $S$  the boundary surface area and  $F$  the macroscopic force acting on it. Moreover, the macroscopic strain is  $\Delta/L$  with  $\Delta$  the change in separation of the macroscopic sample boundaries and  $L$  the absolute distance between them. The displacement  $\Delta$  is measured in the direction of the applied force inducing it. Therefore, and since  $|\mathbf{f}^u\rangle$

represents the mesoscopic direction of a force of magnitude unity ( $F = 1$ , see Section V B), we define  $\Delta = \langle \mathbf{f}^u | \mathbf{u} \rangle$  as a measure of the resulting displacement. We recall here that  $|\mathbf{f}^0\rangle$  was constructed to apply only on the boundary, so  $\langle \mathbf{f}^u | \mathbf{u} \rangle$  really extracts the displacement of the boundaries. Consequently, we write Eq. (27) on the mesoscopic level as

$$\frac{F e^{i\omega t}}{S} = E(\omega) \frac{\langle \mathbf{f}^u | \mathbf{u}^0 \rangle e^{i\omega t}}{L}. \quad (29)$$

Using Eq. (28), as well as  $f_n^0 = F f_n^u$  and  $f_n^u = \langle \mathbf{f}^u | \mathbf{v}_n \rangle$  (see Section V B), the dynamic modulus follows as

$$E(\omega) = \frac{L}{S} \left[ \sum_{n=1}^D \frac{f_n^{u2}}{\kappa_n(\omega)} \right]^{-1} \quad (30)$$

which does not depend on the macroscopic force intensity  $F$  and in the case  $\omega = 0$  recovers Eq. (18). Since  $\kappa_n(\omega)$  is a complex number,  $E(\omega)$  is complex as well and we can separate it into storage and loss components  $E(\omega) = E'(\omega) + iE''(\omega)$ . We remark that in the static case we always find  $E''(\omega = 0) = 0$  by definition [see Eq. (24)].

On the macroscopic level, Eq. (30) is connected to the Kelvin-Voigt model, which correctly describes the properties of permanently crosslinked polymers on long times scales, i.e., small  $\omega$ . This is clear in a limit case when a single mode, e.g.,  $n = 1$ , has a relaxation time, e.g.,  $\tau_1 = c/\lambda_1$ , much longer than the other modes. Then, the long-frequency dynamics is dominated by this mode which gives, in fact, the largest contribution to the sum in Eq. (30). Eventually, in this case one would find  $E(\omega) \propto \kappa_1(\omega) = \lambda_1 + i\omega c$ , which is precisely the form of the dynamic modulus in the Kelvin-Voigt model.<sup>89,90</sup>

In the following, we will apply the present approach to different particle distributions, addressing the dynamic elastic moduli for varying  $\omega$  and  $m$ . Although we will display the behavior of the dynamic moduli up to relatively large values of  $\omega$ , one should keep in mind our focus on overdamped motion. At maximum our approach is meaningful up to a frequency  $\omega_{max} = \lambda_{max}/c$ , where  $\lambda_{max}$  is the largest eigenvalue of  $\mathcal{H}$ .

The limit becomes visible from calculating the spectrum, i.e., the density of states  $g(\omega)$ .<sup>91</sup> It is defined by

$$g(\omega) = \frac{1}{D} \sum_{n=1}^D \delta\left(\omega - \frac{\lambda_n}{c}\right), \quad (31)$$

with  $\delta$  the Dirac delta function. To determine it from our numerical calculations, we replace the Dirac delta function by a narrow normalized Gaussian. We chose the Gaussians as narrow as possible to achieve a smooth representation of the density of states.

We always find  $g(\omega)$  to drop significantly beyond a maximum value  $\omega_{max}$ . The latter is of the order of a few  $k/cl_0$ , see Fig. 4. Consequently, and because of our focus on the overdamped regime, it is not sensible to take into account the behavior for  $\omega \gtrsim 10k/cl_0$ .

First, the exemplary case of a simple cubic lattice will be studied. After that, we consider an fcc particle arrangement, before we finally move on to the case of disordered and more realistic particle arrangements. For simplicity, we will always

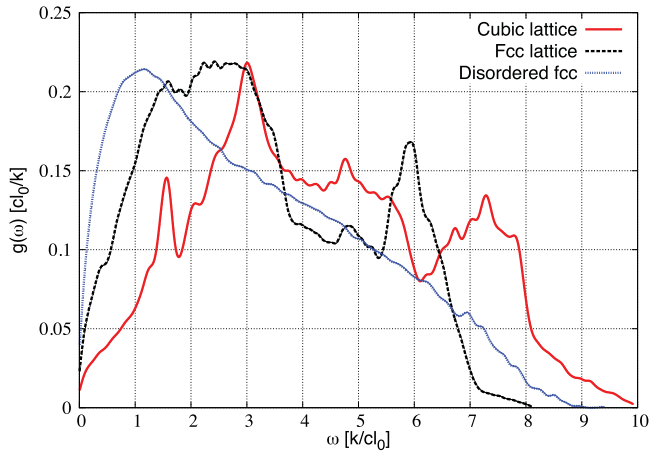


FIG. 4. Density of states  $g(\omega)$  at vanishing  $m$  of a cubic lattice with springs up to second-nearest neighbors (see Section VIII), an fcc lattice with only nearest-neighbor springs taken into account (see Section IX), and a disordered distribution (see Section X) made of 4913, 6084, and 6084 particles, respectively. The density of states is shown from  $\omega = 0$  to the highest  $\omega_{max}$  obtained from the Hamiltonian spectrum, which is usually  $\lesssim 10 k/c l_0$ . The standard deviation of the narrow Gaussians used to approximate the Dirac deltas appearing in Eq. (31) is chosen as  $0.005\omega_{max}$ .

keep the magnetic moment  $\mathbf{m}$  oriented in the  $z$ -direction. We measure the Young moduli in the perpendicular ( $E_{xx}$  and  $E_{yy}$ ) and parallel ( $E_{zz}$ ) directions. Likewise, the shear moduli will be calculated in the three possible orientations depicted in Fig. 5: (a) shear corresponding to  $G_{xy}$  does not directly modify distances along the  $\mathbf{m}$ -direction; (b) while  $G_{xz}$  is measured the macroscopic shear displacements are oriented along  $\mathbf{m}$ ; and (c) the shear plane contains  $\mathbf{m}$ , but the macroscopic shear displacements are perpendicular to  $\mathbf{m}$  when  $G_{zy}$  is determined. Moreover, we here have  $G_{yx} = G_{xy}$ ,  $G_{xz} = G_{yz}$ , and  $G_{zx} = G_{zy}$ .

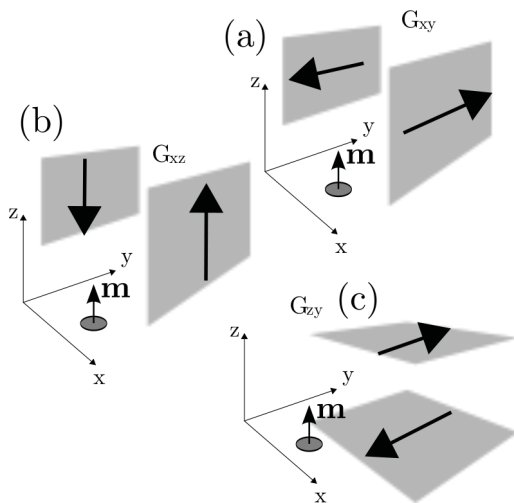


FIG. 5. Illustration of the three principal shear geometries.  $\mathbf{m}$  is rigidly oriented in the  $z$ -direction. Shear forces can be applied to different boundaries and in different directions, giving origin to three main geometries (top to bottom): (a) for  $G_{xy}$  forces are perpendicular to  $\mathbf{m}$ , but the driven boundary planes contain  $\mathbf{m}$ ; (b) for  $G_{xz}$  both shear forces and driven boundary planes are parallel to the  $\mathbf{m}$  direction; (c) for  $G_{zy}$  the driven boundary planes and shear forces are perpendicular to  $\mathbf{m}$ . We here define stresses directly via the forces acting on the indicated planes along the desired directions.

## VIII. CUBIC LATTICE

As a first prototype, we consider the simple exemplary case of a 3D cubic lattice with  $N = 3375$  particles. Magnetic particles on the lattice are linked by springs up to second-nearest neighbors. Corresponding springs along the diagonals of the faces of the unit cells are necessary to avoid unphysical soft-shear modes. The boundaries of the system are simply identified as the outermost layers of particles in the respective directions. As explained in Section II, the lattice parameter and the typical interparticle distance  $l_0$  follow from the number density  $\rho$ . In the case of a simple cubic lattice structure,  $\rho$  is given by one particle per unit cell.

Upon introducing a dipole magnetic moment in the particles, the direct attraction between nearest neighbors causes the system to shrink in the  $\mathbf{m}$ -direction and expand in the perpendicular directions (see Fig. 6). Technically, in our numerical calculations, we gradually increased the magnetic moment to the value under consideration, up to a maximum magnitude of  $m = 0.1m_0$ . In this regime, and despite the overall deformation, the lattice maintains a cuboidlike shape. The magnetic interactions are not as strong as to overcome the elastic springs and the particles do not come into steric contact.

### A. Static moduli

We start by studying the static moduli  $E$  and  $G$  (i.e., the storage components  $E'$  and  $G'$  of the dynamic moduli calculated for  $\omega = 0$ ) for increasing magnitude of the magnetic moment  $m$ , see also Ref. 51. Magnetic interactions between nearest neighbors are attractive in the  $z$ -direction and repulsive in the  $x$ - and  $y$ -direction. These attractive and repulsive

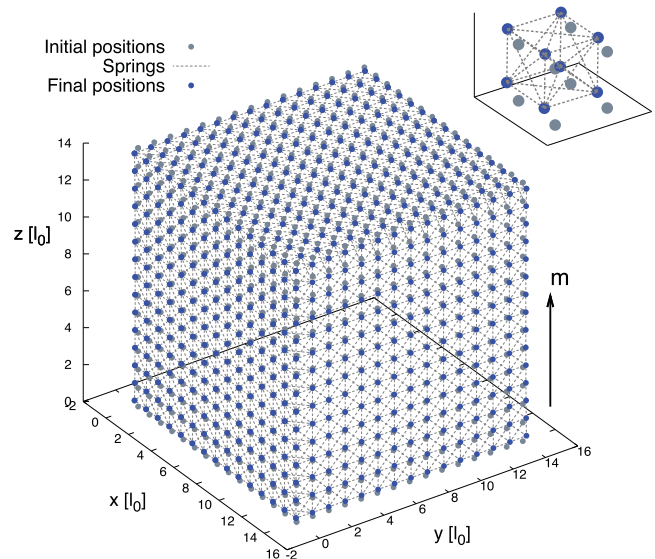


FIG. 6. Deformation of an initially cubic lattice with springs between up to second-nearest neighbors and  $N = 3375$  when a magnetic moment of  $\mathbf{m} = 0.1m_0\hat{z}$  is gradually switched on. For illustrative purposes, only particles on the front, top, and right faces are depicted. Shrinking is observed along  $\mathbf{m}$ , i.e., the  $z$ -direction, and dilation in the perpendicular directions. The inset zooms in onto the deformation of the unit cell at the bottom left corner of the sample.

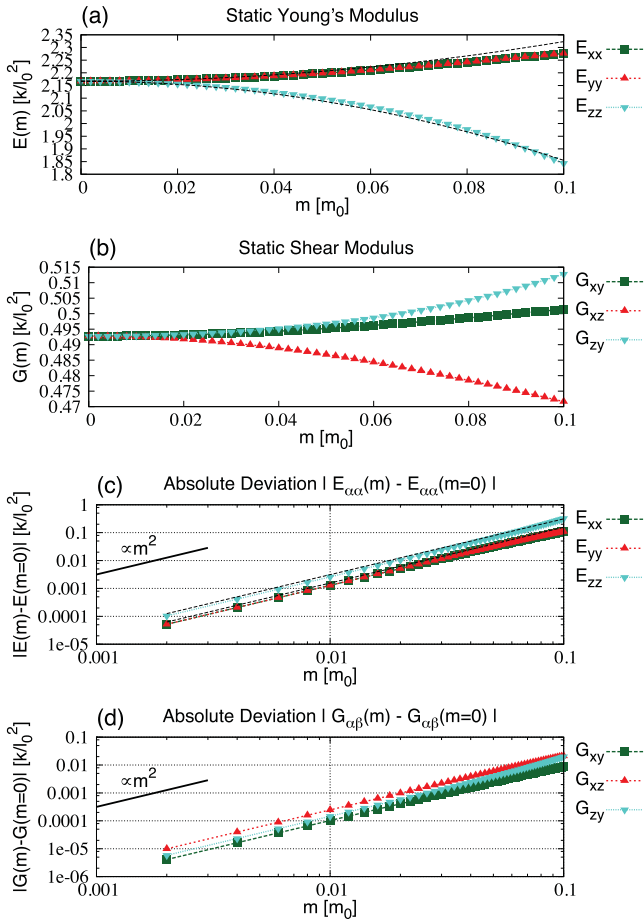


FIG. 7. Static moduli (a)  $E_{\alpha\alpha}(m) = E'_{\alpha\alpha}(\omega=0, m)$  and (b)  $G_{\alpha\beta}(m) = G'_{\alpha\beta}(\omega=0, m)$  ( $\alpha, \beta = x, y, z$ ) of a cubic lattice with  $N = 3375$  for increasing magnetic moment intensity  $m$  ( $\mathbf{m}$  oriented along the  $z$ -direction). (a) The Young moduli in the directions perpendicular to  $\mathbf{m}$  are increased by increasing magnetic moments, whereas in the  $\mathbf{m}$ -direction the modulus is decreased. Black dashed lines in panels (a) and (c) represent the trends in Eq. (32) shifted vertically to compensate for finite-size and boundary effects and to allow for a better comparison of the  $m$ -dependence. (b) The shear modulus  $G_{xz}$  obtained by shear displacements along the  $\mathbf{m}$ -direction decreases for increasing  $m$ , whereas  $G_{xy}$  and  $G_{zy}$  reveal an increasing behavior. (c, d) All elastic moduli as functions of  $m$  show quadratic behavior to lowest order, as required by the necessary  $\mathbf{m} \rightarrow -\mathbf{m}$  symmetry.

magnetic interactions with correspondingly positive and negative second derivatives with respect to nearest-neighbor distances induce decrease and increase, respectively, of the Young moduli.<sup>55</sup> This trend is observed in Fig. 7(a). At vanishing magnetic moment all Young moduli measured along the different directions have the same value, as expected by the cubic lattice symmetry. Then, as  $m$  is slowly increased, this symmetry is broken and  $E_{zz}(m)$  decreases, whereas  $E_{xx}(m)$  and  $E_{yy}(m)$  increase identically, as expected by the unbroken  $x \leftrightarrow y$  symmetry. Moreover, all moduli show to lowest order in  $m$  a quadratic behavior, as demanded by the necessary  $\mathbf{m} \rightarrow -\mathbf{m}$  symmetry,<sup>59</sup> see Fig. 7(c).

More explicitly, the trends of the static Young moduli in the simple cubic case can be explained by considering interactions between neighbors on a regular lattice, see Appendix E. When we focus on small magnetic interactions, i.e.,  $m \ll m_0$ , the dipole-dipole forces are much weaker than

the restoring elastic ones and we can assume they leave the particle positions unaltered.

Considering contributions up to neighbors as distant as  $10l_0$ , we obtain, see Appendix E, the following trends for the Young moduli:

$$\begin{aligned} \frac{E_{xx}(m)}{k/l_0^2} = \frac{E_{yy}(m)}{k/l_0^2} &\approx \frac{9 + 4\sqrt{2}}{7} + 15.61(m/m_0)^2, \\ \frac{E_{zz}(m)}{k/l_0^2} &\approx \frac{9 + 4\sqrt{2}}{7} - 31.21(m/m_0)^2. \end{aligned} \quad (32)$$

The trends provided by these expressions are in good agreement with our numerical results, see Fig. 7(a). They describe, respectively, increasing or decreasing moduli in the directions perpendicular or parallel to  $\mathbf{m}$ . Moreover, Eq. (32) suggests a stronger dependence of  $E_{zz}$  on  $m$  compared to  $E_{xx}$  and  $E_{yy}$ . This agrees with our numerical results, see Figs. 7(a) and 7(c). Furthermore, it confirms the major role played by the second derivatives of neighbor interactions in determining the trends for  $E_{\alpha\alpha}(m)$  of regular distributions, as pointed out in Ref. 55.

In our numerical calculations we obtain different behaviors for the different shear moduli as functions of  $m$ . However, at vanishing magnetic moment they all assume the same value, as expected by lattice symmetry, see Fig. 7(b). Furthermore, as Young's moduli, they are all, to lowest order, quadratic functions of  $m$ , as required by symmetry when  $\mathbf{m}$  is flipped into  $-\mathbf{m}$ , see Fig. 7(d). The shear modulus  $G_{zy}(m)$  shows an increasing behavior for increasing  $m$ . It is, in fact, the only depicted shear deformation that breaks the spatial mutual alignment of the moments in the  $z$ -direction. This is hindered by increasing  $m$ , in agreement with an increasing modulus  $G_{zy}(m)$ . The shear deformation related to  $G_{xz}(m)$ , instead, induces the dipoles to move in parallel to their alignment direction. Nearest neighbors connected by  $l_0\hat{x}$  lie on a maximum of the dipole-dipole interaction, see Eq. (4). Therefore, increasing  $m$  facilitates the displacement induced by  $\sigma_{xz}$ , in agreement with a decreasing shear modulus  $G_{xz}(m)$ , as found in Fig. 7(b). Last, we find an increasing trend for the  $G_{xy}(m)$  shear modulus, slightly weaker compared to the other two examined moduli, as depicted in Figs. 7(b) and 7(d).

## B. Dynamic moduli

We now focus on the dynamic properties, which are the central aim of the present work. As a general trend, we always find the storage moduli to tend to a finite value for large  $\omega$ , see Fig. 8. Yet, as noted before, it is not reasonable to consider the behavior for frequencies larger than  $10k/cl_0$ . Conversely, the loss moduli as functions of  $\omega$  show a linear increase (see Appendix F). This behavior we attribute to our model focusing on overdamped motion. In fact, under oscillatory motion, the damping term in Eq. (19), which is the origin of the loss modulus, increases with frequency  $\omega$ . This conforms with a macroscopic Kelvin-Voigt model<sup>89,90</sup> which predicts an imaginary component of the dynamic moduli linearly increasing with frequency.

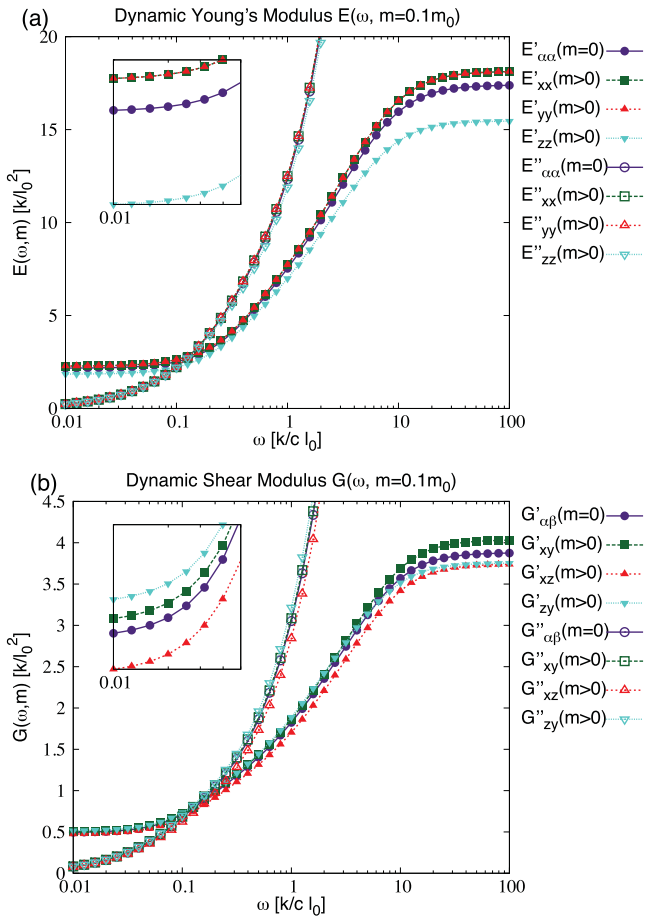


FIG. 8. Dynamic elastic moduli (a)  $E_{\alpha\alpha}(\omega)$  and (b)  $G_{\alpha\beta}(\omega)$  ( $\alpha, \beta = x, y, z$ ) of a cubic lattice with  $N = 3375$  for vanishing magnetic moment (solid line,  $\circ$ ), and  $m = 0.1m_0\hat{z}$  (dashed lines,  $\square, \triangle, \nabla$ ). Filled and unfilled markers correspond to storage ( $E'_{\alpha\alpha}$ ,  $G'_{\alpha\beta}$ ) and loss ( $E''_{\alpha\alpha}$ ,  $G''_{\alpha\beta}$ ) components, respectively. Insets in panels (a) and (b) zoom into the storage parts (a)  $E'_{\alpha\alpha}(\omega)$  and (b)  $G'_{\alpha\beta}(\omega)$  at small  $\omega$  for better resolution (see also Fig. 7).

Similarly, experimental measurements of the loss moduli in polymeric materials<sup>81,85,87,88</sup> are compatible with a Kelvin-Voigt model [i.e., constant storage part and linearly increasing loss part of  $E_{\alpha\alpha}(\omega)$  and  $G_{\alpha\beta}(\omega)$ ] in the low-frequency regime. Furthermore, in the limit  $\omega \rightarrow 0$ , we always find vanishing loss moduli and the storage component to recover the corresponding static elastic modulus, see Eqs. (18), (24), and (30).

The storage Young moduli  $E'_{\alpha\alpha}(\omega)$  ( $\alpha = x, y, z$ ) in Fig. 8(a)—here calculated for  $m = 0.1m_0\hat{z}$ —show at all frequencies the trends as described in the static case, see Fig. 7. The amount of variation with respect to the  $m = 0$  configuration, however, seems to be larger at larger frequencies. Furthermore,  $E'_{xx}(\omega)$  and  $E'_{yy}(\omega)$  show identical behavior as functions of  $\omega$ , as required by the symmetry of this geometry under switching  $x \leftrightarrow y$ . Likewise, at low  $\omega$ , the loss moduli  $E''_{zz}(\omega)$  and  $E''_{xx,yy}(\omega)$  show a decreasing and increasing trend, respectively, when the magnetic moment is switched on and increased. Furthermore, for higher  $\omega$ , all the loss components linearly increase with  $\omega$  with identical coefficients, see also Fig. 17(b) in Appendix F.

The storage shear moduli  $G'_{\alpha\beta}(\omega)$  at low frequencies present the same trends of increase and decrease as in the static case, see Figs. 7(b) and 8(b). We remark that at high frequencies (beyond  $10k/cl_0$ ), while  $G'_{xy}(\omega)$  and  $G'_{xz}(\omega)$  show the same and enhanced trend as in the static case,  $G'_{zy}(\omega)$  now decreases when  $m$  is increased. This graphically results in a crossing between the curves for  $G'_{\alpha\beta}(\omega, m = 0)$  and  $G'_{\alpha\beta}(\omega, m = 0.1m_0)$ . The loss shear moduli  $G''_{\alpha\beta}(\omega)$ , instead, display the same increasing or decreasing trends as the corresponding static  $G_{\alpha\beta}(m = 0)$  both at low and high frequencies (see also Appendix F).

## IX. FACE-CENTERED CUBIC (FCC) LATTICE

We now turn our focus onto the exemplary case of a face-centered cubic (fcc) lattice. Later in Section X, we will generate disordered samples by randomizing an initially fcc particle arrangement. In this setup we introduce springs connecting nearest neighbors only. This is enough to obtain a particle distribution stable under both stretching and shearing. The boundaries of the system are chosen as the outermost layers of particles in a given direction. The typical interparticle distance  $l_0$  follows from the number density  $\rho$ , as explained in Section II, which for the fcc lattice is 4 particles per unit cell.

When magnetic moments are introduced we here observe an elongation of the system in the  $m$ -direction and shrinking in the perpendicular directions, see Fig. 9. The nearest neighbors on the fcc lattice are located along the  $\hat{x} + \hat{y}$ ,  $\hat{x} + \hat{z}$ , and  $\hat{y} + \hat{z}$  directions, i.e., at an angle of  $\pi/4$  with respect to the Cartesian axes. When the system elongates in the  $z$ -direction the angles between the nearest-neighbor directions and  $m$  reduce, thus lowering the magnetic energy  $U^m$ .

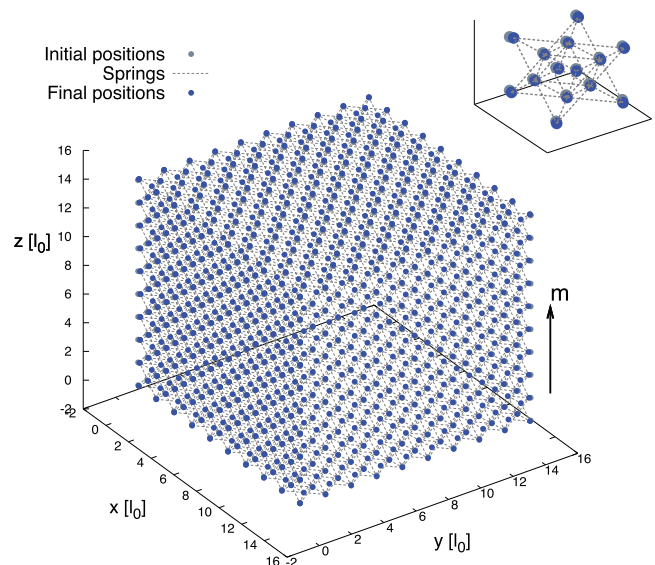


FIG. 9. Deformation of an fcc lattice with springs between nearest neighbors and  $N = 3430$ , when a magnetic moment of  $m = 0.1m_0\hat{z}$  is switched on. For illustrative purposes, only the first two particle layers on the front, top, and right faces are depicted. Elongation is observed in the  $m$ -direction and contraction in the perpendicular ones. Inset zooms in onto the displacements of the particles at the bottom left corner of the sample.

### A. Static moduli

First, we present the behavior of the static moduli as functions of increasing magnetic moment, see also Ref. 51. We always find a monotonic, smooth behavior for increasing  $m$  [see Figs. 10(a) and 10(b)]. In fact, as shown in Figs. 10(c) and 10(d), the elastic moduli as functions of  $m$  are to lowest order quadratic functions, in accord with the  $\mathbf{m} \rightarrow -\mathbf{m}$  symmetry. Again, and as required by lattice symmetry, at  $m = 0$  all Young moduli and the shear moduli in the examined directions coincide, see Figs. 10(a) and 10(b).

Next, we estimate the role played by the relative positions of neighboring particles for the behavior of the Young moduli. We consider the case of a regular fcc lattice and take into account contributions to the Young moduli to lowest order in  $m$ , as explained in Appendix E. Considering terms up to neighbors as far as  $10l_0$  in Eq. (E3), we obtain

$$\begin{aligned} \frac{E_{xx}(m)}{k/l_0^2} = \frac{E_{yy}(m)}{k/l_0^2} &\approx \frac{2^{7/6}}{3} - 13.02(m/m_0)^2, \\ \frac{E_{zz}(m)}{k/l_0^2} &\approx \frac{2^{7/6}}{3} + 28.05(m/m_0)^2. \end{aligned} \quad (33)$$

Comparison with the behavior of the Young's moduli resulting from our numerical calculations, see Fig. 10(a), leads to a good qualitative agreement. The modulus in the  $\mathbf{m}$ -direction  $E_{zz}(m)$  increases with increasing  $m$ , whereas in the perpendicular directions  $E_{xx}(m)$  and  $E_{yy}(m)$  decrease with  $m$ . Thus, the fcc arrangement shows a completely opposite behavior compared to the simple cubic case, see Section VIII A. Moreover, Eq. (33) indicates the  $E_{zz}(m)$  modulus to have a stronger dependence on  $m$  compared to  $E_{xx}(m)$  and  $E_{yy}(m)$ , as also found in our numerical results and shown in Figs. 10(a) and 10(c).

Similarly, the shear moduli are influenced by  $m$  in different ways. Here we find the shear modulus  $G_{xy}(m)$  to increase and  $G_{xz}(m)$  to decrease with increasing  $m$ , analogously to what we observed in the simple cubic case, see Section VIII A. Contrarily to the simple cubic case, the shear modulus referring to displacements perpendicular to  $\mathbf{m}$ ,  $G_{zy}(m)$ , shows a decreasing trend when the magnetic moments increase. Moreover,  $G_{zy}(m)$  displays a weaker dependence on  $m$  compared to the remaining two shear moduli, as depicted in Fig. 10(d).

### B. Dynamic moduli

Finally, we examine the behaviors of the dynamic elastic moduli for various frequencies  $\omega$  and magnetic moment intensities  $m$ . The storage dynamic Young moduli  $E'_{\alpha\alpha}$  ( $\alpha = x, y, z$ ) at all frequencies follow the same behavior as described in the static case (see Fig. 10). In the direction parallel to  $\mathbf{m}$ ,  $E'_{zz}$  increases for increasing  $m$ , whereas  $E'_{xx}$  and  $E'_{yy}$  decrease for the perpendicular directions, see Fig. 11(a) and its inset for a zoom onto the low- $\omega$  behavior. As shown in Appendix F, the loss components  $E''_{\alpha\alpha}$  partially exhibit opposite trends compared to their storage counterparts (see Fig. 18 for a detailed plot). In fact, at low frequencies, the loss modulus for the  $\mathbf{m}$  direction,  $E''_{zz}$ , decreases with increasing  $m$ , whereas  $E''_{xx}$  and  $E''_{yy}$  for the two perpendicular directions increase. At higher frequencies, however, and as in the cubic lattice case, all the loss moduli  $E''_{\alpha\alpha}$  recover the behavior of their storage counterparts and show an identical dependence on  $\omega$  [see Fig. 11(a) and Fig. 18 in Appendix F].

The storage dynamic shear moduli  $G'_{\alpha\beta}$  ( $\alpha, \beta = x, y, z$ ) are displayed in Fig. 11(b). Here, at low- $\omega$  values the changes in the shear moduli for the different geometries reproduce the trends shown in Fig. 10, see the inset of Fig. 11(b). However, when considering the behavior at higher  $\omega$ ,  $G'_{xy}$  turns from increasing to decreasing with  $m$ , while  $G'_{zy}$  turns from decreasing to increasing when compared with the shear modulus at  $m = 0$ . Although we already mentioned that only the behavior for  $\omega \lesssim 10k/cl_0$  should be interpreted, these data suggest the possibility that some dynamic shear moduli could swap their tendency of increasing or decreasing with  $m$  to decreasing or increasing, respectively. Contrarily, the Young

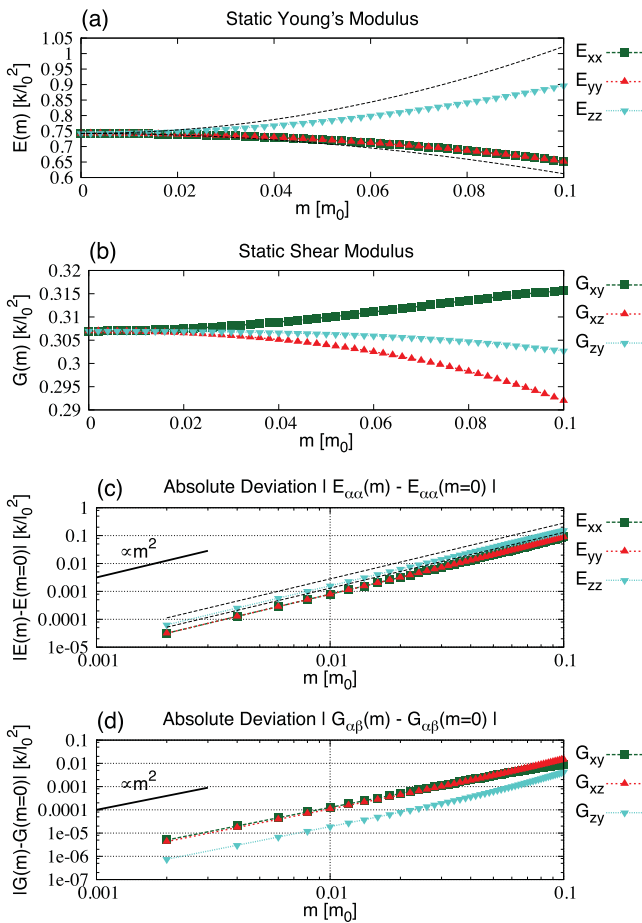


FIG. 10. Static moduli (a)  $E_{\alpha\alpha}(m) = E'_{\alpha\alpha}(\omega=0, m)$  and (b)  $G_{\alpha\beta}(m) = G'_{\alpha\beta}(\omega=0, m)$  ( $\alpha, \beta = x, y, z$ ) of an fcc lattice with  $N = 3430$  for increasing magnetic moment intensity  $m$ .  $\mathbf{m}$  is oriented along the  $z$ -direction. The Young moduli for stretching perpendicular to  $\mathbf{m}$  are reduced by increasing magnetic moments, whereas along the  $\mathbf{m}$ -direction the modulus is increased. Black dashed lines in panels (a) and (c) represent the trends in Eq. (33) shifted vertically to compensate for finite-size and boundary effects and to allow for a better comparison of the  $m$ -dependence. The shear modulus  $G_{xy}$  obtained by applying shear in the  $xy$  plane perpendicular to  $\mathbf{m}$  increases for increasing  $m$ , whereas  $G_{xz}$  and  $G_{zy}$  reveal a decreasing behavior. (c), (d) All elastic moduli as functions of  $m$  show a quadratic behavior to lowest order, in accord with the  $\mathbf{m} \rightarrow -\mathbf{m}$  symmetry and as depicted by the log-log scale plots.

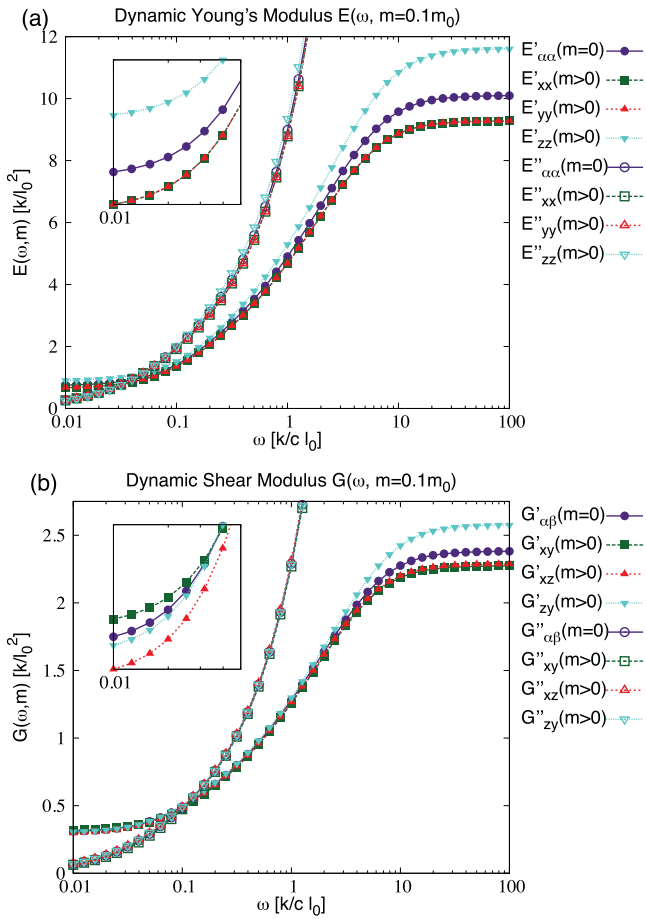


FIG. 11. Dynamic elastic moduli (a)  $E_{\alpha\alpha}(\omega)$  and (b)  $G_{\alpha\beta}(\omega)$  ( $\alpha, \beta = x, y, z$ ) of an fcc lattice with  $N = 3430$  for vanishing magnetic moment (solid line,  $\circ$ ), and  $m = 0.1m_0\hat{z}$  (dashed lines,  $\square, \triangle, \nabla$ ). Filled and unfilled markers correspond to storage ( $E', G'$ ) and loss ( $E'', G''$ ) components, respectively. Insets in panels (a) and (b) zoom onto the storage parts (a)  $E'_{\alpha\alpha}(\omega)$  and (b)  $G'_{\alpha\beta}(\omega)$  at small  $\omega$  to better resolve the different curves (see also Fig. 10).

moduli consistently show a monotonic behavior as functions of both  $\omega$  and  $m$ . Furthermore, at low  $\omega$ , the loss shear moduli  $G''_{\alpha\beta}$  exhibit an opposite behavior when compared with their storage complements. For shear deformations in the plane perpendicular to  $\mathbf{m}$ ,  $G''_{xy}$  decreases with increasing magnetic moment, whereas the other two moduli  $G''_{xz}$  and  $G''_{zy}$  are increased by increasing  $m$ , see also Appendix F, Fig. 18.

### X. 3D DISORDERED SAMPLES

#### A. Numerical generation

We start from a regular three-dimensional fcc lattice. Having a well defined density  $\rho$  and neighbor structure, this lattice allows us to define the average interparticle distance  $l_0$  as described in Section IX. Then we introduce disorder in the lattice by randomly displacing each particle by  $0.5l_0$  in a stochastic direction. After that, we set the elastic springs between nearest neighbors.

In the randomization step, we take care to generate an initially stable disordered system so that magnetic interactions

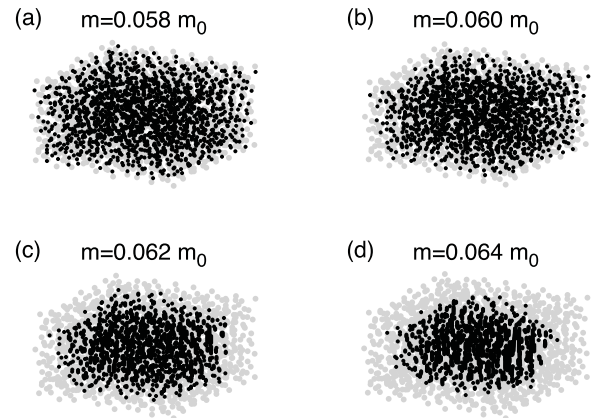


FIG. 12. Example deformation of a randomized particle distribution ( $N = 1688$ ) of initially cubelike shape (gray particles) when a magnetic moment of  $m = m\hat{z}$  is switched on. Panels (a), (b), (c), and (d) show the equilibrated particle distribution (black) as the magnetic moment intensity is gradually increased to  $m = 0.058m_0$ ,  $m = 0.060m_0$ ,  $m = 0.062m_0$ , and  $m = 0.064m_0$ , respectively. Panel (c) represents the onset of chain formation in the  $m$ -direction, see Sections X B and X D.

do not immediately overcome the elastic spring interactions when the magnetic moments are switched on.<sup>54,68</sup> In other words, the formation of collapsed clusters where the particles touch each other in a stuck configuration shall be avoided for low strength of the magnetic interactions. For this purpose, we impose that in the randomized configuration for  $m = 0$  no couples of particles are closer than  $0.5l_0$ . Boundary particles are identified as the outermost layers of the initial fcc lattice in each direction. To help maintain an overall cubelike shape, we move boundary particles by half the amount of other particles. An example of the resulting initial distribution is given by the gray particles in Fig. 12.

Thus, we generate a disordered system of macroscopic cubelike shape with  $N$  non-overlapping magnetic particles. In the following we set  $N = 1688$ . As described, in the initial configuration, the springs are set before the magnetic interactions are switched on. Then, we gradually increase the magnitude of the magnetic moments and at each step find the minimum energy configuration, see Section III. When the equilibrium state for a given  $m$  is reached, we obtain the Young and shear moduli  $E$  and  $G$  as functions of both  $m$  and  $\omega$ , using the methods described in Sections V C and VII.

As the magnitude  $m$  of the magnetic moments increases, we can principally distinguish between two regimes. On the one hand, the behavior for small  $m$  is controlled by magnetic  $U^m$  and elastic  $U^{el}$  energies, see Fig. 13. The deformation is relatively small and the elastic moduli are, to lowest order, quadratic functions of  $m$ , as expected by the necessary  $m \rightarrow -m$  symmetry. On the other hand, when attractive magnetic interactions become as strong as to overcome linear spring repulsion, steric interactions come into play (see Fig. 13). Then, formation of chains is observed, as well as significant changes in the system size (see Fig. 12). Furthermore, the close steric contact between particles generates extra stiffness, which is reflected by a significant change in the elastic moduli. This behavior reflects a “hardening transition” similar

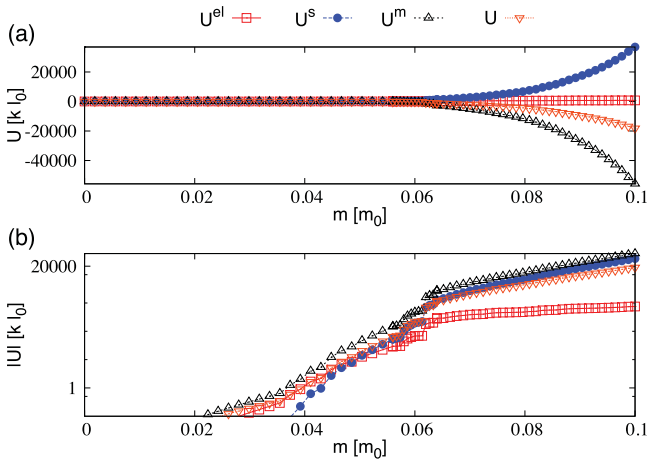


FIG. 13. (a) Equilibrium energies of the disordered fcc system shown in Fig. 12 for increasing magnitude of the magnetic moment  $m$ . (b) Two regimes are identified in a logarithmic plot. Up to  $m \sim 0.05m_0$  the total energy  $U$  mostly comprises elastic  $U^{el}$  and magnetic  $U^m$  contributions. For  $m \geq 0.05m_0$  instead, the steric interaction energy  $U^s$  becomes higher than the elastic energy  $U^{el}$ . This signals the subsequent formation of chains. The pronounced step at  $0.06m_0 \leq m \leq 0.064m_0$  is connected to chain formation.

to the situation described in Ref. 54 for one-dimensional systems.

## B. Static moduli

First, we focus on the static elastic moduli of the randomized system for increasing magnetic moment  $m$ . To extract a general trend we realized 80 different systems following the protocol as described in Section X A. Then we obtain our results by averaging over the moduli for all different randomized realizations, also calculating the standard deviations. The resulting static moduli are depicted in Fig. 14. To lowest order in  $m$  and up to approximately  $m = 0.06m_0$ , the Young moduli of the system [see inset of Fig. 14(a)] show a behavior similar to the fcc case [compare with Fig. 10(a)]: increasing  $\langle E_{zz} \rangle$  for imposed deformations in the  $m$  direction and decreasing  $\langle E_{xx} \rangle$  and  $\langle E_{yy} \rangle$  for the perpendicular cases. Moreover, in this regime the static Young moduli  $\langle E_{\alpha\alpha}(m) \rangle$  ( $\alpha = x, y, z$ ) show a quadratic behavior as functions of  $m$  in accord with the  $m \rightarrow -m$  symmetry, see Fig. 14(c). Similarly, the static shear moduli  $\langle G_{\alpha\beta}(m) \rangle$  ( $\alpha, \beta = x, y, z$ ) in this regime show quadratic behavior, see Fig. 14(d), while the trends for  $\langle G_{\alpha\beta}(m) \rangle$  vary from those of the regular fcc lattice [compare the inset of Fig. 14(b) with Fig. 10(b)].

This behavior changes dramatically for  $m \geq 0.06m_0$ , where magnetic interactions are as strong as to cause the particles to come into steric contact and form chains in the  $m$ -direction. Here we observe a significant increase in all elastic moduli [see Figs. 14(a) and 14(b)]. Still, Young's modulus for imposed deformations in the  $m$ -direction,  $\langle E_{zz} \rangle$ , shows a much larger increase compared to  $\langle E_{xx} \rangle$  and  $\langle E_{yy} \rangle$ , in agreement with experimental observations on anisotropic systems,<sup>38</sup> see also the case of bi-axial tension.<sup>92</sup>  $\langle E_{xx} \rangle$  and  $\langle E_{yy} \rangle$  feature an identical behavior within the standard deviations, as expected by the largely unbroken isotropy of

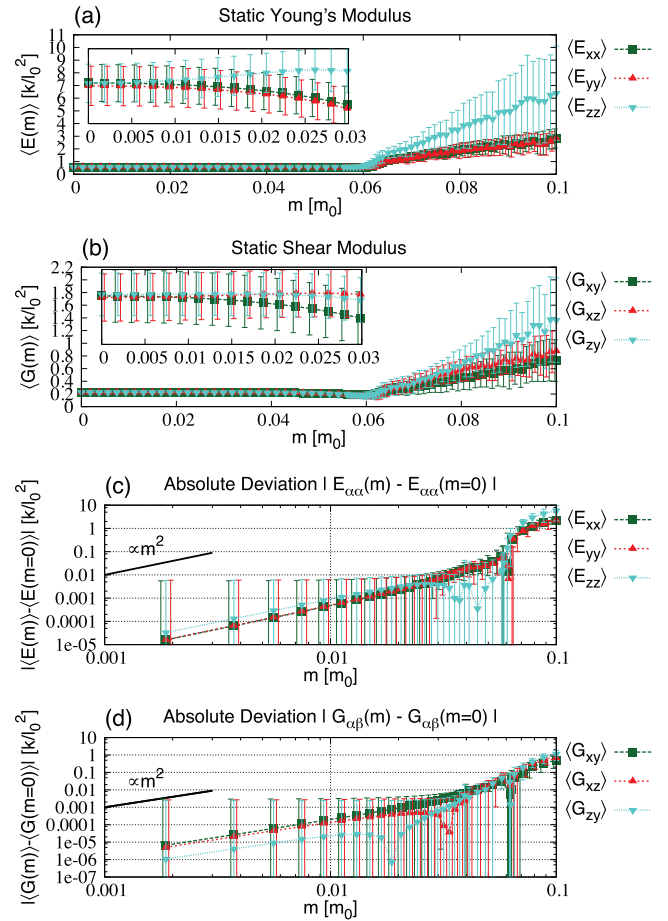


FIG. 14. Static moduli (a)  $\langle E_{\alpha\alpha}(m) \rangle = \langle E'_{\alpha\alpha}(\omega = 0, m) \rangle$  and (b)  $\langle G_{\alpha\beta}(m) \rangle = \langle G'_{\alpha\beta}(\omega = 0, m) \rangle$  ( $\alpha, \beta = x, y, z$ ) of a disordered fcc lattice with  $N = 1688$  for increasing  $m = |m|$ , with  $m$  oriented in the  $z$ -direction. Statistics are collected over 80 differently randomized samples. Data points and bars represent the resulting averages and standard deviations, respectively. (c), (d) All elastic moduli as functions of  $m$  show a quadratic behavior to lowest order for small  $m$ , in accord with the  $m \rightarrow -m$  symmetry. For illustrative purposes we have slightly shifted the bars for different data sets horizontally and reduced the number of points shown in panels (c) and (d) to better distinguish between the individual bars and data points. Dips in panels (c) and (d) occur when  $\langle E_{\alpha\alpha}(m) \rangle \approx \langle E_{\alpha\alpha}(m=0) \rangle$  or  $\langle G_{\alpha\beta}(m) \rangle \approx \langle G_{\alpha\beta}(m=0) \rangle$ . Then, the logarithm of the absolute deviation from the value for  $m = 0$  diverges to  $-\infty$ . The elastic moduli themselves, however, show smooth behavior, as displayed in panels (a) and (b) and the respective insets.

the systems within the  $xy$ -plane. Likewise, the shear moduli show an increase for all investigated geometries. In a purely affine deformation of chains perfectly aligned along  $m$ , the  $zy$  shear geometry would be the only one displayed that leads to distortions of the chains. Therefore it is conceivable that  $\langle G_{zy} \rangle$  grows larger than  $\langle G_{xy} \rangle$  and  $\langle G_{xz} \rangle$ , although the size of the standard deviations does not allow to draw a conclusive result.

Finally, to avoid confusion, we stress that the dips in Figs. 14(c) and 14(d) simply mean that the elastic moduli for  $m \neq 0$  tend to the same values as those for  $m = 0$ . Since in Figs. 14(c) and 14(d) the deviations of the elastic moduli from their values for  $m = 0$  are plotted on a logarithmic scale, the dips are not directly related to a mechanical instability resulting from vanishing elastic moduli. In fact, as shown in

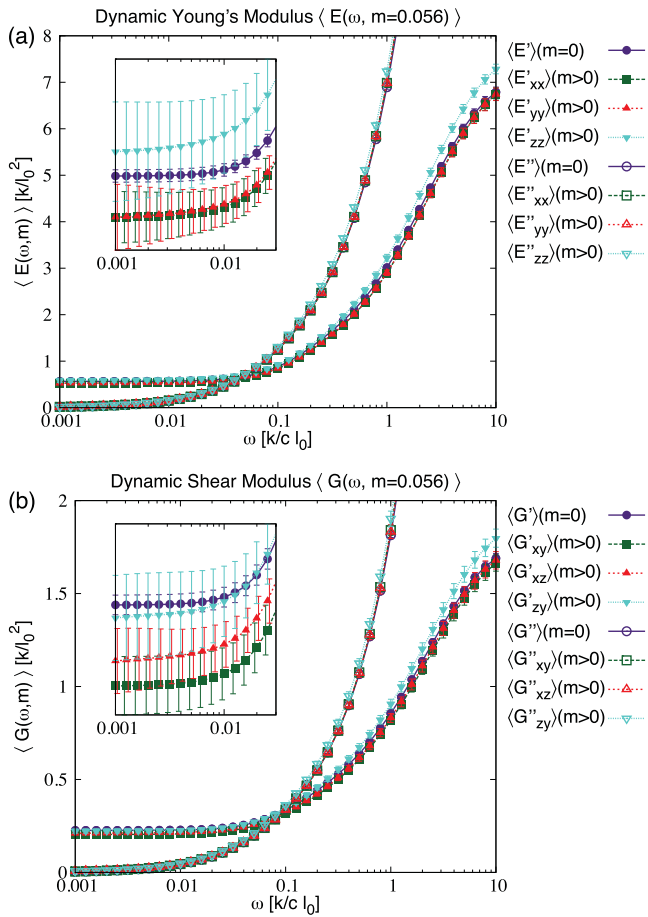


FIG. 15. Dynamic elastic moduli (a)  $\langle E_{\alpha\alpha}(\omega) \rangle$  and (b)  $\langle G_{\alpha\beta}(\omega) \rangle$  ( $\alpha, \beta = x, y, z$ ) of randomized fcc lattices with  $N = 1688$  for vanishing magnetic moment (solid line,  $\circ$ ), and  $m = 0.056m_0\hat{z}$  (dashed lines,  $\square, \triangle, \nabla$ ). Data points and standard deviations are obtained by averaging over 80 differently randomized samples. Filled and unfilled markers correspond to storage ( $E'$ ,  $G'$ ) and loss ( $E''$ ,  $G''$ ) components, respectively. Insets zoom into the storage parts (a)  $\langle E'_{\alpha\alpha}(\omega) \rangle$  and (b)  $\langle G'_{\alpha\beta}(\omega) \rangle$  at small  $\omega$  to better resolve the different curves. For illustrative purposes we have slightly shifted the bars for different data sets horizontally to better distinguish the individual bars.

Figs. 14(a) and 14(b), for a given value of  $m$  the elastic moduli always remain positive.

### C. Dynamic moduli, $m \lesssim 0.06m_0$

We now move our attention to the dynamic properties of our disordered systems. Again, we have collected statistics over 80 different realizations of our randomizing process. The resulting averages and standard deviations are represented as data points and bars in the figures.

First we examine the dynamic moduli for the magnitude of the magnetic moments below the onset of significant chain formation, i.e.,  $m \lesssim 0.06m_0$ . There, the storage parts  $\langle E'_{\alpha\alpha}(\omega) \rangle$  of the dynamic Young moduli for increasing  $m$  show the same trends for the different geometries as the static moduli [see Fig. 15(a) and compare with the inset of Fig. 14(a)]. Conversely, the loss parts  $\langle E''_{\alpha\alpha}(\omega) \rangle$  of the Young moduli feature a trend of increase with increasing  $m$  in all cases [see Appendix F, Fig. 19(a)].

Similarly to the Young moduli, the storage parts  $\langle G'_{\alpha\beta}(\omega) \rangle$  of the dynamic shear moduli approximately follow their

static counterparts at low  $\omega$  [see the inset of Fig. 15(b) and compare it to the inset of Fig. 14(b)]. However, with increasing frequencies  $\omega$  and upon switching  $m$  from  $m = 0$  to  $m > 0$ ,  $\langle G'_{zy}(\omega) \rangle$  switches from a slight decrease to a significant increase with respect to the value at  $m = 0$ , see Fig. 15(b). This results in a crossing between the curves corresponding to  $\langle G'_{zy}(\omega, m = 0) \rangle$  and  $\langle G'_{zy}(\omega, m > 0) \rangle$ . Instead, the remaining two shear moduli,  $\langle G'_{xy}(\omega) \rangle$ , and  $\langle G'_{xz}(\omega) \rangle$  always show a decrease. Analogously to  $\langle E'_{\alpha\alpha}(\omega) \rangle$ , the loss components  $\langle G''_{\alpha\beta}(\omega) \rangle$  are observed to increase at all frequencies when switching on  $m$ , independently of the chosen geometry [see Appendix F, Fig. 19(b)].

### D. Dynamic moduli, $m \gtrsim 0.06m_0$

In the following, we consider the dynamic moduli of the system at magnitudes  $m$  of the magnetic moment at the onset of chain formation [see Fig. 12(c)]. Then steric interactions play a major role in the total interaction energy

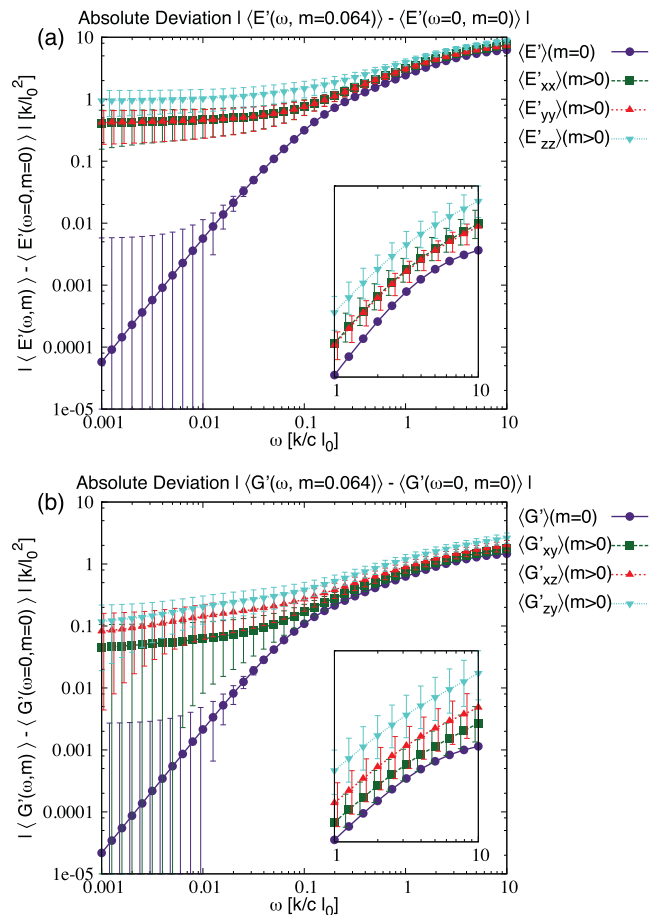


FIG. 16. Storage dynamic elastic moduli (a)  $\langle E'_{\alpha\alpha}(\omega) \rangle$  and (b)  $\langle G'_{\alpha\beta}(\omega) \rangle$  ( $\alpha, \beta = x, y, z$ ) of randomized fcc lattices with  $N = 1688$  for vanishing magnetic moment (solid line,  $\circ$ ), and  $m = 0.064m_0\hat{z}$  (dashed lines,  $\square, \triangle, \nabla$ ). We plot on a double logarithmic scale the absolute deviation from the respective average static modulus at  $m = 0$ . Data points and standard deviations are obtained from statistics over 80 differently randomized samples. For illustrative purposes we have slightly shifted the bars for different data sets horizontally to better distinguish the individual bars. Insets zoom onto the storage parts (a)  $\langle E'_{\alpha\alpha}(\omega) \rangle$  and (b)  $\langle G'_{\alpha\beta}(\omega) \rangle$  at large  $\omega$  to better resolve the different curves. Small values of the curves for the  $m = 0$  cases at low  $\omega$  indicate smooth convergence to the respective static moduli in Fig. 14.

$U$  (see Fig. 13). To better illustrate the behavior of the storage dynamic moduli in this regime it is convenient to plot the *deviation* from the respective static value at  $m = 0$ , as shown in Fig. 16 (for brevity, although deviations are plotted, the curves are still labeled by  $\langle E'_{\alpha\alpha} \rangle$  and  $\langle G'_{\alpha\beta} \rangle$ ). Thus the diminishing behavior of the curves  $\langle E' \rangle(m = 0)$  and  $\langle G' \rangle(m = 0)$  for decreasing  $\omega$  represents a smooth convergence of the moduli to the values for  $\omega = 0$ , similarly to the results in Fig. 15. Experimentally, deviations as small as  $0.01k/l_0^2 - 0.1k/l_0^2$  should be accessible within rheometer sensitivities.

The main difference between the small- and large- $m$  regimes is the qualitative change in  $\langle E'_{\alpha\alpha}(\omega) \rangle$  and  $\langle G'_{\alpha\beta}(\omega) \rangle$  ( $\alpha, \beta = x, y, z$ ) for increasing magnetic moment. For  $m \lesssim 0.06m_0$ , and according to the different geometries, we observed increase or decrease of the elastic moduli with increasing  $m$ . Conversely, for  $m \gtrsim 0.06m_0$  we observe all elastic moduli to increase with increasing magnetic interaction for all frequencies and geometries.

The storage Young's modulus for deformations in the  $m$ -direction  $\langle E'_{zz}(\omega) \rangle$  shows the most significant increase when compared to  $\langle E'_{xx}(\omega) \rangle$  and  $\langle E'_{yy}(\omega) \rangle$ . This trend continues at large  $m$  [see inset of Fig. 16(a)]. In a similar fashion, the large- $\omega$  behavior of the storage modulus  $\langle G'_{zy}(\omega) \rangle$  for shear deformations of the chains aligned along  $m$  [see inset of Fig. 16(b)] suggests a larger increase than for  $\langle G'_{xz}(\omega) \rangle$  and  $\langle G'_{xy}(\omega) \rangle$ . These overall trends of the dynamic moduli are further enhanced and increased for even larger  $m$ .

The loss components of the dynamic moduli, both Young and shear, show again an increase with increasing  $m$  over all frequencies and geometries. Furthermore, the amount of increase follows approximately the same trends as for the corresponding storage components (see Appendix F, Fig. 20).

## XI. CONCLUSIONS

We have described and applied a method to determine the dynamic elastic moduli in discretized mesoscopic model systems representing magnetic elastic composite materials. More precisely, we have confined ourselves to particle-based dipole-spring models<sup>54-59</sup> to characterize the behavior of magnetic gels and elastomers. The magnitudes of Young and shear moduli were evaluated for different frequencies, particle distributions, magnitudes and orientations of the magnetic moments. We find the elastic moduli to lowest order to increase or decrease with the magnitude of the magnetic moment according to the particle distribution, the selected orientation, and the selected frequency.

To summarize our results, we find that increasing magnetic interactions tends to line up the particles in the direction of the magnetic dipoles. This, in regular lattices, can result in different effects according to the considered structure. In general, however, we find the Young modulus in the directions of elongation to increase<sup>51</sup> and, vice versa, to decrease in the directions of shrinking. For randomized particle arrangements we find a "hardened" regime, where dipole-dipole attractions overcome the elastic spring interactions and the elastic moduli significantly

increase. Here, the increase of the storage part of the Young modulus in the direction parallel to the magnetic moments is significantly larger compared to the perpendicular directions, in agreement with experiments reported in the literature.<sup>38,92</sup> Furthermore, for all distributions (except for the randomized arrangements at high  $m$ ) we find the storage part of some of the investigated shear moduli to change tendency from increase to decrease with  $m$  or vice versa, for increasing frequency  $\omega$ . The loss component of the dynamic moduli follows an overall linear behavior for all cases at low and high  $\omega$  with a crossover regime in between. In conclusion, the behavior of the dynamic elastic moduli with varying  $m$  and  $\omega$  strongly depends on the spatial arrangement of the magnetic particles. The angles between the magnetic moments and the directions to find the nearest neighbors are crucial to determine whether, for a selected direction, the system shrinks or elongates when switching on magnetic interactions and whether the elastic moduli increase or decrease.

Our systems were of cubelike shape and finite size. On two opposing boundaries, we imposed prescribed force fields leading to an overall strain response of the whole system. The other boundaries remained unconstrained. Such a geometry is characteristic for experimental investigations using plate-plate rheometers. Assuming particle sizes in the micrometer range, our systems correspond to samples of several ten micrometers in thickness. Such experimental samples can be analyzed using piezorheometric devices.<sup>85,93</sup> In fact, for anisotropic magnetic gels, corresponding piezorheometric measurements were performed already more than a decade ago.<sup>81</sup> It will be interesting to compare our approach in more detail with such experimental investigations in the future.

It is important to model and understand the dynamic response of the materials at different frequencies in the view of many practical applications, from soft actuators<sup>24</sup> to vibration absorbers.<sup>25,26</sup> Our method explicitly connects the relaxational modes of the system on the mesoscopic level<sup>56</sup> with the macroscopic dynamic response.<sup>47,48,50,94</sup> Our approach allows to capture the internal rearrangements of the system under an externally applied stress or magnetic field and to link it to the consequences for the overall system behavior. Furthermore, our technique can be applied to any particle distribution, particularly also to those drawn from experimental analysis of real samples.<sup>55,56</sup>

Generalizations to systems composed of anisotropic particles,<sup>95</sup> as well as including rotational degrees of freedom<sup>36,54</sup> and possibly induced-dipole effects<sup>68,69</sup> could be added to the present framework in subsequent steps. Apart from that, the mesoscopically based dynamic investigations could be extended to more refined approaches, where the elastic matrix between discretized particles of finite volume is described in terms of continuum elasticity theory.<sup>34</sup> As indicated above, it will be possible to use experimental data<sup>44,55,56,96</sup> as input for the initial particle positions and compare calculated dynamic moduli with their measured counterparts, also as a function of magnetic interaction strengths. In a combined effort between experiments and theory, such an approach can serve to devise smarter and new materials with optimized magnetic field dependence and adjusted behavior at different frequencies.

## ACKNOWLEDGMENTS

The authors thank the Deutsche Forschungsgemeinschaft for support of this work through the priority program SPP 1681.

## APPENDIX A: STERIC REPULSION PARAMETERS

The relatively soft steric repulsion between two particles  $i$  and  $j$  at positions  $\mathbf{R}_i$  and  $\mathbf{R}_j$  connected by the vector  $\mathbf{r}_{ij} = \mathbf{R}_j - \mathbf{R}_i$  is modeled by a generic potential  $v^s(r_{ij})$ . Introducing the exponents  $p$  and  $q$ , the functional form of this potential is given by

$$v^s(r) = \varepsilon^s \left[ \left( \frac{r}{\sigma^s} \right)^{-p} - \left( \frac{r}{\sigma^s} \right)^{-q} - \left( \frac{r_c}{\sigma^s} \right)^{-p} + \left( \frac{r_c}{\sigma^s} \right)^{-q} - \frac{c^s (r - r_c)^2}{2} \right] \quad (\text{A1})$$

if  $r = |\mathbf{r}_{ij}| < r_c$  and  $v^s(r) = 0$  otherwise. The parameter  $r_c = \sigma^s (p/q)^{1/(p-q)}$  follows from the condition  $v^s(r_c)' = 0$ , whereas  $c^s$  is chosen such that  $v^s(r_c)'' = 0$ . We find

$$c^s = \frac{p^{-\frac{2+q}{p-q}} (p-q) q^{\frac{2+p}{p-q}}}{(\sigma^s)^2}. \quad (\text{A2})$$

## APPENDIX B: DERIVATIVES OF PAIR INTERACTION POTENTIALS

We consider pair interactions between particles  $i$  and  $j$ , at positions  $\mathbf{R}_i$  and  $\mathbf{R}_j$ , respectively, and connected by  $\mathbf{r}_{ij} = \mathbf{R}_j - \mathbf{R}_i$ . When the particles are linked by a harmonic spring, their harmonic pair interaction potential is

$$v_{ij}^{el} = \frac{k}{2\ell_{ij}^0} (r_{ij} - \ell_{ij}^0)^2, \quad (\text{B1})$$

compare with Eq. (1).  $r_{ij} = |\mathbf{r}_{ij}|$  and  $\ell_{ij}^0$  is the unstrained length of the spring. The gradient components ( $\alpha = x, y, z$ ) follow as (we here drop the  $ij$  subscripts for simplicity)

$$\frac{\partial v^{el}}{\partial r^\alpha} = \frac{k}{\ell^0} (r - \ell^0) \frac{r^\alpha}{r}. \quad (\text{B2})$$

The derivatives appearing below in Eq. (C4) are then

$$\frac{\partial^2 v^{el}}{\partial r^\beta \partial r^\alpha} = \frac{k}{\ell^0} \left[ \frac{r^\alpha r^\beta}{r^2} + (r - \ell^0) \frac{\delta^{\alpha\beta} r^2 - r^\alpha r^\beta}{r^3} \right]. \quad (\text{B3})$$

Furthermore, the steric repulsion pair potential  $v^s$  has been addressed in detail in Appendix A. The gradient components ( $\alpha = x, y, z$ ) of the steric pair potential [see Eq. (A1)] follow for  $r < r_c$  as

$$\frac{\partial v^s}{\partial r^\alpha} = \frac{-\varepsilon^s r^\alpha}{r} \left[ p \left( \frac{r}{\sigma^s} \right)^{-p} - \frac{q}{r} \left( \frac{r}{\sigma^s} \right)^{-q} + c^s (r - r_c) \right] \quad (\text{B4})$$

and vanish for  $r \geq r_c$ . The derivatives below contributing to Eq. (C4) are given by

$$\begin{aligned} \frac{\partial^2 v^s}{\partial r^\beta \partial r^\alpha} = & -\varepsilon^s \left\{ \left( \frac{\delta^{\alpha\beta}}{r^2} - 2 \frac{r^\alpha r^\beta}{r^4} \right) \left[ p \left( \frac{r}{\sigma^s} \right)^{-p} - q \left( \frac{r}{\sigma^s} \right)^{-q} \right] \right. \\ & - \frac{r^\alpha r^\beta}{r^4} \left[ p^2 \left( \frac{r}{\sigma^s} \right)^{-p} - q^2 \left( \frac{r}{\sigma^s} \right)^{-q} \right] \\ & \left. + c^s \left[ \frac{r^\alpha r^\beta}{r^2} + (r - r_c) \frac{\delta^{\alpha\beta} r^2 - r^\alpha r^\beta}{r^3} \right] \right\} \quad (\text{B5}) \end{aligned}$$

for  $r < r_c$  and vanish when  $r \geq r_c$ .

Finally, the magnetic pair interaction potential  $v^m$  as in Eq. (4) reads

$$v_{ij}^m = \frac{m^2 r_{ij}^2 - 3(\mathbf{m} \cdot \mathbf{r}_{ij})^2}{r_{ij}^5} \quad (\text{B6})$$

in using reduced units. The gradient components ( $\alpha = x, y, z$ ) of the previous expression read

$$\frac{\partial v^m}{\partial r^\alpha} = -\frac{3}{r^5} \left[ m^2 r^\alpha + 2m^\alpha (\mathbf{m} \cdot \mathbf{r}) - 5 \frac{r^\alpha (\mathbf{m} \cdot \mathbf{r})^2}{r^2} \right]. \quad (\text{B7})$$

The derivatives appearing below in Eq. (C4) are given by

$$\begin{aligned} \frac{\partial^2 v^m}{\partial r^\beta \partial r^\alpha} = & -\frac{3}{r^5} \left[ m^2 \delta^{\alpha\beta} - 5m^2 r^\alpha r^\beta r^{-2} \right. \\ & - 10(\mathbf{m} \cdot \mathbf{r}) r^{-2} (m^\alpha r^\beta + m^\beta r^\alpha) + 2m^\alpha m^\beta \\ & \left. - 5(\mathbf{m} \cdot \mathbf{r})^2 r^{-2} (\delta^{\alpha\beta} - 7r^\alpha r^\beta r^{-2}) \right]. \quad (\text{B8}) \end{aligned}$$

## APPENDIX C: HESSIAN MATRIX FOR PAIR INTERACTION POTENTIALS

Here we repeat in detail the derivation of the Hessian for a system interacting solely via pair potentials. That is, any two particles  $i$  and  $j$  at positions  $\mathbf{R}_i$  and  $\mathbf{R}_j$  interact through a pair potential  $v$  depending only on the connecting vector  $\mathbf{r}_{ij} = \mathbf{R}_j - \mathbf{R}_i$ . Then we can write

$$U = \frac{1}{2} \sum_{\substack{i,j=1 \\ i \neq j}}^N v(\mathbf{r}_{ij}), \quad (\text{C1})$$

where  $N$  is the total number of particles. Again,  $\mathbf{R}_i$  is the position of the  $i$ -th particle ( $i = 1 \dots N$ ),  $\mathbf{r}_{ij} = \mathbf{R}_j - \mathbf{R}_i$ , and we denote by  $R_i^\alpha$  ( $\alpha = x, y, z$ ) the  $\alpha$ -component of  $\mathbf{R}_i$ . For reasons of symmetry,  $v(\mathbf{r}_{ij}) = v(\mathbf{r}_{ji})$ . The sum in Eq. (C1) together with the prefactor  $\frac{1}{2}$  then runs over all different pairs counting each of them only once. We abbreviate  $v_{ij} = v(\mathbf{r}_{ij})$ . The gradient components ( $\alpha = x, y, z$ ) of the energy  $U$  follow as

$$\begin{aligned} \frac{\partial U}{\partial R_k^\alpha} = & \frac{1}{2} \sum_{\substack{i,j=1 \\ i \neq j}}^N \frac{\partial v_{ij}}{\partial R_k^\alpha} \\ = & \sum_{\substack{j=1 \\ j \neq k}}^N \frac{\partial v_{kj}}{\partial R_k^\alpha} = - \sum_{\substack{j=1 \\ j \neq k}}^N \frac{\partial v_{kj}}{\partial R_{kj}^\alpha}, \quad (\text{C2}) \end{aligned}$$

setting the force  $-\partial U / \partial \mathbf{R}_k$  on the positional degrees of freedom of the  $k$ -th particle.

Next, we obtain the Hessian of the system as

$$\frac{\partial^2 U}{\partial R_i^\alpha \partial R_k^\beta} = \begin{cases} \frac{\partial^2 v_{ik}}{\partial R_i^\alpha \partial R_k^\beta} & (i \neq k), \\ \sum_{\substack{j=1 \\ j \neq i}}^N \frac{\partial^2 v_{ij}}{\partial R_i^\alpha \partial R_i^\beta} & (i = k). \end{cases} \quad (\text{C3})$$

Thus, for pair interactions, the diagonal elements of the Hessian contain the second derivatives of all pair interactions, whereas the off-diagonal elements are given by a single term. Since  $\mathbf{r}_{ij} = \mathbf{R}_j - \mathbf{R}_i$ , the previous equation can be expressed in terms of connecting vectors only,

$$\frac{\partial^2 U}{\partial R_i^\alpha \partial R_k^\beta} = \begin{cases} -\frac{\partial^2 v_{ik}}{\partial r_{ik}^\alpha \partial r_{ik}^\beta} & (i \neq k), \\ \sum_{\substack{j=1 \\ j \neq i}}^N \frac{\partial^2 v_{ij}}{\partial r_{ij}^\alpha \partial r_{ij}^\beta} & (i = k). \end{cases} \quad (\text{C4})$$

#### APPENDIX D: TORQUE-FREE FORCE FIELDS

Our scope is to describe the system behavior for preselected specified orientations. However, both during the search for the corresponding equilibrium state of the system (see Section III) and the implementation of an external force (see Section V B), the system may tend to perform a rigid rotation. We therefore must exclude such rigid rotations. Here we describe a simple method to redefine the generalized force field (or likewise the gradient of the total energy) so that the net overall torque on the system vanishes.

We consider the force field  $\mathbf{f}$  acting on the particles at positions  $\mathbf{R}_i$  with components  $f_i$  ( $i = 1, \dots, N$ ). The net torque  $\boldsymbol{\tau}$  is given by

$$\boldsymbol{\tau} = \sum_{i=1}^N \mathbf{q}_i \times \mathbf{f}_i, \quad (\text{D1})$$

where  $\mathbf{q}_i = \mathbf{R}_i - \mathbf{R}_c$  is the distance of the particle positions  $\mathbf{R}_i$  from the center of mass  $\mathbf{R}_c = \frac{1}{N} \sum_i \mathbf{R}_i$ . To prevent, e.g., a global rotation of the system around the  $z$ -axis, the  $z$ -component of  $\boldsymbol{\tau}$ , i.e.,  $\tau^z$ , must vanish. We define a uniform, counter-clockwise rotational force field around the  $z$ -axis  $\mathbf{P}(\mathbf{q}) = c_R(-q^y, q^x, 0)$ , with  $\mathbf{q}$  a vector in the  $xy$ -plane and  $c_R$  a constant. Next, we determine  $c_R$  by imposing  $\mathbf{P}$  to have the same torque as given by  $\mathbf{f}$ ,

$$\begin{aligned} \sum_{i=1}^N (\mathbf{q}_i \times \mathbf{f}_i)^z &= \tau^z = \sum_{i=1}^N [\mathbf{q}_i \times \mathbf{P}(\mathbf{q}_i)]^z \\ &= c_R \sum_{i=1}^N [(q_i^x)^2 + (q_i^y)^2]. \end{aligned} \quad (\text{D2})$$

We obtain the field  $\mathbf{P}$  by solving for the constant  $c_R$ , leading to

$$c_R = \frac{\tau^z}{\sum_{i=1}^N [(q_i^x)^2 + (q_i^y)^2]}. \quad (\text{D3})$$

Therefore we can make  $\mathbf{f}$  “torque-free” concerning the  $z$ -direction by subtracting  $\mathbf{P}$ , i.e.,  $\mathbf{f}_i \rightarrow \mathbf{f}_i - \mathbf{P}(\mathbf{q}_i)$  ( $i = 1, \dots, N$ ). By repeating the procedure for the remaining directions, we get rid of the rigid rotations induced by  $\mathbf{f}$  and obtain a torque-free force field.

#### APPENDIX E: STATIC YOUNG MODULI OF REGULAR LATTICES

We here present a simple energy argument to interpret the behavior of the Young moduli of the regular lattices presented in Sections VIII and IX. A regular lattice is generated by the basis vectors  $\mathbf{a}_1$ ,  $\mathbf{a}_2$ , and  $\mathbf{a}_3$ . Therefore a lattice point can be written as  $\mathbf{r}_{ijk} = i\mathbf{a}_1 + j\mathbf{a}_2 + k\mathbf{a}_3$ , with  $i, j, k \in \mathbb{Z}$  integers. If the particles interact by the pair potential  $v$ , the total energy per particle in an infinitely extended lattice is given by

$$U_p = \frac{1}{2} \sum_{n \in \mathcal{N}_0} v(\mathbf{r}_n), \quad (\text{E1})$$

where the sum runs over all lattice points (origin excluded) labeled by the discrete index  $n$  contained in the set  $\mathcal{N}_0 = \mathbb{Z}^3 \setminus \{(0, 0, 0)\}$ .

Since we consider the regular lattice to be the ground state of the system, a small deformation that transforms  $\mathbf{r}_n \rightarrow \mathbf{r}'_n$  ( $n \in \mathcal{N}_0$ ) has an energy-per-particle cost that to lowest order reads

$$\Delta U_p = \frac{1}{2} \sum_{n \in \mathcal{N}_0} \frac{1}{2} \mathbf{u}_n^\top \cdot \mathbf{h}(\mathbf{r}_n) \cdot \mathbf{u}_n, \quad (\text{E2})$$

where  $\mathbf{u}_n = \mathbf{r}'_n - \mathbf{r}_n$ ,  $\top$  indicates transposition, and  $\mathbf{h}(\mathbf{r}_n)$  is the Hessian matrix of the interaction  $v(\mathbf{r}_n)$  between the particle fixed in the origin and the  $n$ th neighbor. Its elements are given by  $h^{\mu\nu}(\mathbf{r}_n) = \partial^2 v(\mathbf{r}_n) / \partial r_n^\mu \partial r_n^\nu$ , with  $\mu, \nu = x, y, z$ .

The displacements  $\mathbf{u}_n = \mathbf{D} \cdot \mathbf{r}_n$  corresponding to a uniform strain are given by the constant components of the displacement tensor  $\mathbf{D}$ . The energy of the strain deformation then follows as

$$\begin{aligned} \Delta U_p &= \frac{1}{2} \sum_{\alpha\beta\gamma\delta} C_0^{\alpha\beta\gamma\delta} D^{\alpha\beta} D^{\gamma\delta} \\ \text{with } C_0^{\alpha\beta\gamma\delta} &= \frac{1}{2} \sum_{n \in \mathcal{N}_0} r_n^\alpha h^{\beta\gamma}(\mathbf{r}_n) r_n^\delta, \end{aligned} \quad (\text{E3})$$

where  $\alpha, \beta, \gamma, \delta = x, y, z$ .

In the following we focus on compressive/dilative strains and therefore consider diagonal  $\mathbf{D}$  displacement tensors. For an applied strain  $\varepsilon_{\alpha\alpha}$  along the  $\alpha$ -direction  $D^{\alpha\alpha} \neq 0$  is imposed. The remaining components of  $\mathbf{D}$  are relaxed to minimize the lattice energy

$$\frac{\partial \Delta U_p}{\partial D^{\mu\mu}} = 0, \quad \forall \mu \neq \alpha. \quad (\text{E4})$$

This leads to a system of linear equations the solution of which relates the components  $D^{\mu\mu}$  ( $\mu \neq \alpha$ ) to the imposed deformation  $D^{\alpha\alpha}$ . As a result, we obtain Young's modulus

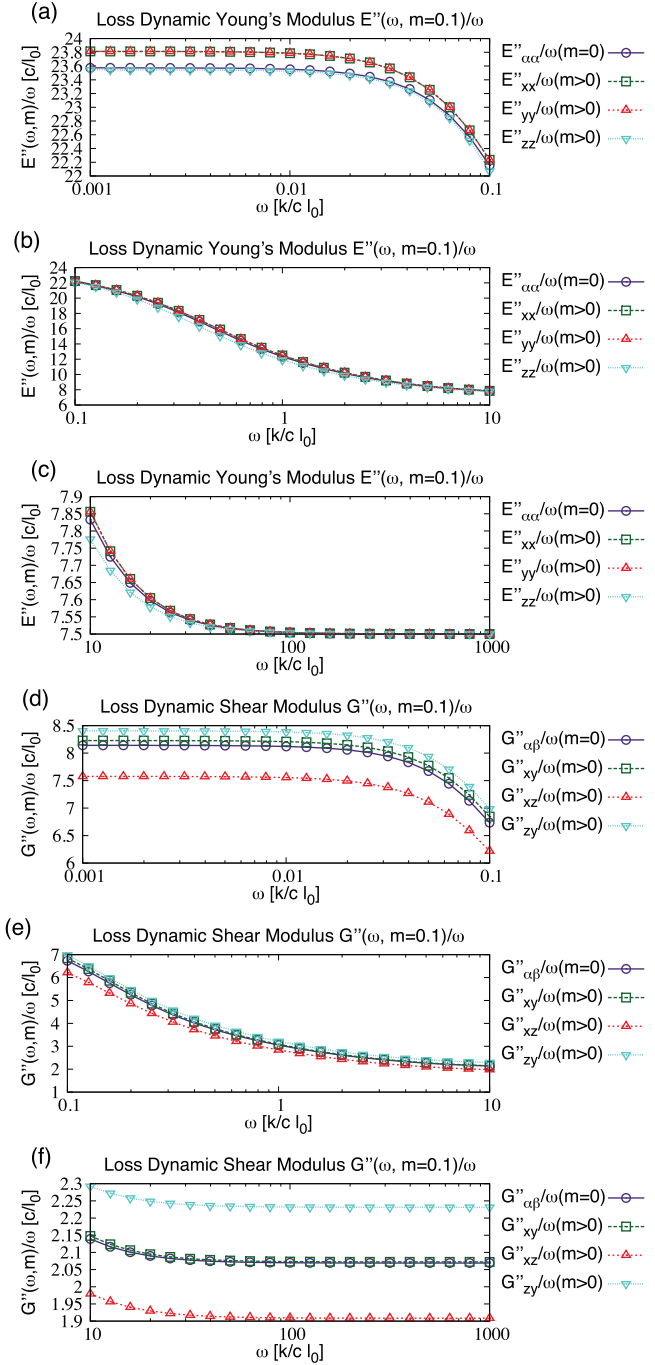


FIG. 17. Loss parts ((a)–(c))  $E''_{\alpha\alpha}(\omega)$  and ((d)–(f))  $G''_{\alpha\beta}(\omega)$  ( $\alpha, \beta = x, y, z$ ) for the dynamic elastic moduli of a simple cubic lattice with  $N = 3375$  for vanishing magnetic moment (solid line,  $\circ$ ), and  $m = 0.1m_0\hat{z}$  (dashed lines,  $\square, \Delta, \nabla$ ). Because of the overall trend of a linear increase with frequency at low and high frequencies, we here present the moduli divided by  $\omega$ . Zoom-ins onto the low-, intermediate-, and high- $\omega$  regions are shown in panels (a) and (d), (b) and (e), and (c) and (f), respectively.

$E_{\alpha\alpha}$  [following the notation as in the main text, see Eq. (16)] given by

$$E_{\alpha\alpha} = \frac{1}{V_p} \frac{d^2 \Delta U_p}{(dD^{\alpha\alpha})^2} = \frac{1}{V_p} (C_0^{\alpha\alpha} - B^\alpha) \quad (E5)$$

$$\text{with } B^\alpha = \sum_{\beta\gamma} C_0^{\alpha\beta} \frac{C_0^{\gamma\gamma} C_0^{\alpha\beta} - C_0^{\alpha\gamma} C_0^{\beta\gamma}}{C_0^{\beta\beta} C_0^{\gamma\gamma} - (C_0^{\beta\gamma})^2} (\epsilon^{\alpha\beta\gamma})^2,$$

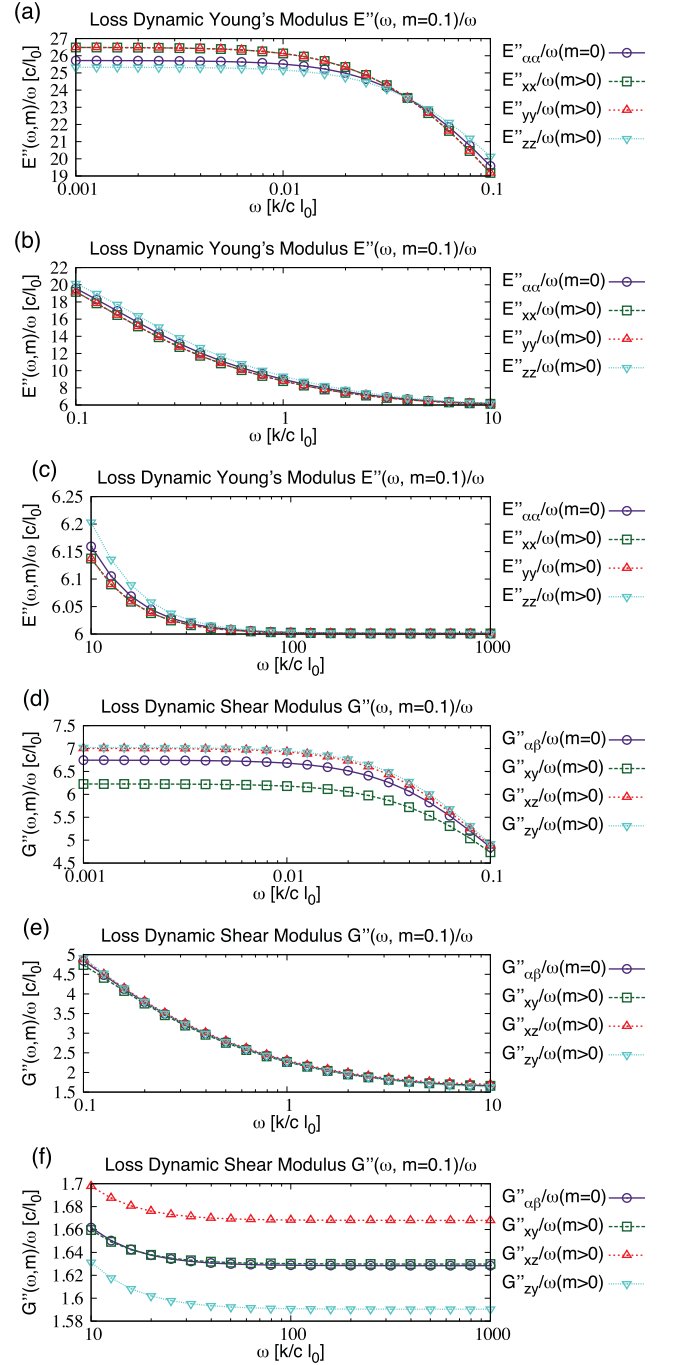


FIG. 18. Loss parts ((a)–(c))  $E''_{\alpha\alpha}(\omega)$  and ((d)–(f))  $G''_{\alpha\beta}(\omega)$  ( $\alpha, \beta = x, y, z$ ) for the dynamic elastic moduli of an fcc lattice with  $N = 3430$  for vanishing magnetic moment (solid line,  $\circ$ ), and  $m = 0.1m_0\hat{z}$  (dashed lines,  $\square, \Delta, \nabla$ ). Since the loss moduli increase linearly with the frequency at low and high frequencies, we here show them divided by  $\omega$ . Zoom-ins onto the low-, intermediate-, and high- $\omega$  regions are shown in panels (a) and (e), and (c), and (f), respectively.

where  $V_p = 1/\rho = V/N$  is the volume per particle, we abbreviated  $C_0^{\alpha\beta} = C_0^{\alpha\alpha\beta\beta}$ , and  $\epsilon^{\alpha\beta\gamma}$  is the Levi-Civita symbol. The contributions  $-B^\alpha$  to the elastic moduli take into account relaxation along the remaining perpendicular axes and lower the moduli.

For small values of the magnetic moment  $m$ , we write, to lowest order in  $m$ ,  $\mathbf{h}(\mathbf{r}_n) = \mathbf{h}_0(\mathbf{r}_n) + m^2 \mathbf{h}_m(\mathbf{r}_n)$ , where the elements of the matrix  $m^2 \mathbf{h}_m(\mathbf{r}_n)$  are as listed in Eq. (B8).

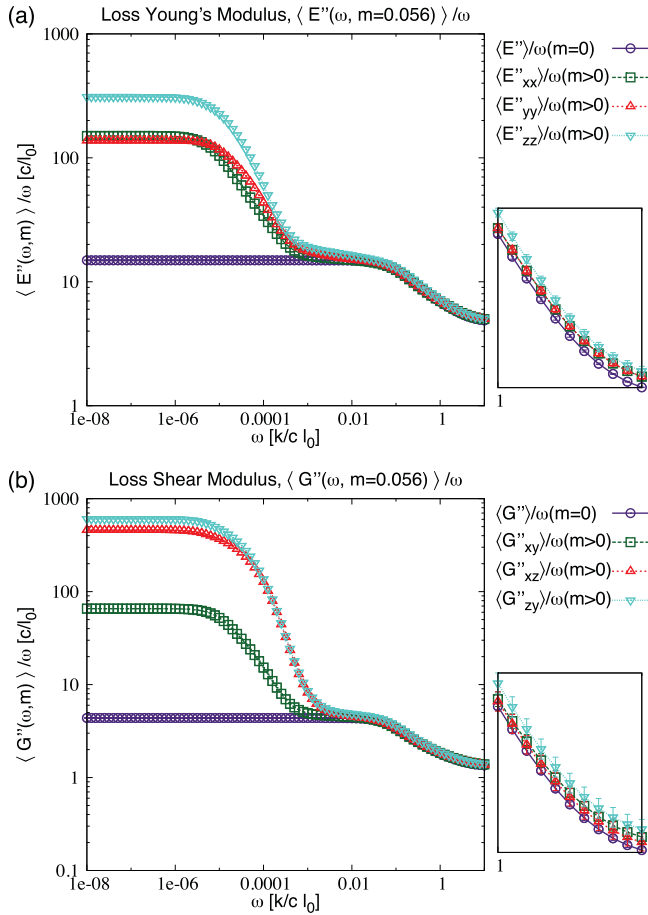


FIG. 19. Average loss parts ((a) and (b))  $\langle E''_{\alpha\alpha}(\omega) \rangle$  and ((c) and (d))  $\langle G''_{\alpha\beta}(\omega) \rangle$  ( $\alpha, \beta = x, y, z$ ) for the dynamic elastic moduli of randomized fcc lattices with  $N = 1688$  for vanishing magnetic moment (solid line,  $\circ$ ), and  $m = 0.056 m_0 \hat{z}$  (dashed lines,  $\square, \triangle, \nabla$ ). Because of the overall trend of a linear increase with frequency at low and high frequencies, we here present the moduli divided by  $\omega$ . Data points and standard deviations are obtained by averaging over 80 differently randomized samples. Because of the different randomizations, the initial slope of the moduli in the  $\omega \rightarrow 0$  limit can vary significantly, thus leading to large bars in the small- $\omega$  regime and for the  $m > 0$  cases, which are not shown here. Insets (a) and (b) zoom in onto the Young and shear loss moduli behavior, respectively, at high frequencies for better resolving the individual curves.

Thus, we can obtain both the static Young's modulus at  $m = 0$  and the initial quadratic behavior for small  $m$ .

## APPENDIX F: ADDITIONAL INFORMATION ON THE LOSS PART OF THE DYNAMIC ELASTIC MODULI

Here we show in more detail the various behaviors of the loss part of the dynamic moduli as functions of frequency  $\omega$  and magnitude of the magnetic moment  $m$  for the different considered geometries. As we have mentioned before, we find as a general trend the loss parts to linearly increase with  $\omega$  at low and high frequencies. It results from our viscous friction term [see Eq. (19)] which, in the case of an oscillatory deformation as in Eq. (22), is proportional to  $\omega$ . Moreover, it is consistent with the predicted loss component of the dynamic moduli in the Kelvin-Voigt model.<sup>89,90</sup> Therefore, and for better illustration, we plot the loss parts after division by  $\omega$ . The agreement with linear behavior is confirmed in this way, i.e.,  $E''_{\alpha\alpha}(\omega)/\omega$  and  $G''_{\alpha\beta}(\omega)/\omega$  ( $\alpha, \beta = x, y, z$ ) converge

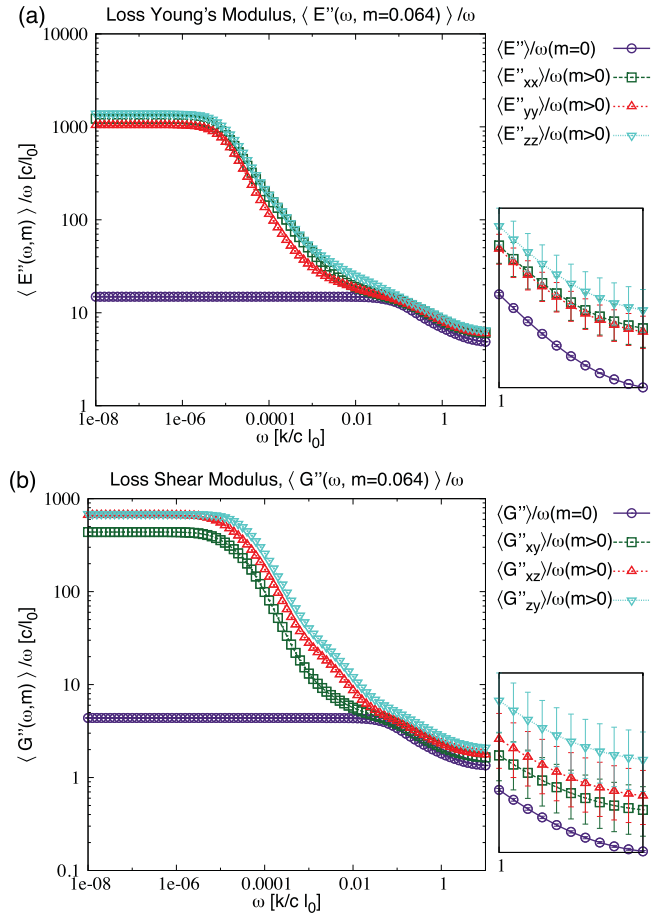


FIG. 20. Average loss parts ((a) and (b))  $\langle E''_{\alpha\alpha}(\omega) \rangle$  and ((c) and (d))  $\langle G''_{\alpha\beta}(\omega) \rangle$  ( $\alpha, \beta = x, y, z$ ) for the dynamic elastic moduli of randomized fcc lattices with  $N = 1688$  for vanishing magnetic moment (solid line,  $\circ$ ), and  $m = 0.064 m_0 \hat{z}$  (dashed lines,  $\square, \triangle, \nabla$ ). Since the loss moduli increase linearly with the frequency at low and high frequencies, we here show them divided by  $\omega$ . Data points and standard deviations are obtained by averaging over 80 differently randomized samples. Because of the different randomizations, the initial slope of the moduli in the  $\omega \rightarrow 0$  limit can vary significantly, thus leading to large bars in the small- $\omega$  regime and for the  $m > 0$  cases, which are not shown here. Insets zoom in onto the (a) Young and (b) shear loss moduli behavior at high frequencies for better resolving the individual curves.

to a finite value in both the low- and high- $\omega$  limit, see Figs. 17–20.

On the one hand, the regular lattices addressed in Sections VIII and IX show different trends for the loss parts as functions of  $m$  and  $\omega$ , as mentioned in the main text and illustrated in Figs. 17 and 18. On the other hand our randomized lattices generally show increasing loss parts with increasing  $m$  for all frequencies, although the amount of gain varies with the selected geometries, see Figs. 19 and 20.

<sup>1</sup>G. Filipcsei, I. Csetneki, A. Szilágyi, and M. Zrinyi, *Adv. Polym. Sci.* **206**, 137 (2007).

<sup>2</sup>A. M. Menzel, *Phys. Rep.* **554**, 1 (2015).

<sup>3</sup>M. Lopez-Lopez, J. D. Durán, L. Y. Iskakova, and A. Y. Zubarev, *J. Nanofluids* **5**, 479 (2016).

<sup>4</sup>S. Odenbach, *Arch. Appl. Mech.* **86**, 269 (2016).

<sup>5</sup>E. Jarkova, H. Pleiner, H.-W. Müller, and H. R. Brand, *Phys. Rev. E* **68**, 041706 (2003).

<sup>6</sup>M. Zrinyi, L. Barsi, and A. Büki, *J. Chem. Phys.* **104**, 8750 (1996).

<sup>7</sup>G. V. Stepanov, S. S. Abramchuk, D. A. Grishin, L. V. Nikitin, E. Y. Kramarenko, and A. R. Khokhlov, *Polymer* **48**, 488 (2007).

- <sup>8</sup>X. Guan, X. Dong, and J. Ou, *J. Magn. Magn. Mater.* **320**, 158 (2008).
- <sup>9</sup>H. Böse and R. Röder, *J. Phys.: Conf. Ser.* **149**, 012090 (2009).
- <sup>10</sup>X. Gong, G. Liao, and S. Xuan, *Appl. Phys. Lett.* **100**, 211909 (2012).
- <sup>11</sup>B. A. Evans, B. L. Fiser, W. J. Prins, D. J. Rapp, A. R. Shields, D. R. Glass, and R. Superfine, *J. Magn. Magn. Mater.* **324**, 501 (2012).
- <sup>12</sup>D. Y. Borin, G. V. Stepanov, and S. Odenbach, *J. Phys.: Conf. Ser.* **412**, 012040 (2013).
- <sup>13</sup>R. E. Rosensweig, *Ferrohydrodynamics* (Cambridge University Press, Cambridge, 1985).
- <sup>14</sup>S. Odenbach, *Colloids Surf., A* **217**, 171 (2003).
- <sup>15</sup>S. Odenbach, *Magnetoviscous Effects in Ferrofluids* (Springer, Berlin, Heidelberg, 2003).
- <sup>16</sup>S. Odenbach, *J. Phys.: Condens. Matter* **16**, R1135 (2004).
- <sup>17</sup>B. Huke and M. Lücke, *Rep. Prog. Phys.* **67**, 1731 (2004).
- <sup>18</sup>P. Ilg, M. Kröger, and S. Hess, *J. Magn. Magn. Mater.* **289**, 325 (2005).
- <sup>19</sup>C. Holm and J.-J. Weis, *Curr. Opin. Colloid Interface Sci.* **10**, 133 (2005).
- <sup>20</sup>S. H. L. Klapp, *J. Phys.: Condens. Matter* **17**, R525 (2005).
- <sup>21</sup>S. M. Cattes, S. H. L. Klapp, and M. Schoen, *Phys. Rev. E* **91**, 052127 (2015).
- <sup>22</sup>S. D. Peroukidis and S. H. L. Klapp, *Phys. Rev. E* **92**, 010501 (2015).
- <sup>23</sup>S. H. L. Klapp, *Curr. Opin. Colloid Interface Sci.* **21**, 76 (2016).
- <sup>24</sup>K. Zimmermann, V. A. Naletova, I. Zeidis, V. Böhm, and E. Kolev, *J. Phys.: Condens. Matter* **18**, S2973 (2006).
- <sup>25</sup>H.-X. Deng, X.-L. Gong, and L.-H. Wang, *Smart Mater. Struct.* **15**, N111 (2006).
- <sup>26</sup>T. L. Sun, X. L. Gong, W. Q. Jiang, J. F. Li, Z. B. Xu, and W. Li, *Polym. Test.* **27**, 520 (2008).
- <sup>27</sup>D. Szabó, G. Szeghy, and M. Zrínyi, *Macromolecules* **31**, 6541 (1998).
- <sup>28</sup>R. V. Ramanujan and L. L. Lao, *Smart Mater. Struct.* **15**, 952 (2006).
- <sup>29</sup>M. Babincová, D. Leszczynska, P. Sourivong, P. Čičmanec, and P. Babinec, *J. Magn. Magn. Mater.* **225**, 109 (2001).
- <sup>30</sup>L. L. Lao and R. V. Ramanujan, *J. Mater. Sci.: Mater. Med.* **15**, 1061 (2004).
- <sup>31</sup>N. Frickel, R. Messing, and A. M. Schmidt, *J. Mater. Chem.* **21**, 8466 (2011).
- <sup>32</sup>E. Allahyarov, A. M. Menzel, L. Zhu, and H. Löwen, *Smart Mater. Struct.* **23**, 115004 (2014).
- <sup>33</sup>M. Kästner, S. Müller, J. Goldmann, C. Spieler, J. Brummund, and V. Ulbricht, *Int. J. Numer. Methods Eng.* **93**, 1403 (2013).
- <sup>34</sup>P. Cremer, H. Löwen, and A. M. Menzel, *Appl. Phys. Lett.* **107**, 171903 (2015).
- <sup>35</sup>S. Huang, G. Pessot, P. Cremer, R. Weeber, C. Holm, J. Nowak, S. Odenbach, A. M. Menzel, and G. K. Auernhammer, *Soft Matter* **12**, 228 (2016).
- <sup>36</sup>R. Weeber, S. Kantorovich, and C. Holm, *J. Chem. Phys.* **143**, 154901 (2015).
- <sup>37</sup>J. L. Mietta, P. I. Tamborenea, and R. Martin Negri, *Soft Matter* **12**, 6430 (2016).
- <sup>38</sup>Z. Varga, G. Filipcsei, and M. Zrínyi, *Polymer* **47**, 227 (2006).
- <sup>39</sup>H. Haider, C. Yang, W. J. Zheng, J. Yang, M. X. Wang, M. Zrínyi, S. Sang, Y. Osada, Z. Suo, Q. Zhang *et al.*, *Soft Matter* **11**, 8253 (2015).
- <sup>40</sup>E. I. Wisotzki, M. Hennes, C. Schuldt, F. Engert, W. Knolle, U. Decker, J. A. Kas, M. Zink, and S. G. Mayr, *J. Mater. Chem. B* **2**, 4297 (2014).
- <sup>41</sup>R. Weeber, S. Kantorovich, and C. Holm, *Soft Matter* **8**, 9923 (2012).
- <sup>42</sup>L. Roeder, P. Bender, M. Kundt, A. Tschöpe, and A. M. Schmidt, *Phys. Chem. Chem. Phys.* **17**, 1290 (2015).
- <sup>43</sup>R. Messing, N. Frickel, L. Belkoura, R. Strey, H. Rahn, S. Odenbach, and A. M. Schmidt, *Macromolecules* **44**, 2990 (2011).
- <sup>44</sup>T. Gundermann and S. Odenbach, *Smart Mater. Struct.* **23**, 105013 (2014).
- <sup>45</sup>J. Landers, L. Roeder, S. Salamon, A. M. Schmidt, and H. Wende, *J. Phys. Chem. C* **119**, 20642 (2015).
- <sup>46</sup>C. Garcia, Y. Zhang, F. DiSalvo, and U. Wiesner, *Angew. Chem., Int. Ed.* **42**, 1526 (2003).
- <sup>47</sup>H. R. Brand, A. Fink, and H. Pleiner, *Eur. Phys. J. E* **38**, 65 (2015).
- <sup>48</sup>H. R. Brand and H. Pleiner, *Eur. Phys. J. E* **37**, 122 (2014).
- <sup>49</sup>A. Y. Zubarev, *Soft Matter* **8**, 3174 (2012).
- <sup>50</sup>S. Bohlius, H. R. Brand, and H. Pleiner, *Phys. Rev. E* **70**, 061411 (2004).
- <sup>51</sup>D. Ivaneyko, V. Toshchevikov, M. Saphiannikova, and G. Heinrich, *Condens. Matter Phys.* **15**, 33601 (2012).
- <sup>52</sup>M. R. Dudek, B. Grabiec, and K. W. Wojciechowski, *Rev. Adv. Mater. Sci.* **14**, 167 (2007).
- <sup>53</sup>D. S. Wood and P. J. Camp, *Phys. Rev. E* **83**, 011402 (2011).
- <sup>54</sup>M. A. Annunziata, A. M. Menzel, and H. Löwen, *J. Chem. Phys.* **138**, 204906 (2013).
- <sup>55</sup>G. Pessot, P. Cremer, D. Y. Borin, S. Odenbach, H. Löwen, and A. M. Menzel, *J. Chem. Phys.* **141**, 124904 (2014).
- <sup>56</sup>M. Tarama, P. Cremer, D. Y. Borin, S. Odenbach, H. Löwen, and A. M. Menzel, *Phys. Rev. E* **90**, 042311 (2014).
- <sup>57</sup>P. A. Sánchez, J. J. Cerdà, T. Sintes, and C. Holm, *J. Chem. Phys.* **139**, 044904 (2013).
- <sup>58</sup>J. J. Cerdà, P. A. Sánchez, C. Holm, and T. Sintes, *Soft Matter* **9**, 7185 (2013).
- <sup>59</sup>D. Ivaneyko, V. Toshchevikov, and M. Saphiannikova, *Soft Matter* **11**, 7627 (2015).
- <sup>60</sup>C. Spieler, M. Kästner, J. Goldmann, J. Brummund, and V. Ulbricht, *Acta Mech.* **224**, 2453 (2013).
- <sup>61</sup>Y. L. Raikher, O. V. Stolbov, and G. V. Stepanov, *J. Phys. D: Appl. Phys.* **41**, 152002 (2008).
- <sup>62</sup>O. V. Stolbov, Y. L. Raikher, and M. Balasoïu, *Soft Matter* **7**, 8484 (2011).
- <sup>63</sup>Y. Han, W. Hong, and L. E. Faidley, *Int. J. Solids Struct.* **50**, 2281 (2013).
- <sup>64</sup>R. Weeber, S. Kantorovich, and C. Holm, *J. Magn. Magn. Mater.* **383**, 262 (2015).
- <sup>65</sup>A. M. Menzel, *J. Chem. Phys.* **141**, 194907 (2014).
- <sup>66</sup>G. Pessot, R. Weeber, C. Holm, H. Löwen, and A. M. Menzel, *J. Phys.: Condens. Matter* **27**, 325105 (2015).
- <sup>67</sup>I. A. Belyaeva, E. Kramarenko, G. V. Stepanov, V. Sorokin, D. Stadler, and M. Shamonin, *Soft Matter* **12**, 2901 (2016).
- <sup>68</sup>A. M. Biller, O. V. Stolbov, and Y. L. Raikher, *J. Appl. Phys.* **116**, 114904 (2014).
- <sup>69</sup>E. Allahyarov, H. Löwen, and L. Zhu, *Phys. Chem. Chem. Phys.* **17**, 32479 (2015).
- <sup>70</sup>J. D. Weeks, D. Chandler, and H. C. Andersen, *J. Chem. Phys.* **54**, 5237 (1971).
- <sup>71</sup>W. W. Hager and Z. Hongchao, *SIAM J. Optim.* **16**, 170 (2005).
- <sup>72</sup>H. Shintani and H. Tanaka, *Nat. Mater.* **7**, 870 (2008).
- <sup>73</sup>L. Rovigatti, W. Kob, and F. Sciortino, *J. Chem. Phys.* **135**, 104502 (2011).
- <sup>74</sup>E. Lerner, E. DeGiuli, G. Düring, and M. Wyart, *Soft Matter* **10**, 5085 (2014).
- <sup>75</sup>D. Frenkel and B. Smit, *Understanding Molecular Simulation*, 2nd ed. (Academic Press, San Diego, 2002).
- <sup>76</sup>D. Frenkel and A. J. C. Ladd, *Phys. Rev. Lett.* **59**, 1169 (1987).
- <sup>77</sup>D. Squire, A. Holt, and W. Hoover, *Physica* **42**, 388 (1969).
- <sup>78</sup>M. Born, *J. Chem. Phys.* **7**, 591 (1939).
- <sup>79</sup>T. Fuereder and P. Ilg, *J. Chem. Phys.* **142**, 144505 (2015).
- <sup>80</sup>M. V. Jarić and U. Mohanty, *Phys. Rev. B* **37**, 4441 (1988).
- <sup>81</sup>D. Collin, G. K. Auernhammer, O. Gavat, P. Martinoty, and H. R. Brand, *Macromol. Rapid Commun.* **24**, 737 (2003).
- <sup>82</sup>L. D. Landau and E. M. Lifshitz, *Elasticity Theory* (Pergamon Press, 1975).
- <sup>83</sup>E. Anderson, Z. Bai, C. Bischof, S. Blackford, J. Demmel, J. Dongarra, J. Du Croz, A. Greenbaum, S. Hammarling, A. McKenney *et al.*, *LAPACK Users' Guide*, 3rd ed. (Society for Industrial and Applied Mathematics, Philadelphia, 1999).
- <sup>84</sup>A. Ivlev, H. Löwen, G. Morfill, and C. P. Royall, *Complex Plasmas and Colloidal Dispersions* (World Scientific, 2012).
- <sup>85</sup>J. J. Zanna, P. Stein, J. D. Marty, M. Mauzac, and P. Martinoty, *Macromolecules* **35**, 5459 (2002).
- <sup>86</sup>M. Sedlacik, M. Mrlik, V. Babayan, and V. Pavlinek, *Compos. Struct.* **135**, 199 (2016).
- <sup>87</sup>E. Roeben, L. Roeder, S. Teusch, M. Effertz, U. K. Deiters, and A. M. Schmidt, *Colloid Polym. Sci.* **292**, 2013 (2014).
- <sup>88</sup>N. Hohlbein, A. Shaaban, and A. M. Schmidt, *Polymer* **69**, 301 (2015).
- <sup>89</sup>F. Mainardi and G. Spada, *Eur. Phys. J.: Spec. Top.* **193**, 133 (2011).
- <sup>90</sup>L. B. Eldred, W. P. Baker, and A. N. Palazotto, *AIAA J.* **33**, 547 (1995).
- <sup>91</sup>N. W. Ashcroft and N. D. Mermin, *Solid State Physics* (Saunders, 1976).
- <sup>92</sup>G. Schubert and P. Harrison, *Smart Mater. Struct.* **25**, 015015 (2016).
- <sup>93</sup>M. Roth, M. D'Acunzi, D. Vollmer, and G. K. Auernhammer, *J. Chem. Phys.* **132**, 124702 (2010).
- <sup>94</sup>A. M. Menzel, *Phys. Rev. E* **94**, 023003 (2016).
- <sup>95</sup>C. Passow, B. ten Hagen, H. Löwen, and J. Wagner, *J. Chem. Phys.* **143**, 044903 (2015).
- <sup>96</sup>S. Günther and S. Odenbach, *Transp. Porous Media* **112**, 105 (2016).



# Paper V Tunable dynamic moduli of magnetic elastomers: from X- $\mu$ CT characterization to mesoscopic modeling

Reproduced from

Giorgio Pessot, Malte Schümann, Thomas Gundermann, Stefan Odenbach,  
Hartmut Löwen, and Andreas M. Menzel.

Tunable dynamic moduli of magnetic elastomers:  
from X- $\mu$ CT characterization to mesoscopic modeling  
*arXiv:1711.04165 [cond-mat.soft] (Submitted to Smart Mater. Struct.).*

Because of copyright reasons, the full manuscript cannot be reproduced here. The full version of this manuscript can be found under the link <https://arxiv.org/abs/1711.04165>.

## Authors' Contributions

All authors contributed to the writing of the manuscript. Malte Schümann, Thomas Gundermann, and Stefan Odenbach performed the experiments and provided the three-dimensional input data for our particle-resolved model. Hartmut Löwen and Andreas M. Menzel supervised the modeling. I performed the numerical calculations based on the dipole-spring model. I estimate my total contribution to this work to approximately 75%.

## Copyright and Permission Informations

ArXiv is granted from the authors a non-exclusive license to distribute this article. ArXiv does not claim exclusive right to the article. See <https://arxiv.org/help/license> and <https://arxiv.org/licenses/nonexclusive-distrib/1.0/license.html>.



### 3 Conclusions

Ferrogels and magnetic elastomers are composite materials that stand out for their ability of reversibly changing shape and stiffness under the action of an external magnetic field. One way to obtain such materials is to crosslink a polymeric solution in which magnetic particles have been dispersed. The magnetic particles are then trapped in or attached to the polymer network [36, 102, 103]. Under the effect of a magnetic field, they apply forces and torques onto each other, which are counterbalanced by the embedding elastic matrix.

The magnetic interactions lead directly to relative displacements of the particles, which, in turn, cause overall deformations [40–43, 104] as well as changes in the stiffness [10, 11, 44–50] of the material. This effect is often referred to as “magneto-mechanical” coupling [36–38]. The central, appealing feature of such a coupling is that strain and elastic moduli are reversibly tunable by external magnetic fields in a non-invasive way. In the present thesis we have outlined a path to model magnetoelastic materials starting from the microscopic description of polymer chains, moving to particle-resolved mesoscopic models, and heading towards a final scale-bridging goal to calculate the macroscopic properties such as strain and elastic moduli.

First, the entropic origin of elasticity is extracted from via molecular dynamics simulations [75], see Paper I. In a first, simplified model, the polymer-mediated interactions between two magnetic particles are investigated by simulating two particles connected by a chain of linked beads, each representing a coarse-grained piece of the polymer. By collecting statistics of the motion of the polymer chain, one can coarse-grain it into an entropic potential between the two magnetic particles. From this procedure we obtain an effective interaction as a function of interparticle separation and relative angles of the particle orientations. Some of these degrees of freedom are strongly correlated with each other, resulting, for instance, in a characteristic “wrapping effect” [117].

Simulation-derived potentials represent the foundation to build models involving more than two magnetic particles. As a first step in increasing complexity, we have investigated the exemplary case of one-dimensional chains of paramagnetic particles embedded in a soft elastic matrix and buckling under a perpendicular external magnetic field [12], see Paper II. The problem is reduced to two dimensions because the plane containing the buckling deformation is entirely determined by the initial chain orientation together with the direction of the external field. We transfer the description of the particle chain to a continuum representation and describe its deflection in terms of a smooth polynomial function. The interaction with the surrounding polymer matrix is phenomenologically modeled by energetic terms opposing bending and displacements. Then, following a variational approach and in agreement with experimental investigations, we find that longer chains buckle with more oscillations. This is a straight consequence of the energetic competition between magnetic and elastic effects. The former favor alignment along the field direction and the latter tend to restore the initial straight profile of the chain. The good agreement between the modeled and observed buckling morphologies evidences the strong coupling between the embedded particles and the matrix.

The next level in increasing complexity consists of two dimensional arrangements of magnetic particles [90], see Paper III. We adopt a basic dipole–spring model: each particle carries a magnetic dipole and is connected to its neighbors via harmonic springs, mimicking the surrounding elastic medium. The principal advantage of this description is to combine the particle-resolved, explicit description of the distribution of magnetic inclusions with computational efficiency. Furthermore, the dipoles are set parallel to each other, a situation representative of paramagnetic particles in a saturating external field or ferromagnetic ones under a strong aligning field. We look at deformations and changes in the elastic moduli for regular as well as non-regular particle arrangements and different orientations of the overall magnetization. As a result, we prove that the positioning of the nearest neighbors with respect to the direction of the magnetization is critical in determining whether the system elongates or contracts, stiffens or softens with increasing magnetic interactions. Moreover, the implications of assuming affine deformations of the system are investigated. In an indefinitely extended system, affine and non-affine deformations are equivalent for regular lattices, as demonstrated in section 1.7. However, in finite or less regular arrangements assuming affine deformations can lead to growing quantitative and even qualitative errors.

For most possible applications, e.g., tunable vibration absorbers or soft actuators, it is crucial to investigate the time dependent material properties. The key quantities are the dynamic elastic moduli. They provide the relation between periodic stresses and strains for a given oscillation frequency. The time relaxation of magnetic elastomers had been investigated in Ref. 105, where the normal modes of the system and their spectrum were described for varying strength of the magnetic interactions. In the last two papers presented in this thesis the description in terms of normal modes is connected with the linear response of the system and the dynamic moduli are calculated.

For this purpose, we consider three-dimensional dipole–spring arrangements. The decomposition into normal modes allows us to calculate the linear response of the system under axial or shear deformations [123], see Paper IV. By construction of appropriate mesoscopic force fields we calculate the Young and shear elastic moduli for various particle distributions and strengths of the magnetic interactions. The comparison with the analytical moduli calculated for regular lattices confirms the correctness of our normal-modes approach. After that, we assume an overdamped, linearized type of motion and extend our method to compute the frequency-dependent moduli in the case of an oscillating external stress. As the frequency of the mechanical stress increases, the response of the system changes over different combinations of modes. The dynamic moduli vary as well, reflecting the different responses, and can increase or decrease when switching on magnetic interactions between the particles, depending on the particle distribution. In the case of regular distributions and especially at low frequencies, the behavior of the moduli follow in good agreement the qualitative arguments of Paper III. Quantitative calculations are presented in Paper IV. In the case of strong magnetic interactions, the formation of chain-like structures, stabilized by steric repulsion, is followed by large increases in the elastic moduli, which has also been observed experimentally [10].

---

In our final Paper V we use experimental data as input for the positions and volumes of our magnetic particles [122]. The final goal of the scale-bridging description is to calculate macroscopic properties of real systems depending on their mesoscopic properties and particle arrangement. We particularly focus on a homogeneous, isotropic particle distribution of magnetic particles with volume fraction 5.6%. Initially, the system elongates to a small degree in the direction of magnetization [98, 119]. However, for larger amounts of magnetization, the dipole–dipole attraction prevails making the particles enter into steric contact and form extensive chain-like aggregates parallel to the magnetic field [8, 10, 124–126]. This aggregation mechanism results in a significant overall contraction in the field-direction [120, 121]. Furthermore, at low to moderate magnetization, the elastic moduli can show a slight amount of decrease. However, when magnetic interactions are as strong as to form chain-like aggregates, the investigated Young and shear moduli strongly increase, in qualitative agreement with experimental observations [10, 11, 46]. Interestingly, the dynamic moduli can present unexpected, non-monotonous behaviors. For instance, increasing magnetic interactions can strengthen a storage shear modulus at low-frequencies, whereas at intermediate frequencies it is reduced.

In conclusion, improving the existing models of ferrogels and magnetic elastomers can help us to develop materials with optimized, customized properties. In this thesis we have outlined a scale-bridging route. Simulations resolving the polymer chains set the foundations of pair elastic potentials which, in turn, can later be incorporated into mesoscopic many-body systems to calculate overall macroscopic properties. With the aim of optimizing the material response, mesoscopic particle-resolved models are irreplaceable because they can explicitly take into account the impact of different particle arrangements. For this purpose, extending in the future the combined effort with particle-resolved experiments [8, 10] will allow us to test different particle arrangements and shed further light onto the properties of the magnetomechanical coupling. With the final goal of devising components featuring dynamic properties optimized down to the microscopic scale, our investigations can provide insight from multiple viewpoints into the behavior of these fascinating materials.



# Acknowledgments and Thanks

First and foremost, my deep gratitude goes to Prof. Dr. Hartmut Löwen for giving me the opportunity to study and do my Ph.D. in Düsseldorf. His help and encouragement have made the route to this point much easier.

Working at the *Institut für Theoretische Physik II* has been a maturing experience also thanks to all the present and past members I had the honor and pleasure to interact with. In particular, I would like to expressly thank Joachim Wenk, Jörg Bartnick, Peet Cremer, and Mate Puljiz for all the helpful, stimulating discussions about physics and many more topics.

Many of the published articles are the result of cooperation with researchers from outside our institute, whom I kindly thank. A shoutout goes to Rudolf Weeber and Shilin Huang, who put a great effort and passion in their work.

I must acknowledge with special emphasis the huge support of Priv.-Doz. Dr. Andreas M. Menzel, whose competence as a supervisor is matched only by his kindness. I owe him much for pointing out my mistakes, many brilliant ideas, and a vast amount of hours spent proofreading.

A heartfelt and much deserved thank goes to to my parents Laura and Ferdinando for all the support, love, and for raising me as a tolerable human being. Finally, I am profoundly grateful to my beloved Mariana for enduring me everyday, her support in the small and big things, and all the chocolate she gifted me.



# Bibliography

- [1] A. Ivlev, H. Löwen, G. Morfill, and C. P. Royall. *Complex Plasmas and Colloidal Dispersions*. World Scientific, 2012.
- [2] A. M. Menzel. Tuned, driven, and active soft matter. *Phys. Rep.*, 554:1, 2015.
- [3] G. Strobl. *The Physics of Polymers*. Springer Berlin / Heidelberg, 2007.
- [4] Material selection and processing [<http://www-materials.eng.cam.ac.uk/mpsite/>] (Last updated: 25/02/2002).
- [5] E. D. Keoke and K. M. Porterfield. *Encyclopedia of American Indian Contributions to the World: 15,000 Years of Inventions and Innovations*. Checkmark Books, 2002.
- [6] P.-G. De Gennes and J. Badoz. *Fragile Objects: Soft Matter, Hard Science, and the Thrill of Discovery*. Springer Science & Business Media, 2012.
- [7] M. L. Selker, G. G. Winspear, and A. R. Kemp. Brittle point of rubber upon freezing. *Ind. Eng. Chem.*, 34:157, 1942.
- [8] T. Gundermann, P. Cremer, H. Löwen, A. M. Menzel, and S. Odenbach. Statistical analysis of magnetically soft particles in magnetorheological elastomers. *Smart Mater. Struct.*, 26:045012, 2017.
- [9] E. I. Wisotzki, M. Hennes, C. Schuldt, F. Engert, W. Knolle, U. Decker, J. A. Kas, M. Zink, and S. G. Mayr. Tailoring the material properties of gelatin hydrogels by high energy electron irradiation. *J. Mater. Chem. B*, 2:4297, 2014.
- [10] M. Schümann and S. Odenbach. In-situ observation of the particle microstructure of magnetorheological elastomers in presence of mechanical strain and magnetic fields. *J. Magn. Magn. Mater.*, 441:88, 2017.
- [11] Z. Varga, G. Filipcsei, and M. Zrínyi. Magnetic field sensitive functional elastomers with tuneable elastic modulus. *Polymer*, 47:227, 2006.
- [12] S. Huang, G. Pessot, P. Cremer, R. Weeber, C. Holm, J. Nowak, S. Odenbach, A. M. Menzel, and G. K. Auernhammer. Buckling of paramagnetic chains in soft gels. *Soft Matter*, 12:228, 2016.
- [13] M. D. Frogley, D. Ravich, and H. D. Wagner. Mechanical properties of carbon nanoparticle-reinforced elastomers. *Compos. Sci. Technol.*, 63:1647, 2003.
- [14] A. Kumar, A. Srivastava, I. Y. Galaev, and B. Mattiasson. Smart polymers: Physical forms and bioengineering applications. *Prog. Polym. Sci.*, 32:1205, 2007.

- [15] I. A. Anderson, T. A. Gisby, T. G. McKay, B. M. O'Brien, and E. P. Calius. Multi-functional dielectric elastomer artificial muscles for soft and smart machines. *J. Appl. Phys.*, 112:041101, 2012.
- [16] E. Allahyarov, H. Löwen, and L. Zhu. A simulation study of the electrostriction effects in dielectric elastomer composites containing polarizable inclusions with different spatial distributions. *Phys. Chem. Chem. Phys.*, 17:32479, 2015.
- [17] E. Allahyarov, H. Löwen, and L. Zhu. Dipole correlation effects on the local field and the effective dielectric constant in composite dielectrics containing high- $\kappa$  inclusions. *Phys. Chem. Chem. Phys.*, 18:19103, 2016.
- [18] L. Tian, L. Tevet-Deree, G. deBotton, and K. Bhattacharya. Dielectric elastomer composites. *J. Mech. Phys. Solids*, 60:181, 2012.
- [19] J. A. Rogers. A clear advance in soft actuators. *Science*, 341:968, 2013.
- [20] T. G. McKay, B. M. O'Brien, E. P. Calius, and I. A. Anderson. Soft generators using dielectric elastomers. *App. Phys. Lett.*, 98:142903, 2011.
- [21] S. Odenbach. Ferrofluids—magnetically controlled suspensions. *Colloids Surf., A*, 217:171, 2003.
- [22] B. Huke and M. Lücke. Magnetic properties of colloidal suspensions of interacting magnetic particles. *Rep. Prog. Phys.*, 67:1731, 2004.
- [23] C. Holm and J.-J. Weis. The structure of ferrofluids: A status report. *Curr. Opin. Colloid Interface Sci.*, 10:133, 2005.
- [24] J. P. Embs, S. May, C. Wagner, A. V. Kityk, A. Leschhorn, and M. Lücke. Measuring the transverse magnetization of rotating ferrofluids. *Phys. Rev. E*, 73:036302, 2006.
- [25] P. Ilg, M. Kröger, and S. Hess. Structure and rheology of model-ferrofluids under shear flow. *J. Magn. Magn. Mater.*, 289:325, 2005.
- [26] P. Ilg, E. Coquelle, and S. Hess. Structure and rheology of ferrofluids: simulation results and kinetic models. *J. Phys.: Condens. Matter*, 18:S2757, 2006.
- [27] P. J. Camp. The effects of magnetic fields on the properties of ferrofluids and ferrogels. *Magnetohydrodyn.*, 47:123, 2011.
- [28] T. I. Volkova, V. Böhm, V. A. Naletova, T. Kaufhold, F. Becker, I. Zeidis, and K. Zimmermann. A ferrofluid based artificial tactile sensor with magnetic field control. *J. Magn. Magn. Mater.*, 431:277, 2017.

- 
- [29] R. L. Bailey. Lesser known applications of ferrofluids. *J. Magn. Magn. Mater.*, 39:178, 1983.
- [30] G. Filipcsei, I. Csetneki, A. Szilágyi, and M. Zrínyi. Magnetic field-responsive smart polymer composites. *Adv. Polym. Sci.*, 206:137, 2007.
- [31] M. T. Lopez-Lopez, J. D. G. Durán, L. Y. Iskakova, and A. Y. Zubarev. Mechanics of magnetopolymer composites: a review. *J. Nanofluids*, 5:479, 2016.
- [32] S. Odenbach. Microstructure and rheology of magnetic hybrid materials. *Arch. Appl. Mech.*, 86:269, 2016.
- [33] M. A. Cantera, M. Behrooz, R. F. Gibson, and F. Gordaninejad. Modeling of magneto-mechanical response of magnetorheological elastomers (MRE) and MRE-based systems: a review. *Smart Mater. Struct.*, 26:023001, 2017.
- [34] J. Embs, H. W. Müller, C. Wagner, K. Knorr, and M. Lücke. Measuring the rotational viscosity of ferrofluids without shear flow. *Phys. Rev. E*, 61:R2196, 2000.
- [35] L. M. Pop and S. Odenbach. Investigation of the microscopic reason for the magnetoviscous effect in ferrofluids studied by small angle neutron scattering. *J. Phys.: Condens. Matter*, 18:S2785, 2006.
- [36] N. Frickel, R. Messing, and A. M. Schmidt. Magneto-mechanical coupling in CoFe<sub>2</sub>O<sub>4</sub>-linked PAAm ferrohydrogels. *J. Mater. Chem.*, 21:8466, 2011.
- [37] M. Kästner, S. Müller, J. Goldmann, C. Spieler, J. Brummund, and V. Ulbricht. Higher-order extended FEM for weak discontinuities – level set representation, quadrature and application to magneto-mechanical problems. *Int. J. Numer. Meth. Eng.*, 93:1403, 2013.
- [38] E. Allahyarov, A. M. Menzel, L. Zhu, and H. Löwen. Magnetomechanical response of bilayered magnetic elastomers. *Smart Mater. Struct.*, 23:115004, 2014.
- [39] O. V. Stolbov, Y. L. Raikher, and M. Balasoiu. Modelling of magnetodipolar striction in soft magnetic elastomers. *Soft Matter*, 7:8484, 2011.
- [40] M. Zrínyi, L. Barsi, and A. Büki. Ferrogel: a new magneto-controlled elastic medium. *Polym. Gels Netw.*, 5:415, 1997.
- [41] X. Guan, X. Dong, and J. Ou. Magnetostrictive effect of magnetorheological elastomer. *J. Magn. Magn. Mater.*, 320:158, 2008.
- [42] X. Gong, G. Liao, and S. Xuan. Full-field deformation of magnetorheological elastomer under uniform magnetic field. *Appl. Phys. Lett.*, 100:211909, 2012.

- [43] Z. Varga, G. Filipcsei, A. Szilágyi, and M. Zrínyi. Electric and magnetic field-structured smart composites. *Macromol. Symp.*, 227:123, 2005.
- [44] M. R. Jolly, J. D. Carlson, B. C. Muñoz, and T. A. Bullions. The magnetoviscoelastic response of elastomer composites consisting of ferrous particles embedded in a polymer matrix. *J. Intell. Mater. Syst. Struct.*, 7:613, 1996.
- [45] G. V. Stepanov, S. S. Abramchuk, D. A. Grishin, L. V. Nikitin, E. Y. Kramarenko, and A. R. Khokhlov. Effect of a homogeneous magnetic field on the viscoelastic behavior of magnetic elastomers. *Polymer*, 48:488, 2007.
- [46] M. Kallio, T. Lindroos, S. Aalto, E. Järvinen, T. Kärnä, and T. Meinander. Dynamic compression testing of a tunable spring element consisting of a magnetorheological elastomer. *Smart Mater. Struct.*, 16:506, 2007.
- [47] H. Böse and R. Röder. Magnetorheological elastomers with high variability of their mechanical properties. *J. Phys.: Conf. Ser.*, 149:012090, 2009.
- [48] B. A. Evans, B. L. Fiser, W. J. Prins, D. J. Rapp, A. R. Shields, D. R. Glass, and R. Superfine. A highly tunable silicone-based magnetic elastomer with nanoscale homogeneity. *J. Magn. Magn. Mater.*, 324:501, 2012.
- [49] D. Y. Borin, G. V. Stepanov, and S. Odenbach. Tuning the tensile modulus of magnetorheological elastomers with magnetically hard powder. *J. Phys.: Conf. Ser.*, 412:012040, 2013.
- [50] G. Schubert and P. Harrison. Equi-biaxial tension tests on magneto-rheological elastomers. *Smart Mater. Struct.*, 25:015015, 2016.
- [51] T. I. Volkova, V. Böhm, T. Kaufhold, J. Popp, F. Becker, D. Y. Borin, G. V. Stepanov, and K. Zimmermann. Motion behaviour of magneto-sensitive elastomers controlled by an external magnetic field for sensor applications. *J. Magn. Magn. Mater.*, 431:262, 2017.
- [52] Y. Wang, S. Xuan, B. Dong, F. Xu, and X. Gong. Stimuli dependent impedance of conductive magnetorheological elastomers. *Smart Mater. Struct.*, 25:025003, 2016.
- [53] J. D. Jackson. *Classical Electrodynamics*, volume 3. Wiley New York, 1962.
- [54] T. Gundermann, S. Günther, D. Borin, and S. Odenbach. A comparison between micro-and macro-structure of magnetoactive composites. *J. Phys.: Conf. Ser.*, 412:012027, 2013.
- [55] T. Gundermann and S. Odenbach. Investigation of the motion of particles in magnetorheological elastomers by X- $\mu$ CT. *Smart Mater. Struct.*, 23:105013, 2014.

- 
- [56] D. Günther, D. Y. Borin, S. Günther, and S. Odenbach. X-ray micro-tomographic characterization of field-structured magnetorheological elastomers. *Smart Mater. Struct.*, 21:015005, 2012.
- [57] S. R. Gorodkin, R. O. James, and W. I. Kordonski. Magnetic properties of carbonyl iron particles in magnetorheological fluids. *J. Phys.: Conf. Ser.*, 149:012051, 2009.
- [58] J. De Vicente, G. Bossis, S. Lacis, and M. Guyot. Permeability measurements in cobalt ferrite and carbonyl iron powders and suspensions. *J. Magn. Magn. Mater.*, 251:100, 2002.
- [59] See Supplemental Material at [<https://pdfs.semanticscholar.org/15b4/068cdeee613acd1849c71cfe87933164877a.pdf>] for a complete listing.
- [60] A. Shankar, A. P. Safronov, E. A. Mikhnevich, I. V. Beketov, and G. V. Kurlyandskaya. Ferrogels based on entrapped metallic iron nanoparticles in a polyacrylamide network: extended Derjaguin-Landau-Verwey-Overbeek consideration, interfacial interactions and magnetodeformation. *Soft Matter*, 13:3359, 2017.
- [61] Z. Varga, G. Filipcsei, and M. Zrínyi. Smart composites with controlled anisotropy. *Polymer*, 46:7779, 2005.
- [62] J. I. Gittleman, B. Abeles, and S. Bozowski. Superparamagnetism and relaxation effects in granular Ni-SiO<sub>2</sub> and Ni-Al<sub>2</sub>O<sub>3</sub> films. *Phys. Rev. B*, 9:3891, 1974.
- [63] J.-F. Berret, O. Sandre, and A. Mauger. Size distribution of superparamagnetic particles determined by magnetic sedimentation. *Langmuir*, 23:2993, 2007.
- [64] L. Schäfer. *Excluded volume effects in polymer solutions: as explained by the renormalization group*. Springer Science & Business Media, 2012.
- [65] A. Gut. *An Intermediate Course in Probability*. Springer Science & Business Media, 2009.
- [66] R. Weeber, S. Kantorovich, and C. Holm. Ferrogels cross-linked by magnetic nanoparticles – Deformation mechanisms in two and three dimensions studied by means of computer simulations. *J. Magn. Magn. Mater.*, 383:262, 2015.
- [67] R. Weeber, S. Kantorovich, and C. Holm. Ferrogels cross-linked by magnetic particles: Field-driven deformation and elasticity studied using computer simulations. *J. Chem. Phys.*, 143:154901, 2015.
- [68] M. Born and V. Fock. Beweis des Adiabatenatzes. *Z. Phys.*, 51:165, 1928.

- [69] J.-P. Hansen and H. Löwen. Effective interactions for large-scale simulations of complex fluids. In P. Nielaba, M. Mareschal, and G. Ciccotti, editors, *Bridging Time Scales: Molecular Simulations for the Next Decade*, volume 605 of *Lecture Notes in Physics*, page 167 ff. Springer Berlin / Heidelberg, 2002.
- [70] V. A. Harmandaris, D. Reith, N. F. A. Van der Vegt, and K. Kremer. Comparison between coarse-graining models for polymer systems: Two mapping schemes for polystyrene. *Macromol. Chem. Phys.*, 208:2109, 2007.
- [71] J. D. Weeks, D. Chandler, and H. C. Andersen. Role of repulsive forces in determining the equilibrium structure of simple liquids. *J. Chem. Phys.*, 54:5237, 1971.
- [72] H. R. Warner. Kinetic theory and rheology of dilute suspensions of finitely extendible dumbbells. *Ind. Eng. Chem. Fundam.*, 11:379, 1972.
- [73] P. A. Sánchez, J. J. Cerdà, T. Sintès, and C. Holm. Effects of the dipolar interaction on the equilibrium morphologies of a single supramolecular magnetic filament in bulk. *J. Chem. Phys.*, 139:044904, 2013.
- [74] M. A. Annunziata, A. M. Menzel, and H. Löwen. Hardening transition in a one-dimensional model for ferrogels. *J. Chem. Phys.*, 138:204906, 2013.
- [75] G. Pessot, R. Weeber, C. Holm, H. Löwen, and A. M. Menzel. Towards a scale-bridging description of ferrogels and magnetic elastomers. *J. Phys.: Condens. Matter*, 27:325105, 2015.
- [76] T. Borbáth, S. Günther, D. Y. Borin, T. Gundermann, and S. Odenbach. X- $\mu$ CT analysis of magnetic field-induced phase transitions in magnetorheological elastomers. *Smart Mater. Struct.*, 21:105018, 2012.
- [77] M. Schümann, D. Y. Borin, S. Huang, G. K. Auernhammer, R. Müller, and S. Odenbach. A characterization of the magnetically induced movement of NdFeB-particles in magnetorheological elastomers. *Smart Mater. Struct.*, 26:095018, 2017.
- [78] M. Puljiz, M. Orlishausen, W. Köhler, and A. M. Menzel. Thermophoretically induced large-scale deformations around microscopic heat centers. *J. Chem. Phys.*, 144:184903, 2016.
- [79] M. Puljiz, S. Huang, G. K. Auernhammer, and A. M. Menzel. Forces on rigid inclusions in elastic media and resulting matrix-mediated interactions. *Phys. Rev. Lett.*, 117:238003, 2016.
- [80] M. Puljiz and A. M. Menzel. Forces and torques on rigid inclusions in an elastic environment: Resulting matrix-mediated interactions, displacements, and rotations. *Phys. Rev. E*, 95:053002, 2017.

- 
- [81] A. M. Menzel. Force-induced elastic matrix-mediated interactions in the presence of a rigid wall. *Soft Matter*, 13:3373, 2017.
- [82] L. D. Landau and E. M. Lifshitz. *Elasticity Theory*. Pergamon Press, 1975.
- [83] Z. Varga, J. Fehér, G. Filipcsei, and M. Zrínyi. Smart nanocomposite polymer gels. *Macromol. Symp.*, 200:93, 2003.
- [84] F. Mainardi and G. Spada. Creep, relaxation and viscosity properties for basic fractional models in rheology. *Eur. Phys. J., Spec. Top.*, 193:133, 2011.
- [85] J. J. Zanna, P. Stein, J. D. Marty, M. Mauzac, and P. Martinoty. Influence of molecular parameters on the elastic and viscoelastic properties of side-chain liquid crystalline elastomers. *Macromolecules*, 35:5459, 2002.
- [86] D. Collin, G. K. Auernhammer, O. Gavot, P. Martinoty, and H. R. Brand. Frozen-in magnetic order in uniaxial magnetic gels: preparation and physical properties. *Macromol. Rapid Commun.*, 24:737, 2003.
- [87] M. Roth, M. D’Acunzi, D. Vollmer, and G. K. Auernhammer. Viscoelastic rheology of colloid-liquid crystal composites. *J. Chem. Phys.*, 132:124702, 2010.
- [88] D. R. Squire, A. C. Holt, and W. G. Hoover. Isothermal elastic constants for argon. Theory and Monte Carlo calculations. *Physica*, 42:388, 1969.
- [89] D. Ivaneyko, V. Toshchevikov, and M. Saphiannikova. Dynamic moduli of magneto-sensitive elastomers: a coarse-grained network model. *Soft Matter*, 11:7627, 2015.
- [90] G. Pessot, P. Cremer, D. Y. Borin, S. Odenbach, H. Löwen, and A. M. Menzel. Structural control of elastic moduli in ferrogels and the importance of non-affine deformations. *J. Chem. Phys.*, 141:124904, 2014.
- [91] H. R. Brand, P. Martinoty, and H. Pleiner. Physical properties of magnetic gels. In *Cross-linked Liquid Crystalline Systems: from Rigid Polymer Networks to Elastomers*, page 529 ff. CRC Press, 2011.
- [92] M. Doi and S. F. Edwards. *The Theory of Polymer Dynamics*. Oxford University Press, 1988.
- [93] K. Zimmermann, V. A. Naletova, I. Zeidis, V. Böhm, and E. Kolev. Modelling of locomotion systems using deformable magnetizable media. *J. Phys.: Condens. Matter*, 18:S2973, 2006.
- [94] M. M. Schmauch, S. R. Mishra, B. A. Evans, O. D. Velev, and J. B. Tracy. Chained iron microparticles for directionally controlled actuation of soft robots. *ACS Appl. Mater. Interfaces*, 9:11895, 2017.

- [95] H.-X. Deng, X.-L. Gong, and L.-H. Wang. Development of an adaptive tuned vibration absorber with magnetorheological elastomer. *Smart Mater. Struct.*, 15:N111, 2006.
- [96] T. L. Sun, X. L. Gong, W. Q. Jiang, J. F. Li, Z. B. Xu, and W. H. Li. Study on the damping properties of magnetorheological elastomers based on cis-polybutadiene rubber. *Polym. Test.*, 27:520, 2008.
- [97] S. Abramchuk, E. Kramarenko, D. Grishin, G. Stepanov, L. V. Nikitin, G. Filipcsei, A. R. Khokhlov, and M. Zrínyi. Novel highly elastic magnetic materials for dampers and seals: part II. material behavior in a magnetic field. *Polymer. Adv. Tech.*, 18:513, 2007.
- [98] D. Szabó, G. Szeghy, and M. Zrínyi. Shape transition of magnetic field sensitive polymer gels. *Macromolecules*, 31:6541, 1998.
- [99] R. V. Ramanujan and L. L. Lao. The mechanical behavior of smart magnet-hydrogel composites. *Smart Mater. Struct.*, 15:952, 2006.
- [100] M. Sedlacik, M. Mrlik, V. Babayan, and V. Pavlinek. Magnetorheological elastomers with efficient electromagnetic shielding. *Compos. Struct.*, 135:199, 2016.
- [101] T. I. Becker, K. Zimmermann, D. Y. Borin, G. V. Stepanov, and P. A. Storozhenko. Dynamic response of a sensor element made of magnetic hybrid elastomer with controllable properties. *J. Magn. Magn. Mater.*, 2017.
- [102] R. K. Bose, N. Hohlbein, S. J. Garcia, A. M. Schmidt, and S. van der Zwaag. Relationship between the network dynamics, supramolecular relaxation time and healing kinetics of cobalt poly(butyl acrylate) ionomers. *Polymer*, 69:228, 2015.
- [103] J. Landers, L. Roeder, S. Salamon, A. M. Schmidt, and H. Wende. Particle–matrix interaction in cross-linked PAAm-hydrogels analyzed by Mössbauer spectroscopy. *J. Phys. Chem. C*, 119:20642, 2015.
- [104] M. Zrínyi, L. Barsi, and A. Büki. Deformation of ferrogels induced by nonuniform magnetic fields. *J. Chem. Phys.*, 104:8750, 1996.
- [105] M. Tarama, P. Cremer, D. Y. Borin, S. Odenbach, H. Löwen, and A. M. Menzel. Tunable dynamic response of magnetic gels: Impact of structural properties and magnetic fields. *Phys. Rev. E*, 90:042311, 2014.
- [106] P. Cremer, H. Löwen, and A. M. Menzel. Tailoring superelasticity of soft magnetic materials. *Appl. Phys. Lett.*, 107:171903, 2015.

- 
- [107] P. Cremer, H. Löwen, and A. M. Menzel. Superelastic stress–strain behavior in ferrogels with different types of magneto-elastic coupling. *Phys. Chem. Chem. Phys.*, page 26670, 2016.
- [108] E. Jarkova, H. Pleiner, H.-W. Müller, and H. R. Brand. Hydrodynamics of isotropic ferrogels. *Phys. Rev. E*, 68:041706, 2003.
- [109] S. Bohlius, H. R. Brand, and H. Pleiner. Macroscopic dynamics of uniaxial magnetic gels. *Phys. Rev. E*, 70:061411, 2004.
- [110] K. Morozov, M. Shliomis, and H. Yamaguchi. Magnetic deformation of ferrogel bodies: Procrustes effect. *Phys. Rev. E*, 79:040801, 2009.
- [111] A. M. Menzel. Bridging from particle to macroscopic scales in uniaxial magnetic gels. *J. Chem. Phys.*, 141:194907, 2014.
- [112] Y. Han, W. Hong, and L. E. Faidley. Field-stiffening effect of magneto-rheological elastomers. *Int. J. Solids Struct.*, 50:2281, 2013.
- [113] P. Metsch, K. A. Kalina, C. Spieler, and M. Kästner. A numerical study on magnetostrictive phenomena in magnetorheological elastomers. *Comput. Mater. Sci.*, 124:364, 2016.
- [114] D. Romeis, P. Metsch, M. Kästner, and M. Saphiannikova. Theoretical models for magneto-sensitive elastomers: A comparison between continuum and dipole approaches. *Phys. Rev. E*, 95:042501, 2017.
- [115] K. A. Kalina, J. Brummund, P. Metsch, M. Kästner, D. Y. Borin, J. M. Linke, and S. Odenbach. Modeling of magnetic hystereses in soft MREs filled with NdFeB particles. *Smart Mater. Struct.*, 26:105019, 2017.
- [116] D. Ivaneyko, V. P. Toshchevikov, M. Saphiannikova, and G. Heinrich. Magneto-sensitive elastomers in a homogeneous magnetic field: a regular rectangular lattice model. *Macromol. Theor. Simul.*, 20:411, 2011.
- [117] R. Weeber, S. Kantorovich, and C. Holm. Deformation mechanisms in 2D magnetic gels studied by computer simulations. *Soft Matter*, 8:9923, 2012.
- [118] M. Zrínyi, L. Barsi, D. Szabó, and H.-G. Kilian. Direct observation of abrupt shape transition in ferrogels induced by nonuniform magnetic field. *J. Chem. Phys.*, 106:5685, 1997.
- [119] G. Diguët, E. Beaugnon, and J. Y. Cavallé. Shape effect in the magnetostriction of ferromagnetic composite. *J. Magn. Magn. Mater.*, 322:3337, 2010.

- [120] G. Y. Zhou and Z. Y. Jiang. Deformation in magnetorheological elastomer and elastomer–ferromagnet composite driven by a magnetic field. *Smart Mater. Struct.*, 13:309, 2004.
- [121] E. Coquelle and G. Bossis. Magnetostriction and piezoresistivity in elastomers filled with magnetic particles. *J. Adv. Sci.*, 17:132, 2005.
- [122] G. Pessot, M. Schümann, T. Gundermann, S. Odenbach, H. Löwen, and A. M. Menzel. Tunable dynamic moduli of magnetic elastomers: From X- $\mu$ CT characterization to mesoscopic modeling. *arXiv:1711.04165 [cond-mat.soft]* (Submitted to *Smart Mater. Struct.*), 2017.
- [123] G. Pessot, H. Löwen, and A. M. Menzel. Dynamic elastic moduli in magnetic gels: Normal modes and linear response. *J. Chem. Phys.*, 145:104904, 2016.
- [124] A. Y. Zubarev, D. N. Chirikov, D. Y. Borin, and G. V. Stepanov. Hysteresis of the magnetic properties of soft magnetic gels. *Soft Matter*, 12:6473, 2016.
- [125] S. D. Peroukidis and S. H. L. Klapp. Spontaneous ordering of magnetic particles in liquid crystals: From chains to biaxial lamellae. *Phys. Rev. E*, 92:010501, 2015.
- [126] S. D. Peroukidis, K. Lichtner, and S. H. L. Klapp. Tunable structures of mixtures of magnetic particles in liquid-crystalline matrices. *Soft Matter*, 11:5999, 2015.